THE AGE OF THE MILKY WAY GALAXY FROM WHITE DWARF CHRONOMETRY

APPROVED BY
DISSERTATION COMMITTEE:

R. Edward Nather, Supervisor

Donald E. Winget

Edward L. Robinson

William H. Jefferys

Jim Liebert

Copyright

by

Charles F. Claver, B.A.

1995

Dedication

To my family; Jack, Paulette, and Jeanne

in memory of

Chet, Harlan, Maria, and Steve.

THE AGE OF THE MILKY WAY GALAXY FROM WHITE DWARF CHRONOMETRY

by

CHARLES FREDERICK CLAVER, B.A.

DISSERTATION

Presented to the Faculty of the Graduate School of

The University of Texas at Austin

in Partial Fulfillment

of the Requirements

for the Degree of

DOCTOR OF PHILOSOPHY

THE UNIVERSITY OF TEXAS AT AUSTIN

May, 1994

Acknowledgements

When I left California to come to Texas I knew I wanted to pursue astronomy, but I had no idea I was taking the first step to the most chalenging and interesting phase of my life to date. The first astronomer I met was Ed Nather. I described to him my telescope making hobby and interests and by the time we were through, without ever having seen me before, Ed gave me a place in his lab to continue my work. From this moment on Ed became my mentor. Ed always gave me a great deal of freedom, but also seemed to know when it was necessary to step in and help, discipline, or correct me. I cannot express enough how grateful I am to Ed for allowing me to do what I love most – astronomy. Thank you Ed, for your faith in me, and for giving me the opportunity and guidance that helped me fulfill a lifelong dream.

Equally inspiring to me was Don Winget. I first met Don at McDonald Observatory while I was working on my senior thesis project in 1986. I asked Don what he did. He proceeded to give me very excitedly a synopsis of the white dwarf field. I asked him what was the most important problem in the study of white dwarfs. Don replied "numbers". With that simple response, Don is directly responsible for igniting the fire of curiosity in me which led to my total commitment to professional astronomy. Without Don's continued support and

help to keep this fire alive I would never had made it through graduate school. Thank you, Don.

The "Lab" environment that Ed and Don cultivate is second to none. It may seem hopelessly chaotic at times, but in reality it is vibrantly alive with science, philosophy, and life. Of the truly unique friends and collaborations to emerge from this environment are truly unique I have been blessed by many. In particular, I am grateful to have met my professional "big brother", Matt Wood and through him his wife Clara. Matt is someone I admire, looked up to, and can always rely on for straight answers. Other good friends from the lab include Butler Hine, Chris Clemens, Scot Kleinman, Judi Provecal, Paul Bradley, Atsuko Nitta, Mike Montgomery, Usama Aziz, and Todd Watson.

I could not have asked for a better family than the one I have. All throughout my life they have supported my interests, encouraged me to learn new things, and have always been willing to help in anyway they could. Most parents would not have driven their son 60 miles every Friday night for 5 years (until I learned to drive) to the Telescope Makers Workshop at Chabot Observatory so that I could rub two pieces of glass together with sand in between. Thank you Mom and Dad for your love, patience, understanding, and most of all for your confidence and trust in me. Jeanne, my sister, you are one of my best friends. Our many conversations have been and continue to be a very important part of my life. Thanks for listening.

I am also blessed with another family, my chosen one, who have been equally supportive in ways parents and siblings cannot. These are the people I grew up with, and are collectively known as "The Newton Way Gang" – after the street we lived on. Over the years this chosen family has grown as we each meet new people and include them in our lives. Even though we are spread accross the country, the love that is shared among us only continues to strengthen. So to you: Mike Cadigan, Terry and Lynne Shapliegh, Larry Cadigan. Rob and Jamie Loud, Greg Sosa, Mo and Lisa, Dan and Vickie, and Chris Klinger I am truly thankful to know you. It is part of life that sometimes we lose a member of the family. This dissertation is, in part, dedicated to one who I knew so briefly, but showed me how to savor the special moments life has to offer. Steve, wherever you might be – Haaayyyyy!

While attending the University of Texas I have also met some truly exceptional people who have helped me along the way towards my degree. I first met Dean Hines on the last day of orientation for the new incoming graduate class. Having spent the past three years at Texas as an undergraduate, I didn't feel like I needed to be oriented. This did nothing to dispel wild rumors of who this Claver guy was, which came to an abrupt halt when Dean and I showed up that day in full Grateful Dead attire. We've been dear friends ever since; thanks Dean. Later that year I met Mark Cornell, and more recently his new wife Debbie. Mark has taught me a sharpness of thinking I would never have developed otherwise. In addition to this, Mark and Debbie are just genuine good people to know - thanks you two!

I cannot really explain how it was that Phillip MacQueen and I became friends and collaborators. I can only say that without Phillip the Prime Focus Camera would never have happened – it is as much his instrument as it is mine. Working with Phillip has been, and continues to be, an education and an inspiration, and just plain fun. Thanks Phillip, for your herculean efforts over the years., and my appologies to your wife if I've kept you out too late :). I am truly indebted to you.

Someone who will always hold a special place in my heart is A–Lan Reynolds, who I met during her second Masters program at the University of Texas. We seem to be cut from the same piece of cloth, albeit opposite ends. A–Lan, you were a brilliant shining light during my darkest years as a graduate student. Even now, as things seem much brighter to me, your light is blinding and your warmth unending. Miao. Op. Po.

To Luke and Sherri – ogidy ogidy ogidy. Thank you for the wonderful T–shirt, but most of all thanks for all the wonderful outdoor experiences we've shared. May there be may many more to come. Thanks to Gary Hansen for all the instructive and enlightening conversations over the years, and for including me in your outdoor experiences with Chris and your newest family member, Carli.

I would also like to express my sincerest thanks to Frank Bash, Tom Barnes, and the entire staff of McDonald Observatory for their support during the construction of the Prime Focus Camera. At Mt. Locke, I am especially grateful to Dave Doss, Ed Barker and Mark Adams, Jerry Martin, Ed Dutchover, and George Grub (and his crew) for their help and support over the years.

I owe special thanks to Jimmy Welborn and George Barzcark for welcoming me into their work place and sharing their knowledge of machining while I built the Prime Focus Camera.

To David Way and his family, thanks for your support both in the department and away. Our trips to the lake listening to SRV while the sun set on a warm Summer's night went a long way towards easing the strain of graduate school.

Finally, but not in the least, I am forever indebted to Beth Clark. If it weren't for Beth this dissertation would not have been completed with my sanity intact. Everyday she does something seemingly small that makes a very big difference in my life. I love you, Beth with all my heart, thanks for everything – big and small.

THE AGE OF THE MILKY WAY GALAXY FROM WHITE DWARF CHRONOMETRY

Publication No._____________

Charles Frederick Claver, Ph. D.
The University of Texas at Austin, 1995

Supervisor: R. Edward Nather

The age of our own Galaxy – the Milky Way – is one of the principal pieces of information we have to constrain our understanding of how the Universe evolved to its current state. With the assumption that our Galaxy is no different than any other of its type and that our locale in the Universe in not unique, the age of the Milky Way places constraints on how much time has elapsed since galaxies and the Universe were first formed. Estimates for the Galaxy's age have ranged from 10 to 20 billion years, but this age spread is too large to constrain the models we have describing the evolution of the Universe. Perhaps the most accurate way we have of estimating ages comes from the white dwarf stars – the cooling remnants of stellar evolution. The difficulty is that there are too few white dwarfs known for us to fully exploit them as the accurate chronometers they are.

In the first part of this work I present new instrumentation and photometric techniques designed specifically to search for and identify the oldest white dwarf stars. In collaboration with Phillip MacQueen I have converted the 0.76m Boller and Chivens telescope at McDonald Observatory into a highly sensitive digital $f/3$ Prime Focus Camera. I have also extended the standard *UBVRI* photometry system to isolate the unique color signatures of cool degenerate white dwarf stars.

Using these new tools I have surveyed 2.1 square degrees around the Praesepe star cluster and identified its white dwarfs, which I have used to estimate its age at 1.0 ± 0.3 billion years. From the same data set I have simultaneously obtained an age of 0.85 ± 0.10 billion years for the cluster from main sequence stellar isochrones. I have also used the preliminary data from the Hipparcos mission to estimate an isochrone age for the Galactic Disk of 15 ± 2.5 billion years. From these results I present a calibration of stellar isochrone ages to white dwarf cooling times and conclude that the Milky Way is 11 ± 2 billion years old.

Finally I use my estimated age of the Milky Way to place a value on the age of the Universe: 12 ± 2 billion years.

Table of Contents

Table of Contents xii

List of Figures xv

List of Tables xxii

1 Introduction: A Review of the Galaxy's Age 1
    1.1 What We Think We Know About Ages in the Galaxy 5
    1.2 Models for Galaxy Formation and Predicted Age Relations 8
    1.3 The Stellar Components of the Galaxy 11
        1.3.1 z < 700 Parsecs 14
        1.3.2 700 < z < 2000 Parsecs 16
        1.3.3 z > 2000 Parsecs 18
        1.3.4 Summary 20
    1.4 Techniques for Estimating ages in our Galaxy. 20
        1.4.1 Cluster Isochrone Ages 20
            Open Clusters 23
            Globular Clusters 25
        1.4.2 Nuclear Age Estimates 27
        1.4.3 White Dwarf Cooling Times 28
    1.5 Summary of Ages 31

2 The White Dwarf Luminosity Function 34
    2.1 Pre-White Dwarf Stellar Evolution 35
    2.2 The Current State of the Observed White Dwarf Luminosity Function 41
        2.2.1 Disk White Dwarfs 43
            The PG Sample 45
            The LHS 0.8 Sample 48
        2.2.2 Other WDLF Estimates 51
        2.2.3 The Halo White Dwarf Population 56

2.3 Theoretical Interpretation of the WDLF 58

2.3.1 White Dwarf Structure 58

2.3.2 The Mestel Luminosity Function 60

2.4 Modifications to Mestel Theory 68

2.4.1 Neutrino Luminosity 69

2.4.2 Convection 70

2.4.3 Crystallization 72

2.5 Summary 75

2.5.1 A Systematic Search for Cool White Dwarfs 77

3 Instrumentation for a Digital Survey: The Prime Focus Camera 81

3.1 The Prime Focus Camera 85

3.1.1 Optical Design 88

3.1.2 Mechanical Design 101

Optics Tube Assembly 102

Spider and Truss Assemblies 107

CCD Enclosure Design 113

3.2 PFC Performance and Data Reduction 116

3.2.1 Characteristics of the Loral-Fairchild 2048^2 CCD 117

3.2.2 Imaging Performance 119

3.2.3 Reducing Data from the PFC 124

Biases, Zeros, and Darks 125

Shutter Correction 130

Flat Field and Illumination Correction 134

4 Photometric Identification of White Dwarf Stars 138

4.1 Broadband Colors of Hot White Dwarfs 141

4.1.1 Synthetic Model Colors 143

4.1.2 Comparison of Computed and Observed Colors and Magnitudes 152

4.2 Identification of Cool White Dwarfs 159

4.2.1 Hydride Photometry: Principles 162

4.2.2 Hydride Photometry: System Definition 164

4.2.3 Hydride Photometry: Trial Observations 168
4.3 Summary 173

5 Calibration of Stellar Ages: A Case Study of the Praesepe 174
5.1 Why the Praesepe? 176
5.2 Observational Material and Data Reduction 179
5.2.1 Observing Stategy and Data Acquisition 179
5.2.2 Standard Star Photometry and Photometric Calibration 185
5.2.3 Program Photometry of the Praesepe 193
5.2.4 An Aside: Galactic Structure in the Direction of the Praesepe 204
5.3 Analysis of the Praesepe Photometry 207
5.3.1 The Praesepe's Main-Sequence Age and Distance 207
5.3.2 White Dwarf Candidate Selection from Photometry 211
5.3.3 Astrometry: Cluster Membership of Photometric Candidates .. 219
5.4 Other Praesepe White Dwarf Candidates 223
5.5 Calculated Isochrones For DA White Dwarf Stars 223
5.6 Discussion of Results: The Praesepe's White Dwarf Age 230
5.6.1 Predicted White Dwarf Numbers in the Praesepe 232
5.6.2 Estimating the White Dwarf Age. 235
5.7 Concluding Remarks 239

6 White Dwarf Chronometry of the Galaxy 241
6.1 What We Know Now 241
6.2 Age of the Disk from Preliminary Hipparcos Results 243
6.4 Calibration and Constraints of Ages 250
6.4.1 Conclusions 253

Appendix A 255

Appendix B 264

References 268

Vita 277

List of Figures

Figure 1.1: A schematic diagram of the Milky Way galaxy. 12

Figure 1.2: Model isochrones in the theoretical bolometric magnitude versus $\log(T_{eff})$ plane (VandenBerg 1985). 22

Figure 1.3: Color-Magnitude diagram of the Praesepe (M44). 24

Figure 1.4: The color-magnitude diagram for the globular cluster Messier 5. 26

Figure 1.5: The effects of age in model white dwarf luminosity functions for Disk ages of 8, 9, 10, and 11 Gyrs (Wood 1992). 30

Figure 2.1: The evolutionary track of a representative model 5 $M_\odot$ star. 37

Figure 2.2: The observed white dwarf luminosity function from the Palomar–Green (PG) survey and the Luyten Half arcSecond (LHS) proper motion survey. 44

Figure 2.3: The WDLF from the APM Proper Motion Project (Evans 1992 52

Figure 2.4: The WDLF from the AAT and Edinburgh Cape (open squares) surveys compared with the PG/LHS WDLFs. 54

Figure 2.5: The preliminary estimate of the WDLF from the CPMB survey of Oswalt and Smith (1994). 55

Figure 2.6: The preliminary WDLFs for the Galactic Halo from the high velocity stars in LDM89 and the Common Proper Motion Binary survey of Oswalt and Smith. 57

Figure 2.7: The observed WDLF from the PG and LHS surveys compared with the analytic Mestel LF. 66

Figure 2.8: An analytic representation of the WDLF compared with the observations. 77

Figure 2.9: The space density detection limits of a hypothetical survey for white dwarfs complete to magnitude 23 over 1 and 100 square degrees of the sky. 79

Figure 3.1: The Prime Focus Camera and its major components. 86

Figure 3.2: The optical ray paths for the PFC's corrector on axis and at the edge of the field 0.55 degrees off axis. 90

Figure 3.3: Transverse and sagital ray fan diagrams showing the residual aberrations in the corrector design. 93

Figure 3.4: Point spread functions for the corrector design as a function of field position and wavelength. 95

Figure 3.5: The optical ray path diagram for the PFC (corrector+primary). 97

Figure 3.6: Light loss through the tertiary's central hole from illumination by off-axis sources. 98

Figure 3.7: Optical ray path diagrams for the nine primary ghost images. 100

Figure 3.8: A cutaway view of the Optical Tube + CCD Dewar assemblies. 103

Figure 3.9: Cutaway view of the Invar Field Lens Cell and tertiary mirror insert. 105

Figure 3.10: The PFC's Truss and Spider assemblies. 108

Figure 3.11: A block diagram of the hardware devices which make up the active focus assembly. 111

Figure 3.12: The effectiveness of the active focus on the PFC is evident in this series of images. 113

Figure 3.13: Cutaway view inside the CCD Dewar showing the location of major parts. 115

Figure 3.14: The detector quantum efficiency for LF1 coated with Lumigen and bare. 117

Figure 3.15: Variance versus signal level with the linear fit to compute read noise and electronic gain of LF1 on the PFC. 119

Figure 3.16: The FWHM as measured in four filters across the PFC's field versus column number. 121

Figure 3.17: The measured FWHM as in Figure 3.16 but as a function of row number. 122

Figure 3.18: The radial dependence of measured FWHM in the four different filter band passes. 123

Figure 3. 19: A raw image from the PFC prior to removing its instrumental signatures. 126

Figure 3.20: A typical column plot of LF1's overscan region averaged by rows. 127

Figure 3.21: The master zero image to date from LF1. 129

Figure 3.22: The average shutter correction map for the PFC (units are 10^{-4} seconds). 133

Figure 3.23: The master flat in the V filter from the PFC. 136

Figure 3.24: The data shown in Figure 3.19 fully reduced – the PFC's instrumental signature has been removed. 137

Figure 4.1: The conventional UBV color-color diagram showing the location of white dwarfs relative to the field main sequence population. 142

Figure 4.2: The response functions for the UBVRI system as defined by Bessell (1990). 144

Figure 4.3a,b,c: Broadband colors versus effective temperature for Bergeron's DA model atmospheres along with black body colors for comparison. 146

Figure 4.4: $U-B$ versus $B-V$ DA model color sequences for log(g)=7.5, 8.0, and 8.5. 148

Figure 4.5: $U-V$ versus $V-I$ DA model color sequences for log(g)=7.5, 8.0, and 8.5. 149

Figure 4.6: Comparison between the observed and model $U-B$ versus $B-V$ two color diagram from white dwarfs. 153

Figure 4.7: Absolute visual magnitude (M_v) versus $V-I$ from Monet et al. (1992) white dwarfs with trigonometric parallaxes from the USNO. 155

Figure 4.8a,b: Comparisons of the calibrated absolute visual magnitudes with observed values as a function of $B-V$ and $U-V$. 157

Figure 4.9: $B-V$ versus $V-I$ two color photometry of cool white dwarfs and field stars. 161

Figure 4.10: The response function of the two intermediate band filters centered on 5095Å and 6860Å compared to the standard BVI responses from Bessell (1990). A spectrum of an intermediate subdwarf is also shown as an example of the absorption features sampled by the two interference filters. 165

Figure 4.11: The MgH absorption index for known white dwarfs and subdwarfs plotted against $B-V$. 170

Figure 4.12: The CaH absorption index for known white dwarfs and subdwarfs plotted against $V-I$. 172

Figure 5.1: The residuals from the standard star photometry on 10 Feb. 1994 and 16 Feb. 1994 plotted against the observed V magnitude. 191

Figure 5.2: Same as in Figure 5.1, except the standard star residuals are plotted against their colors. 192

Figure 5.3: The sky map of the area surrounding the Praesepe showing the individual field locations and the boundary of the survey. 197

Figure 5.4: V vs U-B color-magnitude diagram for all stars measured in the survey of the Praesepe. 200

Figure 5.5: V vs B-V color-magnitude diagram for all stars measured in the survey of the Praesepe. 201

Figure 5.6: V vs V-I color-magnitude diagram for all stars measured in the survey of the Praesepe. 202

Figure 5.7: Normalized predicted star counts versus distance modulus for a two component exponential density distribution (see text). 205

Figure 5.8: The B-V CMD from the short exposure set and Johnson's (1952) photoelectric photometry. 208

Figure 5.9: The V-I CMD from the short exposure image set. 209

Figure 5.10: The grand V-I CMD of the Praesepe fields as in Figure 5.6 with VandenBerg's isochrones and the mean white dwarf evolutionary track from Monet et al. (1992). 212

Figure 5.11a,b: The UBVI two color diagrams for the objects passing the first criterion of hot white dwarf selection: $U-V \leq 0$ and $B-V \leq -0.3$. 214

Figure 5.12: The V-I CMD for Praesepe white dwarf candidates satisfying both $U-V \leq 0$ and $B-V \leq -0.3$ color excess and UVI colors consistent with those of white dwarfs. 216

Figure 5.13: The instrumental proper motion vector point diagram for the photometric white dwarf candidates and stars selected near the Praesepe main-sequence. 221

Figure 5.14: Wood's evolutionary models for $0.4-1.0 M_{\odot}$ white dwarfs with the interpolated $0.6-2.0 Gyr$ isochrones. 224

Figure 5.15: The M_v versus M_{bol} data from Liebert, Dahn, and Monet (1988) fitted with a 4th order polynomial. 226

Figure 5.16: Calculated white dwarf isochrones in the M_v versus U-B color-magnitude plane. 227

Figure 5.17: The same calculated WD isochrones as in Figure 5.16 transformed to the M_v versus B-V color-magnitude plane. 228

Figure 5.18: The same calculated WD isochrones as in Figure 5.16 transformed to the M_v versus V-I color-magnitude plane. 229

Figure 5.19: The mean open cluster luminosity function from Taff (1974) normalized to the observed Praesepe LF of Jones and Stauffer (1991). 233

Figure 5.20: The V versus $V-I$ color–magnitude diagram for the white dwarfs and candidates listed in Table 5.6. 236

Figure 5.21: The V versus B-V color magnitude diagram for the Praesepe white dwarfs and candidates. 237

Figure 6.1: The preliminary Color-magnitude diagram of the solar neighborhood from the Hipparcos mission. 244

Figure 6.2: The color–magnitude diagram from the Hipparcos mission of the local field population with the ZAMS and isochrones from VandenBerg (1985) for 5, 10, and 15 Gyrs overplotted. 246

Figure 6.3a,b: The Morphological Age Index (δV) for the Hipparcos CMD (left) is compared to the cluster data from Janes and Phelps (1994 right). 250

Figure 6.4: A preliminary look at the cross–calibration of white dwarf ages and stellar evolution ages. 251

List of Tables

Table 1.1: Ages for the Universe given H_0 estimates from various investigators for the Milne and Einstein – de Sitter models. 4

Table 1.2: The ages of the different populations are summarized by what method was used to obtain them. 33

Table 3.1: Optical prescription for the PFC's corrector. 89

Table 5.1: Journal of Observations. Summarized here are the individual observations of the Praesepe. 181

Table 5.2: Summary of the photometric coefficients. 190

Table 5.3: Summary of the field centers, integration times, and area for the 3 short exposure image sets. 194

Table 5.4: Summary of field centers, total integration times, and area for the 5 long exposure image sets. 196

Table 5.5: Photometrically selected white dwarf candidates from the Praesepe survey. 217

Table 5.6: The final composite list from this survey and the literature of white dwarfs and candidates for the Praesepe cluster. 231

Table 6.1: The ages of the different populations are summarized by what method was used to obtain them. 254

Table A.1: $U - B$ colors versus T_{eff} for blackbody energy distribution (bb) and Bergeron et al. (1990) $\log(g) = 7.5$, 8.0, and 8.5 model DA atmospheres. 255

Table A.2: $B-V$ colors versus T_{eff} for blackbody energy distribution (bb) and Bergeron et al. (1990) $\log(g) = 7.5$, 8.0, and 8.5 model DA atmospheres. 258

Table A.3: $V-I$ colors versus T_{eff} for blackbody energy distribution (bb) and Bergeron et al. (1990) $\log(g) = 7.5$, 8.0, and 8.5 model DA atmospheres. 261

Table B.1: 0.6 Gyr isochrone for carbon core white dwarfs. 264

Table B.2: 0.8 Gyr isochrone for carbon core white dwarfs. 264

Table B.3: 1.0 Gyr isochrone for carbon core white dwarfs. 265

Table B.4: 1.2 Gyr isochrone for carbon core white dwarfs. 265

Table B.5: 1.4 Gyr isochrone for carbon core white dwarfs. 266

Table B.6: 1.6 Gyr isochrone for carbon core white dwarfs. 266

Table B.7: 1.8 Gyr isochrone for carbon core white dwarfs. 267

Table B.8: 2.0 Gyr isochrone for carbon core white dwarfs. 267

1

Introduction: A Review of the Galaxy's Age

One of the more fundamental questions we can ask about our Galaxy is: How old is it? The age of our own Galaxy – the Milky Way – is one of the principal pieces of information we have to constrain our understanding of how the Universe evolved to its current state. According to the standard Big Bang cosmology model the Universe started as a cosmic fireball, filling all space with opaque energy. As the early Universe expanded this energy cooled, quickly formed matter and shortly thereafter became transparent - the period of recombination. The residual radiation from this fireball can still be seen as the Cosmic Microwave Background, and has a nearly perfect 2.736±0.017K (Mather *et al.* 1990) blackbody distribution. We can also describe the matter continuing to expand according to Hubble's law,

$$v = H_0 r \tag{1.1}$$

where H_0 is Hubble's constant and v is the expansion velocity at a distance r. As this matter expands it must also slow down due to its mutual gravitational attraction. The amount of this deceleration is determined by the density of matter in the Universe and is characterized by the parameter q_0. If the amount of matter in the Universe is sufficient to stop the expansion given infinite time the density is said to be critical and q_0=1/2; the Universe is considered closed for $q_0 \geq 1/2$. This form of the Big Bang with q_0=1/2 is called the Einstein – De Sitter model. However, if the matter in the Universe is negligible then the Universe would continue to expand forever with little deceleration and q_0=0. This is the Milne model for the Universe. Most cosmologists believe that the actual Universe lies somewhere between the Einstein – De Sitter and Milne models.

Within the standard model, Hubble's constant and the age of the Universe, t_0, form a dimensionless constant – $H_0 t_0$. The value of this constant is dependent on the nature of the Universe's geometry, by the amount space is curved (if it is at all), and the value of Einstein's cosmological constant (Λ)[1] and the value of q_0. In the Einstein - de Sitter version of the Big Bang model the value for $H_0 t_0$=2/3. This model assumes that the curvature of space and the cosmological constant, Λ, are insignificant and the deceleration parameter, q_0, is 1/2 (Rowan–Robinson 1977). The value of $H_0 t_0$ is <1 if the cosmological constant is not important, or can be >1 if it is significant and the Universe is flat (*e.g.* Peebles *et al.* 1991). In the Milne model, where the mass density is insignificant, $q_0 = 0$ and the value of $H_0 t_0$=1. Thus any cosmology model makes a prediction on the value of $H_0 t_0$ which, if H_0 and t_0 can be determined observationally, can be tested.

---

[1] The cosmological constant was added by Einstein to keep the expansion in his model criticaly damped given a low density of matter in the universe. It can be understood in terms of the gravitation equivelent of empty space, to provide the ncessary attraction to halt the expansion of the universe in infinite time given less than critical mass density.

In addition, there are several basic observational boundary conditions we can place on our cosmology models. First, the model must explain the current state of the universe - the way we see it now. Second, the results from COBE (COsmic Background Explorer) must be satisfied - that is by accepting the Big Bang as a premise then the model must include the near, but not perfectly, smooth nature of the Cosmic Background Radiation as observed by COBE (Wright *et al.* 1992). Third, the model must satisfy both the first and second conditions within the time scales allowed by various estimates for the Universe's age.

The age of our Galaxy serves to place constraints on our third boundary condition from the simple relation,

$$t_0 = t_f + t_g \tag{1.2}$$

where t_f is the time from the Big Bang until the time galaxies start to form and t_g is the amount of time from galaxy formation to the present day. With the assumption that our Galaxy is no different from any other of its type and that our locale in the Universe in not unique and that all galaxies formed at the same time, then $t_g \approx t_G$ ($t_G \equiv$ age of the Milky Way). We can then use the age of our own Galaxy as a yardstick with which to measure the age and evolution of the Universe.

Many investigators have undertaken efforts to determine H_0 with a wide range of results. Reviews by van den Berg (1989), Tully (1990), and others give significantly different estimates for the value of H_0, which will ultimately be reconciled from other observations. Table 1.1 lists the values of H_0 obtained by various researchers and the implied age of the Universe for the Milne and

Table 1.1: Ages for the Universe given H_0 estimates from various investigators for the Milne (H_0t_0=1) and Einstein – de Sitter (H_0t_0=2/3) models assuming $\Lambda = 0$.

Investigators	H_0 (km s^{-1} Mpc^{-1})	t_0 Gyr (H_0t_0=1, q_0=0)	t_0 Gyr (H_0t_0=2/3, q_0=1/2)
Pierce, M. J. (1994)	87 ± 7	11.5	7.7
Tully, B. (1990)	87±10	11.5	7.7
van den Berg (1989)	67±8	14.9	10.0
Rowan-Robinson (1988)	66±10	15.1	10.1
Tammann (1988)	56±9	17.8	11.9

Einstein – de Sitter cosmology models. Within the large uncertainties of estimating H_0 and t_f (usually near 1 Gyr (10^9 years), but possibly as large as ~5 Gyrs) the age of the Galaxy provides important constraints to the value of $H_0 t_0$, hence on the models we use to describe the evolution and formation of the Universe and its galaxies.

1.1 WHAT WE THINK WE KNOW ABOUT AGES IN THE GALAXY

Age estimates for the Galaxy are based on the ages of its constituent components - namely the stars. There are three independent methods for estimating the ages of stellar populations in our Galaxy which come from a variety of sources encompassing all stages of stellar evolution. Traditionally these have been: stellar isochrone fits to open and globular star cluster color–magnitude diagrams, radioactive decay and nucleosynthesis, and most recently the turndown found in the white dwarf luminosity function (Winget *et al.* 1987, Wood 1992).

The term isochrone comes from the Greek root *chron,* meaning time, and the prefix *iso*, meaning uniform. Stellar Isochrones are formed by computing a set of numerical models for the evolution of stars distributed by mass, beginning each at the same time, all with the same chemical make up, and then at some fixed later time examining how the sequence of model stars are distributed in brightness and temperature. An isochrone is the resulting distribution. Because stars of different mass evolve at different rates, the more massive ones evolving quicker than less massive ones, the shape of the isochrone is a function of when we examine our models – age.

The method of radioactive decay uses a similar approach, relying on knowledge of the decay rates of specific isotopes. We can use these decay rates to estimate ages by measuring the current abundance ratios of two different isotopes with different decay rates. Then if we either know *a priori*, or make some assumption about the initial abundance ratio, we can compute the elapsed time since those isotopes were formed. For stellar ages we usually assume the isotopes were formed very early on in the history of the Galaxy, over a brief time interval (*i.e.* the first epoch of star formation), and their initial ratios can be determined from theoretical calculations.

These two methods are analogous to a foot race between two runners, one is six feet tall and the other is four feet tall. If we know how much faster the taller racer runs over the shorter, then at any time in the race the distance measured between the two runners tells us how long the race has been going on. However, it is apparent that stellar isochrone and nuclear ages are sensitive to assumptions and to the initial conditions at the beginning of the "race" (*i.g.* both runners started from the same place at the same time).

The white dwarfs are different from stellar isochrone and nuclear chronometers in that their cooling times are insensitive to initial conditions. This comes about because white dwarfs, when formed, are very hot and evolve simply by cooling. Their initial high temperature means that the cooling rate of white dwarfs is very fast, hence they spend very little time in their initial condition. The analogy here is: By placing a piece of steel in a fire it will get hot and start to glow. If we know how fast the piece of steel cools and how hot the fire was, then by measuring the temperature of the steel we know how long ago it was in the fire

– an age. Furthermore, suppose it takes only a few seconds for the steel to drop its temperature by half when we first remove it from the fire, and thereafter it takes another hour for the temperature to halve again. This implies that even if we are wrong in estimating the initial temperature by a factor of two we will have misjudged the length of time the steel has been out of the fire by only a few seconds. This is why white dwarfs make superb stellar clocks. In addition, from our understanding of how stars evolve we believe every stellar population forms white dwarfs, therefore in principal white dwarfs can be used for a self–consistent picture of the age of the Galaxy and its stellar populations.

These three methods produce a wide spread in estimates for the Galaxy's age ranging between 10 and 20 Gyrs (1 Gyr = 10^9 years). Even though this spread in ages is still too large to accurately constrain the age and formation of our Galaxy, it is remarkable that results from the wide variety of techniques used are not more discrepant. In most instances these ages for the Galaxy have been addressed in piecemeal fashion. Most reviews on the subject admit that there are discrepancies between the various techniques, but do little to attempt to rectify these differences other than suggesting possible reasons. In this thesis I intend to address the problem using the white dwarf stars which, as I will show in this chapter, provide the necessary connection between the other age techniques. The remainder of this chapter will be a review of the ages of the Galaxy as predicted from different kinds of formation models, observations, and techniques used.

1.2 MODELS FOR GALAXY FORMATION AND PREDICTED AGE RELATIONS

One of the earliest comprehensive models for galaxy formation came from Eggen, Lynden-Bell, and Sandage (1962, hereafter ELS). In their model, the galaxy formed from the rapid collapse of a larger proto-galactic cloud. The model predicts a correlation between the orbits, kinematics, and abundances of the stellar populations (*e.g.* Sandage 1990). The rapid collapse idea of the ELS model, as originally stated, would lead to little age difference between the inner and outer parts of the Galaxy. But this assumes the density of the proto-Galaxy was uniform and that there was only one collapse time scale as $t \propto (\rho \cdot G)^{-0.5}$, essentially a dynamical free fall. If there was a hierarchy of densities in the proto-galactic cloud (Searle and Zinn 1978), then it follows that the collapse times for the Galaxy would also be hierarchical. This modification to the basic ELS model would predict a significant, but continuous, age spread in the various parts of the Galaxy. Specifically, if this kind of model is correct, there should be a relation between distance from the Galactic center and age – the outer portions being older than the inner.

Larson (1976) proposed an alternative to the various forms of dynamical collapse models in the form of a pressure supported collapse galaxy formation. Larson's model attempts to explain the existence of both spherical and disk-like components in the galaxy, which the ELS model has difficulty doing. This is accomplished by having a two component infall; one nearly free fall as in ELS in order to explain the existence of the Galactic spheroid, the other is delayed through some support mechanism to explain the existence of the disk. This would also predict that the outer part of the Galaxy is older than the inner part. This particular class of model therefore suggests an age gap between the outer and inner portions of the Galaxy.

Besides these two collapse models there are two more general concepts for galaxy formation. Searle and Zinn (1978) suggest that the Galaxy was built up over several Gyrs from a chaotic clumpy merging of individual mass fragments of the original protogalactic cloud. These fragments would have then chemically evolved independently and, as stars began forming, expelled any left over gas. This gas eventually began to collapse and form the Galactic Disk. Searle and Zinn formulated their model primarily to explain the patchy density distribution in the outer Halo and the abundance patterns they observed. In such a model the stars in the outer parts of the Galaxy would be systematically older than the Disk, but not uniformly so.

Finally, the last type of model we will consider is one where the initial protogalactic cloud collapses and begins massive star formation (Berman and Suchov 1991). The enormous star formation rate temporarily halts the collapse from winds driven by supernovae and causes as much as 50% mass loss from the original protogalaxy. These winds would also carry processed material enriched with metals back into the remaining protogalactic cloud and possibly outward into intergalactic space. In addition, the interaction of this wind with the gaseous material would heat up the gas, causing it to expand. As a result of the expansion there would be a hiatus in star formation activity followed by a more gradual collapse of the remaining material. If this model describes our own Galaxy there should be a distinct age gap in an age versus metal abundance as well as some stellar tracers of the first massive epoch of star formation. It strikes me that this model may be very difficult to test from stellar ages alone. Although, if there is appreciable mass loss from the protogalaxy then there ought to be observable consequences. In my opinion this model is not applicable to our Galaxy as a whole, but might be useful in some form to explain the enriched metal abundance in the Galactic Bulge and to slow the initial collapse in an ELS-type model to form the Galactic halo and later the Disk.

The models summarized above no doubt are simplifications of a complex process, but I believe each holds elements of truth and perhaps a workable model would come from combining these models and taking advantage of the elements that seem to work. Recently Larson (1990) and Sandage (1990) presented reviews concerning their version of galaxy formation, building on their classes of models. Larson still maintains that disk and spheroid formation are due to very different processes. He contends that disks can only be formed from *gaseous dissipation* and are most likely to be built upon over a long period of time, continuing to the present day. However, Sandage maintains that the original ELS model, with realistic modifications, adequately accounts for the observed properties of the Milky Way. From these reviews we see that there could be multiple processes at the fundamental level which determine how galaxies are formed.

From the example models discussed here it is evident that the relative ages for the Galaxy's components are as interesting in constraining galaxy formation and evolution models, as its absolute age is in constraining models of Cosmology. However, the details of these basic models are in a state of continuous change while researchers try to keep pace with current observations. Until the observations themselves are on firmer foundations this state of flux is not soon to stabilize. By establishing the relative ages within the Galaxy in a self-consistent way we can test and constrain these models for the formation of galaxies. We are left then with two fundamental questions: How old is the Galaxy? and How long did it take to form? What, if anything, do the current state of observations have to say about these questions? Before going on to address the age of the Galaxy we will describe its content and present structure.

1.3 THE STELLAR COMPONENTS OF THE GALAXY

Historically, the Milky Way Galaxy has been regarded as having two major systems of stellar populations, Population I and Population II, characterized by significant differences in their overall properties (Baade 1944). In general, Population I stars tend to have nearly Solar abundances, are in more or less circular orbits around the center of the Galaxy, and are concentrated to within a few hundred parsecs above and below the Galactic plane. In addition, Population I stars are relatively young and continue to form even as this is written. This is in contrast to Population II stars which tend to have abundances from 10 to ~1000 (-1 < [Fe/H] < -2.3) times less than Solar[2], are in highly elliptical orbits around the Galactic center, and have distributions several kiloparsecs about the Galactic

---

[2] When astronomers refer to abundances it is usually on a logarithmic scale referenced against the sun. It is also standard practice to gage the abundance of elements heavier than Hydrogen or Helium by the ratio of Iron abundance to Hydrogen. The notation used is [Fe/H], and is defined as

$$[Fe/H] = \log \frac{N_{Fe}}{N_H} - \log\left(\frac{N_{Fe}}{N_H}\right)_{\odot}.$$

The [Fe/H] notation for abundance will be used throughout the remainder of this work.

plane. These two populations themselves can be further divided into several significant subsystems. Figure 1.1 shows a schematic representation of how we think the Galaxy appears, and the location of the various stellar systems of which it is comprised. Identified are: the Disk, the Open Clusters, the Nucleus, the Bulge, and the Globular Clusters in the Halo. It is these subsystems which will be

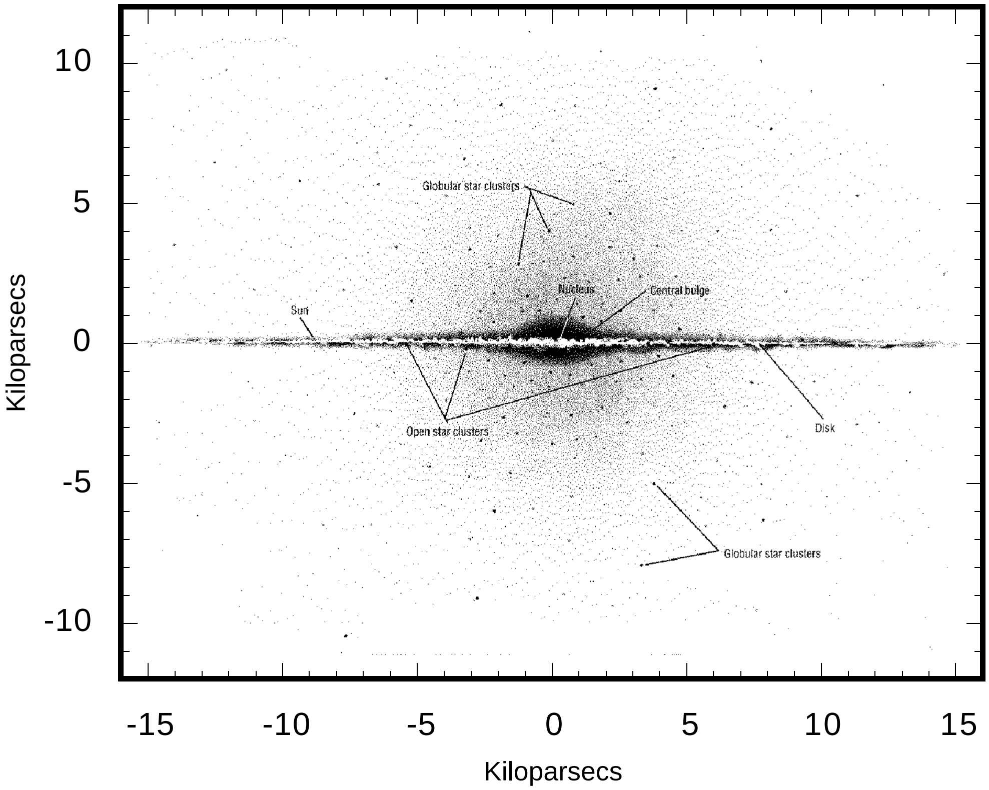
10
5
0
-5
-10
Kiloparsecs
Globular star clusters
Nucleus
Central bulge
Sun
Open star clusters
Disk
Globular star clusters
-15
-10
-5
0
5
10
15
Kiloparsecs

Figure 1.1: A schematic diagram of the Milky Way galaxy showing the major stellar components and the relative location of our Sun.

the focus of this discussion on the Galaxy's structure, evolution, and the techniques used for estimating their ages.

The distinction between Population I and II has become somewhat muddled and out of date in recent times. This has been caused primarily by the discovery of an intermediate population having abundances similar to Population I and kinematics and ages similar to Population II. The new population is known as the Thick Disk (Gilmore and Reid 1983; Gilmore and Wyse 1985; Fenkart 1989; Gilmore, Wyse, and Kuijken 1989). The existence of the Thick Disk supports the idea that there is essentially a continuum of stellar populations, extending outward from the Disk to the Halo, from the Bulge to the outer parts of the Disk. If this is true, then it too will have something to say about the way the Galaxy formed. In addition, the discovery of young stars with nearly solar abundances in the outer parts of the Galaxy has further blurred the distinction between Population I and Population II. In an effort to keep from confusing the matter entirely, when possible I will refer to the individual stellar populations by their accepted names.

This section is not meant to be a comprehensive review of stellar populations, but more a definition of terms. This is so that the reader and I have some common understanding of what is meant when I refer to a specific population by its proper name. Below I summarize the characteristics of each stellar system in order of increasing scale height[3] about the Galactic plane.

---

[3] By definition the scale height is the distance from the Galactic plane where the density of stars has decreased by a factor of 2.718282 - the natural number 'e'. The scale height is most commonly denoted by - z.

1.3.1 z < 700 Parsecs

The first 700 parsecs within the Galactic plane is a very dynamic place as stellar evolution goes. Here we find stars which are nearly as old as the Galaxy itself and those that are still in the process of being formed. We also find dense molecular clouds which have yet to start the process of star formation, but are clearly on their way. When we look up at the night sky what we see is entirely dominated by the Galaxy's content within the first 300 parsecs of scale height. This is primarily because the density of objects occupying this region is several orders of magnitude higher than any of the other populations. The stellar content in this part of the Galaxy is better characterized by an additional scale length of 2000 parsecs for the *e*–folding distance from the Galactic center. The comparatively large radial scale length and the small scale height gives this part of the Galaxy a flattened disk–like appearance — hence the term Disk.

With regard to stellar ages there are two primary components which make up the Disk, the open (Galactic) cluster system and the single isolated field stars. Each of these components share similar properties, but within these properties there are differences linked mostly by differences in age. Overall, the stars in the Disk have circular orbits, low velocity dispersions about these orbits, and nearly solar abundances. The circular orbit of the open clusters within the plane of the Galaxy means that unless they are tightly bound, these clusters will be disrupted over a fairly short period (over a few Galactic revolutions), contributing their stellar contents to the field population. In this way, it is not at all surprising that the open clusters and Disk field stars have similar properties.

The youngest stars of the Disk are found in the spiral arms. The spiral arms contain the dense molecular gas clouds just beginning to form stars and the very young OB associations (*i.e.* the Orion Trapezium complex). The scale height of the spiral arms is thought to be roughly 120 parsecs, to have solar or slightly greater metallicities, and a vertical velocity dispersion of 15 km sec^{-1}. The open cluster pair h and χ Persei at an age of 1.5×10^{7} years are representative of this population, which is too young to contain many evolved stars.

The field stars in the Disk, which permeate the spiral arms and the spaces in between, span a range of scale heights from approximately 200 parsecs for the youngest to nearly 700 parsecs for the oldest. Along with increasing scale height the velocity dispersion also increases from 25 to 80 km sec^{-1} respectively. While the peak metallicities remain near solar, the number of stars with lower metal abundance increases with increasing age and scale height. There are open clusters whose properties seem to follow this gradient in characteristics found in the Disk field stars. At the young end of the spectrum there are clusters like the Hyades and Praesepe whose ages we estimate to be near 1Gyr. The Hyades cluster is also an example of a cluster in the process of dissociation, sending its stellar content into the field. At the other extreme in age, we find the old open clusters NGC–188 and NGC–6791, which appear to have survived because their compactness makes them more tightly bound than other open clusters. The estimated ages for the clusters is still somewhat in dispute, ranging from 6.5 (Demarque *et al.* 1992) and 10–12 Gyrs (VandenBerg 1985; Iben, 1967) for NGC–188. For NGC–6791 Demarque *et al*. obtain an age of 6.5–7.5 Gyrs or 0–1 Gyr older than NGC–188, but contend that it could be younger than NGC–188 depending on metallicity.

1.3.2 700 < z < 2000 Parsecs

The Galaxy in this intermediate range of scale height is an intriguing place simply because we know so little about it. Here again we find two stellar populations, but with very different characteristics – the Thick Disk and the Galactic Bulge. The mysteries surrounding these two populations come primarily from the difficulties in observing them as pure populations, uncontaminated by intervening material or background stars.

The Galactic Bulge occupies the volume of space immediately surrounding the nucleus of our Galaxy. Because of the Sun's position, the Galactic Bulge must be viewed through large portions of the Disk. In most instances the dust and gas found in the disk totally obscure our view of the Bulge. However, there are several windows where the column density of material from the disk along the line of sight towards the Bulge is very low. One such window is called Baade's window, located at Galactic coordinates $\ell = 0^\circ, b = -3.9^\circ$. From the shape of the Red Giant Branch viewed through Baade's Window (Terndrup 1988) and from abundance analysis of individual stars (Rich 1988) we know that much of the Bulge is very metal–rich. The range in metallicity observed is $-1 \geq [Fe/H] \geq +1$, with evidence of a gradient toward lower metallicities with increasing distance from the Galactic center. The stars in the bulge have a velocity dispersion of ~113 km sec^{-1} and have a scale height of approximate 400 parsecs.

The age of the Bulge is thought to be quite old. This is based on the observed high ratio of evolved stars to main sequence stars, as well as color magnitude diagrams in the low extinction windows. From color magnitude diagrams Terndrup (1988) derives an age for the Bulge of 11–14 Gyrs. Rich (1993) suggests that the existence of RR Lyrae stars in the Bulge implies its age must be at least 10 Gyrs old. Recently images from the Hubble Space Telescope have been used to obtain a color magnitude diagram in Baade's Window which indicates a mean age of 9 Gyrs.

In the region near the solar neighborhood the Thick Disk is only just now being rigorously studied. The emergence of the "Thick" Disk as a viable and separate stellar population has come about mainly from the analysis of star count data. Gilmore and Reid (1983) showed that there was an excess of stars at scale heights of ~1–2 kiloparsecs which could not be accounted for by the usual two component distribution. If the scale height for the Bulge is correct, then it is difficult for the Thick Disk to be the result of an extension of the Bulge over the Disk as suggested by Sandage (1990). The peak density of stars in the Thick Disk is roughly 4% that of the Disk field stars with a mean metallicity of $\left[Fe/H\right] \sim -0.6$ (Gilmore, Wyse, and Kuijken 1989).

Estimating the age of the Thick disk is extremely difficult because of problems in obtaining a pure Thick disk sample. According to Gilmore *et al*. (1989) any sample selected on either abundances or kinematics will include a substantial fraction of old Disk stars or Halo stars (as defined below). In spite of this difficulty, Noris and Green (1989) have argued that the age of the Thick Disk is on the order of 8–11 Gyrs. However, Gilmore *et al*. (1989) raise the suggestion that if the Thick Disk is related to the inner globular cluster systems (see below) then its relative age is known reasonably well.

1.3.3 z > 2000 Parsecs

In the outer parts of the Galaxy is the region termed the *Halo*. Janes (1993), in a review article, gives a multifaceted way of defining the Halo through kinematics, spatial location, chemical composition, and age. If a star has a velocity of > 63 km sec^{-1} relative to the local standard of rest or a metallicity of $[Fe/H] < -1$, it is classified as part of the Halo. In Addition, we classify stars as belonging to the Halo when they are located more than 1000 parsecs above the Galactic plane or when they are older than ~10 Gyrs.

Within this definition the most prominent constituents of the Halo are the globular clusters, although they represent only about 1% of the total population. Much of what we know about the Halo, and everything we know about its age, comes from these star systems simply because they are easily distinguished and their distances are easily estimated. Globular clusters are dense systems composed of roughly $10^5 - 10^6$ stars in a nearly spherical shape spanning 40–100 parsecs. From their color–magnitude properties it is clear that globular clusters are old. Just how old remains a topic of vigorous research. From the present day, models of the oldest globular clusters produce ages near 17 Gyrs, and the overall age scale is uncertain by roughly 3–4 Gyrs (Hesser 1993). I would add here that this uncertainty is purely internal to the globular cluster absolute ages and does not reflect possible differences between other stellar age estimation techniques.

It is accepted today by most astronomers working on Galactic structure that there are two distinct systems of globular clusters in terms of spatial distribution and abundance patterns. Armandroff (1993) summarizes the inner, sometimes called Disk, globular cluster characteristics as having a highly flattened compact distribution, with rotational velocities nearly that of the Thick Disk (approximately 190 km sec^{-1}), and a low vertical velocity dispersion of 60 km sec^{-1}. For this reason Armandroff argues that these clusters are actually part of the Thick Disk. According to Armandroff the break in kinematics and spatial distribution between systems occurs at $[Fe/H] = -0.8$, therefore any globular cluster with a metallicity less than this value is defined as a member of the inner population. The prototype cluster for the inner system is 47 Tucanae. The outer globular clusters are nearly spherically distributed about the Galactic center and show kinematics with low rotational velocities and high vertical velocity dispersions of ~40 and ~115 km sec^{-1} respectively. The example prototype is Messier 92.

In addition to the cluster systems there is a population of metal poor isolated field stars, which in many ways have characteristics similar to the globular clusters. These are the Halo subdwarfs, so called because of where they lie in a Hertzprung–Russell diagram (*e.g.* Monet *et al.* 1992). These stars can be recognized within the local stellar population from their high proper motions as their highly elliptical orbits take them through the Galactic Plane. It is difficult to characterize any individual Halo subdwarf within the range of parameters exhibited by the Globular clusters. Because of this it is very difficult to obtain ages for the Halo field population, but it is most likely old and perhaps as old as 17-18 Gyrs. Furthermore, there is no obvious direct progeny of these field stars with globular clusters, as there appears to be for the Disk field stars and open clusters.

1.3.4 Summary

There are several key points that should be emphasized regarding stellar populations and their ages. First, there is a strong connection between the Disk field stars and the open cluster system. Therefore, the ages of the open clusters are representative of the Disk itself, but it is uncertain whether the oldest clusters formed in the disk are still intact or have been dynamically disrupted. Because of problems defining a "pure" sample for the Thin Disk, it will be difficult to accurately evaluate its age with any method. Finally, in the Halo it is not obvious that the field stars and globular clusters are related to each other as are the Disk field stars and open clusters. It follows, then, that the Halo field stars and Globular clusters could have very different ages.

1.4 TECHNIQUES FOR ESTIMATING AGES IN OUR GALAXY.

Currently there are three independent methods in use for estimating stellar ages. These are: stellar isochrones or some variant, abundance patterns of radioactive isotopes, and white dwarf cooling times. For each of the stellar populations discussed above one or more methods have been used for estimating their ages. In the sections that follow I will review these techniques along with their strengths and weaknesses.

1.4.1 Cluster Isochrone Ages

Perhaps the most widely used method for obtaining ages of stellar populations is from the use of model stellar isochrones fitted to some set of observational data, typically a color–magnitude diagram of a star cluster. In Figure 1.2 I show such a set of calculated isochrones for ages of zero, called the zero age main sequence (ZAMS), through 15 Gyrs (1Gyr $= 1\times10^9$ years) for solar abundances (VandenBerg 1985). The essence of the isochrone age technique is the location of the main sequence turnoff point (indicated by arrows in Figure 1.2). The position of the turnoff is mostly a function of age, becoming less luminous and cooler with increasing age. This is because the massive, hotter, more luminous stellar models evolve more quickly than their lower mass cousins.

One of the principal difficulties with stellar isochrones is that we do not observe the calculated values – luminosity (M_{bol}) and effective temperature (T_{eff}). Instead, what we do observe are the apparent brightness and colors. Fortunately, star clusters satisfy some of the same conditions we assumed in calculating our model isochrones, and so we can easily translate between observable quantities and ones calculated from our models. Within the age of all but the youngest clusters, the time spanning the formation of its stars is small, therefore we are not in serious error if we assume all the stars were formed at the same time. We can also assume that the cluster was formed from a single cloud with a uniform chemical composition so that its stars also have this same uniform chemical make up. Finally, for all but the nearest clusters, the physical size of the cluster is small compared to its distance from us, hence we assume all stars in a given cluster are at the same distance. This allows us to easily compare apparent brightness of the cluster stars with their true luminosity.

One remaining difficulty is in translating the computed effective temperature into observable quantities. Here, we must rely on a second set of numerical models for the wavelength dependence of model atmospheres in the evolutionary models. Through the use of these model atmospheres we can

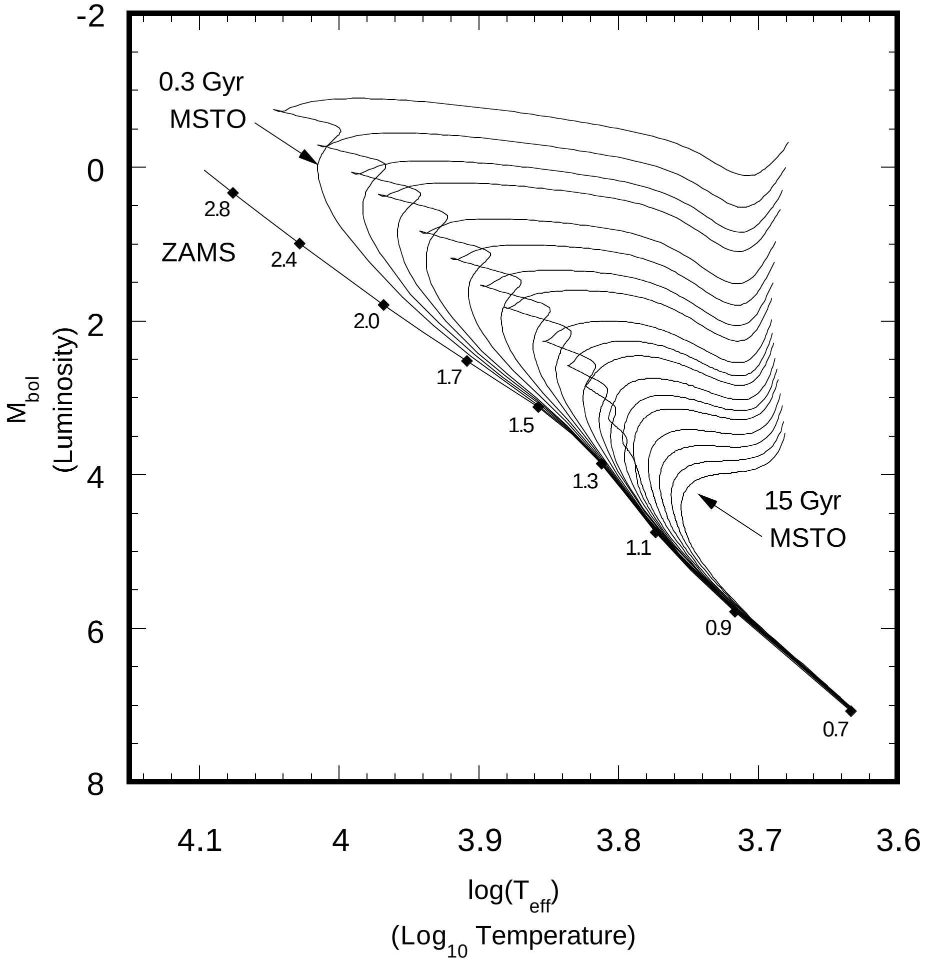

Figure 1.2: Model isochrones in the theoretical bolometric magnitude versus $\log(T_{eff})$ plane (VandenBerg 1985). The effect of increasing age can clearly be seen as lower mass stars evolve away from the Zero Age Main Sequence (ZAMS). The numbers along the ZAMS indicate stellar mass in solar masses $(M/M_{\odot})$. The composition is solar, where $Z = 0.0169$ and $Y = 0.25$[4].

---

[4] The fractional abundances of hydrogen, helium, and all other heavier elements is sometime described by the symbols X, Y, and Z respectively. By definition X+Y+Z=1.

translate effective temperature to an observable color index, usually $B-V$ or $V-I$. The exact relationship between effective temperature and color depends on the chemical composition of the model atmosphere, as does the evolution rates of our model stars. For this reason small differences in estimates for the chemical abundances of a cluster can have a large effect on its isochrone age. The net effect of decreasing the overall model abundance is $\Delta[Fe/H]/\Delta t \approx 0.5-0.7$, where Δt is in Gyrs (see VandenBerg 1988).

Open Clusters

The morphology of open cluster color–magnitude diagrams (CMDs) is usually characterized by a well defined main sequence and a bright blue turnoff. In the older open clusters enough stars have evolved to begin populating the red giant branch. Such is the case for the CMD shown in Figure 1.3 for the Praesepe cluster. It is clear from the diagram that the Praesepe has evolved beyond the zero age main sequence. The Praesepe is a member of the Disk population and is a middle aged cluster at approximately 0.9 Gyr old as indicated by the isochrones overploted on Figure 1.3. The lack of a well defined turnoff point for the young open clusters makes it difficult to obtain better than 20% internal precision from stellar isochrones. However, the oldest known open clusters have had sufficient time to evolve, and have color magnitude diagrams resembling those of globular clusters (shown below).

The two oldest known open clusters that are well studied are NGC–188 and NGC–6791. Demarque *et al.* (1992), using isochrones calculated from models with enhanced oxygen to iron abundances, estimate their ages to be 6.5

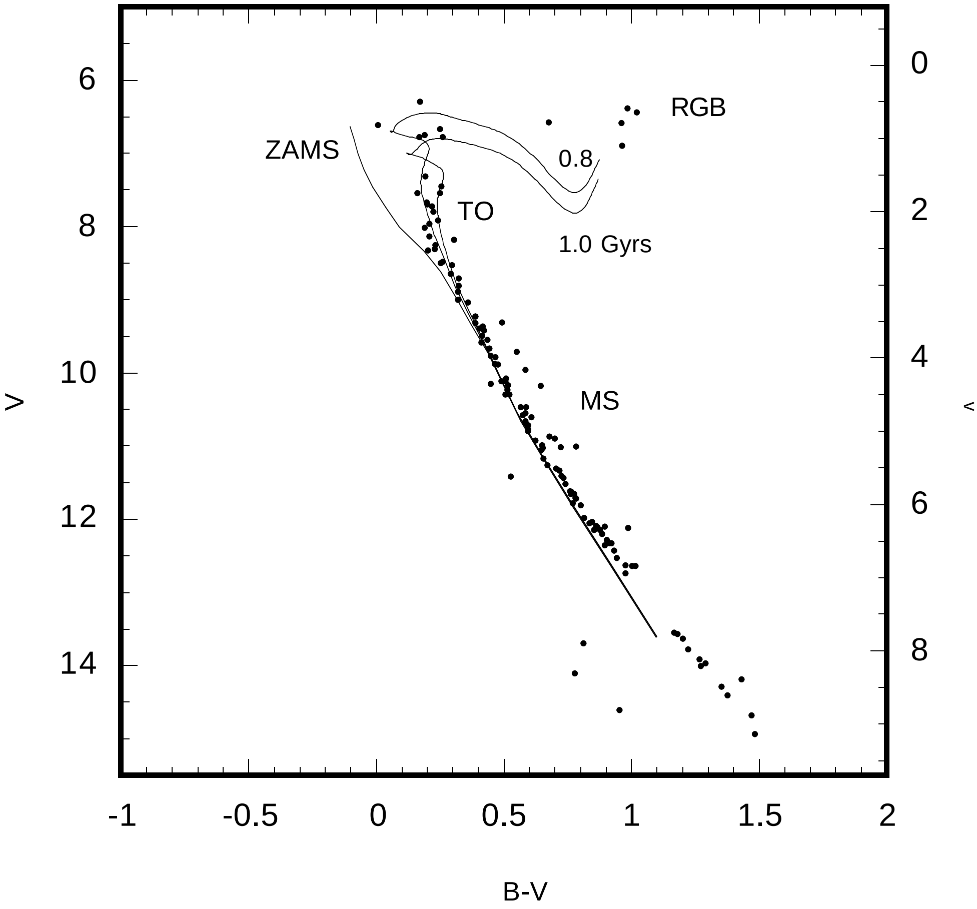

Figure 1.3: Color-Magnitude diagram of the Praesepe (M44) open cluster showing the location of the main sequence (MS), the red giant branch (RGB), and the main sequence turnoff (MSTO) point. The observations are from H. L. Johnson's photoelectric work (1952). Two isochrones at 0.8 and 1.0 Gyr from VandenBerg (1985) have been superimposed. The cluster's age is estimated from these isochrones to be between 0.8 and 1.0 Gyr.

and 6.5–7.5 Gyrs, respectively. VandenBerg (1992) notes that by changing the $[O/Fe]$ abundance ratio by 0.25 in stellar evolution models affects a computed isochrone by decreasing its age 1 Gyr. Without oxygen enhancement the ages for NGC–188 and NGC–6791 are estimated near 10–12 Gyrs. These two clusters are important for estimating the age of the Galaxy if in fact they represent the oldest clusters formed in the Disk.

Globular Clusters

In contrast to the relatively young open clusters, the effects of age can clearly be seen in the color magnitude diagram of an older globular cluster shown in Figure 1.4. Characteristic of all globular clusters is the pronounced turnoff point. In principle this enhanced turnoff would allow a more precise age estimate, but globular clusters pose their own difficulties. For example, according to Renzini (1986) the precision in estimating distance moduli to globular clusters is limited to ~0.2 magnitudes, which translates to a 3 Gyr uncertainty in the globular cluster isochrone ages. This represents the majority of the limiting uncertainty in obtaining absolute isochrone ages from globular clusters, estimated to be $\pm 3-4$ Gyrs (VandenBerg 1991). The oldest globular clusters have isochrone ages of ~17 Gyrs from recent models (see Bencivenni *et al*. 1991; Chaboyer *et al*. 1992). There is the possibility of systematic errors in stellar evolution calculations, resulting in globular cluster ages too old by several Gyrs. It seems that our understanding of stellar evolution is sufficient to model the relatively *static* zero–age main–sequence, but small uncertainties compound to produce large errors in ages – particularly for the oldest stars. If Hubble's constant is somewhere near 75,

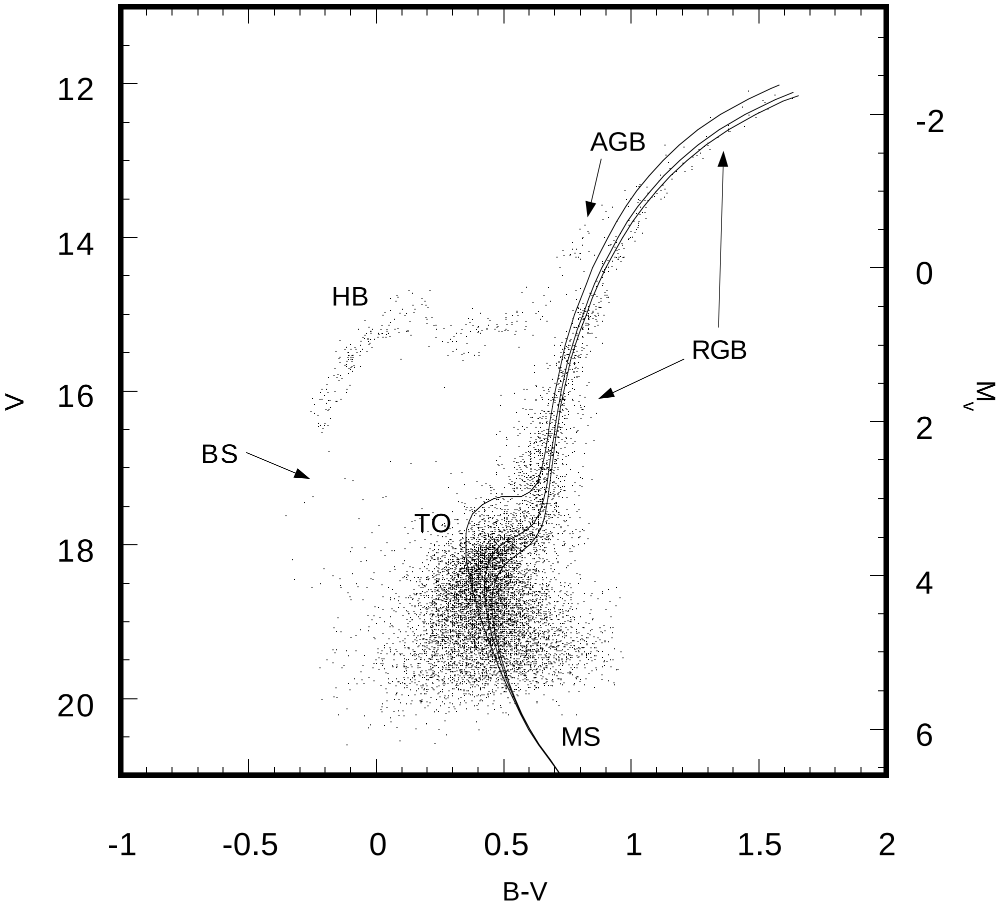

Figure 1.4: The color-magnitude diagram for the globular cluster Messier 5. Superimposed on the observed photometry are the oxygen enhanced model isochrones from Bergbusch and VandenBerg (1992) for 8, 14, and 18 Gyrs at a distance of 7600 parsecs. Also indicated are the cluster's main sequence (MS), turnoff point (TO), blue stragglers (BS), horizontal branch (HB), red giant branch (RGB), and the asymptotic giant branch (AGB).

a value which various researchers seem to be converging upon, then it becomes increasingly difficult to fit the old globular cluster isochrone ages within a Big Bang cosmology.

More recently, a differential approach has been used to investigate the apparent spread in absolute ages of globular cluster systems (VandenBerg 1990; Sarajedini and Demarque 1990). The method uses the difference in color between the positions of the turnoff point and the base of the red giant branch, which is essentially independent of abundance differences (Bolte 1992). From this method Da Costa *at al.* (1992) finds the inner cluster system to have a large age spread of $3-5$ Gyrs, whereas the outer metal–poor clusters have an age spread of ~0.5 Gyr.

1.4.2 Nuclear Age Estimates

Another common method for estimating the Galaxy's age comes from the radioactive decay of long lived isotopes. By measuring the abundance ratios of various isotopes it is possible to estimate the time elapsed since the isotopes were originally formed. In lecture papers, Fowler (1987) and Fowler and Meisl (1986) assume that nucleosynthesis in the solar system was frozen in at the formation time. From the abundances of elements $^{232}\mathrm{Th}$, $^{235}\mathrm{U}$, and $^{238}\mathrm{U}$ currently found from terrestrial observations they estimate that 5.4 ± 1.5 Gyrs passed prior to the formation of the solar system. By adding to this time the age of the solar system, 4.6 ± 0.1 Gyrs (Wasserburg *et al*. 1977), Fowler estimates the Galaxy's age to be 10.0 ± 1.5 Gyrs. By including beta–delayed fission, this age can be calculated to be considerably larger, between 12.4 and 14.7 Gyrs (Cowen, Thielaman, and Truran 1986).

A similar and somewhat more direct application of this technique is used by Butcher (1987) who measured the abundance ratio of $^{232}\mathrm{Th}$ (with a half life of 14 Gyrs) to Nd (Neodymium) in 20 stars of various suspected ages, up to 19 Gyrs. In his sample no star shows an age older than 11–12 Gyrs based on the observed spectral line ratio $^{232}\mathrm{Th}/\mathrm{Nd}$. Similar results have been obtained from other isotope ratios which are reviewed by Schramm (1990). In my opinion this calls into question the extreme ages claimed for the globular clusters and Halo field stars. Furthermore, inferring the overall age of the Galaxy from this method is perhaps a bit of a stretch. How the Galaxy actually did form and what nuclear process went on at that time will no doubt affect these ages. It is probably safe to assume the ages measured are for the Galactic Disk but not for the whole Galaxy.

1.4.3 White Dwarf Cooling Times

White dwarf stars are the cooling remnants of stellar evolution for most stars having masses $\leq 8M_{\odot}$. The rate at which they cool depends mostly on their mass - the more massive white dwarfs cooling more slowly than the less massive ones. This is caused by the inverse mass – radius relation ship for white dwarfs making the more massive ones smaller with less surface are to radiate their energy. When they are first formed, white dwarf stars are extremely hot, with surface temperatures exceeding 100,000 Kelvin, and they cool very quickly - spending little time in their initial hot state. Because of this, the age of an old cool white dwarf star is essentially independent of what temperature it started from. Furthermore the amount of time the oldest white dwarfs have spent cooling is long enough that their earlier time spent as "normal" nuclear burning stars is but a small fraction of their total age. For these reasons and others, described in detail in Chapter 2, white dwarf stars make excellent chronometers to measure the history of star formation and evolution in our Galaxy.

Maarten Schmidt (1959) first suggested that the age of the Disk could be found by comparing the luminosity of the coolest white dwarfs with the age–luminosity relation of Mestel (1952). Later, Greenstein (1971) predicted that the finite age of the Disk should cause an observable deficiency of white dwarfs at low luminosities. Following this, D'Antona and Mazzitelli (1978) first laid the mathematical groundwork for computing a theoretical white dwarf luminosity function which included a finite Galaxy age. After several failed attempts, it was Liebert (1979, 1980) who demonstrated that indeed there was a significant and real turndown in the observed white dwarf luminosity function. Winget *et al.* (1987) first applied this technique to a preliminary version of the white dwarf luminosity function presented by Liebert, Dahn, and Monet (1988) to obtain a Disk age of 9.3 ± 2.0 Gyr.

Since these first estimates of white dwarf ages, various efforts have been made to improve on the precision of numerical models used to compute the age–luminosity relation. Most notable has been the efforts of Iben and Laughlin (1989) and Wood (1992, 1994). The effects of age on his computed luminosity functions can be seen in Figure 1.5, where models having ages of 8, 9, 10, and 11 Gyrs are shown along with the observed luminosity function (In Chapter 2 that follows, I discuss these observations and calculations in detail). Wood's (1992) "best guess models" indicate an age between 8 and 11 Gyrs for the Galactic Disk, or more precisely the population of its field stars. Currently most of the

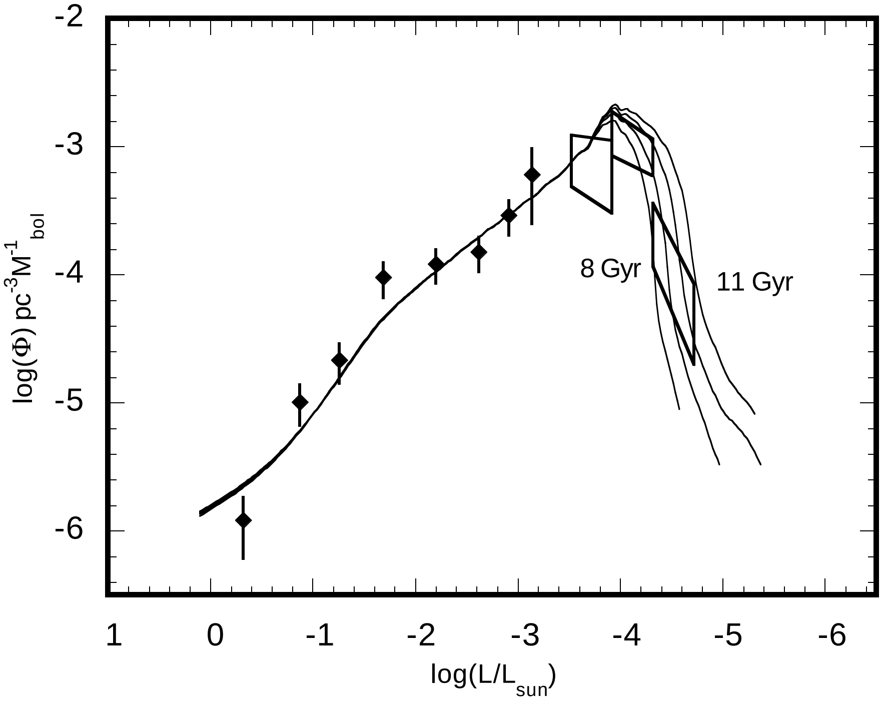

Figure 1.5: The effects of age in model white dwarf luminosity functions for Disk ages of 8, 9, 10, and 11 Gyrs (Wood 1992). For comparison the observed WDLF from Liebert, Dahn and Monet (1988) is also shown (filled diamonds and boxes).

uncertainty of this method lies in the uncertainties in estimating bolometric corrections appropriate for cool degenerate white dwarfs, necessary to translate between observed brightness and luminosity.

One of the main observational difficulties with white dwarfs is that they are very faint and therefore hard to detect. The coolest white dwarfs, the oldest ones used for ages, are some 50,000 times fainter than the age sensitive stars near the turnoff in the oldest globular clusters. Because of this we are currently limited to only those white dwarfs near enough to be seen, which means within 100 parsecs of the sun. In spite of this it is important to note that Liebert (1989) and Oswalt and Smith (1994) have discovered a handful of white dwarfs possessing Halo–like properties within the local stellar population. This implies an intriguing possibility of estimating the age of the Halo field population from white dwarf cooling times. This led several investigators to explore theoretically the possible forms of the luminosity function for Halo white dwarfs, which in terms of space densities range from very high (Tanamaha *et al.* 1990), to moderate (Mochkovitch *et al.* 1990), to quite low (Wood, 1990). Presently, the observational data are unable to constrain any of these models.

1.5 SUMMARY OF AGES

The isochrone age for the Disk is currently based on its two oldest open clusters, NGC–188 and NGC–6791. Depending on the assumed $[O/Fe]$ abundance ratio, we obtain considerably different ages for these two important clusters. With enhanced $[O/Fe]$ their ages are 6.5–7.5 Gyrs, while without this enhancement their isochrone ages are 10–12 Gyrs. If the enhanced $[O/Fe]$ model ages are correct then there appears to be a possible discrepancy between the isochrone Disk age and the age obtained from white dwarf cooling times of 8–11 Gyrs. One way to account for this is by supposing that the oldest open clusters observed are not among the first formed, these having been dynamically disrupted over their many orbits around the galaxy. The nuclear ages, if they are only measuring the Disk age, would tend to support this hypothesis.

Globular cluster ages from isochrones range between 13–18 Gyrs, the oldest of these placing an upper limit on the age of the Galaxy. At first glance this would indicate that the Disk of the Galaxy is considerably younger than the globular clusters and the Galactic Halo. However, if as Sandage (1990) suggests, we let inner globular clusters with disk–like properties (*i.e.* 47 Tucanae with an age of 14 Gyrs) set the age for the Galactic disk then there is no significant age difference between the disk and halo. This would lend support to the original model of Eggen, Lynden–Bell, and Sandage which suggested that the Galaxy formed from collapse of a larger cloud of material and that the collapse was rapid (10^8 years).

In Table 1.2 I have summarized the confusion of ages in the Galaxy, which existed prior to this thesis. It is clear that we are a long way off from obtaining an overall self-consistent picture of the Galaxy's age from these estimates. It might appear that since stellar isochrones have been used for every population except the Disk field stars, they are the only key to reconciling a self-consistent picture of the Galaxy's age. I do not believe this to be so. This is because there are too many variables which produce a wide range in estimated ages. Also, with stellar isochrones there is no way to estimate ages for all the populations using a *single* set of models. So, what can we do to build a coherent and consistent description of the Galaxy's age?

Because of the relative insensitivity of white dwarf cooling times to initial conditions, white dwarfs offer the best chance of obtaining our goal, either directly or by using their cooling times to calibrate the other methods. In addition, the homogeneity of white dwarf compositions (Clemens 1994) allows us to use a single set of models for estimating their ages. This fact eliminates the possibility of systematic differences in estimated ages between populations of differing abundances, as is almost certainly the case for stellar isochrones. Finally, within our understanding of stellar evolution, we believe that white dwarfs are formed by every stellar population. Therefore, if we can find them it should be possible to exploit the white dwarf stars to determine their ages and to construct a self–consistent picture of the Galaxy's age.

Table 1.2: The ages of the different populations are summarized by what method was used to obtain them. If no age estimate has been made a "?" is indicated.

	Age Method (Gyrs)		
Stellar Population	Isochrones	Nuclear	White Dwarf
Disk – Field Stars	?	10–14	8–11
Disk – Open Clusters w Fe/O	6.5–7.5	?	?
w/o Fe/O	10–12		
Thick Disk	8-11	?	?
Halo – Field Stars	<17–18	?	?
Halo – Globular Clusters (Inner)	13–14	?	?
Halo – Globular Clusters (Outer)	13–17	?	?

2

The White Dwarf Luminosity Function

In the field of astronomy making the connection between observation and theory has always been somewhat difficult. The difficulty arises from the vast distances between ourselves and the things we study, making it impossible to apply the usual scientific method: Observation – Theory – Experimentation – Observation which leads eventually to understanding. In most scientific disciplines investigators can design and implement experiments which are created solely to test and probe specific theories. These researchers are able to postulate, "If X is true then when we do Y we should get Z", they design and build the apparatus to perform Y on their subject and observe whether they get the expected result Z or not. Thus in these fields there is an intimate connection between what is observed and what theoretical concepts are being tested via the experiment.

In astronomy, however, we must arrive at "understanding" almost exclusively without the experiment. We are limited to observation and theory. We can design new instruments to observe the universe in new ways, but we cannot alter by design an astronomical system to see if it will respond according to our theoretical models. Because of our limitations we must, therefore, exercise extreme caution when we attempt to project our interpretations of theory and observation onto the real world as true understanding. Furthermore, it follows that any theory which does not make observable predictions cannot be tested and is therefore useless.

This chapter is meant to establish both the observational and theoretical framework for my interpretation of the age and evolution of our Galaxy as it has been recorded by the white dwarf stars. I will point out where our theoretical descriptions succeed and where they fail, as well as where the observations appear to be real and where they appear to be jaded by some sort of bias.

2.1 PRE-WHITE DWARF STELLAR EVOLUTION

In Chapter 1 I described how the white dwarf stars could provide a coherent, self-consistent link between the ages of different populations in the Galaxy. Before I discuss in detail the luminosity function for white dwarf stars and its relevance to Galactic history, it will be instructive to know where the white dwarf stars come from. Specifically, I will pay particular attention to the time spent in the major stages of stellar evolution leading to the formation of white dwarfs, and to the total time necessary for a progenitor star to become a white dwarf. For a detailed description of how we think stars evolve I recommend the many articles by Icko Iben Jr., *Structure and Evolution of the Stars* by Martin Schwartzschild (1958), *Principles of Stellar Structure* by J. P. Cox and R. T. Giuli (1968), and *Principles of Stellar Evolution and Nucleosynthesis* by Donald D. Clayton (1968).

White dwarf stars are the final stage of evolution for most stars having masses less than ~8 $M_\odot$. This upper mass estimate for the white dwarf progenitor stars is based mostly on theoretical models with some support from observational studies (Anthony-Twarog 1982, 1984; and Weidemann and Koester 1983, 1984). While the exact path a given star takes in the H-R diagram depends on its initial mass, the 5 $M_\odot$ evolutionary track shown in Figure 2.1 represents the major phases through which most stellar models with less than 8 $M_\odot$ go prior to becoming white dwarfs.

These model white dwarf progenitor stars spend most of their time on the stellar main sequence. At this stage these model stars are undergoing nuclear fusion of hydrogen into helium in their cores via the p-p chain or CN – CNO bi-cycle - depending on the initial mass of the star, where the division occurs near $1.8 M_\odot$. In either case, the time scale for main-sequence evolution is set by the amount of fuel available and its rate of consumption in the stellar core is approximately proportional to the total stellar mass as expressed by

$$\tau_{MS} \propto \left(\frac{M}{M_\odot}\right)^{-2.5}. \tag{2.1}$$

For a star having a mass of 5 $M_\odot$ this first phase of evolution lasts $\approx 6\times 10^7$ years (points 1-2 in Figure 2.1). This time scale is determined by balancing the energy production rate needed to support the model star against its gravity and the total amount of fuel available to provide this energy.

As the star expends its supply of hydrogen, the total number of particles in the core is decreased as four hydrogen atoms ultimately combine to produce a single helium atom – hence reducing the available support and causing the core to

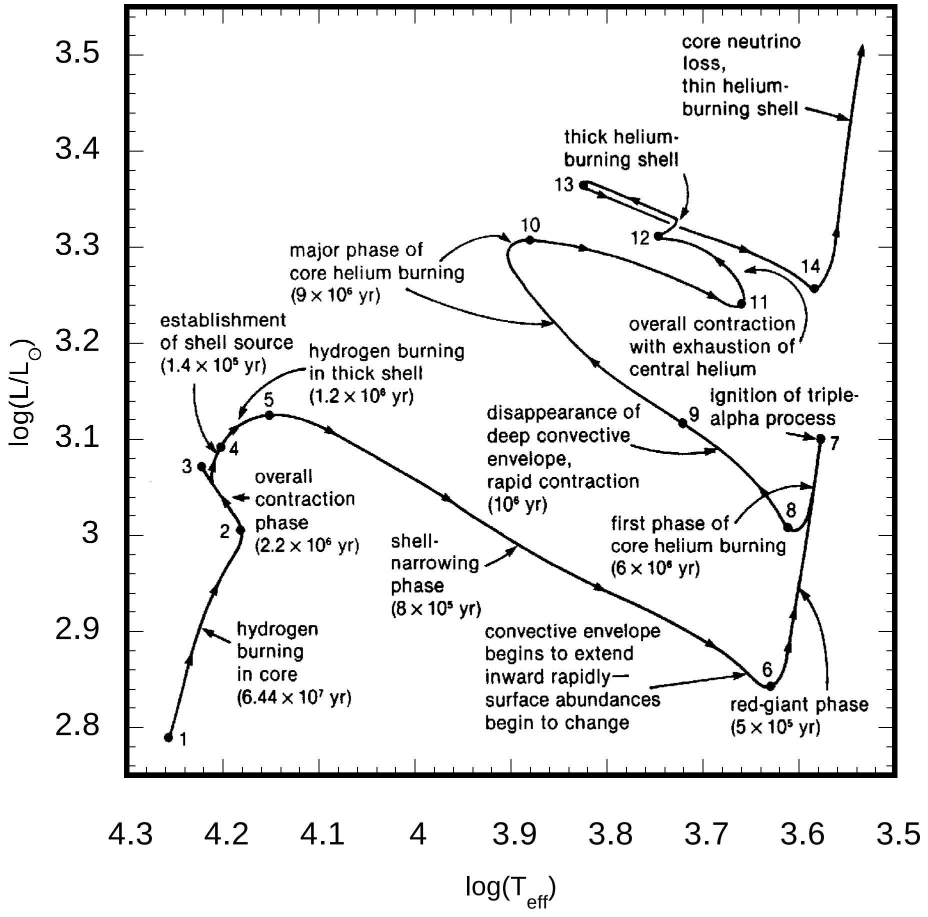

Figure 2.1: The evolutionary track of a representative model 5 $M_\odot$ star. Indicated between the numbered points are the major physical processes and time scales governing the star's evolution. (adopted from *The Astrophysics of Stars* by Bowers and Deeming)

contract. The contraction of the core produces gravitational energy, which is released into the outer layers of the star. In order to dissipate this *extra* energy the outer layers must expand to increase the radiating surface area of the star. This marks the beginning of the Red Giant phase of stellar evolution (points 6-7) and lasts for roughly 10^6 years.

The next lengthy stage of evolution follows the ignition of helium in the stellar core at the tip of the red giant branch (points 7-10 in Figure 2.1). The exact nature of the helium ignition depends on the total mass of the star. For a $5\,M_\odot$ star the helium core contracts and ignites the He triple-α process quiescently, quickly settling on the "helium main sequence". This is also called the Horizontal Branch because of where these stars lie in a color–magnitude diagram (see Figure 1.4). At this point the model star is burning hydrogen in a shell and helium into carbon in the core. If the star is not very massive, ($M \leq 3M_\odot$) by the time the helium core has contracted and heated to the point of ignition it has become degenerate. Upon ignition, the isothermal degenerate core does not expand to cool - hence the helium burning process is unregulated, resulting in a momentary runaway nuclear reaction. This is called the *helium flash,* and is halted when enough energy has been produced in the core to lift its degeneracy. It is believed that the core He flash happens many times while the star is at the tip of the red giant branch until the core finally ignites quiescently and evolves onto the Horizontal Branch. The time a star spends on the Horizontal Branch is roughly 10% of its main-sequence life time – of order 10^7 years for $5\,M_\odot$ star.

Following its stay on the Horizontal Branch, the star's core, exhausted of helium and with fewer particles, contracts once again causing the star to increase its luminosity – ascending the Asymptotic Giant Branch (the AGB is located beyond point 14 in Figure 2.1 – Iben and Renzini 1984; Mazzitelli 1989; Dorman *et al.* 1993; Iben 1994). Also by this point some of the carbon formed in the helium triple-α process has been fused to oxygen by the reaction $^{12}C(\alpha,\gamma)^{16}O$ (Fowler *et al.* 1975; D'Antonna and Mazzitelli 1990) leaving a carbon/oxygen core in the AGB star. However, the distribution and total mass fraction of carbon and oxygen are not well known. The exact amount of oxygen and other heavier elements depends on knowing precisely the internal state of these stars and the nuclear reaction rates forming these elements.

From the AGB the star begins to lose mass and enters the short lived post AGB phases. Primarily because it is a dynamical process on a short time scale, the exact nature of the mass loss process is poorly understood. The primary evidence we have that there must be considerable mass loss comes from the observed difference in the masses of white dwarf stars (averaging near $0.6M_\odot$) and their progenitor stars ($8M_\odot$ and less; see Weidemann 1990). Additional observable evidence we have for this mass loss comes mainly from the existence of planetary nebulae and the bipolar nebulae around some of the AGB stars (Trammell 1994). Planetary nebulae display a very hot central star with an emission nebula more or less symmetrically distributed around it. The name — *Planetary Nebula* — stems from the discovery observations, where the central star was not visible and only the nebula showed as a circular disk much like a planet. Planetary Nebulae (PN) are formed when the outer layers of a star are ejected, expanding radially away from the hot central core. The driving mechanism behind PN ejection is not well understood, but it seems to play a role in creating the uniformly thick ($10^{-4} M_\odot$) hydrogen layers in DA white dwarfs (Clemens 1994).

Model calculations estimate that in roughly $10^4 - 10^5$ years the PN dissipates, leaving behind the very hot remnant core of the progenitor star as a pre-white dwarf. As the pre-white dwarf star settles onto the white dwarf cooling track the chemical elements which differ significantly in atomic weight become fully stratified, through gravitational settling and diffusion. The remaining pre-white dwarf is left with a structure of hydrogen over helium, wrapped around a degenerate carbon-oxygen core. The actual structure of real white dwarfs is highly dependent on the details of the processes outlined above

These subsequent stages of stellar evolution, following initial core hydrogen burning, up to the point of white dwarf formation requires approximately 30–40% of the main-sequence time. For a $5\,M_\odot$ this amounts to approximately 8.6×10^7 years, which implies a proportionality constant to equation 2.1 of $\sim 5 \times 10^9$ years. There are two important consequences from these evolutionary time scales regarding white dwarf stars. First, the monotonic relation between mass and evolutionary time scale implies white dwarfs are formed sequentially by progenitor mass — the more massive progenitors form their white dwarfs first. Secondly, the oldest white dwarfs in the Galaxy have cooled many *e*–folding times from their original hot pre–white dwarf stage, and thereby have long since forgotten their origins. From this we can infer that the evolution of a cool white dwarf is *insensitive* to its initial conditions — the details of its earliest state.

2.2 THE CURRENT STATE OF THE OBSERVED WHITE DWARF LUMINOSITY FUNCTION

The space density of a given class of objects is determined by how many of this class are made in any given time interval and how long these objects spend as that class. A luminosity function (LF) is defined according to how the space density of the objects in question varies as a function of intrinsic luminosity. This can be described by a convolution of formation rates and class duration times. In general the classical luminosity function estimator, given by

$$\Phi_C(l) = \left.\frac{N}{V}\right|_l = \frac{dn}{dL}, \tag{2.2}$$

(Lamb and Van Horn 1975; Felton 1976, Iben and Laughlin 1989), as we will see in §2.3, will be our connection between observation and theory. It is absolutely critical that one has a statistically complete, or tractable,if not complete, sample from which to estimate the true space density of objects. Otherwise it is possible to make gross systematic errors and completely misinterpret the inferred physics and astronomy.

What we usually observe to estimate the LF of a class of objects are the numbers of this class found in surveys of known volume. Unfortunately we typically have too few objects or have systematic biases in our sample which preclude effective application of equation 2.1. We are thus forced to estimate the luminosity function in some other way which makes best use of the information available.

The technique most widely used in white dwarf studies is the $1/V_{\max}$ method developed by Schmidt (1975). When the $1/V_{\max}$ is applied to a group of objects each object does not contribute equally to the estimate of space density as implied by equation 2.2. Instead, each object is weighted by the maximum volume a selected object could occupy and still be included within the survey's limits. The straight $1/V_{\max}$ method implicitly assumes that the distribution of objects in the survey volume is uniform and that the sample is complete. As part of the $1/V_{\max}$ technique the completeness is tested under the assumption of a uniform distribution by

$$\sum_{i=1}^{N} \left. \frac{V_{obs}}{V_{\max}} \right|_i \approx \frac{1}{2}, \tag{2.3}$$

where i is the object index, N is the total number of objects in the sample, and V_{obs} is the volume of the survey at the observed distance for a given object.

For most white dwarf surveys we do not make serious errors by assuming that the sample is uniformly distributed. This is because the faintness of white dwarf stars has prohibited sample volumes large enough such that changes in Galactic structure affecting the distribution of stars are significant. However, as new surveys probe to fainter limits and begin discovering objects at greater distances, the effects of Galactic structure do become important. To first order we can correct for this by modifying the volume determination by $V_{eff} = V \exp^{-(z/z_0)}$, where z_0 is the scale height of the Disk perpendicular to the Galactic Plane. Strictly speaking, if there were a very large deep survey there would have to be an additional correction applied to the volume as a function of Galactic position, accounting for non-spherical geometry and geometric projection effects on the scale height.

In addition, the white dwarf luminosity function (WDLF) is of little value in constraining Galactic evolution and stellar ages unless we can compare it to our numerical models. For this reason the observed WDLF is transformed from space density versus M_v to space density versus $\log L/L_\odot$. In this section I describe the current state of the observed WDLF and the limitations imposed by its sources and its transformations.

2.2.1 Disk White Dwarfs

Early estimates for the space density of white dwarf stars stemmed from the proper motion work of Luyten (1958) and the compilations of Eggen and Greenstein (1965, 1967). Weidemann (1967) used these samples to estimate the observed luminosity function using 167 objects. Although these samples were seriously affected by observational biases the Weidemann, and later the Kovetz and Shaviv (1976) LFs, clearly showed the trend to be increasing space densities at lower luminosities. The significance of this work is the confirmation that white dwarf stars are basically only cooling as they evolve, as first described by Mestel (1952). Sion and Liebert (1977) reconstructed the WDLF from a larger sample of 424 spectroscopically identified white dwarf stars. They used their observed LF to compare with the theoretical LF sequences of Lamb and Van Horn (1975) showing at least moderate agreement between the two. Sion and Liebert (1977) also investigated the space velocities of their sample, finding that within statistical scatter all spectral types had more or less the same kinematics of the Disk population. However the 424 stars in Sion and Liebert (1977) did not come from a homogeneous source, making precise statistical study difficult.

The observed white dwarf luminosity function for the Galactic disk is currently best described by the white dwarf samples from two sources. Figure 2.2 shows the combined luminosity function from the Palomar–Green survey white dwarfs and those found in the Luyten Half Second proper motion survey having proper motions >0.8"/yr.

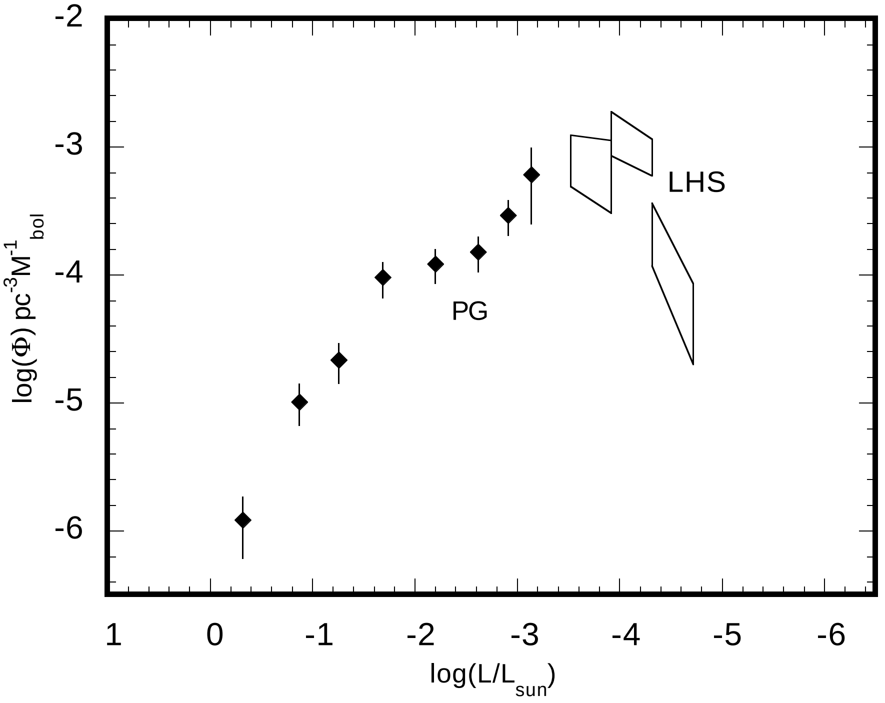

Figure 2.2: The observed white dwarf luminosity function from the Palomar–Green (PG) survey and the Luyten Half arcSecond (LHS) proper motion survey. The filled points with their error bars are from the PG survey sample, while the boxes are from the LHS >0.8″/year sample. The boxes represent uncertainties in both space density (mostly from small number statistics) and luminosity determination arising from ambiguous bolometric corrections.

The PG Sample

In Figure 2.2 the WDLF resulting from the Palomar–Green survey is represented by filled diamonds and their corresponding error bars. The Palomar–Green Survey (Green *et al.* 1986) was primarily conducted to search systematically for quasars, but as a result of the search technique many white dwarf stars were also found. The Palomar–Green (PG) Survey photographed 10,714 square degrees in the equivalent of broad band U and B filters using the 18 inch Schmidt telescope at Mt. Palomar. In the PG Survey, Green selected objects on the basis of ultraviolet (UV) excess, singling out those objects having $U - B < -0.36$. On the basis of this UV excess criterion the PG survey uncovered some 1874 objects to a mean limiting magnitude of B=16.2.

Because the PG survey was conducted in a systematic way, the limitations and selection techniques of this survey were well enough understood such that quantitative statistical analyses could be made on the objects discovered. Based on reliable completeness estimates for the 1874 objects selected, Green determined that 1715 represented a statistically complete sample. Through spectroscopic follow-up, 448 of these objects were discovered to be white dwarf stars, mostly of spectral type DA[1], many more than in any previous statistical study. For these reasons the PG white dwarf sample represents the best data for estimating the white dwarf luminosity function.

---

[1] White dwarf stars are separated into different spectral classes on the basis of the elements found in their optical spectra (Sion *et al.* 1983; Liebert and Sion 1994). By far the most comman spectral type is that of DA which show only hydrogen absorption; the second most common is type DB having lines of helium I; the other spectral types DC, DZ and DQ (continuum dominated spectra, metalic spectral features and strong carbon Swan bands repectively) are not nearly so common. Finally the hottest white dwarfs and pre-white dwarfs showing lines of helium II and other highly ionized metals are classified as spectral type DO.

However, by its nature, the UV excess selection technique used by Green limited the PG survey to only the hotter white dwarfs. The $U-B<-0.36$ criterion effectively limits the complete sample to those white dwarfs hotter than $\sim 10{,}000\mathrm{K}$ or $M_v \approx 13.25$. For a DA white dwarf this corresponds to a luminosity of $\log(L/L_\odot) = -3.2$, well short of where the predicted turndown from the Galaxy's age should be. In spite of these limitations, the PG white dwarf sample made a significant step forward in estimating the WDLF and the overall white dwarf space density.

Green (1980) presented a preliminary WDLF using a complete subset of 89 white dwarfs from the PG survey. This was later improved on by Flemming, Liebert, and Green (1986 – here after FLG86), who used the full sample of 353 spectroscopically identified DA white dwarfs to estimate the WDLF. FLG86 used empirical relations to multi–channel colors (Greenstein 1976, 1984), Strömgren colors (Green, 1980), broad band UBV colors (Sion and Liebert 1977), and their own Hβ relation to estimate absolute visual magnitudes (M_v) for all 353 DA white dwarfs in the PG sample. The resulting WDLF for DA white dwarfs was estimated by FLG86 using the $1/V_{\max}$ method corrected for an exponential density distribution with a characteristic scale height of 250pc. The DA WDLF was then corrected with the observed ratio between DA and non-DA white dwarfs (Liebert *et al.* 1986), to estimate the WDLF for *all* spectral types. FLG86 presented their WDLF in the density (Φ) versus M_v plane, in units of $pc^{-3}0.5mag^{-1}$ over the range of $7.7 \geq M_v \geq 13.0$. The WDLF from the PG survey shown in Figure 2.2 is the FLG86 WDLF transformed by Liebert, Dahn, and Monet (1988) onto the Φ versus $\log(L/L_\odot)$ plane using their $M_v \Rightarrow M_{bol}$ relation.

To date, this represents the best estimate for the WDLF in the range of $0.0 \leq \log(L/L_\odot) \leq -3.2$.

The primary limitation of the PG WDLF is the number of white dwarfs in the sample. Although the PG WDLF is sufficient to constrain the overall physics of white dwarf cooling theory, it is still too coarsely sampled to map out the Galaxy's past star formation history (see Figure 16 in Wood 1992). The 0.5 magnitude bin size of the FLG86 WDLF is limited by the number of objects in the sample – smaller bins would result in too few objects, hence large density uncertainties for each bin, to be scientifically useful. Therefore, if we are to exploit this record of the Galaxy's past, *many* more white dwarfs must be discovered in statistically meaningful surveys.

There are several possible sources of error in the PG WDLF. Difficulties in estimating M_v and M_{bol} for white dwarfs with temperatures $> 70,000\mathrm{K}$, affect the first bin in the presented WDLF. Although it does not impact our overall understanding of white dwarf cooling physics, it would affect the interpretation of the star formation rate corresponding to that epoch. A more serious source of systematic error is the correction to $1/V_{\max}$ for an exponential density distribution. If there is a significant change in scale height of the Galactic Disk over the range of ages covered by the PG WDLF, its slope would be misrepresented by a single scale height correction. Such an error in the WDLF slope affects the implied constraints on the physics of white dwarf cooling in this luminosity range. Here, again, with a larger sample we could estimate scale heights as a function of luminosity and directly correct for any scale height changes.

The LHS 0.8 Sample

White dwarfs which have evolved and cooled below $\log(L/L_{\odot}) \approx -3.2$ pose a special problem for their discovery. Because they have cooled below 10,000K, they no longer have a unique UV excess signature and they have also become so faint that it is difficult to search large volumes of space for them. This means that any that we do see will be relatively nearby. Their proximity allows us to use proper motions and reflex motions (parallax) for identification and analysis as white dwarf stars.

Liebert, Dahn, and Monet (1988 – hereafter LDM88) used the Luyten Half arcSecond (LHS – Luyten 1977, 1979) catalog of objects having proper motions ≥ 0.5 arcseconds per year to search for "cool" white dwarfs in the solar neighborhood. Out of the LHS catalog LDM88 selected a subset of stars with proper motions $\geq 0.8''$/year, finding 43 spectroscopically identified white dwarfs with $M_v \geq 13.0$ and above -20° declination. From these stars LDM88 estimated the WDLF below $\log(L/L_{\odot}) \approx -3.2$ with the following assumptions: 1) the LHS catalog is complete for proper motions $\geq 0.8''$/year to $V < 19$, and 2) there is a 20% incompleteness factor due to the lack of Galactic Plane fields in Luyten's original work.

Where available, LDM88 used trigonometric parallaxes to determine M_v, otherwise they used photometric parallaxes. LDM88 found that there is a significant decrease in the number of white dwarfs fainter than $M_v \sim 16.5$, and none with $M_v > 17$ to the density limits of their sample. Using the $1/V_{\max}$ method LDM88 constructed the WDLF for these 43 cool white dwarfs, showing conclusively for the first time the predicted turndown caused by the finite age of the Galaxy.

Unlike the hotter PG white dwarfs, converting the cool white dwarfs from M_v to $\log(L/L_\odot)$ is very difficult. The difficulty arises from the low temperatures of these stars: the coolest of these (LHS-69 (LP701-29), LHS-342 (LP161-66), and LHS-2673 (LP322-800)) have surface temperatures of $\sim 3750\mathrm{K}$. Below a temperature of approximately 10,000K the hydrogen lines in DA white dwarfs become increasingly weak, making it more difficult to identify the atmospheric composition. Without a clear idea of the principle constituents in the white dwarf atmosphere it is unclear which type of bolometric correction to apply. To complicate things more, at these low temperatures the role of molecules and ionic collisions in the atmosphere become important (Bergeron *et al.* 1994), and are very difficult to model in the high gravity environment of white dwarfs. Therefore, the bolometric correction between M_v and M_{bol} is uncertain even when we do know the atmospheric composition.

In an attempt to constrain the solutions to these problems LDM88 used two different estimates for the bolometric correction (BC): 1) BCs derived from hydrogen model atmospheres for DA white dwarfs and Plank's blackbody for non-DA, and 2) BCs derived directly from surface temperature estimates using

$$L = 4\pi R^2 \sigma T_{eff}^4 . \tag{2.5}$$

In Figure 2.2 the WDLF from LDM88 is represented by 4–sided polygons, where the left side is determined from case 1 BCs and the right side from case 2 BCs.

The box is formed by connecting the associated errors in the vertical direction between the two $M_v \Rightarrow M_{bol}$ transformations.

The transformed WDLF in either case clearly shows the turndown near $\log(L/L_\odot) \approx -4.5$ due to the age of the Galaxy. However, the exact location of this turndown is sensitive to what the true BCs are, hence this ambiguity in BCs translates directly into uncertainties in the age of the Galactic Disk inferred from the WDLF (see Figure 1.5). Liebert, Dahn, and Monet (1989 – hereafter LDM89) improved the precision of the LDM88 WDLF with refined trigonometric parallaxes reducing the errors in density, but this does not significantly affect the BC uncertainties. A potential source of significant error in the LHS WDLF is the systematic failure to include objects with low tangential velocities, falling below the proper motion limit set by LDM88. LDM89 indicates that the effect of missing low velocity objects could cause the WDLF in LDM88 to underestimate the space density of cool white dwarfs by as much as 100% by number or 0.3 in $\log(\Phi)$. If this bias is present in the LDM88 sample it is also most likely to be a function of luminosity; the more luminous bin in the LDM88 WDLF is more affected than the fainter bin. This would cause the overall shape of the WDLF in the range of $-3.5 \leq \log(L/L_\odot) \leq -4.7$ to be altered, affecting both the inferred age of the Galactic Disk and the constraints placed on white dwarf cooling physics in this domain (*i.e.* crystallization of the white dwarf core).

From their data LDM89 contend that the reality of the turndown in the WDLF is not an issue by the fact that the space density of white dwarfs with $17.0 \geq M_v \geq 17.5$ must be down an order of magnitude from the WDLF peak. However, the LDM88 sample does not explore enough volume to say anything about the space density of white dwarfs with $M_v > 17.5$, which would be older and could possibly belong to the Galactic halo. However, Ruiz (1994) may have found a white dwarf with $M_v \sim 17.5$. It is uncertain if this object is a very old Disk white dwarf, a high mass object, or an old halo white dwarf. It will be extremely interesting and important to determine population membership of this object. If a WDLF for cool white dwarfs is constructed from a deep, photometrically selected sample, it is possible to overcome the limitations in the LDM WDLF. However, prior to this thesis, there did not exist an effective photometric technique for the discovery of faint cool white dwarf stars.

2.2.2 Other WDLF Estimates

There have been other estimates of the WDLF from recent surveys that have resulted in important confirmation of the PG/LHS WDLF. In my opinion one of the more important contributions has been from the APM (Australian Proper Motion) project (Evans 1992; 1989). The limiting proper motion from which Evans draws his sample is $0.04''$/ year and has a limiting O magnitude of ~21 (the O bandpass is defined by the blue response of Kodak "103–a O" emulsion and is roughly equivalent to broad band B). From the APM sample Evans used reduced proper motions versus color (equivalent to M_v versus color) to select 123 white dwarf candidates (see Figure 10 in Evans 1992).

Using the $1/V_{\max}$ method Evans constructed a luminosity function for the APM white dwarf stars, which along with the PG/LHS WDLF is shown in Figure 2.3. The most significant aspect of the APM WDLF is that its luminosity range covers both that of the kinematically unbiased PG and the LHS luminosity

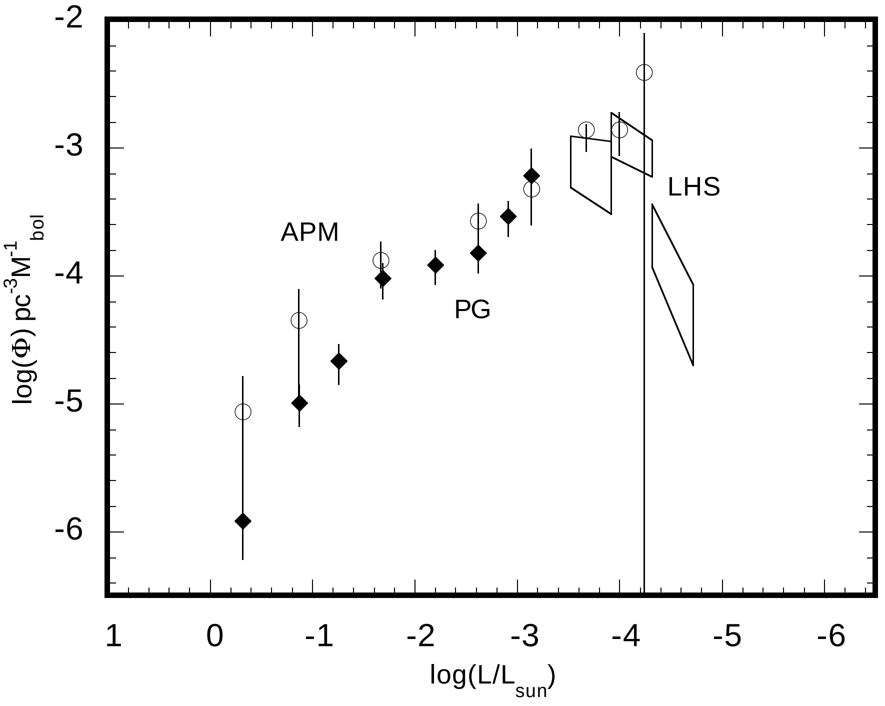

Figure 2.3: The WDLF from the APM Proper Motion Project (Evans 1992; open circles with error bars) shown with the Liebert *et al.* (1988) WDLFs (filled diamonds with error bars and 4–sided polygons). The most significant feature of the APM WDLF is the consistent agreement with the Liebert *et al* WDLF across the PG – LHS boundary.

functions. The APM WDLF is in good agreement with both the PG and LHS WDLFs at the boundary of the later. This would indicate that within the errors of the three WDLFs there is no serious discontinuity between the PG and LDM WDLFs caused by missing low velocity white dwarfs. Although, if we examine the data at face value the location of the Evans datum near $\log(L/L_{\odot}) \approx -3.6$ is approximately 0.3 in $\log(\Phi)$ above the mid-point of the LDM88 datum. While not statistically significant, this is interesting given that the APM limits significantly reduce the possibility of missing low velocity white dwarfs as mentioned above.

Unfortunately the APM WDLF fails to verify the turndown seen in the LDM88,89 WDLF, primarily because of the limitations in using reduced proper motions for candidate selection. In the plane of reduced proper motion versus color, the white dwarf locus at low luminosities becomes confused with the locus of the low metalicity Halo population. This confusion renders reduced proper motion an ineffective selection technique for white dwarfs near the WDLF turndown and beyond.

For the hot white dwarfs covered by the PG sample there are many other estimates for the WDLF. Most notable are the WDLFs from the AAT QSO (Anglo-Australian Telescope Quasi-Stellar Object) survey (Boyle 1989) and the Edinburgh–Cape UVX (UltraViolet eXcess) survey (O'Donoghue *et al.* 1993). I have transformed the AAT and Edinburgh–Cape (EC) WDLFs onto the bolometric scale following the techniques in FLG86 and LDM88, correcting for the ratio of DA to non-DA and the difference in bin widths between M_v. These are shown in Figure 2.4. Both estimates for the WDLF from the AAT and EC surveys are in at least reasonable agreement with the PG sample, although the errors in the AAT data in some places do not overlap those for the PG data. No errors were given for the EC data. In addition, the smaller Downes survey in the Galactic plane (Downes 1986) and the Kiso Schmidt UVX (Ishida *et al.* 1982) survey have also produced luminosity functions which are in good agreement with the PG WDLF.

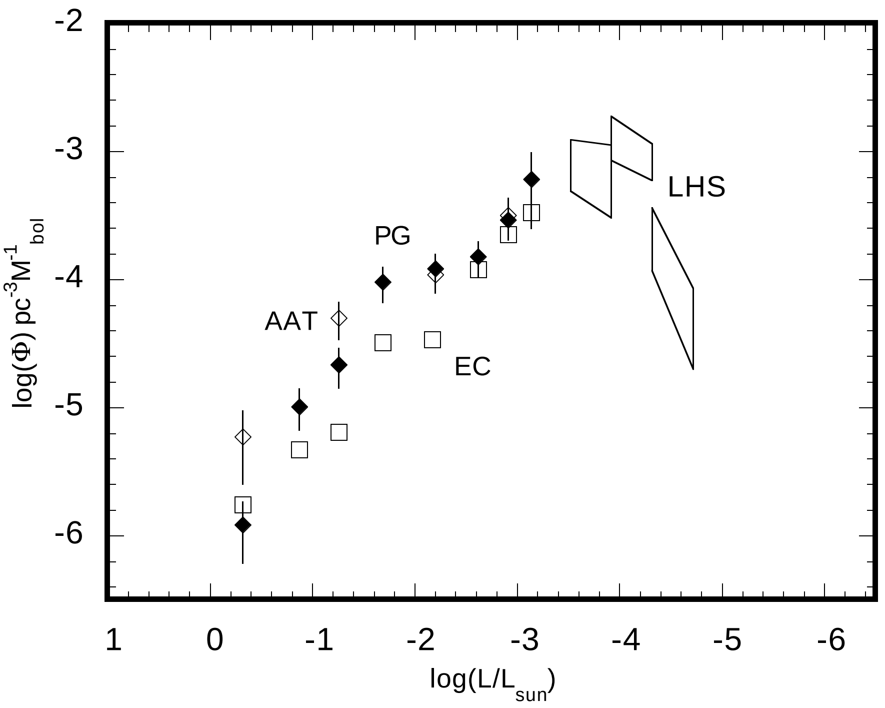

Figure 2.4: The WDLF from the AAT (open diamonds) and Edinburgh Cape (open squares) surveys compared with the PG/LHS WDLFs (filled diamonds and polygons).

Up until now I have exclusively discussed the luminosity functions for single isolated white dwarfs. There remains one other significant contribution to the WDLF from the project undertaken by Oswalt and Smith (1994). Their project involves searching for white dwarf companions in common proper motion binaries (CPMB). For their source Oswalt and Smith used the CPMB lists from the proper motion catalogs of Luyten (mainly the LP survey) and Giclas. In this work they have discovered some 274 white dwarfs, from which they have used 66 to construct a preliminary LF for CPMB white dwarfs. In Figure 2.5 I have transformed the Oswalt–Smith CPMB WDLF onto the same bolometric scale as the previous plots. The two sets of data are their raw data (open squares) and the same data corrected for incompleteness (open circles) in their sample. The overall slope and shape agree well with the PG/LHS WDLF although the CPMB WDLF does not show signs of a turndown at the low luminosity end. This is not yet significant since the last data point in the CPMB WDLF is represented by a single object.

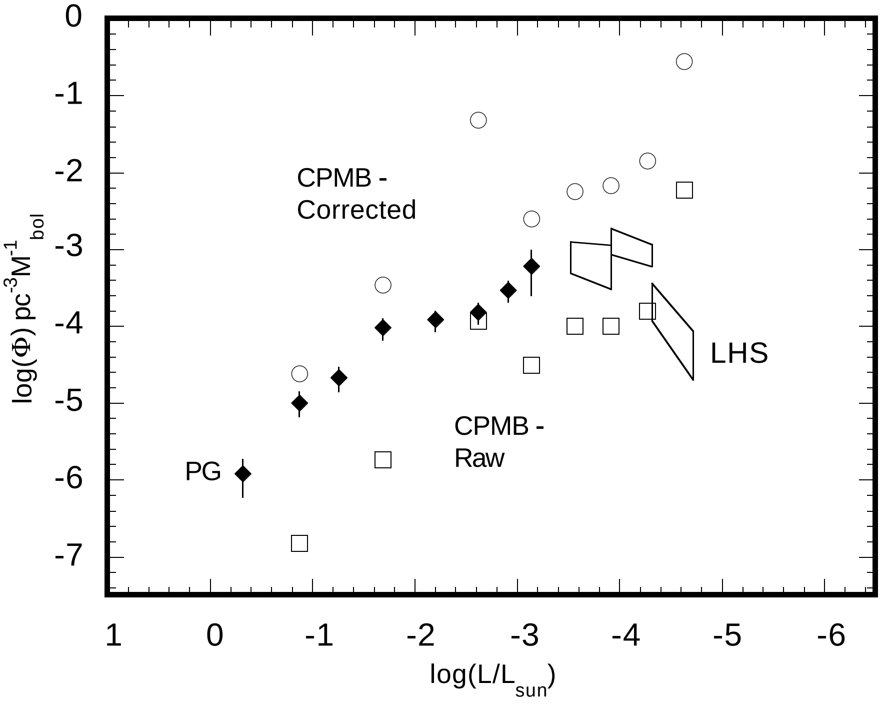

Figure 2.5: The preliminary estimate of the WDLF from the CPMB survey of Oswalt and Smith (1994) containing 66 stars. The two data sets shown are the uncorrected (open squares) and completeness corrected (open circles) LFs.

In addition, there are two very interesting features to note in the Oswalt–Smith LF. First, the large and apparently significant peak near $\log(L/L_\odot) = -2.6$ indicates an excess in white dwarfs above a constant birthrate. Secondly, the incompleteness corrected LF shows that the overall space density for CPMB white dwarfs is higher than for single isolated WDs. This is interesting because it is difficult to account for with any simple explanation. Certainly there is the issue of completeness of the proper motion samples, while true for the proper motion samples it is probably not true for the PG sample. The APM WDLF supports this and suggests that the LHS sample is not seriously incomplete or that the APM and LHS samples share identical selection effects. Clearly there is something to be learned here from the difference in overall space densities for single isolated and CPMB white dwarfs.

2.2.3 The Halo White Dwarf Population

There are currently two estimates of the WDLF for the Galactic Halo population. A preliminary WDLF for the Halo has been estimated by LDM89 from the original LHS > 0.8"/yr white dwarfs. Oswalt and Smith (1994) also estimate a Halo WDLF from objects found in their common proper motion survey.

LDM89 examined the kinematics of the 49 cool white dwarfs in their sample updated from their earlier paper. They found 6 objects having tangential velocities exceeding 250 km/sec indicating that they belong to the Halo (as defined in Chapter 1). Of these, five are fainter than $M_v \sim 13$, which they used to estimate the Halo WDLF. The resulting WDLF translated to the bolometric scale is shown in Figure 2.6. Here again, it is possible that this sample is significantly biased by missing low $V_{\tan}$ objects, perhaps exceeding in magnitude the similar effect in the disk sample. This is because a Halo white dwarf with $V_{\tan} < 250\,km/\sec$ but having a proper motion with the survey's limits would be detected, but would be misidentified as belonging to the Disk.

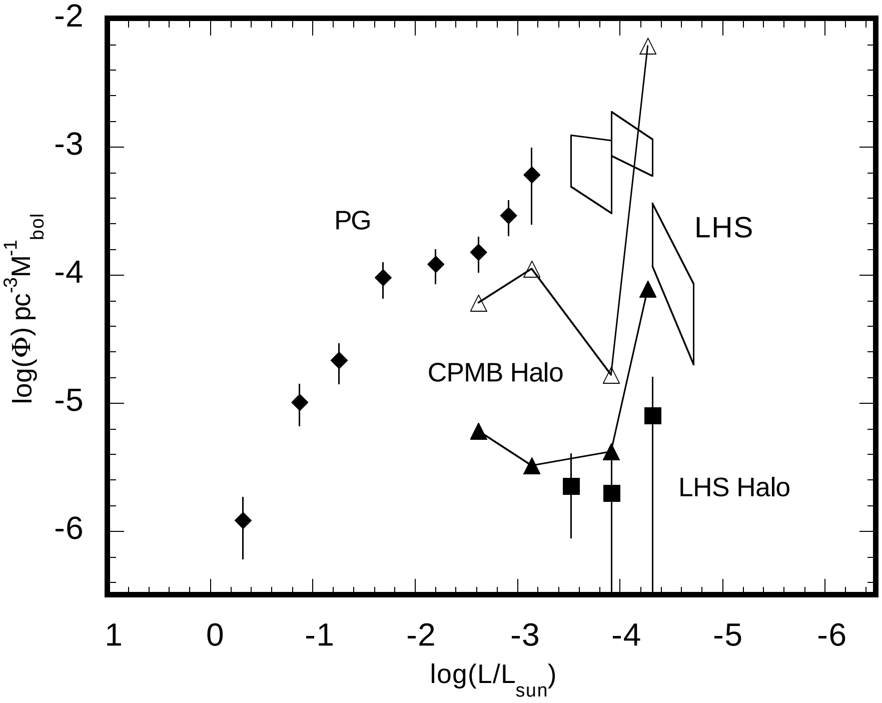

Figure 2.6: The preliminary WDLFs for the Galactic Halo from the high velocity stars in LDM89 (filled squares) and the Common Proper Motion Binary survey of Oswalt and Smith (raw – filled triangles; completeness corrected – open triangles; 1994).

The work by Oswalt and Smith (1994) on white dwarfs in common proper motion binaries has uncovered another source for "Halo" white dwarfs. They have found in their sample of 274 white dwarfs in binaries that 7 have companions which are classified spectroscopically as Halo main-sequence stars. These stars show spectral features indicating abundance patterns consistent with the low metalicity Galactic Halo. This criterion for identifying halo white dwarfs is interesting because no additional kinematic restrictions are necessary once a sample has been selected by proper motion (as in what was done by LDM89, for example). From the abundance patterns of these companion stars it is assumed that they are part of the Halo.

2.3 THEORETICAL INTERPRETATION OF THE WDLF

2.3.1 White Dwarf Structure

By way of a bit of history we can begin to understand the internal structure of white dwarf stars, from which we base our current understanding of the WDLF. It was immediately apparent from the discovery observations that white dwarf stars were not composed of normal matter. The first known white dwarf stars – 40 Eridani B, Van Maanan 2, and Sirius B – were all singled out because of their high temperatures and low luminosities, indicating that they were unusually compact. Sirius B gave us the first conclusive evidence that these stars were made from matter some 2000 times more dense than Platinum (Eddington 1926). In the early part of the 20th century W. S. Adams, knowing the distance to Sirius and the effective temperature of Sirius B, was able to show that the radius of Sirius B was roughly 100 times smaller than our Sun – roughly 10^9 cm (Adams 1914, 1915). This was paramount to determining the nature of these stars because both our Sun and Sirius B have nearly the same mass, with Sirius B actually being slightly more massive.

We were enlightened with an explanation of the unusual physical properties white dwarf stars possess by the work of Fowler (1926). Fowler explained the small size and high density of white dwarfs using Fermi-Dirac statistics to suggest that *degenerate electrons* were responsible for their support. The detailed equations describing the behavior of electron degeneracy explicitly for white dwarfs were presented by Chandrasekhar (1939, 1984). From his work we get the two expressions for electron degeneracy pressure for non-relativistic and relativistic conditions

$$P_e = \begin{cases} \dfrac{1}{20}\left(\dfrac{3}{\pi}\right)^{2/3} \dfrac{h^2}{m(\mu_e H)^{5/3}} \rho^{5/3} \\ \dfrac{1}{8}\left(\dfrac{3}{\pi}\right)^{1/3} \dfrac{hc}{(\mu_e H)^{4/3}} \rho^{4/3} \end{cases} \tag{2.5}$$

respectively. It is important to note that both relations for electron degeneracy pressure are independent of temperature. Furthermore, the conductivity of electron degenerate material is very high causing the material to be essentially uniform in temperature – isothermal, throughout the degenerate interior (Marshak 1940). The degenerate core of a white dwarf also contains more than 99% of its total mass. These properties will have important consequences later when we examine the functional form of the WDLF.

The pressure due to gravity in a white dwarf at some interior point is dependent on the amount of material exterior to a sphere with a radius equal to the point's center distance. From this it follows that going out from the center at some point the gravitational pressure will drop, and with it the density of material, so that the material is no longer degenerate. This defines the region in the star which is called the degeneracy boundary, beyond which is the envelope – composed entirely of non-degenerate gas. The location of the degeneracy boundary can be found by equating the expression of non-relativistic electron degeneracy pressure and the pressure from an ideal gas. This non-degenerate envelope contains roughly 10^{-4} of the total stellar mass and can be ignored as far as estimating the total heat capacity of the star. However, its physical properties cannot be ignored, as it is the envelope which regulates the heat flow from the core out into space and determines the white dwarf cooling rate.

We now have the basic structural components of a white dwarf model from which we can examine the WDLF. To summarize, a white dwarf consists of two basic structural components; the isothermal degenerate *core* surrounded by a thin non-degenerate *envelope*.

2.3.2 The Mestel Luminosity Function

From our basic understanding of white dwarf structure, the overall shape of the white dwarf luminosity function can be readily understood. Using assumptions and simplifications appropriate to white dwarf stars, Mestel (1952) derived an expression for the cooling rate of white dwarfs from a simple analytical evaluation of the equations used to describe stellar structure and evolution. We recall from the beginning of this chapter that the luminosity function can be expressed as dn/dL (equation 2.2) and this is dependent on the evolution time scale and birth rate. Except for perhaps the hottest white dwarf stars there are no energy sources in the core or envelope. Therefore, white dwarfs evolve by dissipating the residual energy in the core through the envelope. The rate of energy dissipation (cooling) is controlled by the physical properties in the overlying envelope (*i.e.* opacities and convection). In the case of white dwarf stars the luminosity function is entirely dependent on their cooling rate plus their birthrate over the white dwarf mass distribution. The white dwarf expression for dn/dL is given by Iben and Laughlin (1989) as

$$\frac{dn}{dL} = -\int_{M_L}^{M_U} \phi(t) \frac{dN}{dM} \frac{dt_{cool}}{dL}\bigg|_M dM\,, \tag{2.6}$$

where $\phi(t)$ is the stellar birthrate, dN/dM is the white dwarf mass distribution, dt_{cool}/dL is the inverse of the white dwarf cooling rate, and the integration limits are determined as: M_U = the maximum white dwarf progenitor mass, and M_L is effectively the main-sequence turnoff mass for the age of the stellar population being considered. The above equation can be greatly simplified if we assume a constant birthrate and a zero width white dwarf mass distribution, so that the LF is approximately expressed by

$$\frac{dn}{dL} = C_0 \frac{dt_{cool}}{dL}\bigg|_{m=\langle m_{wd}\rangle}, \tag{2.7}$$

where C_o is a proportionality constant determined by the assumed birthrate and average white dwarf mass.

To see how the cooling nature of white dwarf evolution translates into a model LF I follow Wood (1990), based on the work of Mestel (1952); Mestel and Ruderman (1967); and Van Horn (1971), by starting with the four basic equations of stellar structure (*cf.* Schwartzschild 1958 and Clayton 1968):

$$\frac{dM_r}{dr} = 4\pi r^2 \rho, \text{ Hydrostatic Equilibrium;} \tag{2.8}$$

$$\frac{dP}{dr} = -\rho \frac{GM_r}{r^2}, \text{ Mass Conservation;} \tag{2.9}$$

$$\frac{dT}{dr} = -\frac{3}{4ac}\frac{\kappa\rho}{T^3}\frac{L_r}{4\pi r^2}, \text{ Radiative Equilibrium;} \tag{2.10}$$

$$\frac{dL_r}{dr} = 4\pi r^2 \rho(\varepsilon - T\frac{\partial s}{\partial t}), \text{ Thermal Equilibrium.} \tag{2.11}$$

Where in these equations M_r is the interior stellar mass encompassed by a sphere with radius r; the material density is ρ; pressure and temperature are indicated by P and T respectively; the luminosity passing through this sphere is L_r; the opacity of the material is κ; the nuclear energy production rate is ε; and the specific entropy is given by s. The constants in the above equations are: G — the gravitation constant; c — the speed of light; $a = 7.565 \times 10^{-15}$ ergs cm^{-3} deg^{-4} — the radiation constant; and π is the number pi. From these equations we want to obtain an analytic expression for the time dependence of total luminosity for a degenerate white dwarf star. Once obtaining the time dependence of luminosity we can then use equation 2.7 to derive our analytic model luminosity functions. Depending on what assumptions we make about the structure of white dwarf stars these equations take on different forms, which allows us to solve them analytically and arrive at our desired expression.

Because most of the mass is contained in the white dwarf core, most of the energy stored as heat is in the core also. The isothermal degenerate core implies there is essentially no temperature structure in the core, hence no radiative transfer and equation 2.10 is not needed. We are left with equation 2.14 to compute the time dependence of luminosity for a white dwarf as

$$L_{WD} = \int_0^{R_{WD}} \frac{dL_r}{dt} \tag{2.12}$$

which can be further simplified using our basic knowledge of white dwarf structure. Since, to a good approximation, there are no energy sources, $\varepsilon = 0$ in equation 2.10. Furthermore, because the pressure from degenerate electrons is independent of temperature the radius of a white dwarf remains essentially constant as it evolves and cools. This allows us to ignore heating from gravitational contraction as an energy source, which leaves us with the white dwarf luminosity dependent only on the time rate of change in entropy. We can write the time derivative of entropy as

$$T\frac{\partial s}{\partial t} = T\left(\left.\frac{\partial s}{\partial T}\right|_{\rho} \frac{dT}{dt} + \left.\frac{\partial s}{\partial \rho}\right|_{T} \frac{d\rho}{dt}\right) \approx C_V \frac{dT}{dt}, \tag{2.13}$$

where C_V is the heat capacity at constant volume and t is time. Because the ions are so much more massive than the degenerate electrons, the heat capacity is that for an ideal gas of atomic mass A, given by

$$C_V = \frac{3}{2}\frac{k}{AH}. \tag{2.14}$$

We can now use these simplifications to evaluate the integral in equation 2.12, noting that the part of the integrand from equation 2.11 simply integrates to the total stellar mass. Because the remainder of the integrand is independent of temperature the time dependence of luminosity for a white dwarf from equation 2.11 becomes

$$L_{WD} = -M_{WD} \frac{3}{2} \frac{k}{AH} \frac{dT}{dt}. \tag{2.15}$$

From our earlier discussion of white dwarf structure we can make the following approximations: $M_{WD} \approx M_{core}$ and $T \approx T_c$. Equation 2.15 shows that white dwarf luminosity depends on the change of its central core temperature. We now need to estimate the rate at which the energy is passed through the controlling non-degenerate envelope to find the age–luminosity relation we desire.

The conditions in the envelope at the degeneracy boundary, as defined above, determine the rate at which energy flows from the core. From the basic stellar structure equations 2.9 and 2.10 we can express the temperature dependence on pressure in the envelope as

$$\frac{dT}{dP} = \frac{3}{16\pi ac} \frac{L_{WD}}{GM_{WD}} \frac{\kappa}{T^3}. \tag{2.16}$$

The important aspect to note here is the only variables in the above equation are the temperature and opacity κ. Following Mestel (1952) by choosing Kramer's law $\kappa \propto \rho / T^{3.5}$ for the expression of opacity, equation 2.16 takes the form

$$\frac{dT}{dP} \propto \frac{L_{WD}}{M_{WD}} \frac{\rho}{T^{6.5}}. \tag{2.17}$$

By eliminating ρ in terms of P using the equation of state for an ideal gas

$$P = \frac{k}{\mu H} \rho T, \tag{2.18}$$

where the atomic mass unit is $H = 1.66044 \times 10^{-24} g$ and μ is the mean molecular weight of the gas. We can integrate equation 2.20 inside the envelope, assuming radiative equilibrium, to obtain the relation between temperature and pressure,

$$P^2 \propto \frac{M_{WD}}{L_{WD}} T^{8.5}. \tag{2.19}$$

At the degeneracy boundary the gas pressure is equal (equation. 2.18) to the non–relativistic (equation. 2.5–top) electron degeneracy pressure. Solving both equations 2.18 and 2.5 for the density, ρ, and equating them we find $P \propto T^{5/2}$, which allows us to solve 2.19 for the white dwarf luminosity

$$L_{WD} \propto M_{WD} T^{3.5}. \tag{2.20}$$

We can now use the above relation to substitute for M_{WD} in 2.15 and integrate over time. The form of the Mestel age–luminosity relation we desire is found by back substituting 2.20 for T into the integral solution yielding

$$\tau_{WD} \propto M_{WD}^{5/7}\left(L_{WD}^{-5/7}(t) - L_{WD}^{-5/7}(t=0)\right), \tag{2.21}$$

where in the usual case the initial white dwarf luminosity at $t = 0$ is much larger than at the time of interest, its effect vanishing with increasing time. This is what we mean by saying a white dwarf quickly "forgets" its past, hence its evolution is insensitive to the initial conditions once it is formed. Furthermore, we can see directly in this form that the cooling rate slows for white dwarfs with increasing mass. This results because the more massive white dwarfs have higher surface gravities making them smaller, hence smaller surface area is available for radiating energy. Also, because the smaller size forces more ions into a given volume element, the material in the more massive white dwarfs have a higher heat capacity than do the less massive ones.

It is now possible to apply equations 2.7 and 2.21 to find the functional form of the Mestel luminosity function. The key point here is the value of the luminosity exponent, which determines the slope of the Mestel LF, such that

$$\Phi \propto -\frac{5}{7}\log\left(L/L_{\odot}\right), \tag{2.22}$$

where the normalization of Φ is dependent on the white dwarf birthrate and the proportionality constant for the cooling time in 2.15. In Figure 2.7 I have plotted the PG and LHS WDLFs along with a normalized Mestel LF showing that for the most part it agrees well with the observations.

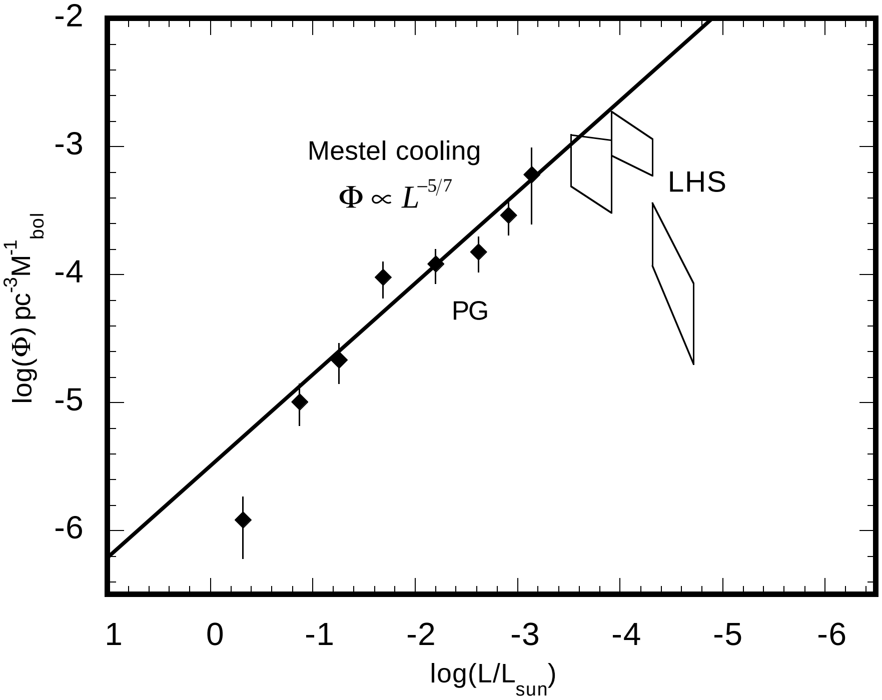

Figure 2.7: The observed WDLF from the PG and LHS surveys compared with the analytic Mestel LF.

To summarize the assumptions and approximations used by Mestel:

- no nuclear sources;
- no gravitational contraction;
- heat capacity is completely contained in the ions;
- the degenerate core is isothermal;
- the envelope acts as an ideal gas and is in radiative equilibrium;
- and the throttling opacity source is expressible by Kramers' law;

when applied to the basic stellar structure equation yield a surprisingly accurate model for white dwarf evolution.

The Mestel age–luminosity relation has several important consequences. From 2.21 we see that luminosity maps into time, but is a function of white dwarf mass. Therefore, in order to obtain this time dependance the white dwarf mass function must be deconvolved out of the WDLF. Because the mass distribution is very narrow (Bergeron, Saffer, and Liebert 1992; Weidemann 1971, 1990) – spanning a width of $\sim 0.05M_{\odot}$, there is basically a one to one correlation between luminosity and white dwarf age, although there is a weak dependence of white dwarf ages on their masses – $\tau_{WD} \propto M^{5/7}$. In this way the luminosity function maps out star formation history in our Galaxy – excesses in the WDLF above a constant birthrate model would indicate a burst of star formation while a deficiency would indicate a quiescent period. We will see in the next section that changes in the physics governing white dwarf cooling rates can also cause excesses and deficiencies relative to the Mestel LF. Furthermore, since the cooling rate of a white dwarf slows with the time, the time resolution in the WDLF in the lower luminosity bins becomes compressed. Therefore, the location of the age dependent turndown in the WDLF is insensitive to small fluctuations in the star formation rate early on in the Galaxy's history. One other important quality of the WDLF to point out is that its construction is an *integral* process, which is inherently resilient against the effects of noise.

Perhaps the most significant prediction of the narrow white dwarf mass distribution and the Mestel age–luminosity relation is that there should be an abrupt cut–off in the WDLF corresponding to the finite age of the Galaxy's Disk. Furthermore, this should be true for any stellar population, not just the population of the Disk. If we normalize the Mestel age–luminosity relation according to Iben and Laughlin (1989) then the drop–off luminosity versus Disk age is

$$\log\left(\frac{L_c}{L_\odot}\right) \approx -\frac{7}{5}\log(\tau_{Disk}) - 14.5, \tag{2.23}$$

where τ_{disk} is the age of the Disk in years from when it first started forming stars to the present day. From this simple relation, we can infer, given the range in stellar ages discussed in Chapter 1, that even the oldest white dwarfs in both the Disk and the Halo should still be luminous and in principle observable — if model calculations of main-sequence lifetimes are correct.

2.4 MODIFICATIONS TO MESTEL THEORY

Mestel theory does well in explaining the general rise of the WDLF and predicting the time scale for white dwarf evolution, suggesting that the WDLF will be truncated at low luminosity due to the finite age of the Galaxy. However, the changes in slope found in the observed WDLF are not well explained and require some modification to general Mestel cooling theory. In the following paragraphs I will outline the necessary modifications to the Mestel approximations needed to perform a similar analysis to the one above. I also include some physical processes affecting white dwarf cooling times that theory says must be present, but because of observational uncertainties are not readily apparent. It is possible with this "Mestel" approach to explain most of the details in the WDLF from first principle physics, to a very good approximation.

2.4.1 Neutrino Luminosity

The first obvious place Mestel theory fails to accurately describe the observed WDLF is at the very hottest end. Mestel theory predicts a LF that is too flat in the regime $\log(L/L_\odot) > -1$, meaning the Mestel model cools too slowly compared to the real stars we observe. Under our assumption of a constant white dwarf birthrate this would imply that there must be another source, other than photons, of luminosity or energy loss. This invalidates our earlier assumption that there are no sources or sinks in our white dwarf model, hence we cannot ignore the ε term in 2.11.

It has been shown, for various chemical compositions, that the source for this luminosity are neutrinos (Van Horn 1971 and references therein) produced by the high temperature dense plasma thought to be in white dwarf cores. Through numerical modeling and analytic calculations (Wood 1990; Lamb and Van Horn 1975; Van Horn 1971) it is predicted that the dominant neutrino luminosity source is in the form of plasmon neutrinos. The luminosities from the other neutrino types — pair, recombination, photon, and Bremsstrahlung — are all down by at least an order of magnitude (see Figure 5 in Lamb and Van Horn 1975). According to Bowers and Deeming (1984 p. 247) in low density plasmas the energy loss rate goes as $\varepsilon_\nu \propto T^3$, where at high densities $\varepsilon_\nu \propto T$. For the interiors of white dwarfs we need only consider the latter. From these calculations we also believe that the neutrino luminosity exceeds the photon luminosity by at least an order of magnitude until $\log(L/L_\odot) \sim -0.5$, where they are equal, and by $\log(L/L_\odot) \sim -1$ it is down by a factor of ~100.

The implication of neutrino luminosity on white dwarf cooling rates is that we gain a factor of T in the thermal equilibrium equation (2.11), whereas before the rate of change in entropy was approximated with a constant. Because the crossection for interaction of neutrinos is extremely small, the material above the core has essentially zero opacity to these neutrinos. The net effect is that the controlling mechanism for the white dwarf cooling rate is dominated by the production rate of neutrinos. With the assumptions above it can be shown, using a Mestel–like approach, that for plasmon neutrino dominated cooling the WDLF takes the form $\Phi \propto L_{WD}^{-2}$ for $\log(L/L_\odot) > -1$. Including neutrinos also has the effect of making the inferred ages from white dwarf luminosities significantly younger by a factor of 10 at $\log(L/L_\odot) = -2$ but by less than 10% at $\log(L/L_\odot) = -4$ (Van Horn 1971).

2.4.2 Convection

While not readily visible with the current observed WDLF, simple calculations lead us to believe that as a white dwarf cools, a convection layer develops in the star's envelope. When first formed, this convection layer has little effect on the white dwarf cooling rate. But as the envelope temperature decreases, the base of the convection layer increases in depth until its base reaches the degeneracy boundary — altering the physical nature of the mechanism throttling the cooling process. Because convective energy transport is more efficient than radiative transport, the energy transport mechanism is governed by conduction between the nearly isothermal core and the base of the convection layer. Therefore, Kramer's Law is no longer appropriate and the throttling mechanism becomes the conductive opacities at the degeneracy boundary, where the conductive opacity is defined as

$$\kappa_c = \frac{4acT^3}{3\rho\lambda_c}. \tag{2.24}$$

For a weakly degenerate gas, the conductivity, λ_c, is dependent on temperature and density as $\lambda_c \propto \rho T^{5/2}$ (see Clayton 1983 p.248). Therefore, instead of using Kramer's formulation for opacity in the radiative equilibrium equation (2.10) for our Mestel analysis we let $\kappa \propto \rho^2 T^{1/2}$.

We can now examine in qualitative terms the consequences of convection changing the throttling mechanism from radiative transport to conduction. The change of the exponent on density, $\rho \to \rho^2$ and the decreased temperature sensitivity of the opacity causes an overall slope change in the calculated WDLF. This is because the conductive opacities at the degeneracy boundary are lower than radiative opacities and the energy transport efficiency for convection is high, effectively speeding the white dwarf cooling process. The net result on the luminosity function is a flatter slope, consistent with the three data points between $-2 \leq \log(L/L_\odot) \leq -3$ in the observed WDLF.

2.4.3 Crystallization

At the cool end of the WDLF in Figure 2.7 we find the Mestel LF once again does not fit the observations well. From $\log(L/L_\odot) \leq -4$ the Mestel LF predicts a cooling rate too slow compared to what is seen in the observed WDLF. There are actually two effects to be concerned with at this end of the WDLF: 1) according to our models the core temperature has fallen considerably since becoming a white dwarf — crystallization and 2) following cyrstallization the onset of rapid Debye cooling. I will discuss each in turn.

As the thermal energy of the ions is bled away over time their Coulomb interactions (the electrostatic attraction or repulsion experienced by like or opposite charges) become important. Expressed in qualitative terms, as the ions lose their thermal energy they begin to feel the effects of the Fermi sea of electrons and their neighboring ion's charge. The density of electrons is sufficient to effectively screen out the nearest ion so that the net Coulomb force between ions is attractive. When this happens the ions try to rearrange themselves in the lowest energy state possible, consistent with their (reduced) thermal motions, and ultimately as the temperature continues to decrease the ions form a Coulomb lattice (Slattery, Doolen, and DeWitt 1982). In the process of becoming a Coulomb lattice the dense plasma passes through the Coulomb liquid phase, and in doing so the heat capacity C_V of the plasma gradually increases from $3k/2AH$ to $3k/AH$. The increased heat capacity of the core means there is more energy available that must be radiated away. This, in turn, causes the cooling rate to slow more than what is predicted by the Mestel relation, thus the slope in the WDLF becomes steeper than the Mestel slope of $-5/7$.

When the ion plasma's Coulomb energy is much greater than its thermal energy, by a factor of ~178 (Lamb and Van Horn 1975), the ions solidify into a crystal lattice. There are two significant effects of crystallization on the model cooling rates of white dwarfs. First, because the ions are now trapped in a Coulomb potential well the number of degrees of freedom they have has been reduced, causing the release of energy – *the latent heat of crystallization*. According to Van Horn (1971) the amount of heat released is $Tds \sim 3kT/4AH$, which in effect adds an energy source to the radiative equilibrium equation (2.14). Since the release of latent heat is relatively sudden compared to the evolution time scale at these luminosities, it can add 50% to the white dwarf cooling times, resulting in a bump in the calculated LF. Where in luminosity the latent heat is released is dependent on what element is crystallizing, and in principle we could use this to determine observationally the internal composition of white dwarf cores. However, the resolution of the observed WDLF is still too coarse for this diagnostic to be applied.

The other main effect crystallization has is to change the heat capacity of the material in the core a second time. The heat capacity of a Coulomb lattice at sufficiently low temperatures is no longer reasonably expressed as a constant, as before, but is strongly dependent on temperature. For a core temperature below the Debye temperature the heat capacity can be described as $C_V \propto T^3 k/AH$, which leads to very rapid cooling called *Debye cooling*. The strong temperature dependence of Debye cooling causes the white dwarf cooling rate to accelerate at lower luminosities, resulting in the LF turning over. If we use the Debye heat capacity for the crystal lattice and follow a Mestel–like analysis we can show that the luminosity function goes as $\Phi \propto L^{1/7}$.

There are still many unresolved issues regarding this regime of white dwarf evolution. It is currently unclear how a white dwarf core of mixed composition crystallizes. Whether crystallization happens as mixture or as a stratified process with the heavier elements crystallizing first, followed by the lighter ones, causing a significant restructuring of the stellar core, is still a debated issue among theorists working on white dwarf structure. According to Chabrier *et al*. (1993) it is possible for the heavier elements to begin crystallizing first and sink towards the center of the star. If this were to happen, along with the latent heat there would be an addition of gravitational potential energy as the mean molecular weight and the structure of the white dwarf core are rearranged. The effect can be rather dramatic according to the models of Segretain *et al.* (1994) and Hernanz *at al.* (1994), causing a rather significant bump in the LF as the white dwarf models spend time radiating this extra energy. Where such a bump occurs in luminosity is dependent on the chemical element being crystallized. According to these models the resulting bump has an amplitude $\log(\Phi) \approx -2.4$ — an excess of 0.6 in the log of space density above observed data at $\log(L/L_\odot) \sim -4$. Given the current resolution and errors, the observed WDLF places few constraints on this theory.

2.5 SUMMARY

The limitations found in the observed WDLF come from essentially three sources: 1) For luminosities $\log(L/L_\odot) > -3$ the WDLF is limited primarily by small number statistics. This is manifested in the large bin widths of the WDLF so that the statistical errors can be kept reasonable. For this reason the potential for the WDLF to map out the past star formation rate in the local Galaxy has yet to be realized. This is also true for luminosities $\log(L/L_\odot) < -3$, where in the LHS sample there are only 43 objects to define the WDLF – the last bin containing just 3 objects. 2) If we are to use the cutoff in the WDLF as an accurate age estimator to the limit of its potential we need to resolve the uncertainties in transforming observed magnitudes and indices to true luminosities. The uncertainties in modeling the atmospheres of cool white dwarfs represents about half of the uncertainty in the WDLF age estimates. 3) The last three bins in the WDLF contain all the information regarding the nature of white dwarf crystallization. The overall shape of this part of WDLF is the key to resolving the nature of the mixed composition crystallization, which can have a 1-2 Gyr effect on the age of the WDLF cutoff. Systematic biases from the proper motion survey across this region plus the small number statistics have kept us from unambiguously constraining the theoretical models of crystallization.

In spite of various surveys for white dwarfs, the quality of the WDLF remains unchanged. Felton (1976), in his review of luminosity function estimators, gives a prescription for combining data from different surveys having different limits to form a composite luminosity function. If combined using this prescription, the various WDLFs described earlier would produce a composite WDLF that I believe would mark a significant improvement — with no new observations necessary. It would be a tedious process and would need the cooperation of many people, but in my opinion is worth the effort.

We can summarize the basic theory of the white dwarf luminosity function from the simple model LF (solid line) shown in Figure 2.8. The stick-figure WDLF shown includes only the three major slope changes in the neutrino, Mestel, and Debye cooling regimes. We obtain a very good fit to the overall LF from back-of-the-envelope first principle physics, giving us some confidence that our understanding of white dwarfs is reasonably correct. I have also included in Figure 2.8 (dotted line) a LF resulting from detailed numerical modeling of white dwarf cooling (Wood 1992). Both the analytic and detailed numerical model fit the data equally well, giving us some degree of confidence in our understanding of how white dwarf stars evolve with time. Debye cooling completely fails to explain the observations at the cool end, which must be accounted for by finite age effects. Finally, within observational errors, the analytic form of neutrino and Mestel WDLF cooling with finite age effects fully accounts for the observed WDLF.

It is clear from these models that the observations are a long way from constraining the details of white dwarf cooling theory. The subtle features and the physics that cause them, found in the model LF, are completely obscured by the limitations in the observed WDLF. However, even though these features currently remain hidden, their effects on the age-luminosity relationship are significant. For this reason the age-luminosity relation generated by the

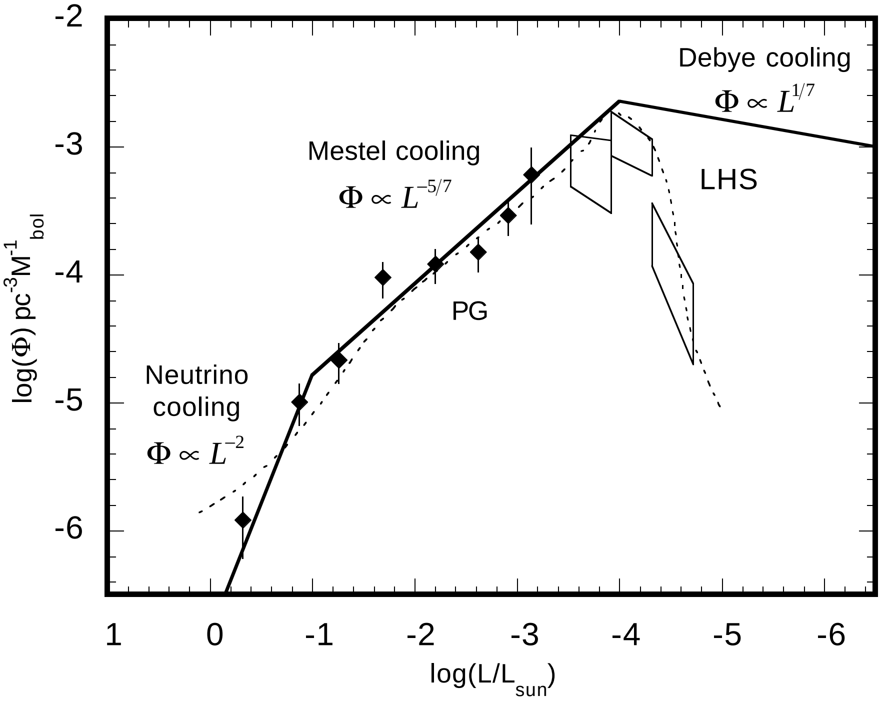

Figure 2.8: An analytic representation of the WDLF (solid line) compared with the observations. In addition a details numerical model WDLF from Wood (1992 – dotted line) is shown, which also includes finite age effects for a Disk age of ~10 Gyrs. (concept from Van Horn and Liebert private communication).

numerical models is of great value, even with the current state of the observed WDLF.

2.5.1 A Systematic Search for Cool White Dwarfs

We can address some of the limitations in the current estimates of the WDLF by continuing to search present data bases for their white dwarf contents, however this too has its limitations. We are either exhausting the white dwarf content of present day databases or the data they contain prevent easy identification of their white dwarfs. Instead, I have chosen to design a set of tools specifically with the goal of searching for white dwarf stars in both the disk and halo of our Galaxy.

For the reasons summarized above we can see that the cool end of the WDLF is in need of more help than the hot end and in terms of ages contains the most information. Therefore, I have investigated what we could expect from a search for cool white dwarfs by comparing a hypothetical survey with what we know of the WDLF. Suppose the combination of instrument and technique allows me to be complete to $V = 23$. I can ask: How many white dwarfs can I expect to find? I have computed and plotted in Figure 2.9 the space density sensitivity limits such a survey would have over 1 and 100 square degrees. The two sets of lines are these limits without a bolometric correction and with the bolometric correction for DA white dwarfs, as in Liebert, Dahn and Monet (1988), to compare with the two cases in the LHS WDLF.

I can estimate the number of white dwarfs we could expect to discover at a given luminosity by taking the difference between the observed WDLF and the limit line. Consider the following example: The difference between the WDLF and the 100 square degree limit without bolometric corrections at $\log(L/L_\odot) \approx -4.7$ is ~0.6. Therefore, the expected number of white dwarfs discovered at $\log(L/L_\odot) \approx -4.7$ in 100 square degrees is $10^{0.6} \approx 4$. In this way we can assess the effectiveness of a survey on improving the WDLF and our understanding of white dwarf evolution.

It is clear from Figure 2.9 that I could improve the observed WDLF for the Galactic Disk with as little area as 1 square degree at 23rd magnitude. I can

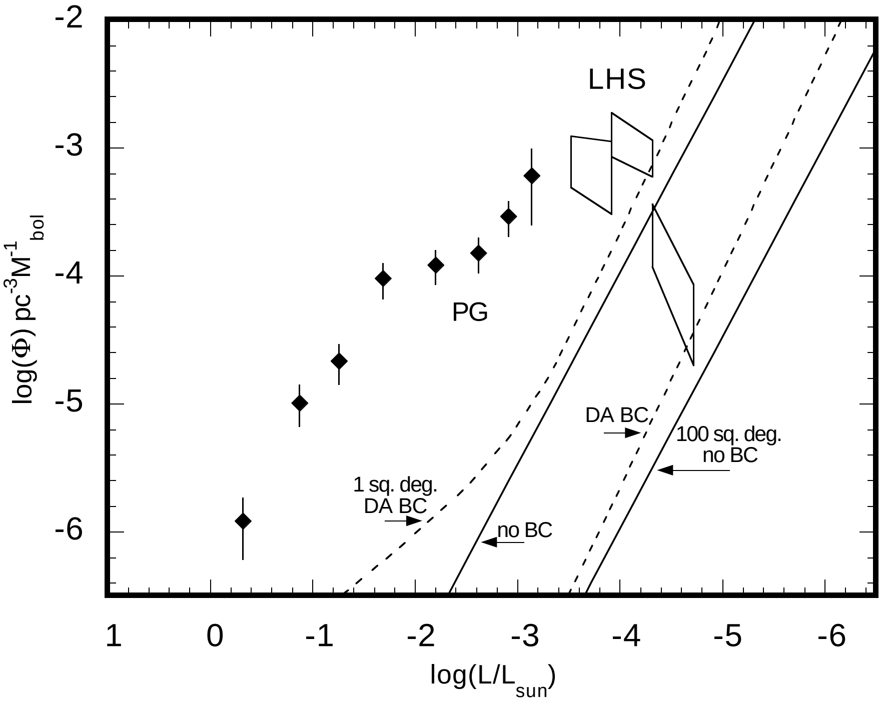

Figure 2.9: The space density detection limits of a hypothetical survey for white dwarfs complete to magnitude 23 over 1 and 100 square degrees of the sky.

expect to find 12–15 white dwarfs at $\log(L/L_{\odot}) \sim 3.2$. With one hundred square degrees of area it is possible to more than double the number of objects in the last bin and increase the number in the previous two bins by two orders of magnitude — adding hundreds of objects to the WDLF below $\log(L/L_{\odot}) \approx -3$. With this amount of data it would be possible to increase the resolution of the WDLF while maintaining small statistical errors, allowing us to test the validity of the numerical models and the interesting physics of crystallizing white dwarf interiors. By clarifying the shape in this part of the WDLF we would also improve the age–luminosity relationship for white dwarfs, improving on our age estimate for the Galaxy using the WDLF. If we examine the limits shown above with the Halo WDLFs in Figure 2.6 we see that we are sensitive to halo white dwarfs after 100 square degrees. Furthermore, if the Galactic Halo is significantly older than the Disk, as suggested from the oldest globular clusters, we are sensitive enough to learn something about where the turndown for the Halo WDLF is located, hence the Halo's age.

We can also direct white dwarf searches to carefully selected targets in order to tie together the white dwarf ages with the mainstay of stellar age estimates — main-sequence stellar isochrones. The same tools which are effective in a survey like the one outlined above would prove most rewarding if trained on carefully selected star clusters. It would then be possible to determine the luminosity of the oldest white dwarfs in these clusters and to compare their ages with the age estimates from model main-sequence isochrones, hence cross–calibrating these two different methods.

If we were to calibrate white dwarf ages and isochrone ages, improve the Disk age estimate by clarifying the shape of the WDLF, and either measure or place limits on the white dwarf turndown age for the Halo, we would be well on our way to having a *fully self-consistent* picture of the Galaxy's age and evolution. To accomplish this, not only will the survey instrumentation need to be very sensitive, but the technique used for selecting cool white dwarf candidates must be free from possible kinematical biases. In other words, the survey would have to employ a photometric system developed specifically for the discovery of cool white dwarfs.

3

Instrumentation for a Digital Survey: The Prime Focus Camera

Astronomical surveys are at the core of the understanding astronomers have developed about the Universe and the Galaxy in which we live. Through the discovery of new objects and the systematic cataloging of those already known, astronomical surveys provide the raw data we use to test our theoretical models describing our view of the universe. Schmidt telescopes and photographic plates have been, and continue to be, the time–honored tools for conducting large area sky surveys. For nearly 50 years the combination of Schmidt telescopes and large format photographic plates have been the instrument/detector of choice for sky surveys. This is primarily because of limits in detector technology, but is also due to the extraordinary wide field coverage capacity offered by Schmidt telescopes. However, technology has changed and so have the tools for astronomical surveys.

The Charge Coupled Device (CCD) represents the greatest advancement in astronomical detectors since the photographic plate replaced the human eye (see Mackay 1986). The sensitivity of a modern CCD is more than 50–100 times better than that of the fastest photographic emulsion, having detection quantum efficiencies (DQE) of 20–30% across most of the visible spectrum. Specially treated CCDs, which have been thinned so that they can be illuminated from behind (rather than through the semi–transparent circuitry they need in order to function) and have been treated with anti-reflection coatings, can have DQEs exceeding 90–95% (Lesser 1994). Unlike photographic emulsions, CCD detectors have excellent linearity in their response to light and as a result of their digital natures can produce images that are directly compatible with fast computer hardware and software.

Yet, with all these benefits, large area optical surveys have not made use of CCDs, mainly because they have been physically too small in size. The typical CCD today is about 30mm on a side (Loral-Fairchild $2048^2 \times 15\mu m$ pixel) and does not lend itself to wide field imaging on typical professional telescopes. The relative efficiency with which a survey gathers information is given by

$$\varepsilon = \Omega D^2 q, \tag{3.1}$$

where the solid angle of the sky on the detector(s) is Ω, the combined efficiency of telescope and detector is q, and the telescope diameter is D. It is clear from the above expression that a CDD, placed in a relatively fast optical system, can compete favorably with the conventional techniques used for sky surveys. It is simply a matter of matching the telescope and detector to the task at hand: a combination that is efficient for survey imaging is not suitable for detailed high resolution imaging.

The obvious place to put a CCD in a fast optical system is in one of the Schmidt telescopes already available. One of the first Schmidt telescopes to use a

CCD detector was the Burrell Schmidt at Kitt Peak (Armandroff 1994), where in 1988 a standard CCD dewar was placed at the telescope's Newtonian focus. The first experiments that used a CCD directly at the prime focus (in lieu of the plate holder) were done in 1989 at Steward Observatory's 18 inch Schmidt on Mt. Bigelow (Claver *et al*. 1990), and concurrently but independently by the Japanese at the Kiso Observatory (Takato *et al*. 1990). Both groups showed that it was feasible to place a cryogenically cooled CCD at the prime focus of a Schmidt telescope, although their methods of cooling were quite different. In my study, I replaced the photographic plate holder with a custom–made dewar containing a 1024×1024 $12 \mu m$ pixel virtual phase CCD manufactured by Texas Instruments of Japan. With this detector, the 18 inch Schmidt imaged a 36×36 arcminute area with a resolution of 2.02 arcseconds. One of the primary concerns with an instrument like this is that the large pixels (relative to the stellar image size, or seeing) might degrade the photometric precision too much for usefulness as a survey camera.

With this instrument I obtained *UBV* images of fields around known white dwarfs from the Palomar–Green survey. From the photometry extracted from these images I showed that the photometric precision obtainable was sufficient to identify the two known white dwarfs, along with several other interesting objects. The internal uncertainty of my photometry was some 3–4 times better than the quoted errors from the Palomar–Green survey, in spite of the large pixels. While this condensed imaging did not prevent reasonable photometry, the large pixels lacked enough spatial information to separate stars from small distant galaxies. Furthermore, the small aperture and UV–opaque corrector glass of the Schmidt did not make it efficient enough for the survey I wanted to conduct. In the end I decided to find a detector/telescope combination that was better optimized for my task.

In order to optimize a telescope for a specific imaging task, we must match its plate scale with the chosen detector's resolution; the exact sampling ratio will depend on what science is sought. For example; the average seeing at McDonald Observatory, roughly 1.2 arcseconds (Gafney and Sneden 1991), would require 0.55 arcsecond pixels to critically sample the point spread function (PSF) – the minimum sampling necessary to retain all of the information. For a CCD with $15\mu m$ pixels this critical sampling would be obtained with a focal length of 5.67m, which is roughly half the focal length of the $f/3.93$ primary mirror of the 2.7m telescope – something to remember when considering possible future imaging instruments for McDonald Observatory. But for survey work it is more important to increase overall efficiency than maintain 100% of the PSF's information. Therefore, the optimum combination for a digital survey is when the plate scale and local seeing are just matched by the detector resolution. At 1.2 arcsecond seeing and $15\mu m$ pixels we can exactly match the plate scale with a focal length of 2.58m.

I began my search for the optimum detector/telescope combination by investigating what instrumentation was available for the telescopes at McDonald Observatory. With its dark skies, McDonald Observatory is an excellent location to conduct a deep sky digital survey. However, none of the telescopes had imaging instruments suitable to cover a large part of the sky in a reasonable amount of time. One of the four telescopes operated by McDonald Observatory, the 0.76m Boller and Chivens reflector, has a primary mirror whose focal length is 2.29m, providing a plate scale of $90.23''/mm$. This plate scale is a close match to both the CCD camera I originally built for the Mt. Bigelow Schmidt and the seeing at McDonald: 1.08 arcseconds per $12\mu m$ pixel. In the Fall of 1990 I approached research scientist Phillip MacQueen, asking about the possibility of designing a corrector for the 0.76m $f/3$ paraboloid so that it could be used with my 1024^2 pixel CCD. Phillip quickly convinced me to abandon this CCD in favor of the larger, higher quality Loral–Fairchild $2048^2 \times 15\mu m$ device. The Loral–Fairchild CCD at the 0.76m prime focus would have a resolution of 1.35 arcseconds and cover a square area 46 arcminutes on a side (0.59 square degrees). We then had a nearly optimum combination of detector and telescope. All we needed to do was correct the aberrations arising from the parabolic primary, and design an instrument to hold everything in place. So began the collaboration between Phillip MacQueen and myself; our goal was to build a prime focus CCD imaging system for the McDonald Observatory's 0.76m telescope.

3.1 THE PRIME FOCUS CAMERA

We designed and built the Prime Focus Camera (PFC) to provide wide field digital imaging capability to the McDonald Observatory specifically to conduct a photometric survey to search for white dwarf stars. The PFC, as an instrument, is composed of several major subsystems: the original telescope and mounting, the corrector, the truss assembly, and the CCD detector. These basic systems are identified in Figure 3.1.

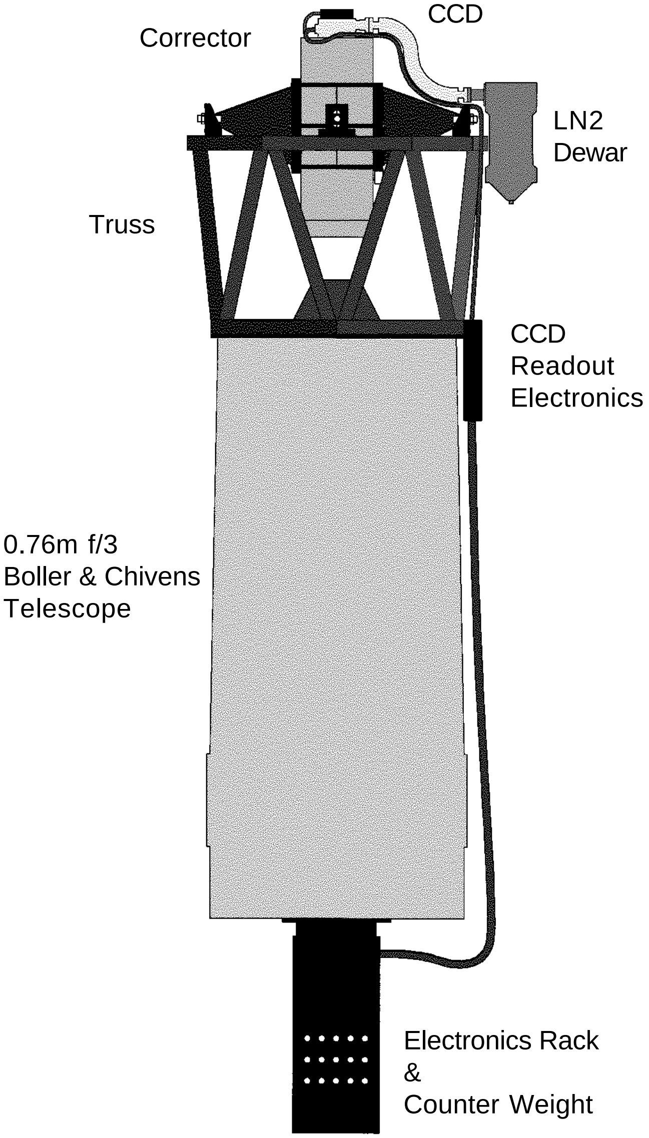
CCD
Corrector
LN2
Dewar
Truss
CCD
Readout
Electronics
0.76m f/3
Boller & Chivens
Telescope
Electronics Rack
&
Counter Weight

Figure 3.1: The Prime Focus Camera and its major components.

The PFC was specifically designed as a replacement for the existing secondary assembly on the 0.76m Boller and Chivens telescope on Mt. Locke. As with any instrument design there were many things one needs to consider, such as the tradeoffs between performance needs, physical constraints, and limits in technology. The optical design of the PFC's corrector is the work of Phillip J. MacQueen, who spent many hours of his own personal time perfecting its performance. At the same time I worked on the mechanical design problems to make full use of the creative optical design Phillip proposed. All through the design process Phillip and I had countless discussions, iterating and constraining the trade-offs between something that could be readily built and something that performed well in the computer simulations of the optical system.

The fabrication of the PFC was done almost entirely "in house" with the exception of the optics. These were contracted out to Don Loomis at Custom Optics in Tucson, Arizona. To keep costs down, I did most of the parts machining myself. The design and construction of the PFC–specific electronics were done jointly by Phillip MacQueen and myself. The CCD electronics used on the PFC were constructed at the McDonald Observatory electronics shop by Doug Edmondston under the direction of Phillip MacQueen.

The PFC is the first instrument at McDonald Observatory to use a 2048^2 CCD array. The 16 bits from each pixel resulted in images over 8 Mbytes in size, which were too large for the existing CCD controlling software, which thus required extensive reworking. Coordination of the software modifications and interfacing of the PFC's control functions were done by Mark Cornell, with the actual code written by Sam Odoms.

3.1.1 Optical Design

In order to design and fully specify an optical system we must first decide on its purpose, and then we identify the design constraints to meet this purpose. The purpose of the PFC's corrector is to enable a 0.76m $f/3$ parabola to be used in conjunction with a CCD for wide–field digital imaging. Because CCDs are physically flat and rigid, they must be used at a flat focal surface. Even though we have chosen our CCD and telescope to match the average seeing at McDonald, we do not want to preclude use of the PFC on nights when the seeing is better than average. The corrector should provide diffraction–limited images, or nearly so, across its entire field of view. The plate scale should be distortion–free across the entire field so that its potential for astrometric use can be easily realized. In order to ensure photometric precision and efficiency, the corrector should provide uniform illumination across the complete field, with low obscuration. Because the primary photometric system used for surveys is the broad band *UBVRI*, the corrector should provide as its optimum passband the wavelengths from 3000Å to 10000Å. The optical design should use industry standard 2" square filters because they are relatively inexpensive, and can be made for practically any wavelength/bandpass combination desired. Finally, the optical design must be feasible, both in terms of optical manufacturing and mechanical realization – in other words, we must be able to build the thing.

P. MacQueen has produced a catadioptric corrector that meets all these specifications, consisting of 5 elements – 2 reflective and 3 refractive. The prescription is listed in Table 3.1 and the physical layout of this design is shown

Table 3.1: Optical prescription for the PFC's corrector.

					Surface Specifications		
	Optic	**Medium**	**Thickness**	**Diameter**	**Radius**	**k**	**Asph.**
0	Object	Air	∞	–	–	–	–
1	Ap. stop	Air	–	762.00	_	_	_
2	Primary	Mirror	-2210.00	762.00	-4544.0	-1.00	–
3	(graphic)	Air	-27.559557	–	–	–	–
4	Filter (front)	UBK7	-5.00	57.15	flat	–	–
5	Filter (back)	Air	-4.00	57.15	flat	–	–
6	#1 Fld. lens	Silca	-3.50	56.00	-47.99880	0.00	–
7	#1 Fld. lens	Air	-23.64395	54.00	-46.55977	0.00	–
8	Prime Focus	Air	-25.76525	43.85	flat	–	–
9	#2 Fld. lens	Silica	-4.00	54.00	64.08389	0.00	–
10	#2 Fld. lens	Air	-545.00	56.00	53.49770	0.00	–
11	Secondary	Mirror	545.00	200.00	1168.479	-3.2732	–
12	Tertiary	Mirror	-570.75	223.00	-1150.451	0.9479	–
13	Fld Flattener	Silica	6.75	60.00	-179.194	0.00	–
14	Fld Flattener	Silica	-7.5	60.00	269.187	0.00	-5.69380E-7
15	CCD Sur.	Vacuum	-21.96	30.0x30.0	flat	–	–

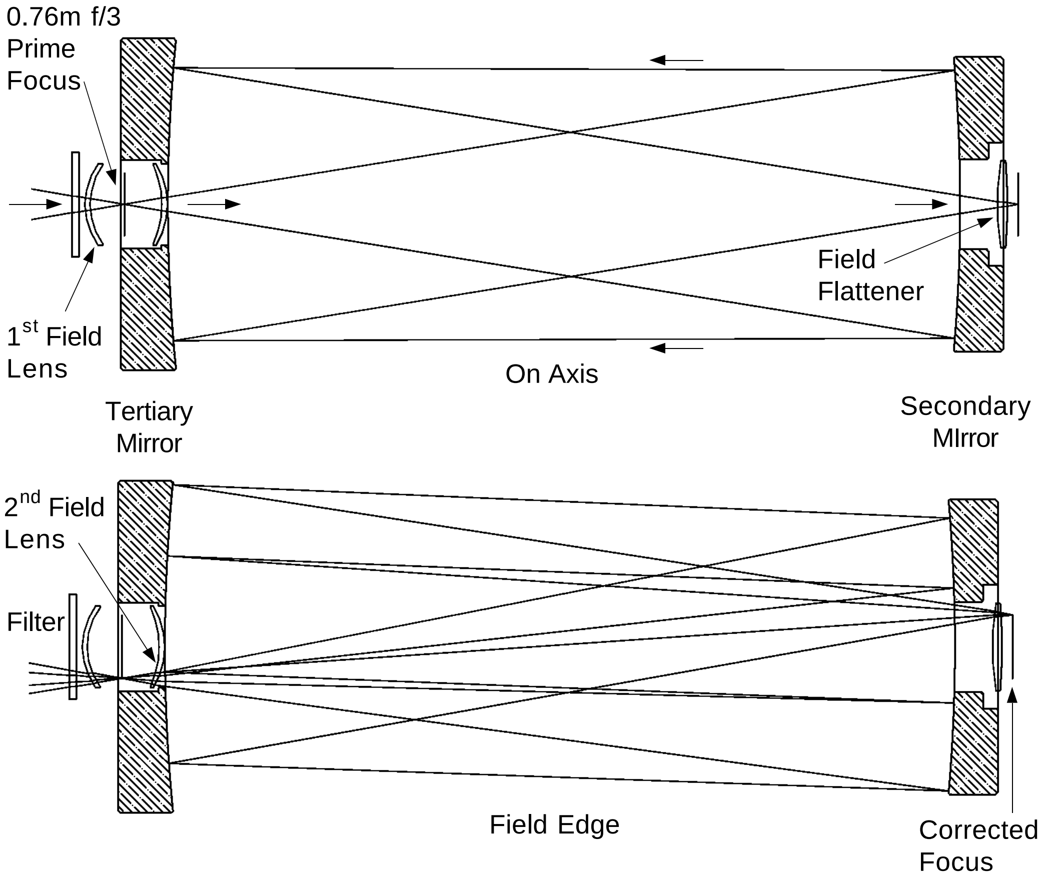
0.76m f/3
Prime
Focus
1st Field
Lens
Tertiary
Mirror
On Axis
Field
Flattener
Secondary
MIrror
2nd Field
Lens
Filter
Field Edge
Corrected
Focus

Figure 3.2: The optical ray paths for the PFC's corrector on axis (top) and at the edge of the field (bottom) 0.55 degrees off axis, defined by the corners of the CCD.

in Figure 3.2. In the Table, all units for thickness, diameter, and radius are in mm, and the positive direction is towards the object. The one aspheric surface on the field flattener is specified in terms of a mean radius and a 4th order coefficient. A medium indicated as a "Mirror" implies a direction change in the optical path but does not change the sense of the thickness values relative to the object. Finally, three of the optical elements have central obstructions not listed in Table 3.1; in diameter they are: 300mm for the primary mirror, 67mm for the secondary, and 57mm for the tertiary.

Light first enters the corrector though the two meniscus field lenses, then is reflected by an oblate secondary mirror onto a hyperboloid tertiary mirror, and finally through an aspheric field flattener onto the CCD detector. By choosing fused silica for all three refractive elements we have maintained a high ultraviolet throughput, while the reflective elements and low dispersion of the refractive elements make the design close to being completely achromatic. As with any optical system as complex as this, there is a great deal of interplay between individual elements going into the system's overall performance. However, each element has a primary function.

Light first enters the corrector system through a pair of field lenses, whose primary function is to control astigmatism. In effect these lenses perform a similar function to that of a Fabry lens in a classical photometer – keeping an image of the primary fixed on the photomultiplier tube. By reimaging the pupil of the primary mirror near the secondary, we keep the illumination of the secondary nearly fixed as a function of field angle, minimizing astigmatism. The slight asymmetry in the field lens pair introduces a small amount of lateral chromatic aberration. This is designed to compensate for lateral chromatic aberration introduced by the field flattener, therefore maintaining the achromatic correction of the two mirrors. Furthermore, these two lenses also introduce a small amount of distortion in an opposite sense to the rest of the system, keeping the overall geometric distortion of the corrector impressively low: <0.01% across the 1.1° diameter corrected field. This low distortion allows us to exploit the CCD's linear geometric properties for high precision astrometric studies not previously possible with digital CCD imagery.

The next two elements in the corrector's optical system are the secondary and tertiary mirrors. These two mirrors serve primarily to achromatically correct the off-axis coma produced by a parabolic primary. These two mirrors are key to the exceptional broadband performance of this corrector design, keeping the coma correction independent of wavelength. In our specific implementation of this design concept the overall magnification is unity, but this need not be so. The net magnification of the corrector is controlled by these mirrors, and could be made different to suit the needs of individual telescope/detector combinations.

The final element in the corrector is the field flattener, which also serves as the window for the evacuated CCD housing. The first surface of the field flattener is spherical, and flattens the small part of the nearly spherical focal surface we accept onto the planar CCD. The second surface of the field flattener, inside the vacuum of the CCD dewar, is strongly aspheric, with nearly 80 waves of 4th order curvature. This aspheric element corrects the higher order distortion left over from the field lenses, resulting in an essentially distortion–free flat focal plane at the surface of the CCD.

The quality of the corrector design can be evaluated by examining the ray fan diagrams shown in Figure 3.3. Shown are the transverse and sagital errors in the focal plane for three different field angles: 0.0 (on axis), 0.7, and 1.0 (edge of field) at 3100, 4500, and 9000Å. These errors measure the distance in the focal

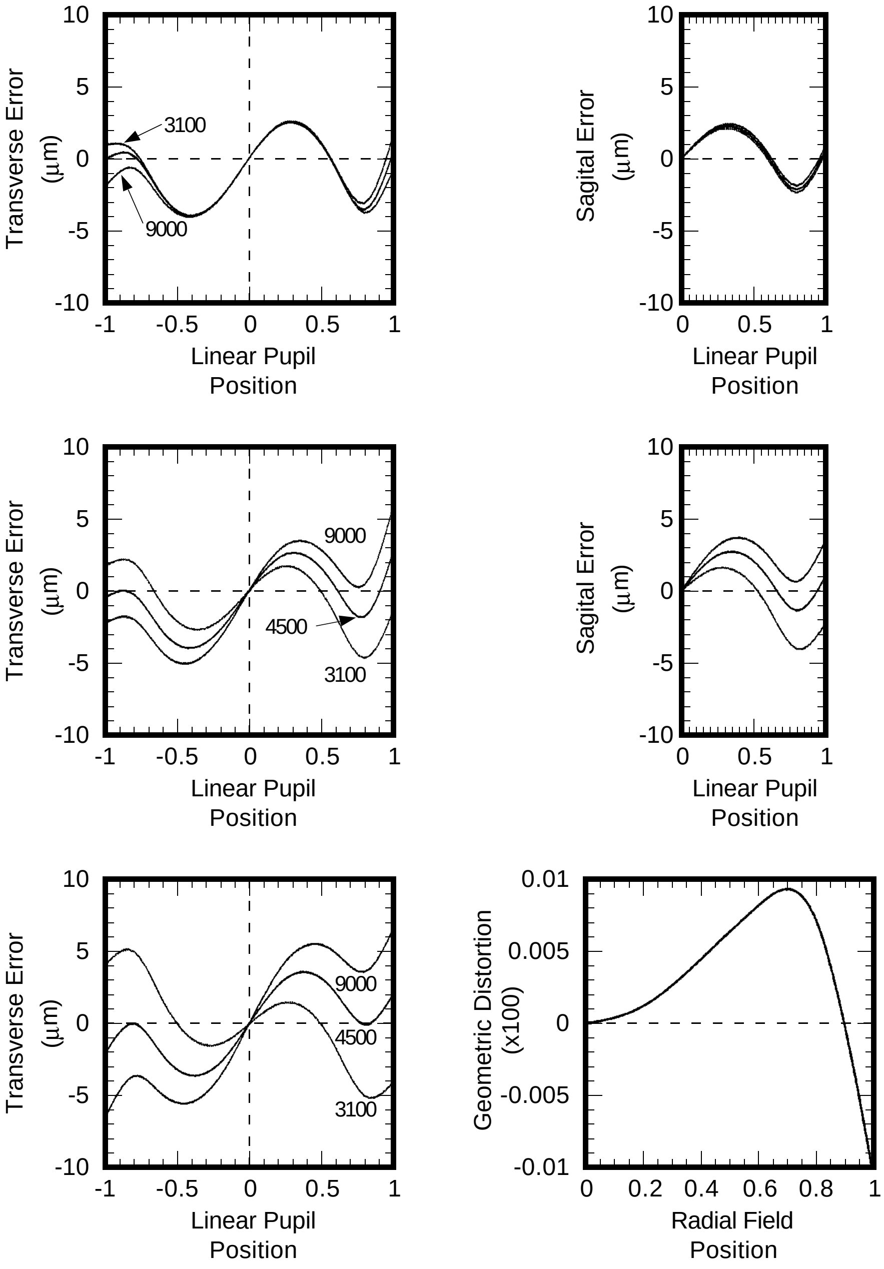

Figure 3.3: Transverse (left) and sagital (right) ray fan diagrams showing the residual aberrations in the corrector design. Also shown is the geometric distortion versus field position (lower right).

plane from a perfect image center to where the transverse or sagital rays intercept the focal plane. In correcting the off-axis coma of the $f/3$ paraboloid we have introduced a small amount of spherical aberration as evident from the "S" shaped curves. In all cases the spherical aberration amounts to $< 5\mu m$ of image blurring. There is also an increased "tilt" in these curves from the field edge (top panels) towards the center (bottom left panel). Because the optical system is axially symmetric, the on-axis sagital error is identical to the transverse error. In conjunction with the increased tilt, the different wavelengths begin to separate. This behavior in ray fan diagrams is interpreted as a slight wavelength–dependent focus shift, amounting to a $1-2\mu m$ additional image blur. Independent of field position or wavelength, the residual aberrations in the corrector design are much less than the $15\mu m$ pixels of our chosen CCD. We also show the amount of geometric field distortion as a function of field position (Figure 3.3, lower right panel). Nowhere in the field does the distortion exceed 0.01%, which at the PFC's plate scale is $< \pm 0.25$ arcseconds.

From the computed point spread functions (PSFs) shown in Figure 3.4 we can further evaluate the imaging performance of the corrector design. In each case the projected square is approximately equivalent in size to the $15\mu m$ pixels in the Loral-Fairchild CCD. Each row of PSFs are for a specified wavelength at the center of one of the *UBVRI* band passes as indicated in the left–most column. For each wavelength we have computed PSFs in three different field positions, 0.0 (on axis), 0.564 – the radius which contains 50% of the CCDs imaging area, and 1.0 at the very corner of the field. Below each PSF is a number expressing its Strehl ratio, where a perfect image has a Strehl ratio of 1.0. An image is

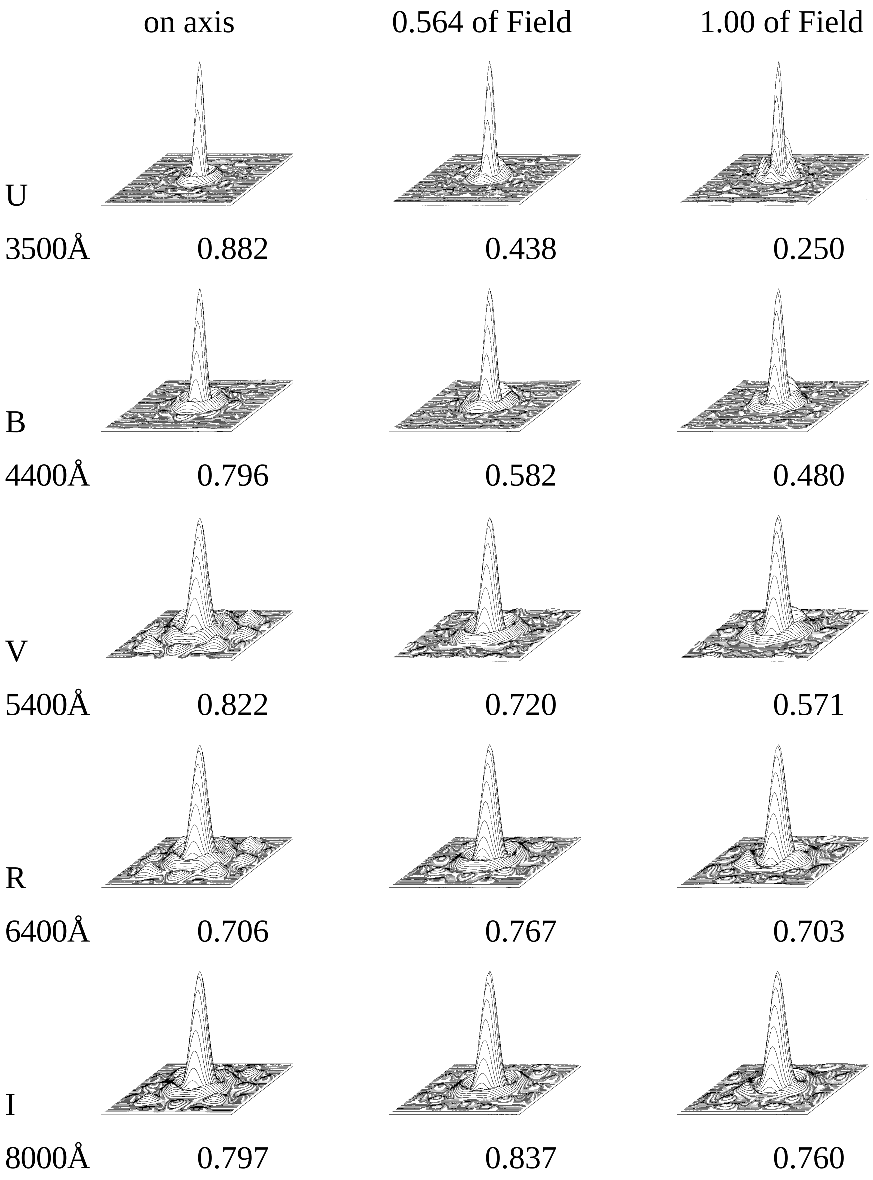

Figure 3.4: Point spread functions for the corrector design as a function of field position and wavelength. Each square is approximately $15\mu m$ on a side and the Strehl ratio for each PSF is listed below it.

considered diffraction limited if its Strehl ratio is more than 0.7. Given this criterion we can see the corrector is diffraction limited, or nearly so, throughout its field and wavelength coverage. Furthermore, in every instance more than 98% of the PSFs encircled energy is contained within a single $15\mu m$ pixel. We could easily use a CCD with smaller pixels with this optical design.

In addition to pure imaging performance, we must consider indirect illumination of the detector, scattered light, and overall efficiency when designing and evaluating an optical system for astronomical purposes. In examining Figure 3.2 and 3.5 (below) we see that there exists the possibility of illuminating the CCD directly through the field lenses and the secondary's central hole. The central obstruction of the PFC is defined by the 12.5 inch diameter mid-ring in the corrector support structure and amounts to ~17% by area. This mid-ring is reimaged for *all* field angles onto, but slightly larger than, the central hole in the secondary mirror, off the primary and through the field lenses. This prevents the sky reflected from the primary from illuminating the CCD. In exchange for this necessity, the central obstruction falling on the tertiary mirror moves with field angle, allowing some of the light at large field angles to fall through its central hole (see Figure 3.6). This in turn causes a slight field dependence on the illumination of the CCD. Furthermore, from inspection of Figure 3.4 we can see that rays are blocked by the telescope tube's top ring, causing a slight amount of vignetting in the extreme field. The combination of variation in obscuration and vignetting produce variations in illumination across the field on the order of 2%, increasing with field angle.

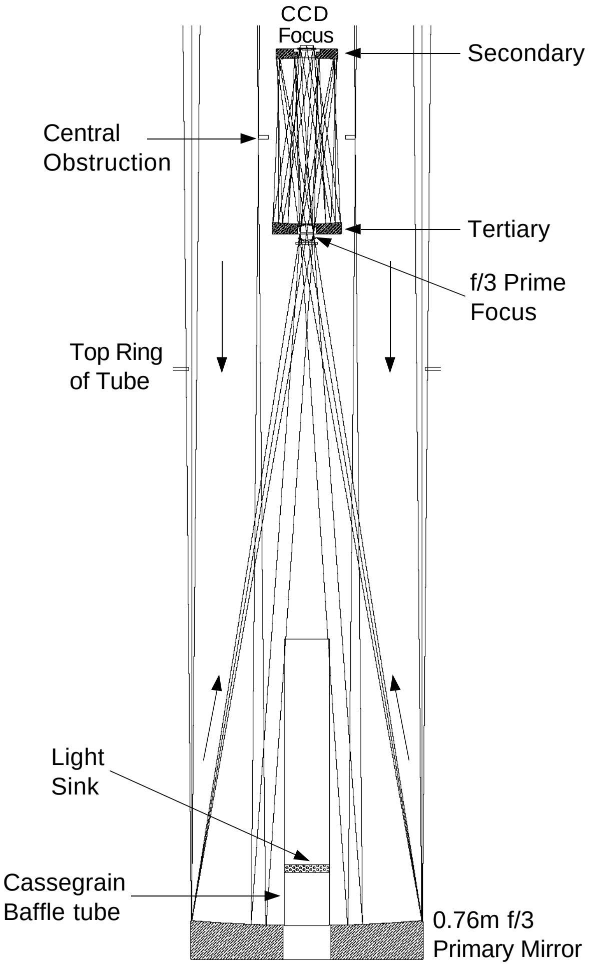
CCD
Focus
Secondary
Central
Obstruction
Tertiary
f/3 Prime
Focus
Top Ring
of Tube
Light
Sink
Cassegrain
Baffle tube
0.76m f/3
Primary Mirror

Figure 3.5: The optical ray path diagram for the PFC (corrector+primary).

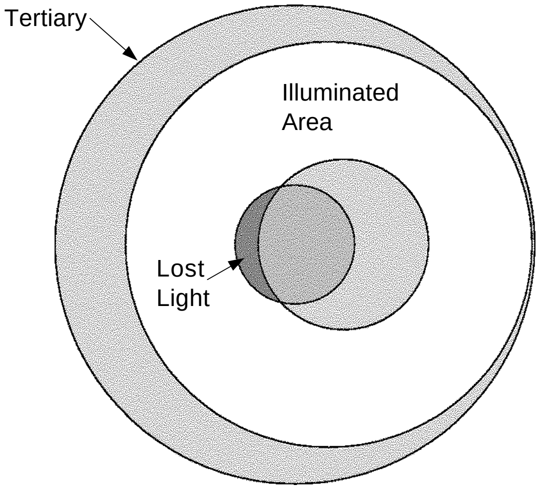

Figure 3.6: Light loss through the tertiary's central hole from illumination by off-axis sources.

Shadowing of the central obstruction on the secondary does not prevent the CCD from "looking" straight through the field lenses into the Cassegrain baffle tube. Each pixel sees a ~12mm diameter spot at the front of the baffle. The sum of these spots from the entire CCD array forms a 142mm circle and is completely contained within the Cassegrain baffle. For this reason we have placed a "light sink", made from open cell foam sprayed with very flat black paint, deep inside the baffle tube (see Figure 3.5). Visual inspection of the open end of the baffle with the "light sink" installed confirms that very little light escapes once it has entered. Thus, we have kept to a minimum non-imaging illumination from ambient surroundings.

There are two places where we control scattered light inside the corrector. The location of the prime focus lies midway between the two field lenses. At this focal plane we have placed a square field stop only slightly larger than the imaging area of the CCD to allow for comatic light at the field edges to pass. The field stop prevents off–axis light from entering the system. Just prior to the secondary mirror the field lenses form a pupil, where we have placed a circular aperture stop. This stop is slightly oversized so that the primary mirror is still the true aperture stop, but serves to stop light grazing off the inside of the corrector tube from getting back onto the CCD.

The design of this corrector is necessarily complex in order to optimize performance. The losses from reflection on the corrector's 6 transmissive surfaces is roughly 19%, with the two filter surfaces adding another 8%. We have applied a custom–made anti–reflection coating specifically manufactured for fused silica to all transmisive surfaces except those on the filters. The multi-layer coating as delivered by Continental Optics has outstanding broadband performance over the bandpass of the corrector, which, when applied to the corrector’s 6 fused silica surfaces, results in about 16% increased throughput. This coating reduces the air/fused silica surface reflectance from 3.5–4.0% to <1.0% from 3100Å through ~8000Å and <3.5% to the red edge of the I band at ~9500Å.

In addition to improving throughput, the anti-reflection coating has substantially improved the ghost images found in any refractive optical system. In the PFC's corrector we have identified nine primary sources for ghost images, which are shown in Figure 3.7. There are six sources from the field lenses, one from the filter, and one from the field flattener. The integrated intensity of these

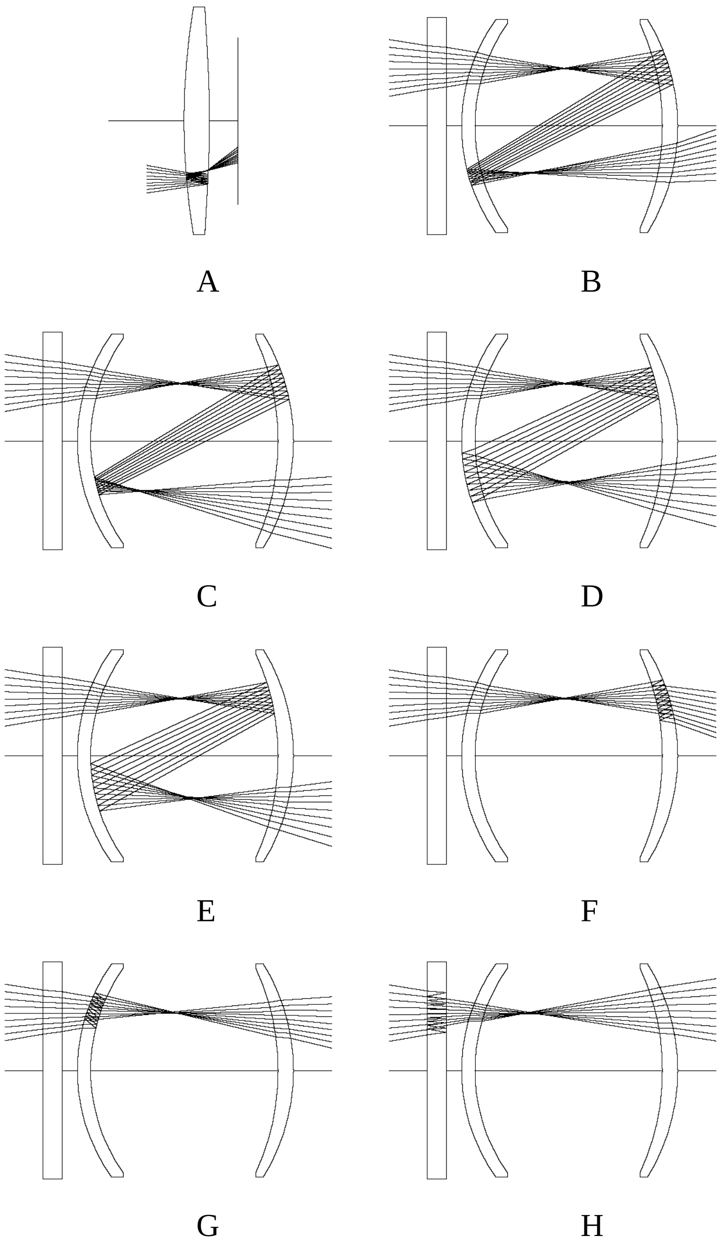

Figure 3.7: Optical ray path diagrams for the nine primary ghost image sources we have identified.

ghost images is related to the square of reflectance. The anti-reflection coating has reduced these by a factor of at least 16 and at some wavelengths by a factor of >40. The relative surface intensity of these ghosts is dependent on how far away their focus is from a true focal plane and field angle, on which the anti-reflection coating has no effect.

3.1.2 Mechanical Design

The foremost principle in instrument design is *function*. We must constantly ask ourselves: does the design allow the instrument to perform the scientific task for which it is meant without detrimental compromise? It is not always possible to prevent compromise in an instrument's performance because of basic design limitations, but we should explore all possible avenues before accepting compromise. The PFC has four primary assemblies that, integrated together, create a functioning instrument. The primary function of the PFC's mechanical structure is to hold the corrector optics in place above the primary mirror. The corrector optics are held in place relative to each other in the Optics Tube, which also supports the CCD Dewar, filter wheel, and shutter. Together, these form a light–tight system at the heart of the PFC. The Optics Tube and CCD Dewar are held above the primary mirror by a four–vane spider and truss assembly. Finally, the Electronics Rack is attached to the old Cassegrain instrument port, which functions primarily as a counterweight.

I also had to keep in mind several global constraints in designing each assembly to perform its function. With any telescope, weight and balance are deeply rooted in the overall functionality and reliability of the system. If an instrument overloads the mount and/or drive system or if it cannot be balanced, then the telescope will track poorly and render the instrument useless. I was particularly sensitive to the total weight of the PFC because the 0.76m (30 inch) Boller and Chivens telescope is already on an undersized mount, originally built for a 24 inch telescope. Related to the weight issue is stiffness: flexure can destroy the usefulness of any astronomical instrument. I also paid close attention to the design of specific parts, keeping them simple and easy to fabricate, resorting to complicated detailed design only when absolutely necessary. I have seen many instances of the "perfectly" engineered part which could not be fabricated or incurs the cost of a small fortune to do so.

Optics Tube Assembly

The primary function of the Optical Tube assembly is to hold the elements of the corrector in place per their prescription and allowable tolerances. In Figure 3.8 I have cut away the outer layers of the Optics Tube and CCD Dewar to show the internal arrangement of cells, shutter, filter wheel, and CCD. The field flattener is completely contained within the secondary mirror, making it impossible to place the shutter in its traditional position immediately in front of the CCD Dewar window. This forced me to place the shutter in front of the field lenses, requiring that the Optics Tube be light tight.

The most sensitive in their placement are the two mirrors, which must be held coaxial to each other to better than 0.1mm translation and 1.5 arcminutes of tip–tilt. Because the secondary cell must bear the load of the CCD dewar, I chose to make this from a single piece of aluminum with a strong "T" shaped

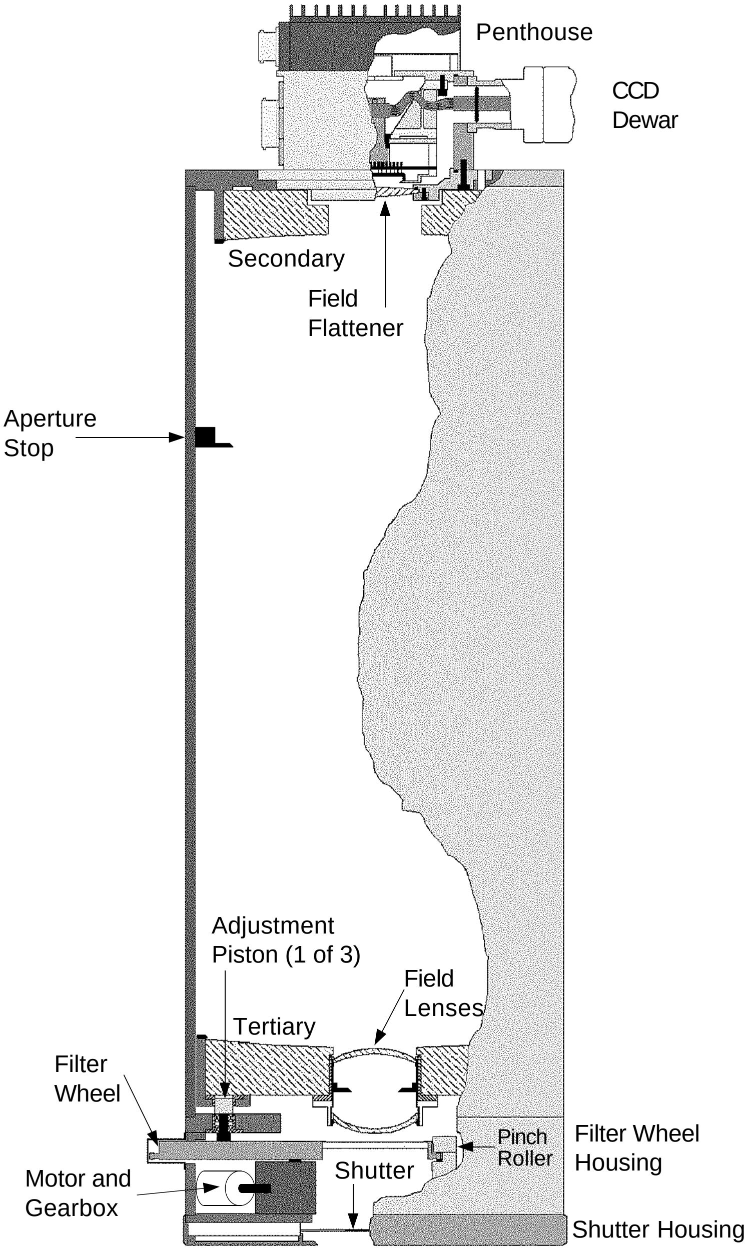
Penthouse
CCD
Dewar
Secondary
Field
Flattener
Aperture
Stop
Adjustment
Piston (1 of 3)
Field
Lenses
Tertiary
Filter
Wheel
Pinch
Roller
Filter Wheel
Housing
Motor and
Gearbox
Shutter
Shutter Housing

Figure 3.8: A cutaway view of the Optical Tube + CCD Dewar assemblies showing the location of the corrector optics, lens and mirror cells, shutter, and filter wheel.

crossection. As a result of this design the secondary cell has a small amount of translation, but no tip–tilt adjustment. Through careful machining tolerances and small adjustment to tip–tilt with shims, the optical axis of the secondary defines the optical axis of the entire system. The tertiary mirror is brought into tolerance by its three point tip–tilt adjustments and push–pull translation adjustments. These adjustments are accessible through ports in the side of the Optics Tube and on the back plane of the tertiary cell.

The cells which hold the field lenses needed special attention. The mirrors were fabricated from ultra–low expansion Zerodur, which is incompatible with the expansion coefficients of most metals. The close quarters between the field lenses and tertiary mirror necessitated a glass–metal–glass interface, without the usual Teflon or cork cushion between glass and metal (see Figure 3.9). Without the proper choice of materials, changes in temperature could put great strain on the glass elements, causing them to lose their designed figures, or at worst actually break. I solved this problem by using a stainless steel alloy called Invar, which has an expansion coefficient nearly the same as Zerodur and fused silica. I fastened the cell insert, also made from Invar, in the tertiary mirror with a thin layer of flexible RTV silicon glue to further guard against movement caused by differential temperature response of the materials.

The filter wheel proved to be particularly troublesome to design. Because I insisted it hold five 2×2 inch filters, it was too big to fit completely within the Optics Tube. The most compact 5 position geometry for square filters results in a star shaped pattern. The necessary location behind the shutter meant this was a potential source for a large light leak. The optical arrangement of the corrector

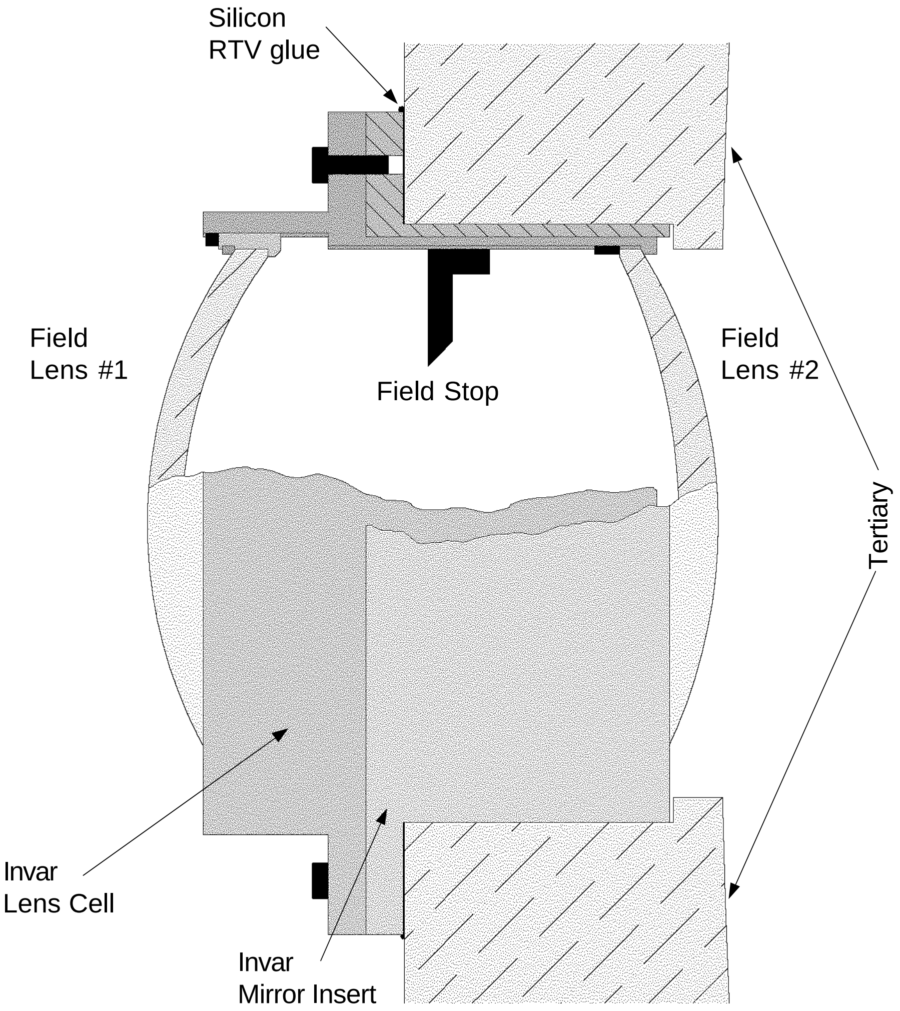
Silicon
RTV glue
Field
Lens #1
Field Stop
Field
Lens #2
Tertiary
Invar
Lens Cell
Invar
Mirror Insert

Figure 3.9: Cutaway view of the Invar Field Lens Cell and tertiary mirror insert.

also meant there was no room outside the Optics Tube for the filter wheel drive motor without protruding into the incoming light beam. The resulting design is necessarily compact but it is also cumbersome to change filter arrangements quickly, as the front end of the Optics Tube must be disassembled. Fortunately filters need not be changed very often. The filter wheel's excursion outside the Optics Tube is made light tight by a cover sealed with a rubber gasket – not an ideal solution, but functional. Electrical signals for the filter motor are passed to the shutter housing through a 4 conductor interconnect on the filter housing's back plane.

It is essential that filters not be allowed to move when in place, so that irregularities (*e.g.* dust) projected onto the focal plane can be consistently and precisely accounted for in the data reduction process. This requirement opposes our desire to be able to change the filters by moving the filter wheel. To accomplish this I have designed a three–point rotation mechanism that allows rotation, but provides complete constraint at each filter position. The lateral motion is constrained by the central bearing of the gearbox while allowing rotational motion. I have constrained the filter tip–tilt by placing a pair of pinch rollers to ride the filter wheel's outer rim. In locating these pinch rollers I formed a right triangle with the rotation axis with the hypotenuse passing approximately midway through the optical path. The pinch rollers and bearings define the plane of rotation. One of the pinch rollers also serves as a detent to provide the necessary rotational constraint while the filter is in position.

Covering the entrance to the Optics Tube is the shutter housing, which is simply a light–tight fixture to hold the shutter in place. Its only other function is to pass the filter control signals (as well as its own signals) to the outside world via an opaque military–style connector. Because the shutter's aperture is oversized, I have designed the housing opening to be just large enough not to vignette the extreme field rays, minimizing the quantity of unwanted light entering the corrector when the shutter is open.

Spider and Truss Assemblies

The fast $f/3$ focal ratio of the primary places severe requirements on the placement of the corrector at prime focus. We must hold the corrector's optical axis colinear with the primary's to within $\pm 500\mu m$ translation and $6-7$ arcminutes of tip–tilt to keep the images inside a $15\mu m$ pixel. A change in focus which causes the image to blur by one diameter of the designed image size is called "the depth of field". The corrector has a depth of field of approximately $\pm 20\mu m$. We have met these requirements by holding the Optics Tube in place with a stressed spider–truss assembly and an active feedback focus servo.

The Truss is fabricated by joining two hexagons, rotationally offset by 30 degrees, at each apex by placing sequentially around its perimeter angled tubular members (see Figure 3.10). I chose this design over other geometries as a compromise between strength, weight, size, and ease of fabrication. The inside dimension of the bottom hexagon circumscribes the front of the existing telescope tube and provides a mating surface identical to the the telescope's original Cassegrain secondary assembly. The size of the upper hexagon was made slightly larger so it did not vignette incoming light from the edge of the field. We fabricated both hexagons by welding together mitered pieces of 2 inch square

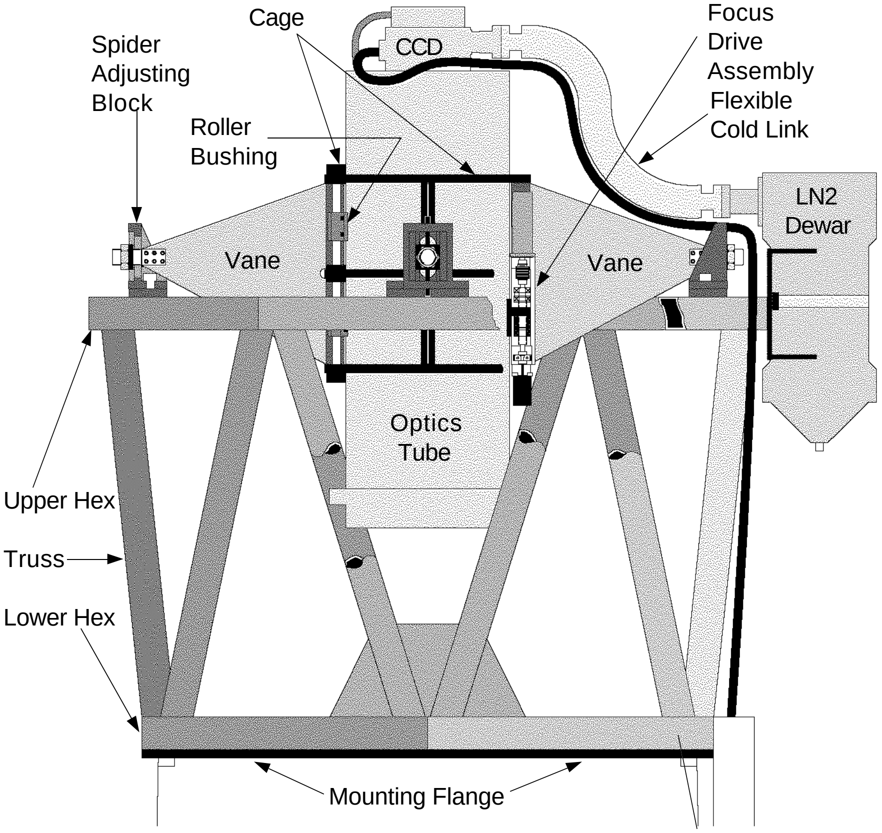
Cage
Spider
Adjusting
Block
Roller
Bushing
CCD
Focus
Drive
Assembly
Flexible
Cold Link
LN2
Dewar
Vane
Vane
Optics
Tube
Upper Hex
Truss
Lower Hex
Mounting Flange

Figure 3.10: The PFC's Truss and Spider assemblies with various items discussed in the text indicated.

aluminum tubing. Similarly we made the truss members from mitered 2 inch round aluminum tube, which were welded in place – two ends at each apex – forming the truss.

The Spider assembly serves as the interface between the Truss and Optics Tube, and is also key to providing the required stiffness for the whole support structure. The Optics Tube is suspended from the upper hexagon inside a three–ring cage containing the focusing mechanism. The cage is joined to the truss at 4 adjustable points through thin aluminum vanes. At the end of each vane there is a 16 threads per inch (TPI) screw which provides lateral centering adjustments and tensioning. By placing the vanes under several hundred pounds of tension I have "pre-stressed" the support structure. In doing this I have made the weight of the Optics Tube and CCD Dewar negligible in terms of flexure in the support structure. The combination between a truss design and pre–stressing makes a very stiff assembly, placing the stiffness limit on the existing telescope tube. At each of the adjustment points the vane screws ride in a push–pull slide, providing the necessary tip–tilt adjustment between the corrector and primary.

The small focus tolerance allowed by the shallow depth-of-field requires high precision control of the corrector's focus motion. For design purposes we set the minimum tolerance of focus to be a quarter of the depth-of-field, totaling $10\mu m$. The effective length of the telescope tube and PFC is approximately 2.59 meters and is made completely of aluminum. Over this length, aluminum will vary its size with temperature at a rate of $\sim 51\mu m/^{\circ}C$ and will put the PFC's focus out of tolerance with a change of only $0.2^{\circ}C$. To keep a constant focus we had to design an active, temperature compensating focus mechanism capable of very fine motion at the micron level.

I obtained the required smooth linear motion using three pillow block style self–aligning roller bearings riding on a pair of precision ground and hardened Thompson shafts. The Thompson shafts are supported in three places by the central cage, with a bushing in between to define the axis of motion parallel to the optical axis. The position along the axis of travel is defined by a stainless steel lead screw and nut made of self–lubricating Ampco bronze. The lead screw has a thread pitch of 56 TPI ($453.57\mu m$ per turn) and is held axially at one end by a pair of duplex bearings which allows the other end to float. The mating nut is flexible in both tip and tilt but is axially rigid and stiff. Thus any error in misalignment between the axis of motion and the lead screw is translated into an acceptable tip–tilt through flexure of both nut and lead screw, rather than binding or flexing of the linear bearings.

Control of the focus mechanism is done through both hardware devices and software programming. In Figure 3.11 I show a block diagram indicating the devices and how they are connected to the mechanical assemblies and host computer. Three "smart" subsystems interact through software control to produce an active focus system which compensates for both temperature changes and filter thickness differences. In choosing RS232 serial communication for the individual control subsystems I have kept the control independent of host computer brand. It also allows me to use a standard terminal for stand–alone testing and verification of each subsystem. The lead screw is driven by a Globe gear motor with a Galil servo controller and positioning feedback is done with an incremental shaft encoder with 4096 steps per revolution. In theory, one step is equivalent to $0.11\mu m$ linear movement of the Optics Tube. However, in practice the smallest increment I have been able to measure consistently is 4 encoder steps – $0.44\mu m$, which I regard as the true focus resolution. Thus, I have exceeded our original design resolution criterion by a factor of ~22.

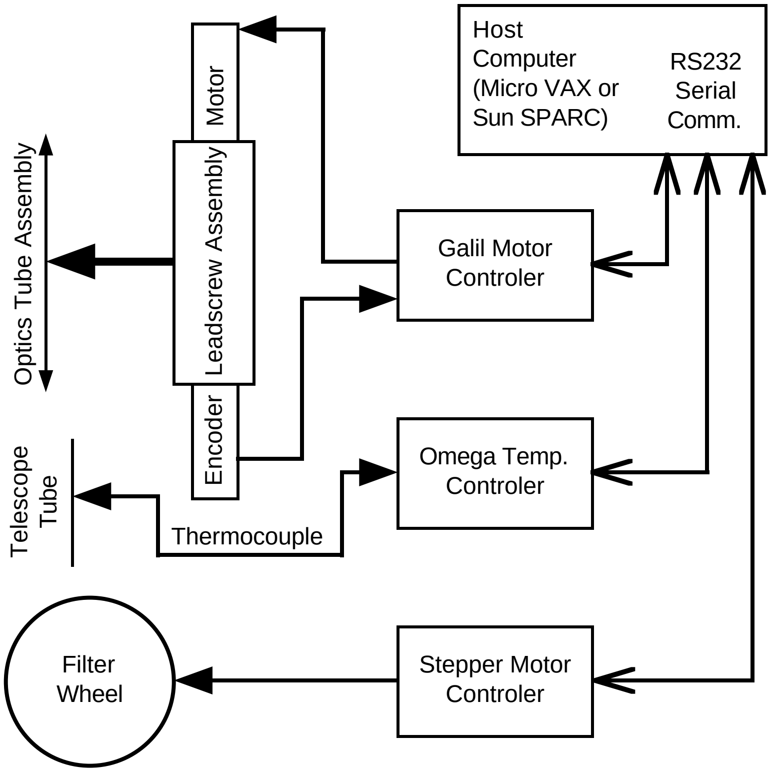
Host Computer (Micro VAX or Sun SPARC)
RS232 Serial Comm.
Motor
Leadscrew Assembly
Optics Tube Assembly
Encoder
Galil Motor Controler
Omega Temp. Controler
Telescope Tube
Thermocouple
Filter Wheel
Stepper Motor Controler

Figure 3.11: A block diagram of the hardware devices which make up the active focus assembly.

Temperature is monitored continuously by an Omega temperature controller through a thermocouple bolted to the telescope's aluminum tube. I have programmed this controller to sample the temperature 10 times per second and to keep a running average over a 10 second window. This information is sent to the computer when it is requested. In this way I have ensured the necessary temperature precision of at least $0.1^{\circ}C$ in order to maintain control of the focus changes. The filter wheel is not strictly part of the focus system, but I have included it here because variations in optical path length through different filters will cause changes in focus. Through a set of user–defined focus offsets for each filter, stored in the host computer, the focus position can be modified for each change in filter position.

The loop between focus position, telescope tube temperature, and filter optical path differences is closed in software by a subroutine in the CCD control program ARGUS. Through a set of commands from the keyboard, the user can manually move the focus by a precise amount. Once the focus is close, the user turns the temperature compensation on and makes the final focus adjustments; this prevents the user from "chasing" fast temperature changes usually present at the beginning of the night. From this point on, or whenever the servo is deactivated, the software will evaluate temperature and filter changes at the beginning of each exposure. Any needed focus position updates are done just before the CCD control program opens the shutter.

The effectiveness of the active focus servo is illustrated in a series of images I took at the beginning and end of a night's observing (Figure 3.12). The first image (left) was taken just after I had focused the instrument at the beginning of the night and set the servo on with a telescope tube temperature of 19.87C. The seeing on this night was not particularly good as can be seen in this first image. By the end of the night the temperature had dropped 5.25C. At this time I turned off the focus servo resulting in the very poor image quality shown in the middle image. I then turned the focus servo back on (right). The improvement is obvious, and illustrates the fact that the focus servo is essential to optimal operation. There was also a slight improvement in seeing between the beginning and end the of the night.

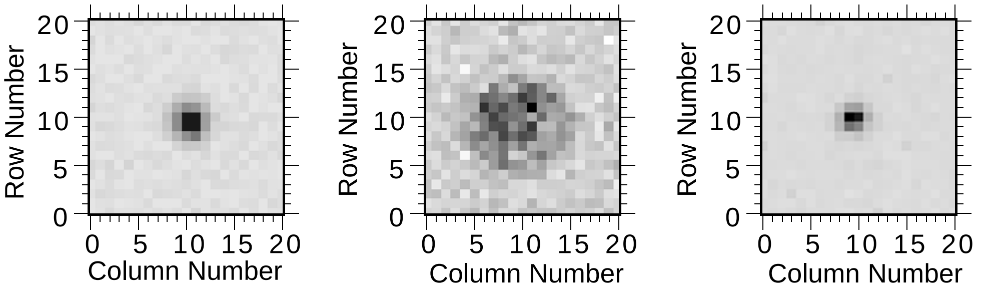

$T_{tube} = 19.87C$
servo set

$T_{tube} = 14.62C$
servo off

$T_{tube} = 14.59C$
servo on

Figure 3.12: The effectiveness of the active focus on the PFC is evident in this series of images. The first image (left) was taken at the beginning of the night when the focus servo was set and activated. The following two images were taken at the end of the night with the servo off (middle) and with the servo back on (right).

CCD Enclosure Design

The primary purpose of the CCD Enclosure (Dewar) is to thermally insulate the cryogenically cooled CCD imager from the ambient surroundings. The typical operating temperature of modern CCDs is near -100C, chosen so that thermal noise from the Silicon substrate doesn't overwhelm the signal created by faint objects. We must keep the CCD inside an evacuated enclosure to keep moisture and carbon dioxide from condensing on its surface.

The enclosure must hold the CCD rigidly in place at the corrected focus of the PFC. Of course the support structure for the CCD must also be thermally insulating as well. A cutaway illustration of the CCD Dewar showing its components is shown in Figure 3.13. In the PFC's dewar I have achieved the required thermal insulation and stiffness by designing a small tripod made of Amoco Torlon. Torlon is a composite material which has the strength of steel but the insulating properties of plastic. The CCD sits on top of a copper cold block which is supported by the tripod. The optical interface between the vacuum inside the CCD enclosure and the outside world is the field flattener, doubling as the dewar window. The center of the CCD is precisely positioned on the optical axis through close mechanical tolerances of the tripod and the registration surfaces mating to the Optics Tube. The entire assembly, including the penthouse electronics box, is about 4.5 inches thick.

Cooling the CCD on the PFC proved to be a bit tricky. The typical method of cooling a CCD is by way of conduction into liquid nitrogen contained in a tank that is part of the CCD dewar. However, I could not use this arrangement with the PFC for two reasons. First, the size and weight of the liquid nitrogen dewars in common use (IR Labs ND-3) prohibited emplacement with the CCD at the end of the corrector. Second, mounting the liquid Nitrogen (LN2) dewar there would allow it to vent cold air into the optical path, seriously disturbing the local seeing conditions. For these reasons I was left with no choice but to mount the LN2 dewar of to the side of the upper hexagon – outside the beam but nearly 24 inches away from the CCD. This meant that the CCD and

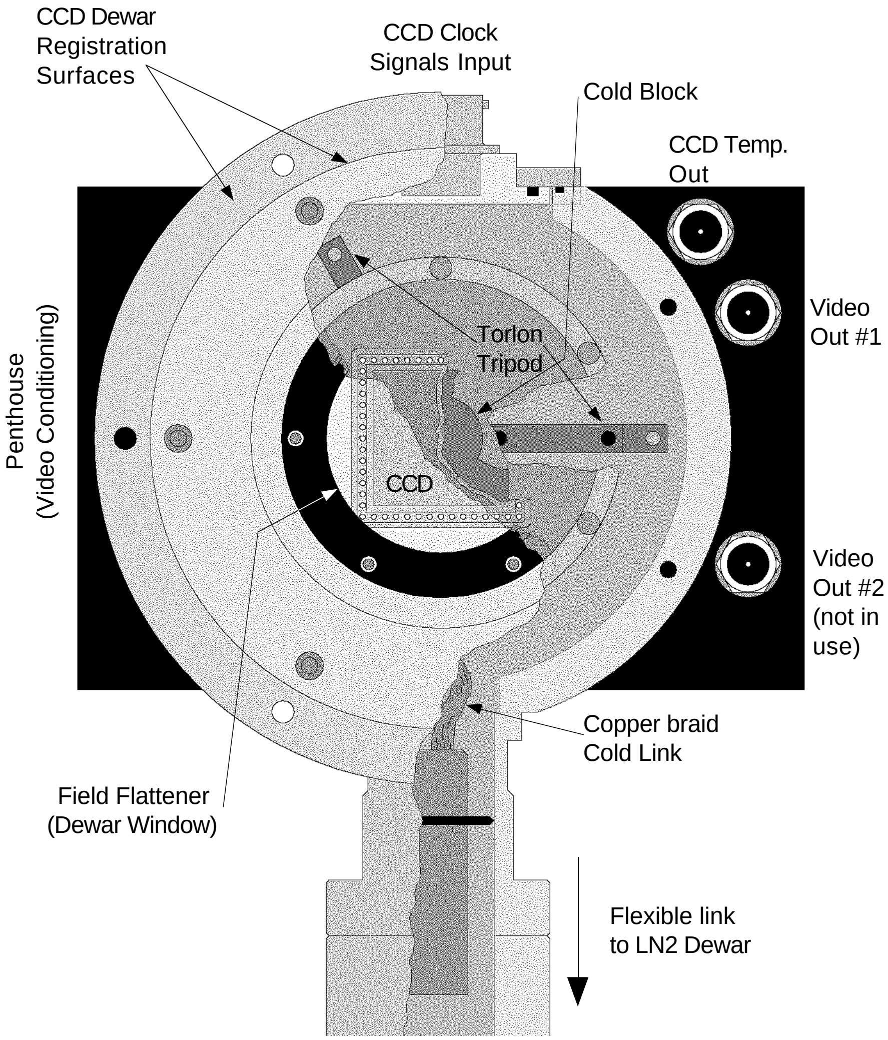
CCD Dewar Registration Surfaces
CCD Clock Signals Input
Cold Block
CCD Temp. Out
Video Out #1
Torlon Tripod
Penthouse (Video Conditioning)
CCD
Video Out #2 (not in use)
Copper braid Cold Link
Field Flattener (Dewar Window)
Flexible link to LN2 Dewar

Figure 3.13: Cutaway view inside the CCD Dewar showing the location of major parts.

LN2 dewars would move relative to each other when the corrector moves during focusing operations.

I solved this problem by using a 5/8 inch diameter copper cable held inside a standard flexible vacuum bellows. The copper cable is kept from shorting against the bellows' side by 6 evenly spaced PVC insulators. One end of the cable is clamped to the cold working surface inside the LN2 dewar, while the other is clamped to the copper cold block underneath the CCD. With this arrangement we must use the LN2 dewar in an inverted orientation, for which it is designed, but as a result we are only able to fill it to half capacity – 1.5 liters. Under a good vacuum, better than 10^{-4} Torr, our holding time on 1.5 liters of liquid nitrogen is approximately 11 hours while running the CCD at its normal operating temperature of -90C. This means the observer must top off the LN2 just before beginning to observe and just before he goes off to sleep for the day. Forgetting to do so will allow the CCD to warm up, which means it must be repumped to recover the vacuum.

3.2 PFC PERFORMANCE AND DATA REDUCTION

There are a number of things that I consider in evaluating an imaging instrument like the PFC. At the top of the list, with equal weight, are image and photometric quality, since these are what the instrument is meant for. For maximum quality we must have a low–noise, high–quality, stable CCD detector. In this section I will discuss the detector, imaging, and data reduction qualities of the PFC. I discuss the photometric qualities of the PFC in Chapter 5, where I describe a deep photometric survey I have conducted of the Praesepe open cluster.

3.2.1 Characteristics of the Loral-Fairchild 2048^2 CCD

Before we can evaluate the imaging and photometric performance of the PFC we must first know what limitations are imposed on us by our detector. The CCD imaging array used in the PFC is a Loral–Fairchild $2048 \times 2048 \times 15\mu m$ pixel device. We have given this CCD the designation LF1. This CCD is a front–side–illuminated thick detector which has been overcoated with Lumigen, a phosphorescent coating to extend the blue response into the ultraviolet. The detector quantum efficiency (DQE) for LF1+Lumigen is shown in Figure 3.14 (adopted from Geary *et al*. 1989). For comparison the DQE for an uncoated CCD identical to LF1 is also shown.

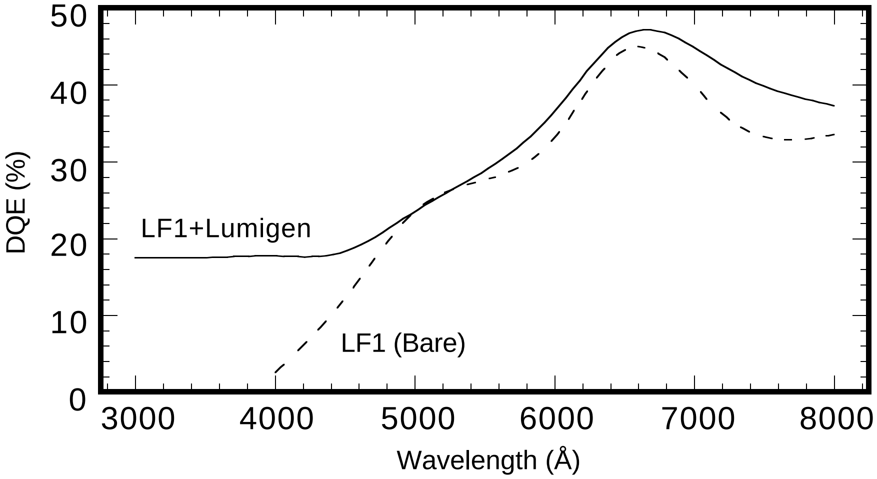

Figure 3.14: The detector quantum efficiency for LF1 coated with Lumigen and bare. The data are taken from Geary *et al.* 1989 based on a Ford Aerospace 2048 CCD, which later became Loral–Fairchild.

Cosmetically LF1 is an outstanding CCD. There are only two bad columns, one hot column seen at low light levels and one dead column seen at higher signal levels. In addition to these columns there are a handful of small charge traps common to most CCDs, but only two of these are severe, being several pixels wide. Also seen in flat exposures and in data where sky is significant is a "Z"–shaped mark across LF1's surface. We don't know where this mark of Zorro came from, but at its maximum it is <10% deep and is removed completely by the flat–fielding process. In all, less than 0.2% of LF1 imaging area is unusable from cosmetic defects.

The noise properties and electronic gain of a CCD system can be evaluated by measuring how the variance in signal changes as a function of signal level. This is expressed by

$$\sigma_{total}^{2} = g^{2} RN^{2} + gS, \qquad 3.2$$

where $\sigma_{\mathrm{total}}^{2}$ is the measured total variance, g is the electronic gain in data number per electron, RN is readout noise measured in electrons, and S is the measured signal level in electrons. The data I obtained from the ARGUS program Autonoise on 8 February 1994 and 14 March 1994 taken with the PFC and LF1 are shown in Figure 3.15. From these data I obtain a readout noise of 5.76 ± 0.02 electrons and an inverse gain of 1.622 ± 0.005 electrons per data number. These are typical values for LF1. The readout noise is not extremely low by today's standards, but it is low enough so that we are always sky–noise limited with modest exposure times through the broadband *UBVRI* filters.

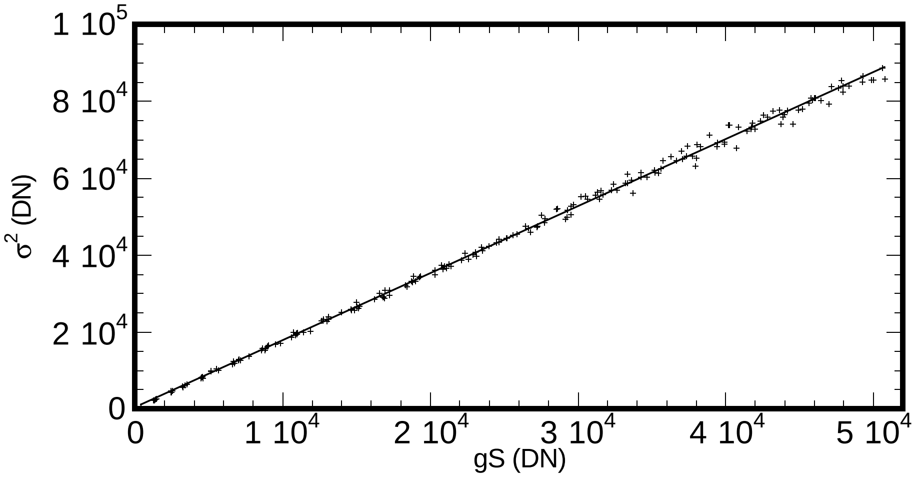

Figure 3.15: Variance versus signal level with the linear fit to compute read noise and electronic gain of LF1 on the PFC.

3.2.2 Imaging Performance

There are essentially only two measures for the imaging performance of an astronomical instrument: 1) image size and shape, and 2) consistency across the field. During our first engineering run in October 1991 we used a visual eyepiece and Ronchi ruling to evaluate the optical performance of the corrector. We were blessed with an exceptional night of steady seeing when we first looked at the star Gamma Andromeda, a triple system having yellow and blue components separated by 10 arcseconds, where the blue component is itself a double star, with components separated by <0.6 arcseconds. Once focused properly we were pleasantly shocked to find that we could clearly see the airy disk and the first two diffraction rings around the brighter yellow star. We then realized that the blue star was indeed 2 points of light separated cleanly with black sky in between. The airy disk of the 30 inch telescope is about 0.3 arcsecond, hence we estimated the seeing to be slightly better than this. These conditions lasted for about 1/2 hour, after which the seeing increased to between 0.4 and 0.7 arcseconds. On subsequent nights we used the Ronchi ruling to verify that the design performance of the PFC optical system was in fact being realized.

Since October 1991 we have not had a night of such excellent seeing at McDonald, and so have not been able to record the PFC's CCD total performance. Further we are still learning how to properly collimate the PFC's complex optical system. The best point–spread function I have personally measured with the PFC is roughly 1.5 pixels full width at half maximum (FWHM), or ~2 arcseconds. We have measured the stability of the images produced by the PFC by computing the FWHM for 600+ stars distributed across its field of view. In the following three figures I show the dependence of the FWHM as a function of column number (Figure 3.16), row number (Figure 3.17), and radial distance from the center of the CCD (Figure 3.18). Each measure was done for four broadband filters – *UBVI* – top to bottom panels. The average FWHM in pixels for full field through the individual filters are: $U = 2.56 \pm 0.26$, $B = 2.37 \pm 0.22$, $V = 2.37 \pm 0.20$, and $I = 2.64 \pm 0.18$. The PFC's imaging is constant to within the measured errors with respect to wavelength, as we designed it to be.

In both Figure 3.16 and 3.17 it is apparent that there are slight low–order trends in image size as a function of column and row number respectively. I have fit the data in each case with a 3rd order polynomial to illustrate these trends. In all cases the systematic variations are smaller than the noise band, but real

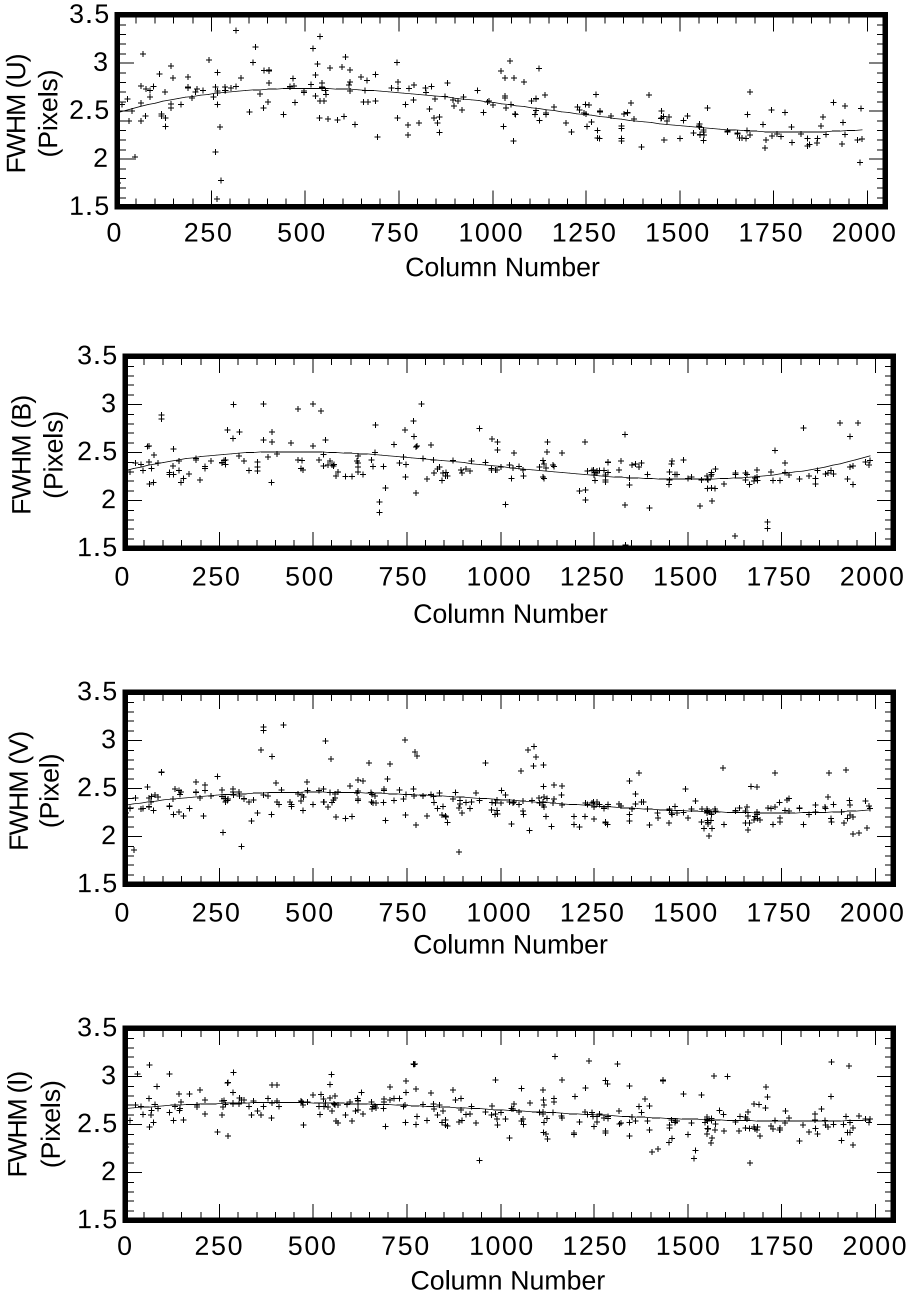

Figure 3.16: The FWHM as measured in four filters across the PFC's field versus column number.

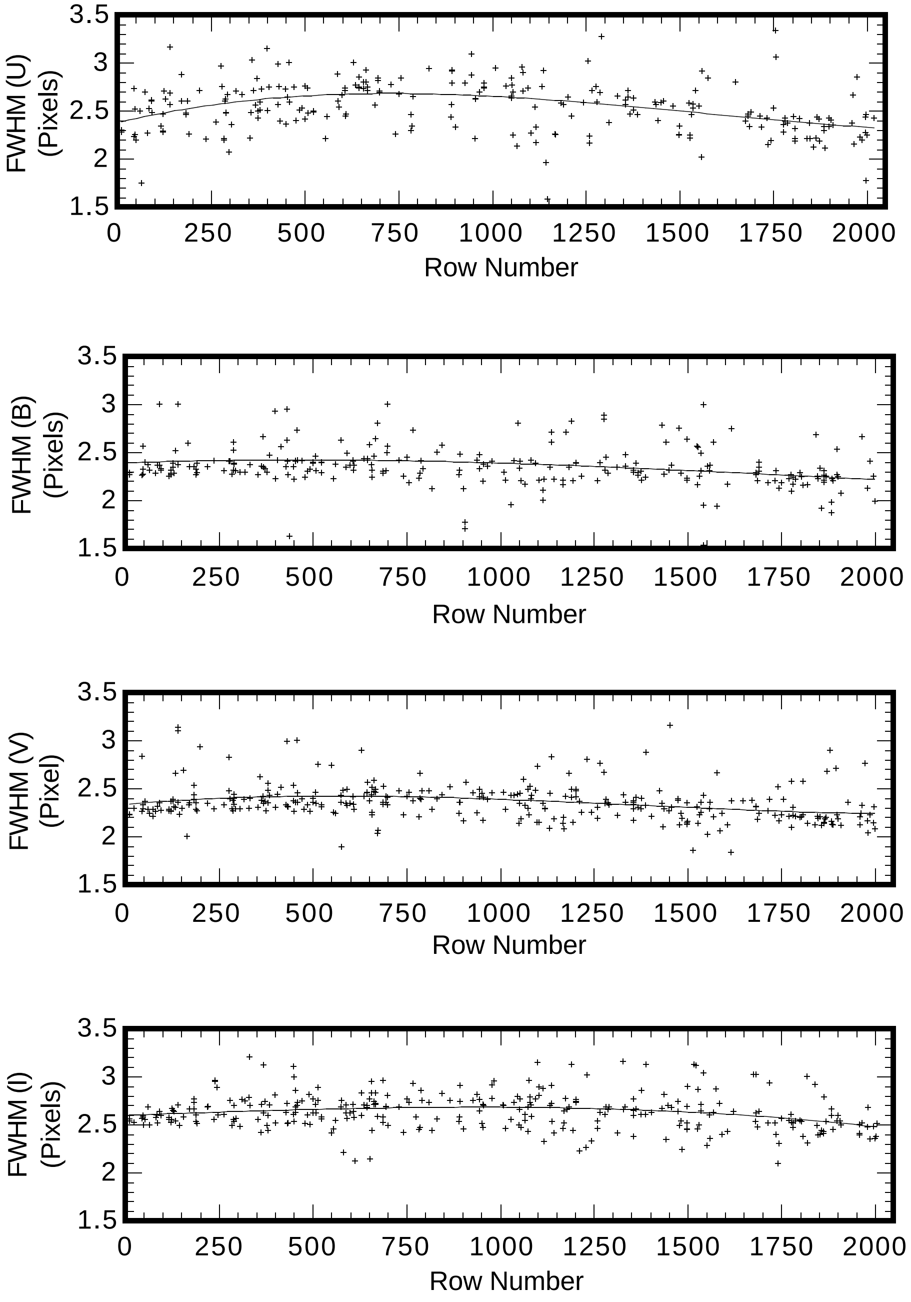

Figure 3.17: The measured FWHM as in Figure 3.16 but as a function of row number.

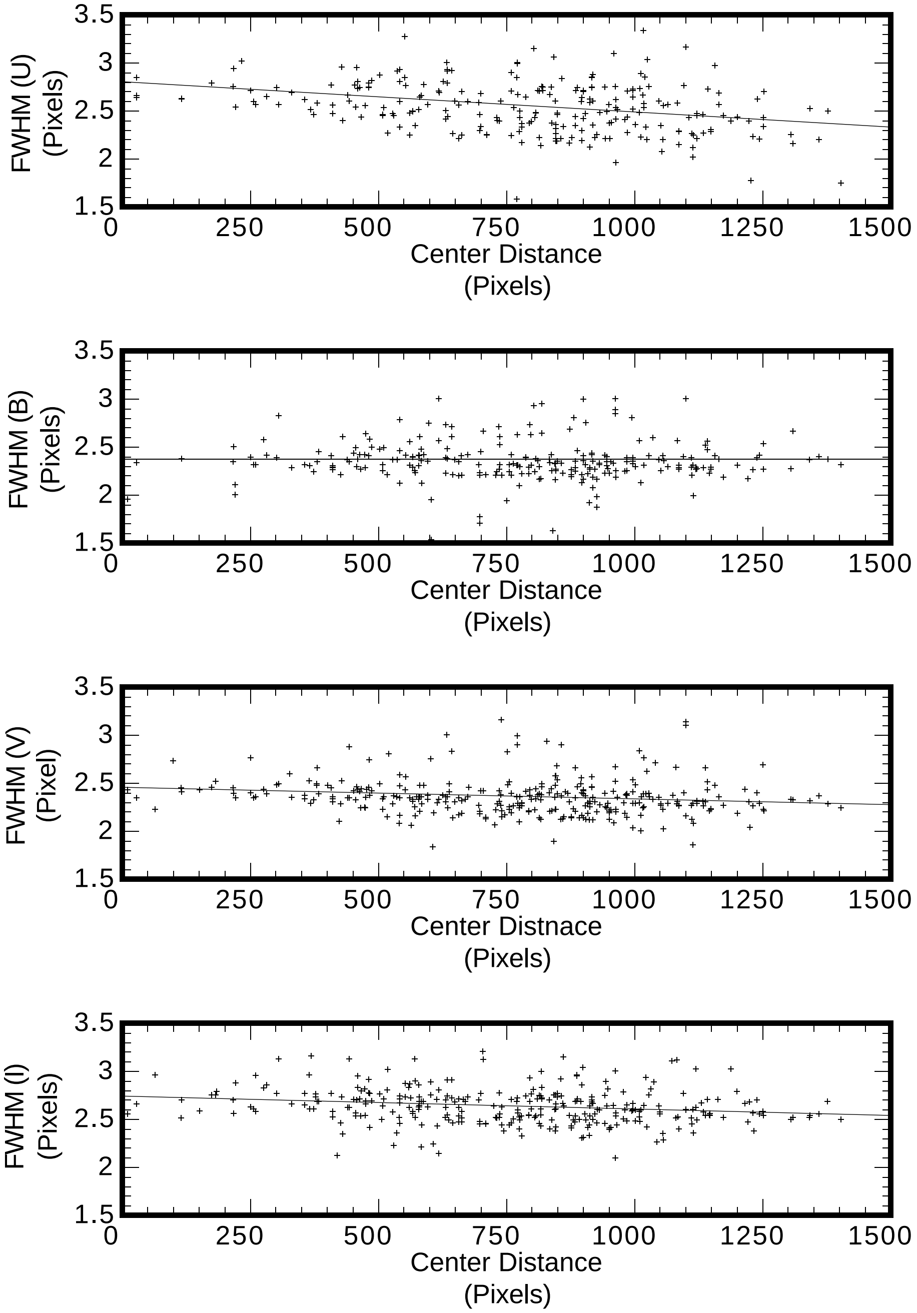

Figure 3.18: The radial dependence of measured FWHM in the four different filter band passes.

nonetheless. As a function of radial distance from the chip center, the data show little more than slight, linear trends. We can only speculate at this point as to what the source of these trends can be. There are many factors which can contribute to such behavior. For example, the CCD may not be perfectly flat, or one of the many optical elements could be slightly out of alignment. However, since optical misalignments tend to produce radial variations, I suspect some of what we are seeing is a result of the CCD not being exactly flat.

3.2.3 Reducing Data from the PFC

The key to success for any instrument making scientific measurement is the removal of its own signature from the data. It is absolutely critical for precise quantitative measurement, using *any* instrument, to accurately account for its instrumental signature. If one is truly successful in this endeavor then we are sure that the resulting data reflect something intrinsic to the properties of the observed objects. However, it is my opinion that to do this well requires *intimate* knowledge of the instrument used to make the measurement.

When dealing with CCD imaging systems there are two basic types of signatures we must account for: 1) the electronic signature generated by the CCD system, and 2) the optical signature produced both by the CCD itself and the optics in front of it. Fortunately, in a well–designed CCD imaging system we can account for these with a great deal of precision. Because of the large field of view of the PFC, the instrument has some unique aspects which must be considered when reducing data, as compared to other CCD imaging systems.

The exact details of how one removes the instrumental signature from a CCD is described in *A Users Guide to CCD Reductions with IRAF* by Philip Massey at NOAO in Tucson, Arizona. This document also describes how many images one must take at the telescope such that instrumental signatures can be assessed. Starting with the raw data, shown in Figure 3.19, I will assume in this discussion that we have followed the guidelines outlined by Massey in obtaining the necessary calibration images. Below I discuss only the specifics related to the PFC in the data reduction process.

Biases, Zeros, and Darks

Every CCD system has an electrical pedestal called bias, which is an additive constant on top of the data. This bias level is measured by reading out more CCD columns than are contained in the imaging area. This creates an "overscan" at the end of each row, showing the bias overscan region. In most CCD controllers there is a piece of circuitry which allows the user to adjust the bias level to some low value, usually near a few hundred counts. This preserves the limited dynamic range of the CCD electronics to its maximum in order to accommodate the much greater dynamic range of the CCD itself. In the PFC's CCD electronics the dynamic range is sufficient to accommodate LF1's dynamic range and noise properties comfortably. Therefore, we have removed the bias adjustment and we let the system run at its "natural" bias level of ~3200 counts. Without these additional electronics the bias level in the PFC's images is extremely stable, never varying by more than a few counts in the mean.

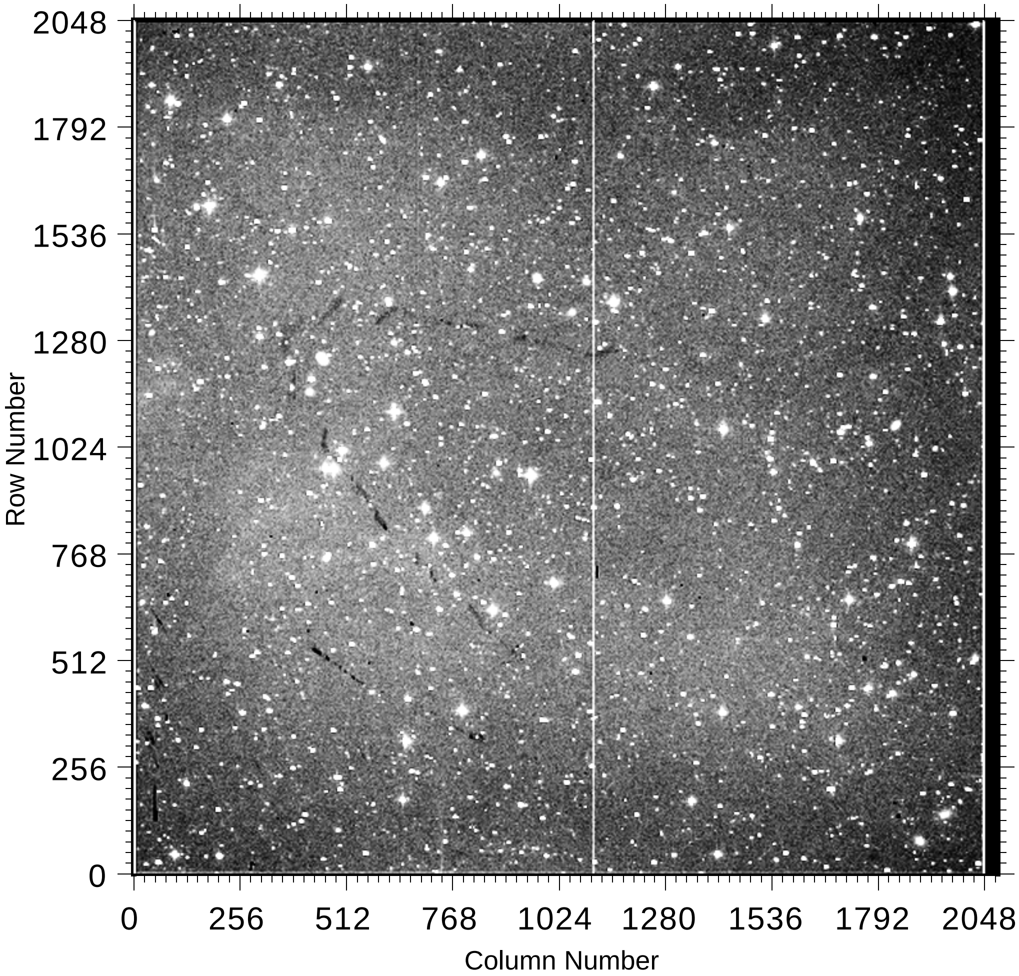
2048
1792
1536
1280
1024
768
512
256
0
Row Number
0
256
512
768
1024
1280
1536
1792
2048
Column Number

Figure 3. 19: A raw image from the PFC prior to removing its instrumental signatures.

In the images from the PFC it is sufficient to fit the overscan region by a single constant as I have shown in Figure 3.20. Even if you are tempted to fit something other than a constant – don't! The reason why will become clear when I discuss the Zero image below. For each image the fitted constant from the overscan region is subtracted from every pixel value in the CCD's imaging area. After this, I usually trim away the overscan region as well as the few misbehaved rows and columns around the perimeter of LF1. The CCD area which I keep is columns 5 through 2045 and rows 4 through 2047.

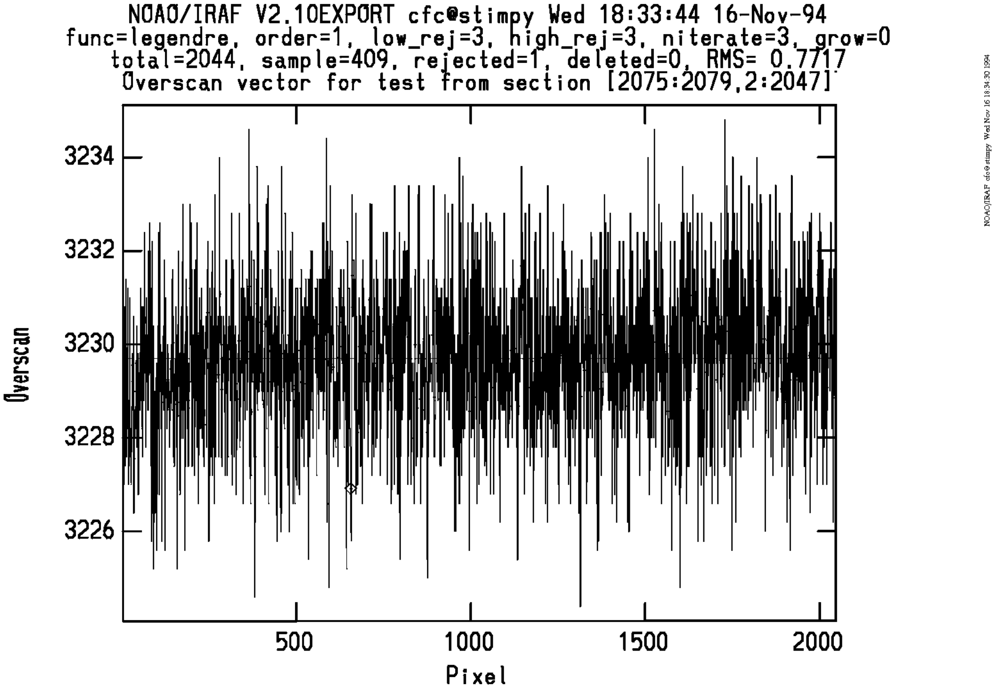

Figure 3.20: A typical column plot of LF1's overscan region averaged by rows.

By fitting the overscan region with a constant I have made no assumptions about the spatial structure of the additive pedestal signature. Because of the stability of LF1's electronics we can accurately measure what structure there might be by taking many frames with zero integration time. These frames are bias subtracted as described above and then averaged. Fitting anything other than a constant to the bias level would cause this spatial information to be lost in the averaging process. I found the average zero to be constant from night to night and run to run. Therefore, I have produced a master zero image (Figure 3.21) made from an average of the zero images of many observing runs, which is essentially noise–free. I subtract this image every frame, along with the bias constant mentioned above.

There are several spatially–dependent features which can be seen in the master zero image . There is a gradient from upper left to lower right, which is really the sum of two gradients of differed charge. Differed charge arises from heating the CCD's electrodes by the clocking signals, knocking loose a small number of electrons with each clock cycle. The two gradients are from the parallel (vertical) and serial (horizontal) clocks and contribute from 0 to 3.5 counts (0 – 5.67 electrons) on average. There is also a small systematic offset of ~1.2 counts between the lowest average zero value and the bias, which is accounted for in the master zero image. In addition to the gradient there are columns which are "hot". These do not subtract out and are categorized as bad areas on the CCD.

The third kind of additive signature we need to consider removing is thermal dark current. Older CCDs show a significant buildup of charge across the

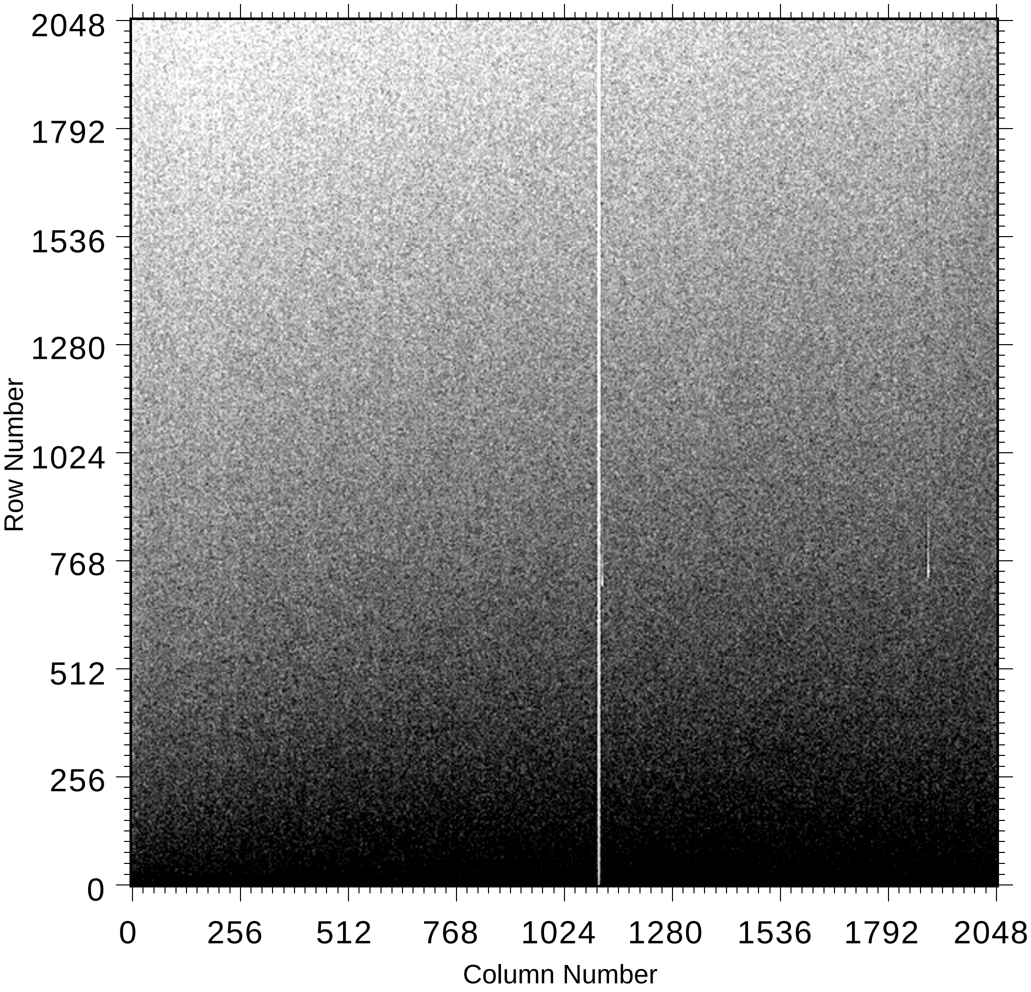

Figure 3.21: The master zero image to date from LF1.

imaging area during long integrations. This is caused by thermal vibrations in the silicon substrate. In more modern CCDs the amount of dark current is quite small, especially in MPP buried–channel devices which allow integration without any voltage applied to the clocks across the image area. The PFC's CCD LF1 is an MPP device and we operate it in this mode. I have measured the dark current from LF1 on several occasions and have found it to average near 2×10^{-4} electrons per second. The longest exposure time practical at the 30 inch telescope site, limited by local radiation in the rock surrounding the dome, is ~1800 seconds. In this time the CCD will have accumulated less than a single electron dark current. This is insignificant compared with the readout noise and differed charge effects and is not a concern. However, the local radioactive rocks *are*, of course, a concern.

To summarize, we can remove, to a high degree of precision, the additive signatures in PFC data with a constant fitted to the bias overscan plus an averaged zero image.

Shutter Correction

If the PFC is to make precision photometric measurement it is essential that the exact time the shutter is open be known. Mechanical shutters give exposure times somewhat different from what is requested by the control computer. This is caused by such things as time lag to fully energize a solenoid to open the shutter, simple mechanical limitations, and systematics in the computer timing controlling the exposure length. Furthermore, because of the wide field in the PFC, the finite transition time from closed to open and back again can be important. This is especially true for short exposures, as one would use in taking flat field and standard star images.

We can exactly measure the differences between requested exposure time and true exposure as a function of field position by taking a series of uniformly illuminated exposures in the following way: The true exposure time at a given pixel, $T(x,y)$, is expressed by

$$T(x,y) = t_{req.} + \delta t(x,y)_{shutter}, \tag{3.3}$$

where t_{req} is the requested exposure time and $\delta t(x,y)_{shutter}$ is the position–dependent shutter correction. By definition the counting rate measured from a constant light source is independent of exposure time. With this assumption we can write the following:

$$\frac{\sum_{1}^{N} I(x,y)_{short}}{\sum_{1}^{N}\left(t_{short} + \delta t(x,y)_{shutter}\right)} = \frac{\sum_{1}^{M} I(x,y)_{long}}{\sum_{1}^{M}\left(t_{long} + \delta t(x,y)_{shutter}\right)}, \tag{3.4}$$

where $I(x,y)$ is an image of measured intensities from a given exposure. By forming a ratio between the image sums we can eliminate nonuniformities in illumination across the field, leaving only the effects from the shutter correction. This ratio image is defined as

$$R(x,y) \equiv \frac{\sum_{1}^{N} I(x,y)_{short}}{\sum_{1}^{M} I(x,y)_{long}}. \tag{3.5}$$

Because the shutter correction is independent of requested exposure time we can combine 3.4 and 3.5, expressing them with like terms collected by

$$R(x,y)\sum_{1}^{M} t_{long} - \sum_{1}^{N} t_{short} = N\delta t(x,y)_{shutter} - R(x,y)M\delta t(x,y)_{shutter}. \qquad (3.6)$$

We can now easily solve 3.6 for the shutter correction, $\delta t(x,y)_{shutter}$, in terms of something we can easily obtain at the telescope, which is given by

$$\delta t(x,y)_{shutter} = \frac{R(x,y)\sum_{1}^{M} t_{long} - \sum_{1}^{N} t_{short}}{N - MR(x,y)}. \qquad (3.7)$$

In principle we can evaluate 3.7 from a single long and short exposure, but in practice it is best to use many of each. Furthermore, the short exposure time should be just long enough for the noise in the signal to dominate over the CCD readout noise.

I have estimated the shutter correction each time we have mounted the PFC on the telescope. I usually take a series of 10 1-second exposures followed by a single 10 second exposure, and repeat this sequentially 4 times. In Figure 3.22 I show the average shutter correction map for the PFC since the instrument has been operational. The heavy contours are labeled in 10^{-4} seconds with the minor contours separated by 5×10^{-4} seconds. This image is applied to *every* image taken with the shutter open. The correction between requested exposure time and true exposure time is give by

$$I(x,y)_{true} = I(x,y)_{obs} \times \frac{t_{req.}}{t_{req.} + \delta t(x,y)_{shutter}}, \qquad (3.8)$$

where $I(x,y)_{true}$ is the corrected intensity image and $I(x,y)_{obs}$ is the raw observed image which has been corrected for additive effects discussed above.

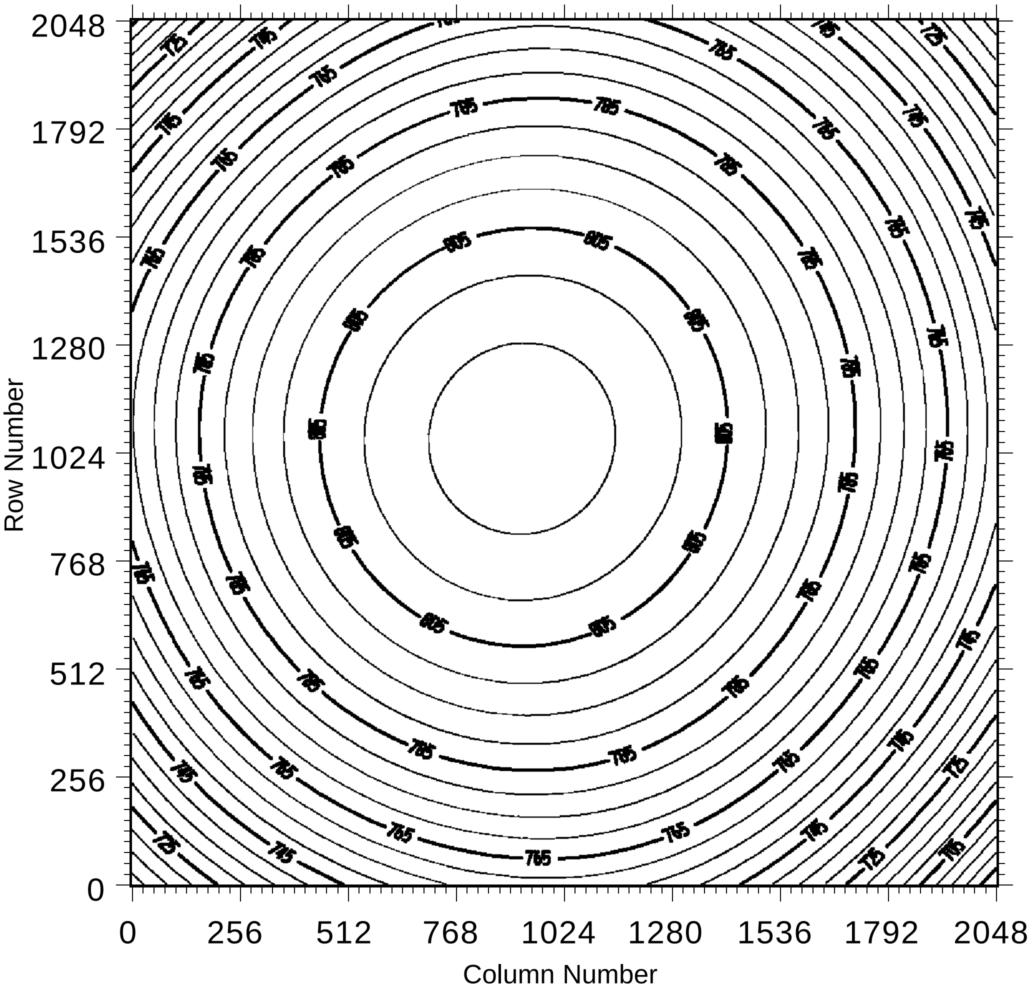

Figure 3.22: The average shutter correction map for the PFC (units are 10^{-4} seconds).

Flat Field and Illumination Correction

We are now in a position to remove the optical instrumental signature from the data. These are all multiplicative effects, which include pixel-to-pixel sensitivity differences, dust on the CCD and/or filters, and illumination differences across the field. The way these are accounted for is by uniformly illuminating the entrance pupil of the telescope and recording the images (called "flats"). This is usually done by exposing to an illuminated white screen on the inside of the dome (dome flats), or by looking at the twilight sky (sky flats). In the case of the PFC it is not practical to use the twilight sky because of the time needed to read out the CCD – more than 3 minutes per image. In a perfect world a dome flat should show the same response as a sky flat, but this is not always the case. First, the sky and dome are at vastly different distances as seen by the telescope. Second, the color of the sky and dome are not the same and can cause systematic effects if they differ widely. In any case, with the PFC we are forced to use dome flats.

The master flat for each filter is obtained by averaging 9 or so exposures of the illuminated dome screen and normalizing them to a mean of 1.0. For most CCD imaging systems this is a trivial and straight–forward process. However, the PFC's wide field makes it very difficult to illuminate the full entrance pupil uniformly . The raw flat frames from the PFC all show strong gradients. It is possible to proceed from here in two ways. We can either use the flats as they are and derive an illumination correction later from the data, or we can try to remove the gradient from the flat before applying them to the data. I prefer the latter, because the gradient is linear and well–behaved and can be removed easily from a fit to a tilted plane. Furthermore, I have a better "feel" this way for how the instrument is performing and whether something else has gone wrong.

I treat the gradient by fitting and normalizing each individual flat image by a tilted planar surface. I compute the master flat for each filter by averaging the individual flats and normalizing the final result by its mean. A typical flat from the PFC is shown in Figure 3.23. The "Z" shaped mark of Zorro mentioned earlier is clearly seen. We can also see systematic low areas in the corners caused by the vignetting and illumination field dependencies discussed in §3.1.1. There is also a slight amount of fringing visible which is also a multiplicative effect and is accounted for in the flat fielding process. The variation in the master flats are <10% in the blackest parts of the image shown. These flats are applied to the data in the usual manner of dividing each image with the appropriate flat for its filter.

The final result of the data reduction process is shown in Figure 3.24, which should be compared with the original raw data in Figure 3.19. The precision with which we have removed the PFC's instrumental signature following the procedure above can be clearly seen in the Praesepe photometry I will present in Chapter 5.

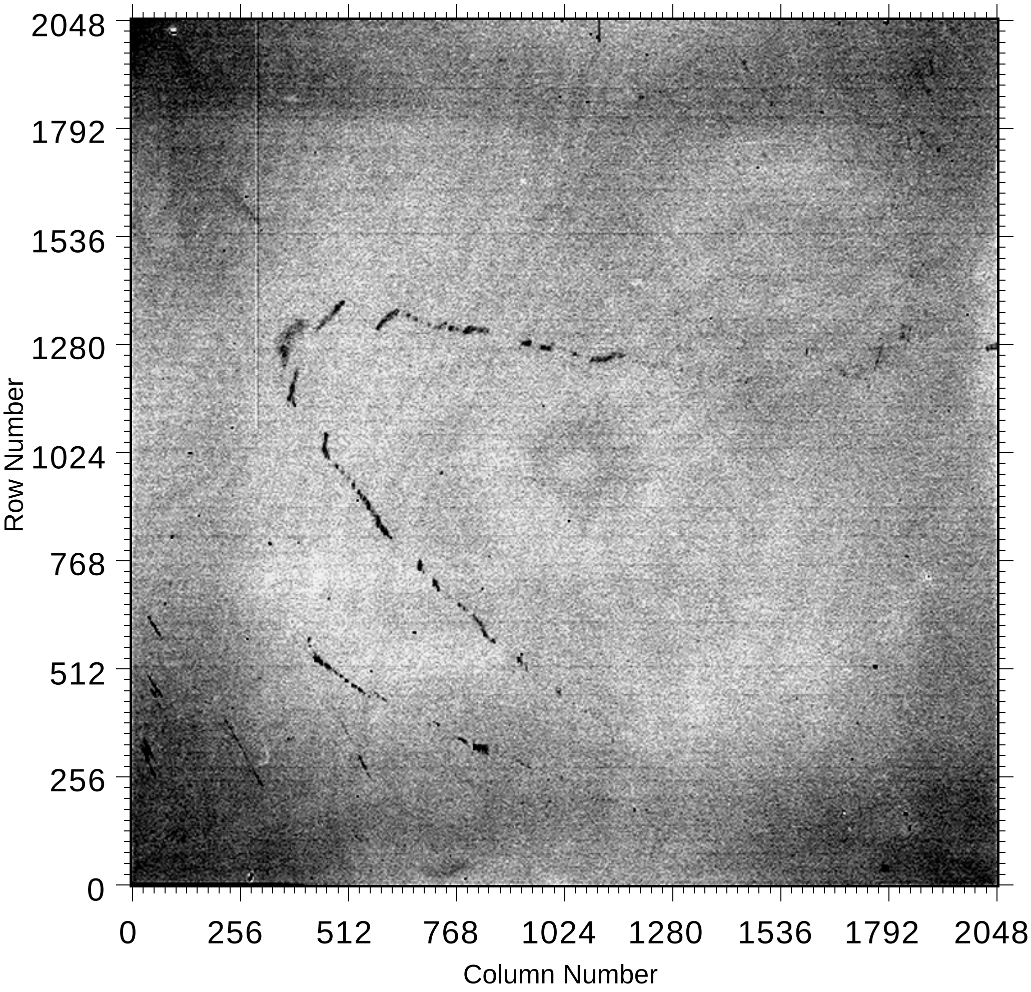
2048
1792
1536
1280
1024
768
512
256
0
Row Number
0
256
512
768
1024
1280
1536
1792
2048
Column Number

Figure 3.23: The master flat in the V filter from the PFC.

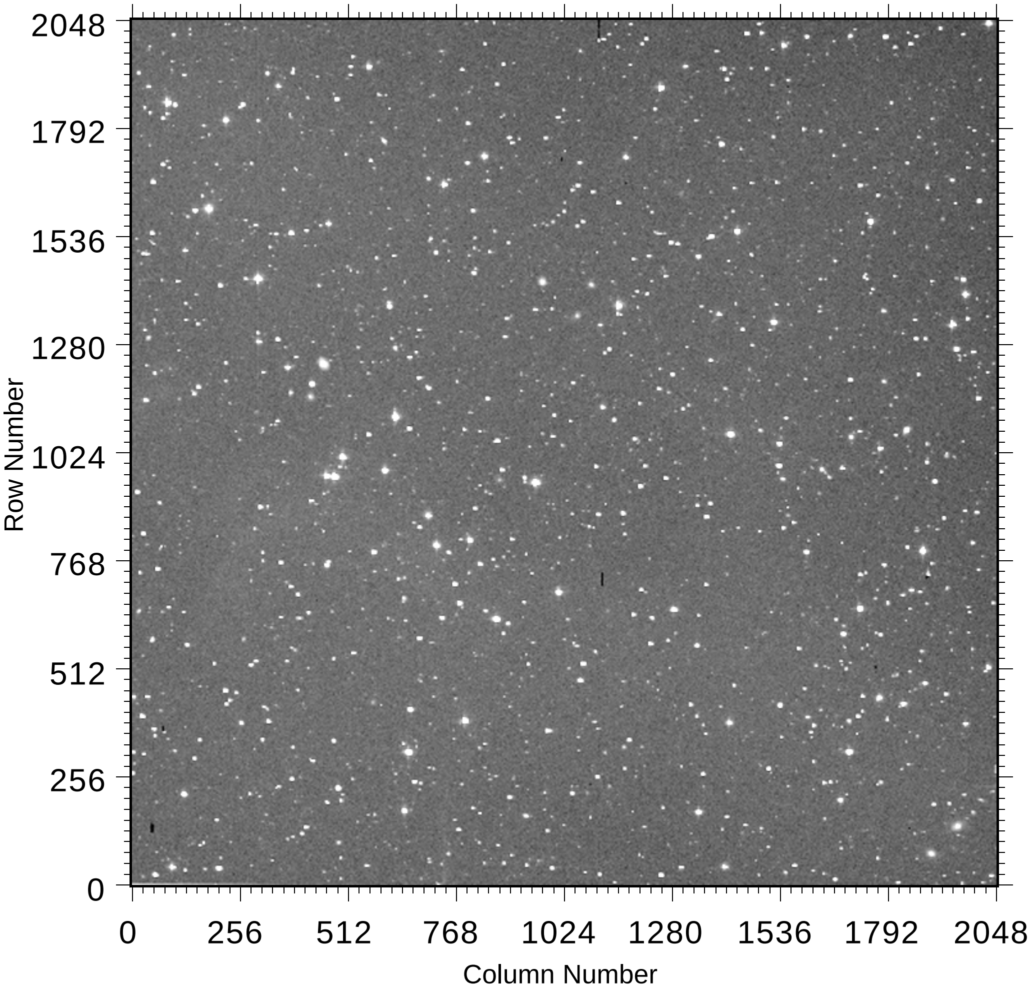
2048
1792
1536
1280
1024
768
512
256
0
Row Number
0
256
512
768
1024
1280
1536
1792
2048
Column Number

Figure 3.24: The data shown in Figure 3.19 fully reduced – the PFC's instrumental signature has been removed.

4

Photometric Identification of White Dwarf Stars

Because they are intrinsically faint, distinguishing a white dwarf from the many thousands of ordinary field stars we see is a difficult task. We can divide the methods which have been used for identifying white dwarfs out of the many other stars in the Galaxy into three categories: kinematic, photometric, and spectroscopic. Each of these methods has at one time or another been applied to large area sky surveys, leading to the discovery of many white dwarfs. However, most of these methods have serious limitations for effective survey use at very faint magnitudes.

Kinematically we can identify white dwarfs through their interaction with a binary companion or from their proper motions against relatively stationary background stars. One of the first extensive compilations of white dwarf candidates was done by Luyten (1962, 1975). Luyten, from his proper motion surveys, produced candidate lists for some 3000 faint blue stars – white dwarf candidates. Similar work done by Giclas (1971) also generated lists of candidate white dwarfs. Many of the known white dwarfs have come from these two sources, but because at their faint luminosities they must be close to be seen; white dwarfs therefore have greater proper motions than do most other stars. The main difficulty in extending proper motion searches to fainter magnitudes is the limitation imposed by the depth of the first epoch data. Unfortunately the early epoch data are on photographic plates from small to medium sized telescopes and do not go faint enough to be useful for further white dwarf searches. In order to detect the small motions of more distant white dwarfs at faint magnitudes it is also necessary to have a long time span between measurements; usually 30–50 years is needed for their apparent motions to be measurable. This time–base requirement also makes it a prohibitively lengthy enterprise (for a graduate student) to begin from scratch using modern detectors and astrometric techniques.

Identification of a white dwarf out of the many other field stars from photometry relies on it having a unique color signature. Of the three photometric systems which have been used to study white dwarfs in detail, only the broad band *UBVRI* system has been used extensively for survey work. The other two, Strömgren (Wegner 1983) and Multi-Color Spectrophotometry (Greenstein 1984 and references therein), are intermediate and narrow band(width) systems: their narrower filters allow more precise evaluation of physical properties in white dwarfs, but they are less useful because the time needed to reach a given faintness is inversely proportional to the bandwidth of the filter used. A survey of equal depth using the intermediate band Strömgren system would take 3–5 times longer than one using the *UBVRI* system.

With its higher "color" resolution over photometry, spectroscopic identification of white dwarfs is based on the detection of specific broad spectral features and sometimes featureless spectra characteristic of the high surface gravities present in these stars. Spectroscopic surveys are usually made photographically with slitless spectra of a large field, using a Schmidt telescope fitted with an objective prism dispersing element. Here again, while objective spectroscopy offers a higher degree of interrogation of the field, much longer integration times are needed to reach a desired faintness. This is because the light from a point source is dispersed over a relatively large area on the detector and without a slit, the individual spectra are badly affected by the night sky background. An additional problem in objective prism surveys is caused by overlapping spectra of crowded objects. At faint limits where the density of stars is quite high, $\sim 5 \times 10^4$ stars per square degree at $V \approx 21$ (Allen 1973), this is a severe problem[1]. Therefore, it is not practical to attempt objective prism type searches fainter than $V \approx 21$.

So how *do* we conduct a deep survey in search of faint white dwarf stars? Considering the arguments I have made above, I contend that the old broad band *UBVRI* photometric system is still the most efficient means to search large parts of the sky in the hunt for white dwarfs. The broad filter bandwidths (1000–1500Å) allow for the desired faintness to be reach in a minimum amount of time and the combination of filters is sufficient to weed out most of the stellar contaminants. It is then practical to obtain individual spectra for detailed analysis of selected candidates in a manner tailored to the specific science one wishes to address. In the remainder of this chapter I first re-examine the well-known broad band photometry of the hotter white dwarfs in the context of recent model atmospheres, then, I describe my extension to the broad band system so that it is useful for identifying the cooler, low luminosity white dwarfs, which because of the confusion in colors that exists at low temperatures *UBVRI* photometry alone can not do.

---

[1] A clever way to minimize the confusion at high densities was suggested by Ed Nather (U. of Texas): Take two exposures on each field using a properly designed instrument such that the dispersion of the first exposure is 90 degrees to the other with a low level zero order image at the intersection of the two spectra. Using appropriately designed software the resulting composite image would be scanned for the location of all stellar images. Each image would serve as the wavelength zero point and the reference for a cross correlation of the spectra with "templates" of known spectral characteristics of the objects being searched for. Even though the integration times would be long the amount of information possible with such a technique, if properly executed, is staggering.

4.1 BROADBAND COLORS OF HOT WHITE DWARFS

Relatively little has changed in terms of broad band *UBV* colors of white dwarfs since Eggen and Greenstein (1965) published their work. They showed that the majority of white dwarfs are well separated from main sequence stars in a $U-B$ versus $B-V$ two color diagram; the peak separation is roughly 0.75 magnitudes in $U-B$ at $B-V\sim 0.2$. This can be readily seen in Figure 4.1, where I have plotted the UBV colors of the white dwarfs from McCook and Sion (1987), field photometry from the 5th Revised Bright Star Catalog, and the Landolt (1983, 1992) photometric standards. The large numbers of hotter white dwarfs (towards the upper left of Figure 4.1) reflects the bias of past searches to preferentially find these stars, even though the luminosity function increases in space density towards lower temperatures and luminosities (lower right in Figure 4.1). It is also clear that the *UBV* broad band colors of the cooler white dwarfs, redward of $B-V\sim 0.6$, become indistinguishable from those of main sequence

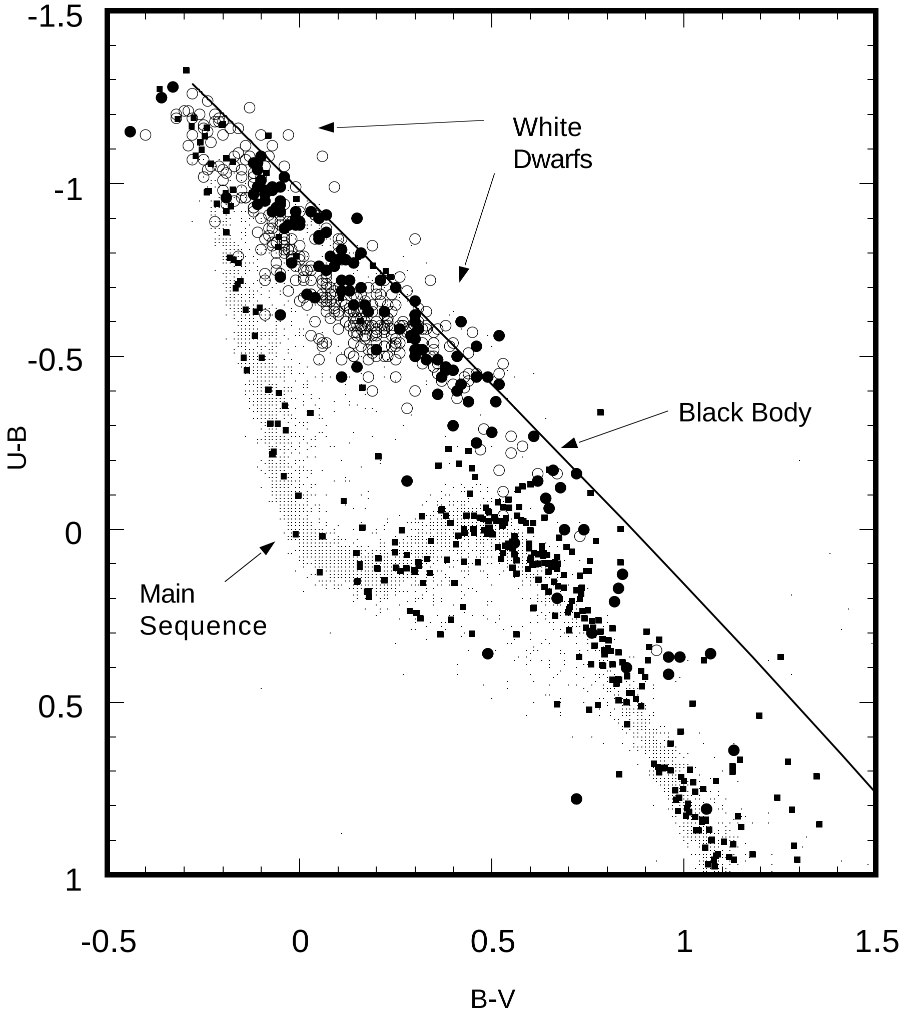

Figure 4.1: The conventional *UBV* color-color diagram showing the location of white dwarfs (open and filled circles) relative to the field main sequence population (small points). The white dwarf photometry was taken from the McCook and Sion (1987) catalog of spectroscopically identified white dwarfs and separated according to spectral type: DA represented by open circles and non-DA by filled circles. I also include for comparison the *UBV* photometry of the Landolt standards (filled squares) used to calibrate modern *UBVRI* data. Note that some of the Landolt standards are themselves white dwarf stars.

stars. This further underscores our need to develop a photometric method for efficiently identifying the cooler white dwarfs.

In the ideal case we would always fit high quality observed spectra with model atmospheres to obtain the physical characteristics for individual white dwarf stars. However, in many cases, and almost always with photometric surveys, we do not initially have such spectral data. Therefore, it is necessary to have a set of synthetic colors based on state-of-the-art atmospheres and filter definitions, to compare with photometry and obtain some indication of the physical nature of white dwarfs found in current photometric surveys. Now that more detailed numerical models exist for white dwarf atmospheres, it is worth while to have a fresh look at the properties of white dwarf measurements in the broad band *UBVRI* system.

4.1.1 Synthetic Model Colors

Within the errror limits obtainable from broad band photometry, results from model atmosphere colors for DA and blackbody colors for non-DA white dwarfs give similar precision in quantifying their physical characteristics. For this reason, I have constructed synthetic *UBVRI* colors for DA white dwarfs using Bergeron's (1991) model atmospheres in conjunction with colors for blackbody distribution at the same effective temperatures. I have adopted the response functions for the *UBVRI* band passes described by Bessell (1990), which are directly related to the Landolt (1983, 1992) standards. These response functions are shown in Figure 4.2 and are approximated by the filters used in the Prime Focus Camera described previously.

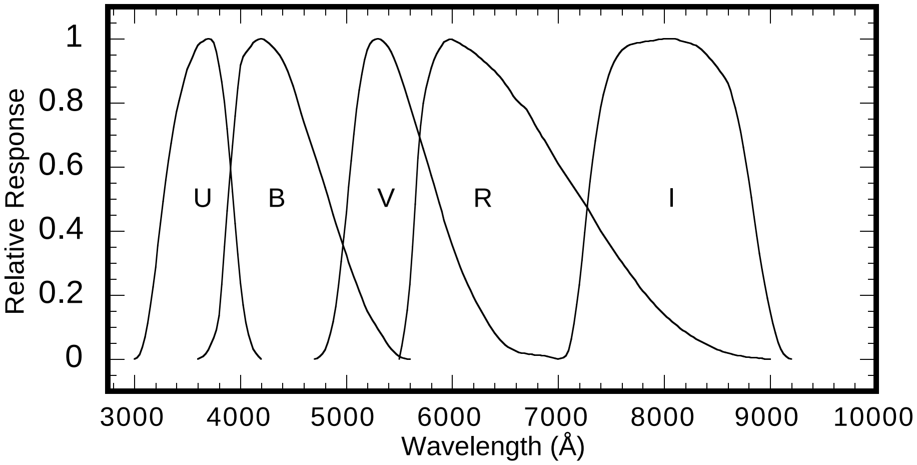

Figure 4.2: The response functions for the *UBVRI* system as defined by Bessell (1990).

I have obtained, from Pierre Bergeron at Montreal, DA model atmospheres which span a temperature range of 50,000K to 5000K at three different gravities of $\log(g) = 7.5, 8.0,$ and 8.5. These models atmospheres give emergent flux as a function of wavelength, which can be convolved with the Bessell filter responses to obtain synthetic magnitudes. The formal definition of the convolution procedure is given by

$$m_\lambda = -2.5\log\left(\frac{\int_0^\infty F(\lambda)R(\lambda)d\lambda}{\int_0^\infty R(\lambda)d\lambda}\right) + C_\lambda, \tag{4.1}$$

where C_λ is a calibration constant to place the computed magnitude (m_λ) onto the standard system, $F(\lambda)$ is the emergent flux from the model calculations, and

$R(\lambda)$ is the response function of the filter for which the magnitude is being computed. I have computed the calibration constants for each filter by evaluating equation 4.1 using the flux measured from Vega (Hayes 1985) as my standard. The colors and magnitudes measured for Vega are from the 5th Revised Bright Star Catalog (Hoffleit and Warren 1991) and are listed as:

$$V = 0.03; \tag{4.2}$$

$$U - B = -0.01; \tag{4.3}$$

$$B - V = 0.00; \tag{4.4}$$

$$V - R = -0.04; \tag{4.5}$$

$$R - I = -0.03. \tag{4.6}$$

I set the constants C_λ so that the computed magnitudes and colors of Vega are identical to the observed ones listed above. I applied the same set of constants in my computation of the model atmosphere and black body colors. The calibration of the computed V magnitude to absolute visual magnitude is addressed later in the following section.

The calibrated colors from my calculations for the three sets of model DA atmospheres and for ablack body are shown in Figure 4.3, where I have plotted the computed colors against the model's effective temperature. Although I have computed synthetic magnitude for all five *UBVRI* filters I have chosen only to present the colors for *UBVI*, since R does not contain much information that isn't already measured by I. While there are many different possible color combinations between *UBVI* magnitudes only $U - B$ (top panel), $B - V$ (middle), and $V - I$ (bottom) contain relevant information for identifying and

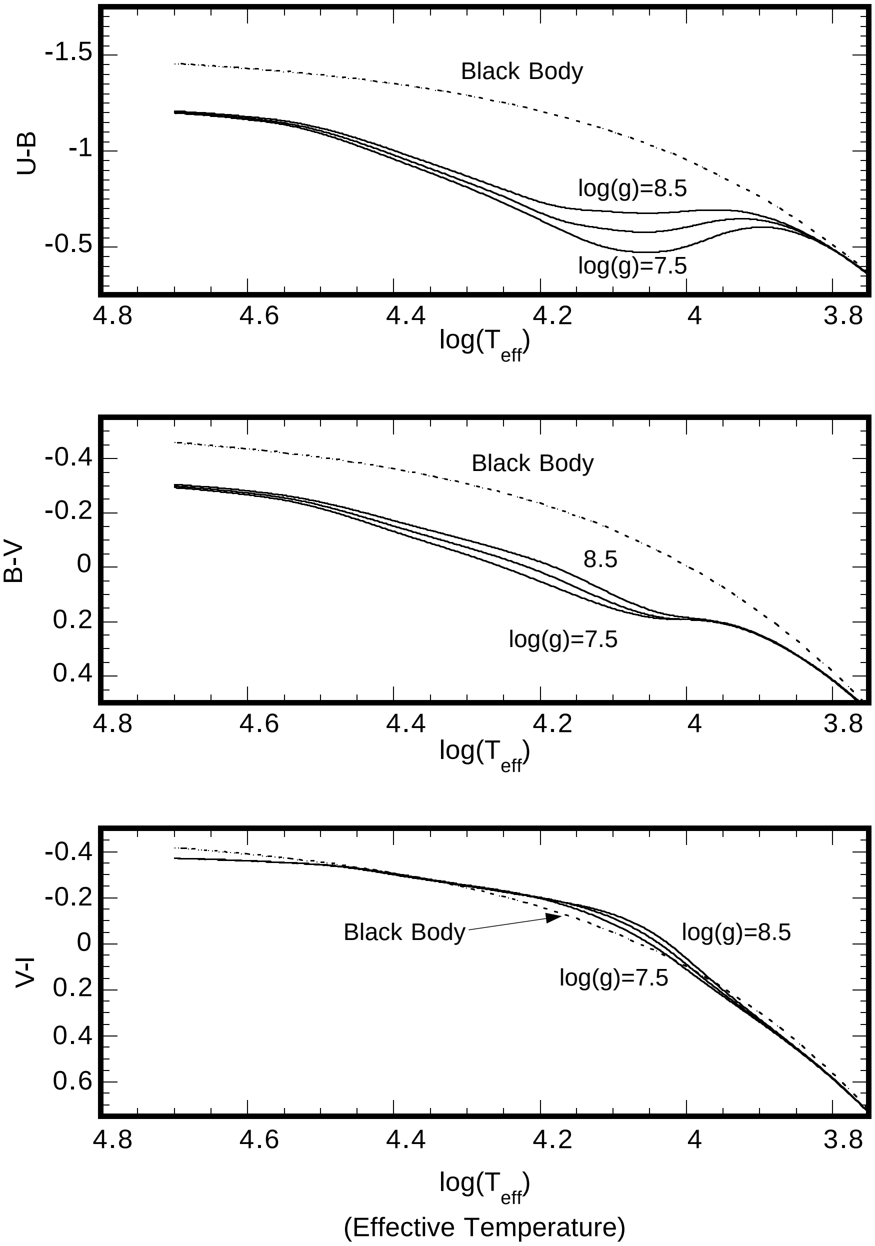

Figure 4.3a,b,c: Broad band colors versus effective temperature for Bergeron's DA model atmospheres (solid lines) along with black body colors (dotted line) for comparison (see text for description).

characterizing white dwarf stars. Clearly evident, regardless of color, is the general trend towards redder (more positive) colors with decreasing temperature. The temperature sensitivity of hydrogen line strengths is also seen in the blue $U-B$ and $B-V$ colors. The strength of the Balmer discontinuity (jump), as measured by $U-B$, can be seen to vary as a function of surface gravity. With increasing gravity the hydrogen ions become crowded to the point that their outer energy levels responsible for the Balmer discontinuity simply no longer exist. This effect is also responsible for the slight gravity dependence of $B-V$, as the higher Balmer lines begin to disappear, weakening the absorption strength through the B filter. Finally, we see that for all models the $V-I$ color index deviates little from black body colors. This implies that $V-I$ is a reasonable estimator for effective temperature. The effect of reprocessed radiation from line blanketing being emitted in the I bandpass can be seen as a slight blue excess of the $V-I$ colors near an effective temperature of 12,500K ($\log(T_{eff}) \sim 4.1$).

From these model colors I have formed the standard two color – $U-B$, $B-V$ – diagram with which we are most familiar (Figure 4.4), in addition to the two color diagrams for $U-V$ and $V-I$ (Figure 4.5). In both figures the DA model color sequences are shown as heavy solid lines with the black body sequence (dashed line) and the average locus for the main sequence (dotted line) shown for reference. The effective temperatures for of the model atmospheres in thousands of degrees Kelvin are indicated by the numbers located below the color sequences. The characteristic 'S' shape in the model sequences from the hydrogen absorption and Balmer discontinuity can be clearly seen in both

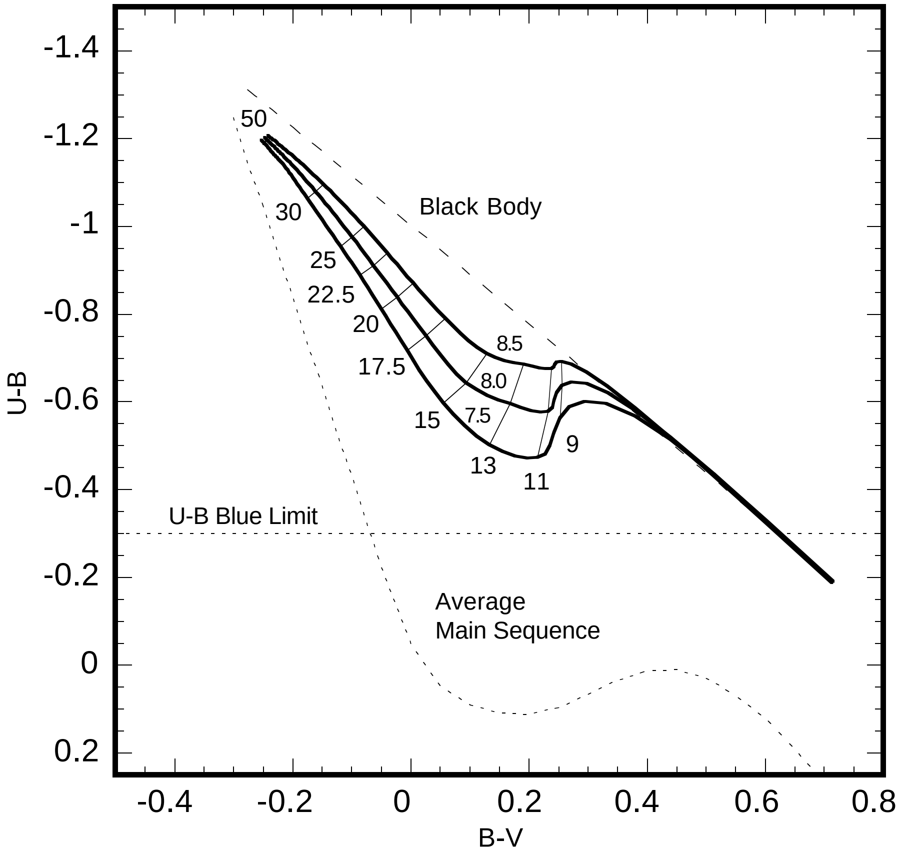

Figure 4.4: $U-B$ versus $B-V$ DA model color sequences for log(g)=7.5, 8.0, and 8.5 (heavy solid lines). The colors for a black body (dashed line) and the average locus for the main sequence stars (dotted line) are shown for comparison. The numbers (9–50) below the lower model sequence represent effective temperature in units of 1000K.

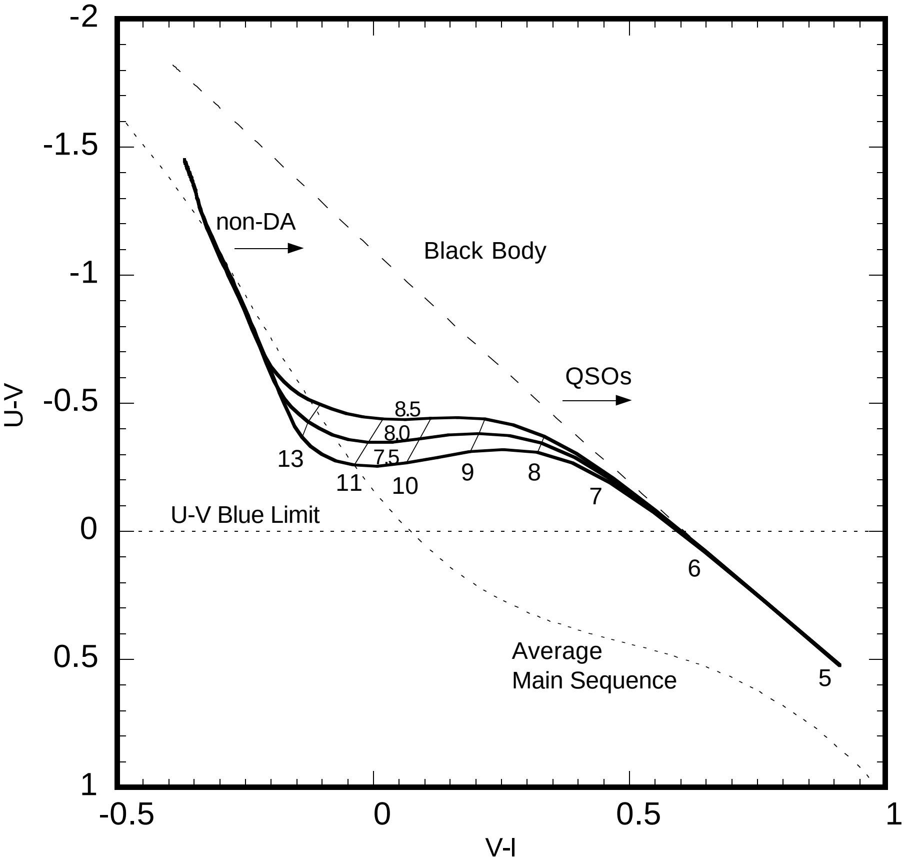

Figure 4.5: $U-V$ versus $V-I$ DA model color sequences for log(g)=7.5, 8.0, and 8.5 (heavy solid lines). The colors for a black body (dashed line) and the average locus for the main sequence stars (dotted line) are shown for comparison. The numbers (5–13) below the lower model sequence represent effective temperature in units of 1000K.

diagrams, as well as its diminished amplitude relative the main sequence caused by the high surface gravity.

We can use the properties of these two color–color diagrams in a sequential three–step process to identify and roughly characterize white dwarf stars in the field hotter than ~7000K. The first step of this process is essentially identical to the classical method using *UBV* colors, selecting objects which are blueward of $U-B \sim -0.3$ while simultaneously bluer than $U-V \approx 0$. Its requires that the candidates selected be bluer than the "Balmer plateau" in both Figures 4.4 and 4.5. It also requires an absolute photometric accuracy better than ± 0.10 in the colors.

The second step is to examine the candidates selected in step one in the two color diagram shown in Figure 4.5. Because the hydrogen model atmosphere colors in Figure 4.5 are independent of gravity above 13,000K we can use this diagram as a diagnostic of spectral type . Allowing for photometric uncertainties, objects with $V-I$ redder than the DA model sequence would be classified as nonDA, while a DA classification would be assigned to those lying within their measured uncertainties of the DA sequence.

The third step is to take those object from step two which we classified as DA and examine them once again in the two color diagram in Figure 4.4. For those with hydrogen atmospheres we can estimate their surface gravities from their $U-B$ and $B-V$ colors. It still remains difficult to estimate the characteristics of nonDA white dwarfs within the limits of broad band photometry alone.

It is apparent from the two-color diagrams there is no clear way of unambiguously identifying the hottest white dwarfs from the field main sequence stars. This is especially true in Figure 4.4 where the main sequence locus crosses the white dwarf models near 11,000K. However, this situation is not entirely hopeless. In a deep survey below 16th magnitude (the limit of the Palomar–Green survey) the surface density on the sky of hot, blue main sequence stars is very low, and would not be a serious contaminant in a selected white dwarf sample. If any were to be discovered at these limits they themselves would be interesting as main sequence O and B type stars in the halo of the Galaxy, indicating there might be recent star formation occurring there.

We also know that, with increasing red shift, the colors of emission line quasars cross the black body sequence and contaminate the white dwarf region in $U-B$ versus $B-V$. The exact red shift at which this occurs is dependent on the Lyman α emission strength as it is red shifted into the U bandpass, but it is usually somewhere between 2 and 2.5. In Figure 4.5, quasars at this red shift remain quite red in $V-I$ and are still found to be right of the black body line. Therefore, it is possible to easily remove the blue quasar contamination from a white dwarf search by using both diagrams as a diagnostic.

While this methodology is not meant as a substitute for spectroscopic analysis, it does allow us to evaluate the basic characteristics of white dwarfs in bulk, based on the kind of first epoch data one might have from a large photometric survey.

4.1.2 Comparison of Computed and Observed Colors and Magnitudes

The first comparison I can make between the observed and my computed colors is in the $U-B$ versus $B-V$ two color diagram. In Figure 4.6 I have combined the observed and model data shown in Figure 4.1 and 4.4 respectively. The DA white dwarf data (small points) and the model colors (heavy lines) agree well through roughly 9000K, where they begin to deviate with cooler temperatures. The nonDA data (small open squares) fall roughly between the blackbody sequence (dashed line) and the model DA colors. The separation between the two spectral types is minimal and could not be made on the basis of these colors alone, as I suggested earlier. I have also included the known variable DAV white dwarfs known as ZZ Ceti stars (open circles). Unfortunately there does not exist a large data set for comparison of $U-V$ and $V-I$ colors for white dwarfs with the model colors.

With an estimate of temperature and surface gravity we would also like to have a way to estimate luminosity. Several attempts have been made to calibrate broad band colors to absolute visual magnitude (M_v), which can then be used to estimate true luminosity. Eggen and Greenstein (1965) obtained a relation between M_v and $U-V$ for stars in their sample which had good trigonometric parallaxes. However, at this time there was the belief that there were two possible sequences for white dwarfs, those with and without thermonuclear reactions. This lead Eggen and Greenstein to incorrectly define two relations between M_v and $U-V$. Later, Sion and Liebert (1977) used a larger sample to derive similar relations between M_v and $B-V$ for both DA and nonDA white dwarfs. Their

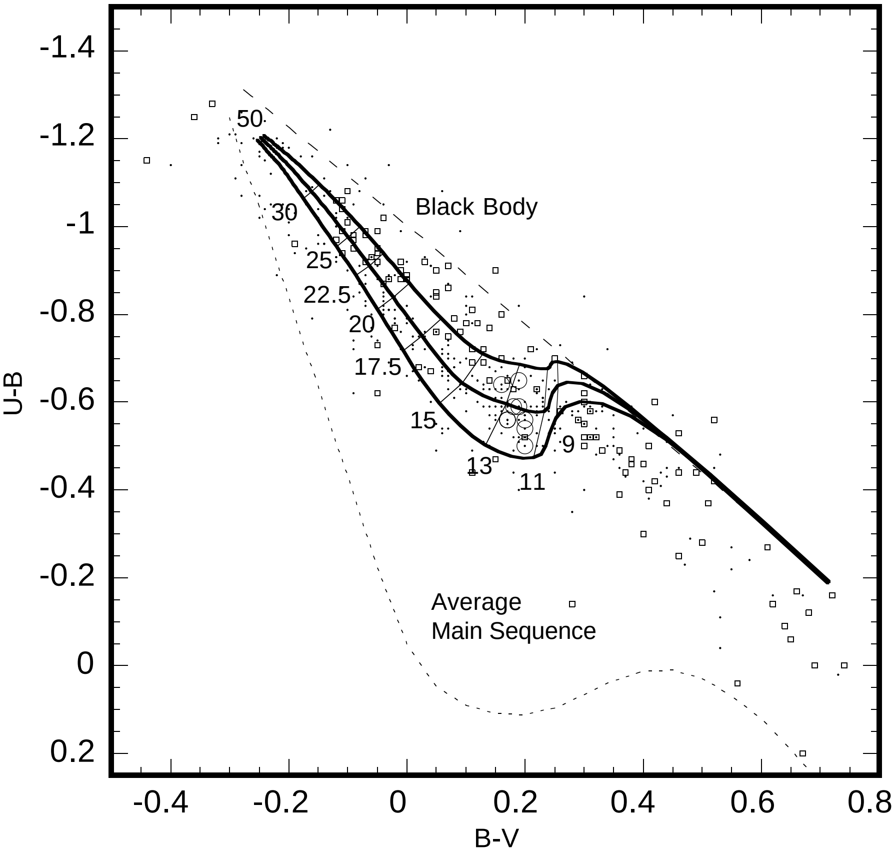

Figure 4.6: Comparison between the observed and model $U-B$ versus $B-V$ two color diagram from white dwarfs. The data are from McCook and Sion (1987) with DA (small points), nonDA (open squares), and ZZ Ceti variable DA (open circles) types indicated.

absolute magnitude scale was determined from Greenstein's (1976) calibration of Multi-Channel Spectrophotometry to trigonometric parallax. Here they correctly separated their white dwarfs by spectral type, but did not recognize a significant feature in M_v for DA types at $B-V \approx 0.25$. As was shown in Figure 4.3b and 4.3c the blue colors are significantly affected by the presence of broad hydrogen lines in DA type white dwarfs. This in turn has caused large systematic errors in their empirical relationships for M_v.

Recently additional trigonometric parallaxes of white dwarfs have been measured by Monet *et al*. (1992) along with their observed broad band *V* and *I* magnitudes. I have already shown the $V-I$ color for white dwarfs is essentially dependent only on temperature. Because of this I have chosen to use the Monet *et al*. data as my reference to calibrate the computed model *V* magnitude scale to M_v. The data from Monet *et al*. (open circles) and a third order polynomial fit (dotted line) are shown in Figure 4.7. The result of the empirical fit is given by

$$M_v = \underset{\pm 0.083}{12.377} + \underset{\pm 0.288}{4.136}(V-I) - \underset{\pm 0.223}{1.196}(V-I)^2, \tag{4.7}$$

where the total RMS is 0.308 magnitudes. I have evaluated the significance of this fit by computing $\Delta\chi^2$ for each additional polynomial term. The best fit was found by increasing the number of terms (degrees of freedom) until the confidence level of $\Delta\chi^2$ drops abruptly, usually from >95% to <70%. I then calibrated the computed V magnitude of the $\log(g) = 8.0$ model to M_v by adding a constant of 1.600, so that the models and fit agree at the hot end, $V-I < -0.1$. This is shown as a heavy solid line in the figure. I did this to avoid problems known to exist in the model atmospheres at cool temperatures and the effects of unknown spectral types in the Monet *et al.* data. The change in the zero temperature radius of a white dwarf for a change in gravity of $\log(g) \approx 0.5$ causes a change of roughly 0.77 in absolute magnitude. I have applied this offset to the M_v calibration above for $\log(g) \approx 7.5$ and $\log(g) \approx 8.5$, which can be seen in Figure 4.7 as dashed lines. Finally, I have calibrated the black body (BB in Figure 4.7) to a radius of $0.012 R_\odot$ at a distance of 10 parsecs.

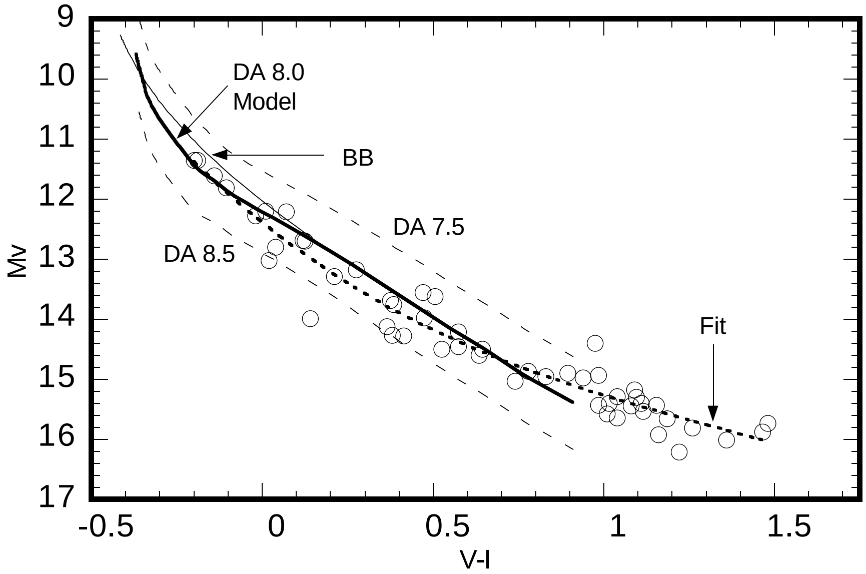

Figure 4.7: Absolute visual magnitude (M_v) versus $V - I$ from Monet *et al.* (1992) white dwarfs with trigonometric parallaxes from the USNO. The computed model (solid line) V magnitude for $\log(g) = 8.0$ has been normalized by a constant to an empirical cubic polynomial fit as is shown by the dotted line.

Using this calibration I have reexamined the absolute visual magnitude data for DA and non DA white dwarf stars from McCook and Sion (1987) in both

$B-V$ and $U-V$. In Figure 4.8a (top) and 4.8b (bottom) I have compared the colors and absolute visual magnitudes with their respective model (heavy solid line) and black body (thin solid line) sequences along with empirical fits to the nonDA data (dashed line). As in Figure 4.6 I have in included some of the known pulsating DAV stars (open circles)

In both colors there is good agreement between the $\log(g)=8.0$ model and the data for spectral type DA white dwarfs at the hot blue end, including the "kink" caused by hydrogen absorption. This presence of hydrogen causes a large change in absolute visual magnitude for a small change in color. In the case of $B-V$ in a span of 0.2 magnitudes centered on $B-V\approx 0.25$ the absolute magnitude changes by approximately 1.75 magnitudes. In $U-V$ it is even worse, where centered on $U-V\approx -0.38$ in a span of 0.1 magnitudes the change in absolute magnitude is roughly 2. This behavior is what lead Eggen and Greenstein (1965) to their erroneous "two" sequence conclusion and can be easily seen in their Figure 5. This feature is also responsible for the systematics in the Sion and Liebert (1977) $M_v, B-V$ relation and is evident as a line of points above and below the DA model in Figure 4.8a.

There is also a clear separation between DA and nonDA spectral types in both colors over the range of colors where hydrogen absorption is significant in DA stars. Otherwise the two spectral types seem to follow the same sequences at the extreme hot and cool ends. The redward deviation of the hotter nonDA from the black body is due, in part, to the majority of these stars being type DB and having strong helium absorption. Since currently there are no model atmospheres available for DB and other nonDA white dwarfs, I have fit the nonDA M_v data to

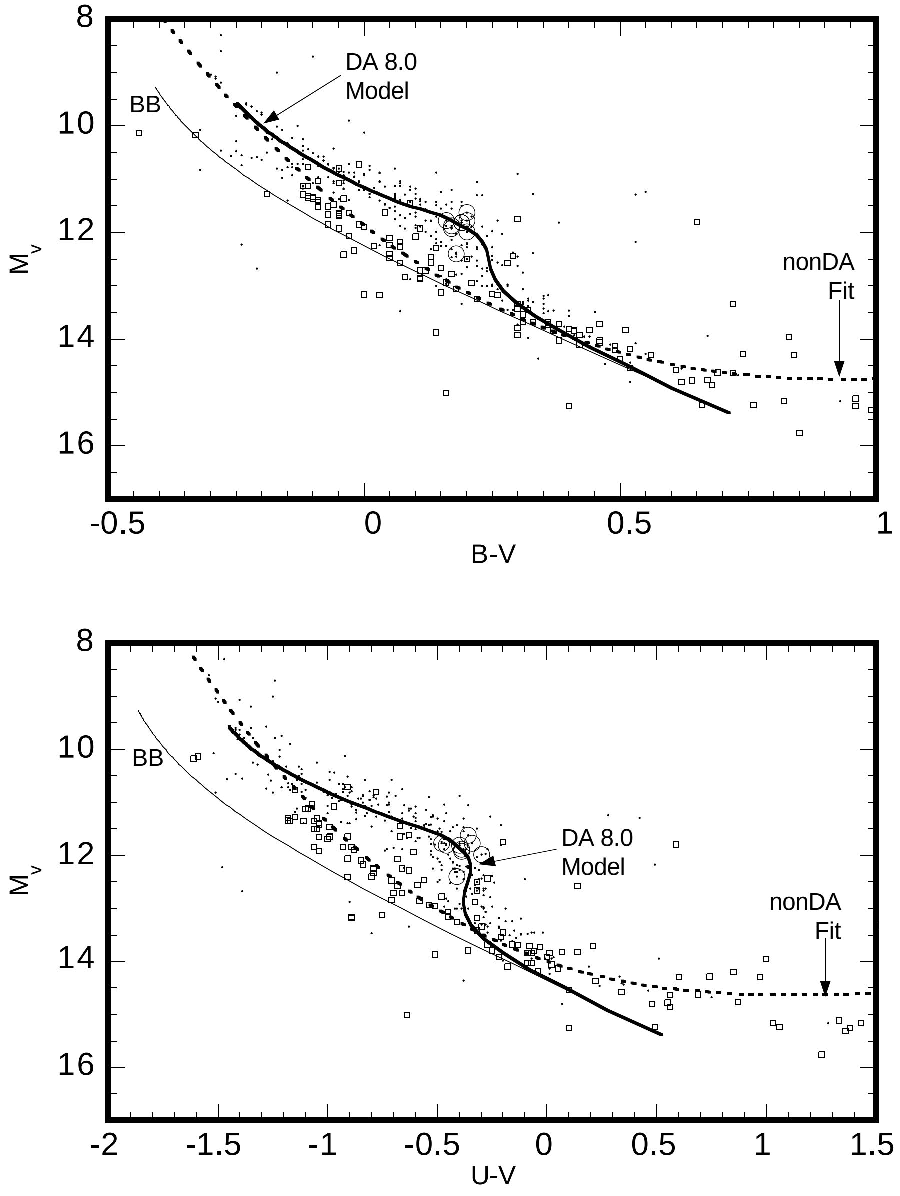

Figure 4.8a,b: Comparisons of the calibrated absolute visual magnitudes with observed values as a function of $B-V$ and $U-V$. The symbols have the same meaning as in Figure 4.6. The heavy solid lines are the DA model sequences, thin lines are a black body at 10 pc with a radius of 0.012 $R_{\odot}$, and the dotted line is an empirical fit to the nonDA data.

cubic ploynomials for both $B-V$ and $U-V$. The result of the nonDA $B-V$ fit is given by

$$M_v = \underset{\pm 0.109}{11.809} + \underset{\pm 0.487}{6.855}(B-V) - \underset{\pm 0.508}{3.739}(B-V)^2, \tag{4.8}$$

which provides a reasonable fit over $-0.2 < B-V < 1.0$ with an RMS error of 0.418. Using the $\Delta\chi^2$ versus degrees of freedom significance test I have evaluated the confidence level of this fit at better than the 99.99%. Adding an additional cubic term in $B-V$ drops the significance to below the 68% confidence level. I obtained a similar result for the nonDA $U-V$ data given by

$$M_v = \underset{\pm 0.125}{13.999} + \underset{\pm 0.187}{1.411}(U-V) - \underset{\pm 0.129}{0.991}(U-V)^2 + \underset{\pm 0.085}{0.214}(U-V)^3, \tag{4.9}$$

where the valid range is $-1.2 < U-V < 1.5$ with a similar RMS error of 0.464. In this case the cubic term is significant to better than the 95% confidence level. In principle, helium model atmospheres should produce a sequence qualitatively similar to the DA sequence, but the "helium kink" will be at higher temperature and bluer color. Beauchamp and Wesemael (1994) at The University of Montreal are currently working on a set of helium atmospheres appropriate for white dwarf stars. When these become available they should provide a better interpretation of the current nonDA data than the empirical fits given here.

At the cool end, neither the atmosphere nor blackbody models fit too well for both spectral types. This is an effect of physics known to be missing in the model atmosphere calculations that become increasingly important at lower temperatures. For example, H^- continuum opacity, which affects the bluer colors first, causes these colors to be redder than is predicted by the model atmospheres or black body. Finally, I note that the location of the variable DAV pulsators coincide with the maximum hydrogen line absorption, owing to their driving mechanism of hydrogen partial ionization.

From this discussion we have learned that, at least, in principle we can learn a great deal about white dwarfs from broad band *UBVI* photometry. As with any photometric technique our ability to learn anything definite depends on the precision of our observations. It is in this area that I believe we have made real progress in the past 20–30 years. It has always been difficult to calibrate photographic photometry to the precision necessary to effectively use the information in the *UBVI* system for detailed analysis. For this reason photographic surveys have had to rely on second epoch observations for detailed analysis of their white dwarf content. And for this same reason little attention has been given to the use of broad band photometry for more than just candidate selection. However, it is now possible to conduct large area sky surveys in search of white dwarfs with the precision provided by Charge Coupled Devices. Because of this improved photometry, we can use the original first epoch discovery data to quantify the basic physical properties of white dwarf stars in such a survey.

4.2 IDENTIFICATION OF COOL WHITE DWARFS

We can see from Figure 4.1 and from my discussion of the classical broad band method above that white dwarfs below approximately 6000K ($B-V>0.5$) pose a special problem for their identification in photometric surveys. The colors of cool white dwarfs are identical to the colors of metal–poor subdwarfs (sdG – sdM). In this system the effect of decreasing metal abundances reduces the amount of line blanketing, causing the subdwarf colors to become bluer, so the subdwarf main sequence and white dwarf sequences coincide at ~6000K. Even if it were theoretically possible to use *UBVI* photometry to identify these cooler white dwarfs, their low temperatures make it exceedingly difficult to obtain the faint *U* band photometry necessary for a deep survey.

These problems are further accentuated when we compare the *BVI* colors of cool white dwarfs with other stars in the field. Without *U* band photometry it is not possible to separate any of the populations in *BVI* colors until very low temperatures ($B-V>1.6$), and even then only the regular solar abundance type dwarfs separate out. This confusion can be easily seen in the two color $B-V$ versus $V-I$ diagram shown in Figure 4.9, where white dwarfs (filled circles) from Liebert, Dahn, and Monet (1988) are plotted with field star photometry from Morrel and Magnanat (1978). In the $B-V$ versus $V-I$ two color diagram we can see it is impossible to distinguish cool white dwarfs from the other stars in the field. I have also included several known cool metal–poor subdwarfs (open circles), noting that they and the white dwarfs follow the same black body (solid line) sequence. In whatever system is developed, this similarity in color sequences must be addressed if we are to explore the possibility of white dwarfs in the Galactic Halo. If the Halo is significantly older than the Disk, these white dwarfs will be cooler and have colors very much like the subdwarfs. We must obtain additional information to identify the cooler white dwarfs. In this case I have the advantage of knowing something about my adversaries – the contaminating main sequence field stars and the metal poor subdwarfs.

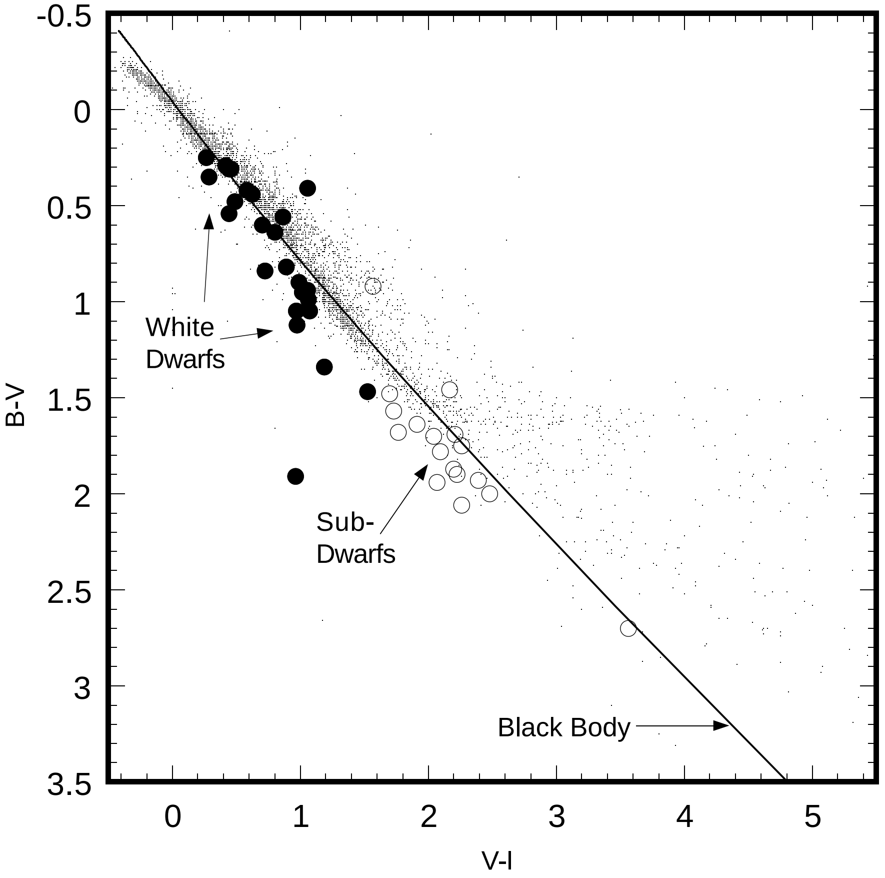

Figure 4.9: $B-V$ versus $V-I$ two color photometry of cool white dwarfs (filled circle – Liebert *et al*. 1988) and field stars (small points – Morel and Magnanat 1978). 16 cool high velocity metal poor subdwarfs (open circles) from various samples (Liebert 1990, Dahn *et al*. 1992, Ruiz *et al*. 1993) belonging to the Halo and the black body sequence (solid line) are also shown . Note that cool white dwarfs and subdwarfs follow essentially the same sequence of colors.

Knowing the spectral properties of these primary contaminants, Jim Liebert suggested I investigate two wavelength regions, centered on the absorption features of magnesium and calcium hydride, that might enable me to sort out the cooler white dwarfs from the field stars. The dwarfs and subdwarfs have absorption features in their spectra that conspire to keep the flux ratios (colors) similar to those of a featureless black body. The resulting colors for these stars typically indicate black body temperatures considerably lower than their true atmospheric temperature. Fortunately, the cooler white dwarfs do not have these absorption features. As the surface temperature of a star gets cooler, the thermal energy of the gas in its atmosphere decreases, allowing molecules to form. However, the high surface gravities in white dwarf stars create large pressures in their atmospheres, preventing the formation of molecules by forcing pressure disassociation. It is this difference in these stars which I have exploited to develop a photometric method for identifying cool white dwarfs.

4.2.1 Hydride Photometry: Principles

It has long been known that the absorption strength of the magnesium triplet (Mgb) near 5174Å is sensitive to surface gravity and can be used as a luminosity indicator (Deeming 1960; Clark and McClure 1979; Guinan and Smith 1985). For cool stars this part of the spectrum also contains the magnesium hydride (MgH) bands of the $\mathrm{A}^2\Pi - \mathrm{X}^2\Sigma$ vibrational system, which is very strong in cool, low metalicity subdwarf stars of the Halo. In more metal rich dwarf stars the blue wing of the MgH band is blended near 4850Å with one of the many titanium oxide (TiO) bands present at low temperatures. The net effect: between roughly 4850–5180Å there is significant absorption in cool stellar spectra regardless of population abundance differences (see bottom panel in Figure 4.10), but not in white dwarfs.

At the low temperature limit of white dwarf identification from broad band photometry the Mgb triplet strength in main sequence dwarfs has become strong enough to measure with an intermediate band filter. By 5500K ($B-V \sim 0.6$) the temperature in subdwarfs is low enough for MgH to form, its absorption strength increasing towards lower temperatures. TiO also begins to show in dwarfs not too much cooler than those beginning to show MgH, and follows the same trend toward increased absorption strength with decreasing temperatures. Although the MgH and TiO band strengths increase with lower temperatures, the amount of available flux in this part of the spectrum decreases rapidly. Therefore, there will be a practical limit to just how cool a temperature this part of the spectrum can be effectively used as a diagnostic. We can estimate where this limit ocurs by examining the behavior of $B-V$ with decreasing temperature. Line blanketing in stars with near–solar abundances causes the flux ratio measured by $B-V$ to remain esentially constant below ~3500K. This can be seen in figure 4.9 as the horizontal spur of points at $B-V \sim 1.6$, and corresponds to spectral type M0. Similarly, the region of MgB+MgH+TiO is affected in the same manner and its effectiveness as a discriminant is limited below ~3500K.

In order to explore the part of the white dwarf luminosity function below the turndown at $\log\left(L/L_\odot\right) \sim -4.2$ we must find a diagnostic feature at redder wavelengths. There are several properties of these still cooler stars that work in my favor here. First, the MgH band has a close relative in calcium hydride (CaH) located near 6846Å and 6908Å. Each of the CaH bands have a red band-head with a broad wing extending blueward like its cousin MgH, but the width of CaH is considerable broader, extending nearly ~200Å. On the blue wing of CaH there is also a TiO band near 6750Å, but somewhat weaker than the one blending with MgH. Additionally there is a TiO band near 6580Å which also contributes to absorption in this region. With the relatively greater flux in cool stars at these redder wavelengths, the CaH and TiO bands combine to form a very strong feature centered near 6825Å. Because if it longer wavelenght than the MgH region, this part of the spectrum should be a sufficient diagnostic well below 3000K for both dwarfs and metal poor subdwarfs.

4.2.2 Hydride Photometry: System Definition

I have designed a pair of intermediate bandwidth interference filters which, when combined with the broad band *BVI* filters, allow me to measure the relative absorption strength in the regions of both MgB+MgH+TiO and CaH+TiO. In designing these filters specifically for use as survey tools I have had to form a compromise between filter width and selectivity. A narrower filter means more selectivity but less depth per unit integration time, where the inverse is true for a wider filter. For the purpose of identifying white dwarfs we do not care to distinguish among subdwarfs, dwarfs, or red giant stars, so I have designed these filters to encompass the entire wavelength span of both regions discussed. The resulting filter widths for the Mgb+MgH+TiO and MgH+CaH regions are 425Å and 435Å respectively at their 50% response levels. In Figure 4.10 I have shown the response traces for these two filters (solid lines) compared with the

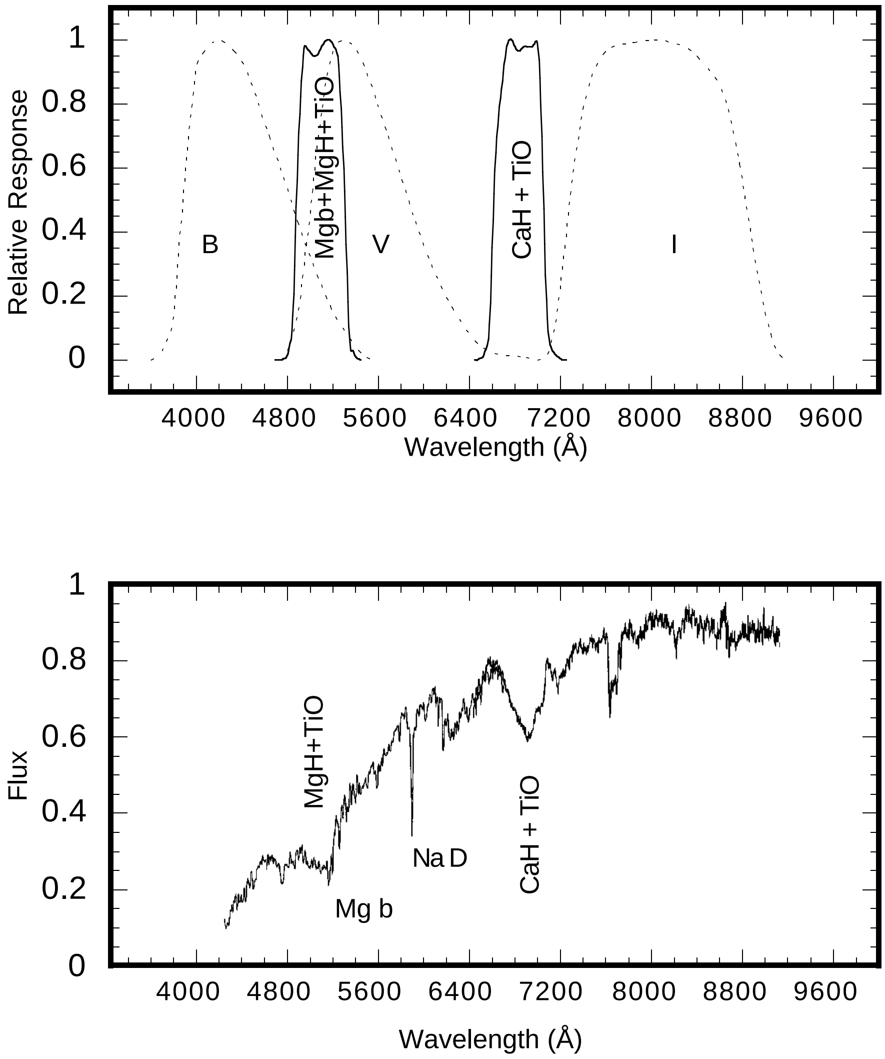

Figure 4.10: The response function (top panel) of the two intermediate band filters centered on 5095Å and 6860Å (solid lines) compared to the standard *BVI* responses from Bessell (1990). A spectrum of an intermediate subdwarf is also shown (bottom panel) as an example of the absorption features sampled by the two interference filters.

standard BVI filters responses (dashed lines). The bottom pannel shows a composite spectrum of a low–metallicity subdwarf with the hydride features evident.

I have defined a relative absorption index by comparing the ratio of measured flux in each of the intermediate band hydride filters to their expected flux from a black body, whose temperature is determined by the encompassing broad band color: $B-V$ for Mgb+MgH+TiO and $V-I$ for CaH+TiO. Using the Mgb+MgH+TiO index, hereafter $\mathrm{A}(MgH)$, as an example: I have expressed $\mathrm{A}(MgH)$ defined this way by

$$\mathrm{A}(MgH) = -2.5\log\left(\frac{F(MgH)_{obs}}{F(MgH)_{BB(B-V)}}\right), \tag{4.10}$$

where F is the integrated flux in the indicated filter and the subscript $BB(B-V)$ denotes the flux from a black body of a temperature governed by the indicated color index. Because it is usually much easier to measure the ratio of two fluxes than the flux in any one filter, I have define these indices in terms of observed and computed flux ratios expressed as

$$\mathrm{A}(MgH) = -2.5\log\left(\left.\frac{F(MgH)}{F(V)}\right|_{obs}\left.\frac{F(V)}{F(MgH)}\right|_{BB(B-V)}\right). \tag{4.11}$$

While 4.10 and 4.11 are not strictly equivalent, the color index of the model black body and observation are, by definition. Thus, to a good approximation both the model black bodies and photometry have equivelent flux in V. In terms of color indices Equation 4.11 is expressed by

$$\mathrm{A}(MgH) = (MgH-V)_{obs} - (MgH-V)_{BB(B-V)}. \tag{4.12}$$

I have fit synthetic $MgH-V$ and $B-V$ colors to a quadradic polynomial, which I use to transform $(MgH-V)_{BB(B-V)}$ to observed $B-V$ resulting in the usable definition of $\mathrm{A}(MgH)$. This is expressed as

$$\mathrm{A}(MgH) = (MgH-V)_{obs} - \left[-0.0723 + 0.278(B-V)_{obs} + 0.0522(B-V)^2_{obs}\right]. \tag{4.13}$$

Similarly, I have used the colors $CaH-I$ and $V-I$ to define the CaH absoption index as

$$\mathrm{A}(CaH) = (CaH-I)_{obs} - \left[-0.0503 + 0.356(V-I)_{obs} + 0.0141(V-I)^2_{obs}\right]. \tag{4.14}$$

With these definitions, objects with black body energy distributions will have the $\mathrm{A}(MgH)$ and $\mathrm{A}(CaH)$ absorption indices of zero. These indices follow the usual astronomical convention of magnitudes, in that less flux in either intermediate band results in a more positive absorption index. The broad band colors serve as crude continuum estimators for the two intermediate bands, which has some predictable consequences. The reddening of $B-V$ from extreme line blanketing in cool stars has the greatest effect on $\mathrm{A}(MgH)$. Line blanketing preferentially absorbs the flux in the blue, causing $B-V$ to underestimate the continuum in the region of MgH, hence for these stars $\mathrm{A}(MgH)$ apears as if it were in excess and takes on negative values. The amount of absorption in main sequence dwarf and subdwarf stars from molecular bands increases all across the visible spectrum, affecting the blue part of the spectrum first, then the red, with lower temperatures. This implies that both $\mathrm{A}(MgH)$ and $\mathrm{A}(CaH)$ have a "saturation" limit, where additional absorption in the intermediate filters are met with an equal amount in the broad band filters. Thus, at some temperature, hotter for $\mathrm{A}(MgH)$ than $\mathrm{A}(CaH)$, the index will remain constant in spite of increased absorption.

4.2.3 Hydride Photometry: Trial Observations

There are two possible ways to explore the behavior of the proposed photometric system for identifying cool white dwarf stars: theoretical modeling or direct observation. Because of the difficulties in accurately modeling atmospheres of cool stars, and my nature as an experimentalist, I chose the direct observational approach.

During the construction of the Prime Focus Camera I obtained *BVI, MgH,* and CaH CCD photometry of 25 known cool white dwarfs and 13 cool subdwarfs. I made these observations using McDonald Observatory's 0.76m telescope White Guider cassegrain CCD camera over the course of several observing seasons from October 1990 through April 1992. The broad band *BVI* photometry was calibrated using Landolt (1983, 1992) standards, while the interference filters were calibrated to synthetic colors and magnitudes computed from spectroscopic flux standards. The computed broad band colors of the flux standards agreed within photometric errors when compared against derived photometry tied to the Landolt standards.

In addition to this individual star photometry I have used photometry obtained during the Prime Focus engineering runs to define the average field sequences in $\mathrm{A}(MgH)$ versus $B-V$ and $\mathrm{A}(CaH)$ versus $V-I$. The field is a

0.5 square degree area centered at 16^h29^m RA and $+56^\circ01'$ Dec. ($\ell = 85.12, b = 41.78$). From this field I have used 575 stars brighter than V=19.5 which had photometric uncertainties less than 0.1 magnitudes to define the mean field sequences used in the analysis below.

The separation of cool white dwarfs, subdwarfs, and the field stars can be seen in Figure 4.11 below. In this diagram I have plotted the absorption index $\mathrm{A}(MgH)$ versus $B-V$ for the program stars described above. The mean field sequence is shown as a dashed line. The predicted effects of line blanketing in the field stars can clearly be seen as an "upward" turn in the field sequence beyond $B-V \sim 1.4$. The very red white dwarf at $B-V = 1.9$ is LHS–69 (LP701–29), which is known to have a large absorption feature in the middle of the *B* bandpass (Dahn *et al*. 1977). This feature has the same effect as line blanketing in the field stars and subdwarfs, causing its $\mathrm{A}(MgH)$ index to be very negative. For this reason this object was not included in my linear fit to the white dwarf data (solid line in Figure 4.11). The slight slope of this line toward more negative $\mathrm{A}(MgH)$ values with redder $B-V$ may be caused by the increased effects of H^- opacity in the blue with lower temperatures.

We can now examine the properties of Figure 4.11 in terms of its usefulness as a search tool for a photometric survey. The maximum difference in $\mathrm{A}(MgH)$ between the white dwarf line and field sequence is approximately 0.35 magnitudes occurring near $B-V \sim 1.4$, with the subdwarfs an additional ~0.075 magnitudes more. The turndown in the WDLF happens to coincide with this maximum separation. Therefore, the coolest white dwarfs defining the shape of

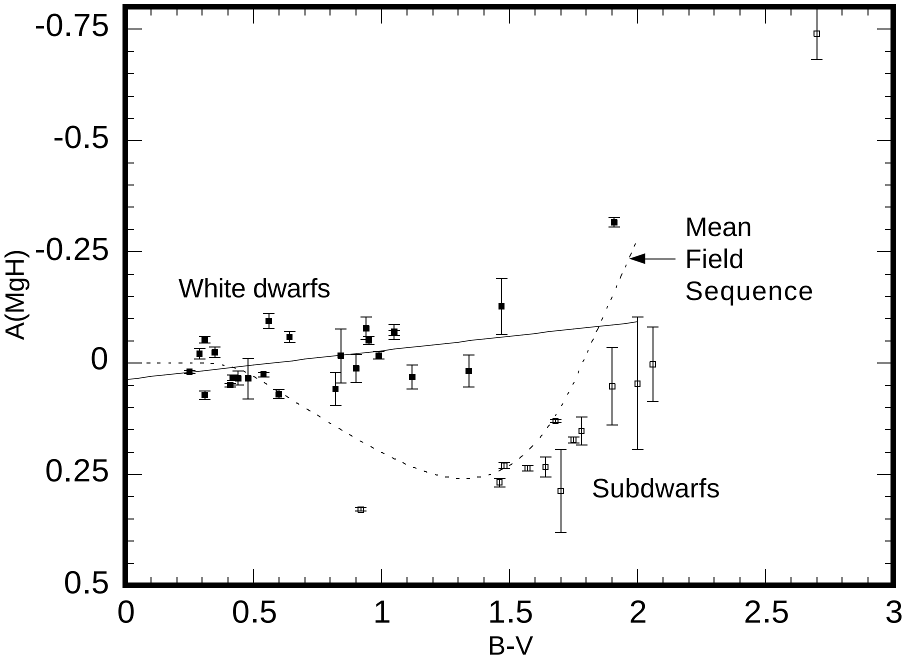

Figure 4.11: The MgH absorption index for known white dwarfs (filled squares) and subdwarfs (open squares) plotted against $B-V$. The mean field sequence from 1629+5601 area (dotted line) and the linear white dwarf fit (solid line) are clearly separated in the range $0.8 < B-V < 1.8$.

the WDLF below $\log(L/L_{\odot}) \sim -3$ should be easily separable from the field stars with modest precision photometry from a CCD based survey. However, even with high precision photometry white dwarfs near $B-V = 0.6$ will be difficult to identify, as would white dwarfs near $B-V = 1.8$. However, white dwarfs near the region of red confusion correspond to effective temperatures below ~3500K, hence will have red $V-I$ colors in excess of 2.0. Therefore, this confusion can be reolved with the $\mathrm{A}(CaH)$ index. In spite of this limitation, the $\mathrm{A}(MgH)$ versus $B-V$ diagram does provide us with a method of photometrically identifying cool white dwarf candidates over most of the luminosity function currently defined by proper motion objects.

Similarly, in Figure 4.12 I have shown $\mathrm{A}(CaH)$ versus $V-I$ for the same program stars as in Figure 4.11. The mean subdwaf sequence (long dashed line) was derived from spectroscopic data obtained by Hartwick *et al*. (1984). In their study of late type dwarfs, Hartwick *et al*. spectroscopically measured the CaH absorption feature sampled by my interference filter for 65 high proper motion objects from the LHS Catalog (Luyten 1979); they classify 19 as Halo subdwarfs. Using Bessell's (1987) transformation of Kron RI to the Cousins RI I have computed a smoothed fit to the Hartwick *et al*. CaH strength versus $V-I$. To obtain the mean subdwarf sequence shown below I scaled their CaH strengths by 0.80, which is effectively a dilution factor between my filter width and the "pure" spectroscopic width of the CaH feature. The agreement of the mean sequence with the photometric data in Figure 4.12 for the subdwarfs is excellent.

The effects of saturation can be seen in both the field stars (short dashed line) and subdwarf mean sequences as a flat red tail. It is clear from this diagram the white dwarfs do not separate from the field stars until possibly beyond $V-I\sim 1.8$. The red limit of the white dwarf separation in $\mathrm{A}(MgH)$ versus $B-V$ corresponds to a $V-I\sim 2$, which is red enough that both the field stars and subdwarfs show significant absorption in $\mathrm{A}(CaH)$. Since there are no white dwarfs yet known with effective temperatures this low I can only speculate where they might fall in this diagram. If the Halo is significantly older than the Disk, as might be suggested by the globular cluster ages, then its white dwarfs would have had sufficient time to cool to this much. If such cool white dwarfs have similar

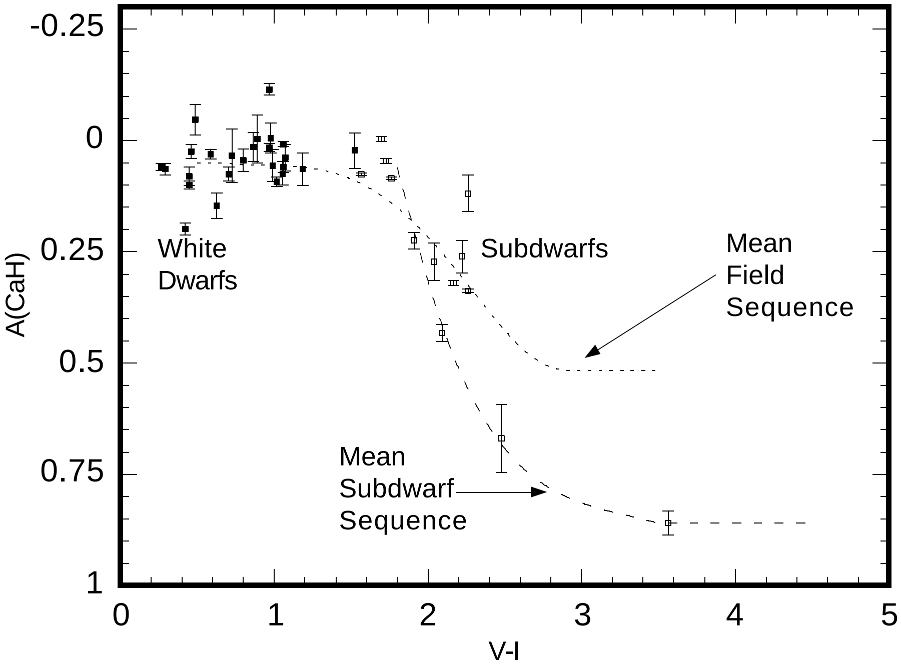

Figure 4.12: The CaH absorption index for known white dwarfs (filled squares) and subdwarfs (open squares) plotted against $V-I$.

photometric properties to those of the Disk, then they too will have nearly zero absorption in $\mathrm{A}(CaH)$. In this case very old cool white dwarfs should be well separated from the field stars and subdwarfs in a $\mathrm{A}(CaH)$ versus $V-I$ diagram. This effect will allow me to explore the region in the white dwarf luminosity function well beyond the observed turndown from finite age effects in the Disk. It is also evident that the $\mathrm{A}(CaH)$ index could be used to separate low temperature late–type Halo subdwarfs from other objects. This would be useful for a investigations of the mass content of the Galaxy.

4.3 SUMMARY

I have shown that CCD*UBVI* photometry is an efficient means of conducting a large area sky survey in search of white dwarf stars . I have also demonstrated that it is possible to estimate the basic physical characteristics of white dwarfs, such as effective temperature and surface gravity, given good model atmosphere calculations and modest precision photometry, made possible with a CCD–based sky survey, . However, *UBVI* photometry alone fails to provide an effective discriminatant for white dwarfs with effective temperatures below ~6000K.

I have designed an intermediate band filter system which can be combined with broad band *BVI* photometry to provide a method for identifying cool white dwarfs. These filters are centered on the absorption features of MgB+MgH+TiO and CaH+TiO at central wavelengths of 5095Å and 6840Å, where degenerate stars lack the absorption features of non-degenerate dwarfs of similar color. Though the filter widths at 424Å and 435Å are narrower than *BVI* filters they are wide enough to be effective at very faint magnitudes. With these filters I have defined two absorption indices, $\mathrm{A}(MgH)$ and $\mathrm{A}(CaH)$, which estimate the strength of the absorption in each of the intermediate band filters. When combined with broad band $B-V$ and $V-I$ colors, these indices can identify cool white dwarfs in the disk and explore their existence in the halo.

5

Calibration of Stellar Ages: A Case Study of the Praesepe

I have demonstrated in Chapters 1 and 2 that white dwarf stars offer a very powerful technique for estimating the age of the Galactic disk and have great potential as a self consistent means to estimate the Galactic Halo's age. It is therefore of great importance to have the white dwarf ages and other stellar ages on the same system so that they are directly comparable. To do this I have initiated a project to empirically calibrate the white dwarf ages with the most popular age estimation technique – stellar evolution isochrones. One of the more obvious places to look for such a calibration of age estimators is in a place where two or more estimators can be applied simultaneously. Because every stellar population creates white dwarf stars, it seems reasonable then to look for white dwarfs in systems where stellar isochrones are used – namely *star clusters*.

Because white dwarf stars are intrinsically faint it is necessary to look at star clusters which are relatively nearby. Unfortunately, the sensitivity of current instrumentation essentially eliminates all of the older globular clusters found in the Galactic halo. These systems are typically far enough away that the oldest white dwarfs have visual magnitudes exceeding 30th – too faint even for the Hubble Space Telescope to see, but possibly reachable with a 3-4 meter class space based telescope. The clusters that remain are the Galactic or Open clusters. These are considered part of the "Disk" and can be found both near and far, one of the nearest being the Hyades. The ages of Galactic clusters as estimated from calculated isochrones range from essentially 0 to 10-12 billion years. It seems natural, then, to use open clusters for calibration of both stellar isochrone *and* white dwarf evolutionary ages.

While the idea of searching for white dwarf stars in Galactic clusters is not new (Koester and Reimers 1989, 1985, 1981; Reimers and Koester 1988, 1982 and Anthony-Twarog, 1982; 1984), the unique qualities of the Prime Focus Camera (PFC) make new search efforts for white dwarf stars in star clusters very rewarding. The wide field digital imagery of the PFC (described in Chapter 3) allows very high precision photometric and astrometric measurements of stars over areas comparable in size to most galactic clusters. In contrast, most prior efforts have been with photographic material, resulting in lower quality photometry at the faint limits, where precision is needed most to distinguish white dwarfs in the cluster from accidentally aligned field stars. Most of these past efforts were also aimed at the different goal of establishing the maximum mass a progenitor star can have and still form a white dwarf. Considering standard errors of measurement, this upper limit is still an open issue. In spite of several well executed searches, the extent of our observational information is that the maximum progenitor mass for white dwarf stars is $\geq 4 - 5M_{\odot}$ (Weidemann 1990).

Theoretical models, however, indicate the upper limit for white dwarf progenitors is $\sim 8M_\odot$ (Romanishin and Angel 1980), and is supported empirically by Koester and Reimers' work. This limit for progenitor mass will be important when I try to estimate the number of white dwarf stars formed by a given mass distribution (*i.e.* a star cluster).

With the wide field digital capability of the PFC I have reobserved an open cluster for white dwarf stars, with the specific goal of locating the very faintest and oldest white dwarfs present. With this instrument it is possible to establish a *white dwarf* age for the cluster in question as well as a stellar isochrone age from the same set of exposures, and thus cross-calibrate these two techniques.

5.1 WHY THE PRAESEPE?

The Praesepe (M-44, NGC-2632, C-0837+201) is an open cluster located in the constellation Cancer at $8^h40^m07^s$ Right Ascension, $19^\circ 59' 49''$ Declination (epoch J2000.0). There are many open clusters known to have white dwarf stars (von Hippel 1994, Weidemann *et al.* 1992, Koester and Reimers 1989 *et seq.*, Anthony-Twarog 1984, 1982, Eggen and Greenstin 1965). Why then choose the Praesepe for an exhaustive study? Of the many open cluster systems known, the Praesepe is one of the best suited for age calibration because it is: a) nearby, b) not too thick, c) sufficiently old, and d) well populated.

The age of the Praesepe from stellar isochrones is estimated at $0.9 \pm 0.1 Gyr$ (Vandenberg 1990). This is old enough that the lifetimes of the progenitor stars, $\sim 0.05 - 0.1 Gyr$, do not seriously affect the zero point of the cooling times for the oldest white dwarfs. At the Praesepe's isochrone age, a

$0.6M_\odot$ DA white dwarf has an approximate luminosity of $\log(L/L_\odot) \approx -3$, and an absolute visual magnitude of $M_v \approx 12.7$. However, in the limit of zero main sequence lifetime the oldest white dwarf progenitor mass most likely is greater than $5M_\odot$, implying that it has a mass exceeding $0.6M_\odot$ and would be somewhat brighter.

The distance to the Praesepe is roughly 174 parsecs, giving it a distance modulus of $m - M_m \approx 6.2$ (ref). Therefore, at this distance the coolest and faintest white dwarfs in the cluster will have apparent visual brightnesses of $V \approx 18.9$. This is near enough that these stars are easily observable both photometrically and spectroscopically, an important fact for further study.

The Praesepe's distance is also sufficiently great that the thickness of the cluster along the line-of-sight is relatively small in comparison. Johnson (1952) estimated from his photoelectric photometry that the Praesepe's thickness was responsible for 0.015 magnitudes of scatter in the V versus B-V color-magnitude diagram. While this might hold true for the brightest cluster members (inside a ~ 2 parsecs radius) it is more realistic to assume a cluster radius of 12 parsecs (Mermilliod *et al.* 1990), which leads to 0.3 magnitudes of thickness. In any case, we expect white dwarfs in the Praesepe to form a fairly well–defined sequence in a color-magnitude diagram. This compares favorably with one of the most extensively studied clusters – the Hyades. At a distance of 47.9 parsecs (Schwan 1991) and an estimated cluster radius of 20 parsecs, the Hyades has a difference of nearly 2 magnitudes from the back to the front of the cluster. This necessitates that distances for cluster members be known on an individual basis, thereby greatly complicating studies of overall cluster properties.

Common to all cluster studies is the issue of membership: Is a given star a true cluster member or a chance superposition of a star in the same line of sight? In systems where the concentration and density of stars is high (*i.e.* globular clusters) it is usually sufficient to examine photometric properties and positions relative to the cluster center in order to determine membership probability. However, this usually does not hold true of the open clusters, whose distribution and numbers are more sparse. In these cases we must resort to other criteria, usually kinematics from proper motion and/or radial velocity measurements, to certify membership. There are but a handful of open clusters known to be common proper motion systems, and the classic example is the Hyades. Among the other few known is the Praesepe, which appears to move roughly 0.037 arcseconds per year (Jones and Cudworth 1983, Jones and Stauffer 1991) in a direction with a position angle of approximately 250 degrees. This provides the opportunity to further constrain cluster membership of white dwarf candidates by requiring that they have proper motions similar to the Praesepe's main-sequence stars. Because of their broad spectral features, obtaining precision radial velocities of white dwarf stars is difficult. This makes radial velocities a poor discriminant for cluster membership and they will not be further addressed herein.

The Praesepe is also sufficiently populated to have formed a significant number of white dwarf stars at its present estimated age of $0.9Gyr$. The Praesepe is already known to contain at least 3 white dwarf stars (Eggen and Greenstein 1965); LB-930 (EG-59), LB-1847 (EG-60) and LB-393 (EG-61). It is clear from the population of the upper main sequence that the Praesepe should have formed more white dwarf stars than these three.

The questions are: *How many more white dwarfs are there and can we use these to estimate the Praesepe age?*

5.2 OBSERVATIONAL MATERIAL AND DATA REDUCTION

5.2.1 Observing Stategy and Data Acquisition

On two observing runs in February and March of 1994 I obtained deep UBVI CCD imagery of the Praesepe and surrounding field for the purpose of conducting a search for faint white dwarf stars. I obtained these data at McDonald Observatory using the modified Boller and Chivens 0.76-m telescope with the Prime Focus Camera (PFC). The detector was a Lumigen coated, frontside illuminated Loral-Fairchild $2048^2 \times 15\mu m$ pixel CCD controlled with a DEC MicroVAX-II computer running ARGUS data acquisition software. The UBVRI filter set in the PFC is per the prescriptions given in Bessell (1990), which uses readily available Schott filter glass to approximate the standard UBVRI bandpasses.

The task of searching for faint stars in nearby open clusters is somewhat hindered by the presence of bright upper main-sequence stars. These stars can cause severe scattered light problems and/or image blooming from saturated charge on the CCD detector. Both of these effects would cause the image of a faint star near one of these bright stars to be obscured or contaminated so that it could not be measured. Therefore, rather than use single exposures to the desired depth, I made a series of at least 6 individual images, where the individual exposure times for each filter were set so that the sky was on the verge of becoming the dominant noise source over the read noise in the background.

There are four advantages of doing this: First, having multiple exposures makes the final coadded imagery very insensitive to cosmic ray events - a must for wide field big-pixel imagery where a single cosmic ray looks very much like a star. Second, by moving the field slightly between each exposure - "dithering" by a few pixels – the final image is not adversely affected by manufacturing defects present in the CCD detector. Third, in keeping the individual exposures as short as possible I kept the charge blooming near bright stars to a minimum and hence maximized the total dynamic range on the final images. Finally, the S/N ratio is not compromised in the final coadded image when each image is exposed such that sky is the dominant noise source.

In addition to these images, I also obtained a set of short exposure frames for the NE, NW and SE fields (see Figure 5.3). These images were useful in obtaining CCD photometry of the upper main sequence of the Praesepe, including the brightest red giants, on the same standard system as the deep images used for the white dwarf search. The details of the individual images are summarized in Table 5.1. The first and sixth columns are the UT date and coordinated UT time at the beginning of each exposure. The second column contains the running catalogue number from all of my CCD observations. The field identification given in the third column is (in terms of compass points) the position of the field relative to the cluster center. The integration times, filter, and beginning airmass for each image are listed in columns 4, 5, and 7 respectively.

I reduced the data for this project using the software tools found in IRAF; FOCAS (Jarvis and Tyson, 1981 and Valdes, 1982), DAOPHOT (Stetson 1987), and PHOTCAL. The details of how to reduce CCD image data and produce

Table 5.1: Journal of Observations. Summarized here are the individual observations of the Praesepe.

Date (UT)	Image No.	Field ID	Integration Time (sec.)	Filter	Start Time (UTC)	Start Airmass
10 Feb. 1994	cc08274	Praesepe NE	1	I	08:12:34	1.139
"	cc08275	"	30	I	08:17:19	1.150
10 Feb. 1994	cc08276	Praesepe NE	30	U	08:22:34	1.163
"	cc08277	"	900	U	08:27:50	1.177
10 Feb. 1994	cc08278	Praesepe NE	5	B	08:47:38	1.237
"	cc08279	"	150	B	08:52:24	1.253
10 Feb. 1994	cc08280	Praesepe NE	2	V	08:59:38	1.279
"	cc08281	"	60	V	09:04:29	1.298
10 Feb. 1994	cc08282	Praesepe NW	30	U	09:13:44	1.338
"	cc08283	"	900	U	09:19:58	1.362
10 Feb. 1994	cc08284	Praesepe NW	5	B	09:40:58	1.478
"	cc08285	"	150	B	09:45:32	1.508
10 Feb. 1994	cc08286	Praesepe NW	2	V	09:52:45	1.556
"	cc08287	"	60	V	09:57:29	1.590
10 Feb. 1994	cc08289	Praesepe NW	1	I	10:07:47	1.671
11 Feb. 1994	cc08332	Praesepe NE	180	V	03:01:01	1.393
"	cc08333	"	180	V	03:12:16	1.336
"	cc08334	"	180	V	03:20:07	1.302
"	cc08335	"	180	V	03:29:21	1.266
"	cc08336	"	180	V	03:38:16	1.234
"	cc08337	"	180	V	03:47:25	1.205
11 Feb. 1994	cc08344	Praesepe NE	180	I	04:43:20	1.081
"	cc08345	"	180	I	04:51:12	1.070
"	cc08346	"	180	I	04:59:31	1.059
"	cc08347	"	90	I	05:07:56	1.050
"	cc08348	"	90	I	05:14:50	1.043
"	cc08349	"	90	I	05:21:12	1.037
12 Feb. 1994	cc08382	Praesepe NW	120	I	02:44:31	1.472
"	cc08383	"	120	I	02:51:56	1.413
"	cc08384	"	120	I	02:58:46	1.378
"	cc08385	"	120	I	03:05:23	1.347
"	cc08386	"	120	I	03:12:04	1.318
"	cc08387	"	120	I	03:18:47	1.290
12 Feb. 1994	cc08388	Praesepe NW	180	V	03:25:53	1.264
"	cc08389	"	180	V	03:33:40	1.236
"	cc08390	"	180	V	03:41:17	1.212
"	cc08391	"	180	V	03:49:10	1.189
"	cc08392	"	180	V	03:56:48	1.168
"	cc08393	"	180	V	04:04:38	1.149
12 Feb. 1994	cc08394	Praesepe NW	300	B	04:12:50	1.130

Table 5.1: Journal of Observations continued.

Date (UT)	Image No.	Field ID	Integration Time (sec.)	Filter	Start Time (UTC)	Start Airmass
"	cc08395	"	300	B	04:24:33	1.107
"	cc08396	"	300	B	04:39:36	1.081
"	cc08397	"	300	B	04:49:17	1.067
"	cc08398	"	300	B	04:59:17	1.055
"	cc08399	"	300	B	05:08:16	1.045
12 Feb. 1994	cc08401	Praesepe NW	900	U	05:39:17	1.024
"	cc08402	"	900	U	06:05::45	1.018
"	cc08403	"	900	U	06:25:00	1.020
"	cc08404	"	900	U	06:44:18	1.029
"	cc08406	"	900	U	07:37:16	1.080
"	cc08408	"	900	U	08:15:47	1.166
"	cc08409	"	900	U	–	–
"	cc08410	"	900	U	09:10:53	1.360
"	cc08411	"	900	U	–	–
13 Feb. 1994	cc08499	Praesepe NE	900	U	03:49:02	1.184
"	cc08500	"	900	U	03:09:22	1.129
"	cc08501	"	900	U	04:31:30	1.088
"	cc08502	"	900	U	–	–
"	cc08503	"	900	U	05:11:04	1.039
"	cc08504	"	900	U	–	–
"	cc08505	"	900	U	05:57:50	1.018
"	cc08506	"	900	U	–	–
13 Feb. 1994	cc08507	Praesepe NE	300	B	07:08:16	1.053
"	cc08508	"	300	B	07:18:54	1.066
"	cc08509	"	300	B	07:32:33	1.085
"	cc08510	"	300	B	07:42:33	1.103
"	cc08511	"	300	B	07:52:25	1.122
"	cc08512	"	300	B	08:02:16	1.143
14 Feb. 1994	cc08533	Praesepe SE	120	I	03:09:47	1.296
"	cc08534	"	120	I	03:12:01	1.269
"	cc08535	"	120	I	03:25:56	1.236
"	cc08536	"	120	I	03:32:36	1.214
"	cc08537	"	120	I	03:39:13	1.195
"	cc08538	"	120	I	03:49:12	1.175
"	cc08539	"	1	I	03:52:46	1.158
14 Feb. 1994	cc08540	Praesepe SE	180	V	03:58:08	1.146
"	cc08541	"	180	V	04:05:48	1.128
"	cc08542	"	180	V	04:13:55	1.112
"	cc08543	"	180	V	04:21:21	1.098
"	cc08544	"	180	V	04:29:01	1.085

Table 5.1: Journal of Observations continued.

Date (UT)	Image No.	Field ID	Integration Time (sec.)	Filter	Start Time (UTC)	Start Airmass
"	cc08545	"	180	V	04:36:36	1.074
"	cc08546	"	3	V	04:44:08	1.064
14 Feb. 1994	cc08547	Praesepe SE	900	U	05:01:22	1.045
"	cc08548	"	900	U	05:21:18	1.029
"	cc08549	"	900	U	05:41:56	1.020
"	cc08550	"	900	U	06:02:54	1.018
"	cc08551	"	900	U	06:25:06	1.023
"	cc08552	"	900	U	06:44:45	1.035
"	cc08553	"	30	U	07:10:19	1.059
14 Feb. 1994	cc08554	Praesepe SE	300	B	07:15:26	1.066
"	cc08555	"	300	B	07:25:00	1.080
"	cc08556	"	300	B	07:45:50	1.116
"	cc08557	"	300	B	07:55:45	1.137
"	cc08558	"	300	B	08:05:25	1.160
"	cc08559	"	300	B	08:15:05	1.185
"	cc08560	"	5	B	08:24:52	1.213
16 Feb. 1994	cc08674	Praesepe Cen.	10	V	03:38:00	1.160
16 Feb. 1994	cc08675	Praesepe Cen.	5	I	03:42:56	1.153
16 Feb. 1994	cc08676	Praesepe Cen.	180	U	03:47:55	1.142
16 Feb. 1994	cc08677	Praesepe Cen.	60	B	03:55:36	1.125
17 Mar. 1994	cc08860	Praesepe NNE	900	U	02:03:26	1.134
"	cc08861	"	900	U	02:24:46	1.092
"	cc08862	"	900	U	02:44:28	1.063
"	cc08863	"	900	U	03:05:27	1.040
"	cc08864	"	900	U	03:25:08	1.026
"	cc08865	"	900	U	03:45:22	1.018
"	cc08866	"	900	U	04:05:31	1.017
17 Mar. 1994	cc08868	Praesepe NNE	300	B	04:59:05	1.045
"	cc08869	"	300	B	05:10:18	1.057
"	cc08870	"	300	B	05:19:58	1.070
"	cc08871	"	300	B	05:30:53	1.084
"	cc08872	"	300	B	05:40:32	1.103
"	cc08873	"	300	B	05:50:16	1.122
"	cc08874	"	300	B	05:59:56	1.143
17 Mar. 1994	cc08875	Praesepe NNE	180	V	06:11:50	1.172
"	cc08876	"	180	V	06:20:10	1.195
"	cc08877	"	180	V	06:28:00	1.219
"	cc08878	"	180	V	06:35:40	1.244
"	cc08879	"	180	V	06:43:22	1.272
"	cc08879	"	180	V	06:51:01	1.302

Table 5.1: Journal of Observations continued.

Date (UT)	Image No.	Field ID	Integration Time (sec.)	Filter	Start Time (UTC)	Start Airmass
17 Mar. 1994	cc08880	Praesepe NNE	120	I	06:58:47	1.335
"	cc08881	"	120	I	07:05:28	1.365
"	cc08882	"	120	I	07:12:08	1.398
"	cc08883	"	120	I	07:18:55	1.434
"	cc08884	"	120	I	07:25:35	1.473
"	cc08885	"	120	I	07:32:31	1.515
18 Mar. 1994	cc08949	Praesepe NNW	900	U	03:19:04	1.025
"	cc08950	"	900	U	03:38:35	1.018
"	cc08951	"	900	U	03:59:01	1.017
"	cc08952	"	900	U	04:18:44	1.022
"	cc08953	"	900	U	04:38:54	1.034
"	cc08954	"	900	U	04:58:37	1.052
18 Mar. 1994	cc09002	Praesepe NNW	300	B	06:18:49	1.225
"	cc09003	"	300	B	06:29:25	1.262
"	cc09004	"	300	B	06:39:06	1.299
"	cc09005	"	300	B	06:49:09	1.342
"	cc09006	"	300	B	06:58:55	1.388
"	cc09007	"	300	B	07:08:27	1.439
18 Mar. 1994	cc09008	Praesepe NNW	180	V	07:18:19	1.497
"	cc09009	"	180	V	07:25:57	1.547
"	cc09010	"	180	V	07:33:35	1.603
"	cc09011	"	180	V	07:41:27	1.664
"	cc09012	"	180	V	07:51:00	1.749
"	cc09013	"	180	V	07:58:40	1.824
18 Mar. 1994	cc09014	Praesepe NNW	120	I	08:06:27	1.910
"	cc09015	"	120	I	08:13:10	1.992
"	cc09016	"	120	I	08:19:48	2.080
"	cc09017	"	120	I	08:26:26	2:179

stellar photometry are well documented in manuals produced by the National Optical Astronomy Observatories. For CCD data reduction the relevant manual is *A Users Guide to CCD Reductions with IRAF* by Phillip Massey, and for stellar photometry *A Users Guide to Stellar Photometry with IRAF* by Phillip Massey and Lindsey Davis. Information regarding the theory and use of FOCAS can be found in *Faint Object Classification and Analysis System* by Francisco Valdes and references therein. In §5.2.2 and §5.2.3 that follow, I list the prescribed steps I took, noting where I have deviated from the usual methods. All images have had the PFC's instrumental signature removed following the procedure outlined in Chapter 3 and are ready for further analysis.

5.2.2 Standard Star Photometry and Photometric Calibration

Of the eight nights I observed during this project, two were photometric; 10 February 1994 and 16 February 1994. The photometric calibration of the entire Praesepe data set rests on these two nights. During these nights I observed the Praesepe along with a total of 58 Landolt (1983, 1992) standard stars in 6 different fields. In order to have the greatest leverage in the photometric solution I chose the standards so that they would cover as wide a range in magnitude and color as possible. Each Landolt field contains many UBVRI standards, therefore I chose each field to contain either an extreme "red" or "blue" standard, with surrounding standards of intermediate colors. I did this so that the amount of time spent obtaining the desired standards was minimized. The standards were observed at multiple airmasses so as to bracket the airmass range of the Praesepe calibration fields themselves.

I used software tools in the IRAF package APPHOT to extract fixed aperture instrumental magnitudes. With PHOT set in its interactive mode I manually measured all standard stars using an aperture fixed at 20 arcseconds ($r_{aper.} \cong 7.5$ pixels) in diameter. The sky value for each star measured was computed locally using the modal value of pixels within an annulus having a 20 arcsecond inner radius and a width of 6.75 arcseconds (5 pixels). I determined these parameters after examining each standard star in the Praesepe calibration image and measuring the spatial extent of the stellar point-spread-function (PSF). I set the aperture size so that in the worst case the aperture contained at least 99.9% of the integrated flux from the PSF. The parameters for the sky annulus were chosen so that 1) at the inner radius of the annulus, the flux in the wings of the PFS were contributing <0.1% to the sky, and 2) the width provided enough pixels (550 in the final annulus) that the histogram of pixel values inside the annulus provided an accurate estimate of the modal sky value.

It is a common practice in CCD photometry to extract the program field photometry with a smaller aperture, $r_{apert} \sim FWHM(PSF)$, which is corrected to the same zero point as the standards by a constant called an *aperture correction*. This is done in order to avoid contamination from nearby stars and to keep the read noise from the CCD electronics as small as possible. It has been my experience that a consistent estimate of the precise value of aperture correction is quite difficult. I have, therefore, extracted the photometry of the Praesepe calibration fields taken on the two photometric nights using the same size aperture and sky annulus as for the standard stars. In doing so I have explicitly forced the standard star and Praesepe calibration photometry to have the same zero points.

The prescription for the U filter using Schott glass (1mm UG1 + 2mm BG39 + 2mm GG395) is known to have a red leak of roughly 0.4% of the mean between the R and I flux (Bessel 1990). This red leak causes the U band photometry to deteriorate rapidly for objects redder than U-B=1.5. In an attempt to minimize this effect I have corrected the instrumental U magnitude by subtracting from the measured U band flux a fraction of the measured I band flux. The instrumental U magnitude is thus

$$U_{inst} = 25 - 2.5\log\left[10^{\left(0.4\left(U_{mea.}-25\right)\right)} - 3.6954\times 10^{-4}\left(10^{\left(0.4\left(I_{mea.}-25\right)\right)}\right)\right], \qquad (5.1)$$

where $U_{mea.}$ and $I_{mea.}$ are the measured magnitudes from PHOT. The amount of I band flux subtracted is determined by scaling the intrinsic 0.4% red leak by the difference in overall throughput efficiency between the U and I bandpasses. All other instrumental magnitudes: B, V, and I are taken to be identical to their measured values from PHOT.

I next transformed the instrumental magnitudes onto the standard system using PHOTCAL to fit the equations 5.2-5.5 shown below,

$$U_{inst} = U_{std} + u_0 + u_1 X + u_2 (U-B)_{std} + u_3 X (U-B)_{std}, \qquad (5.2)$$

$$B_{inst} = B_{std} + b_0 + b_1 X + b_2 (B-V)_{std} + b_3 X (B-V)_{std}, \qquad (5.3)$$

$$V_{inst} = V_{std} + v_0 + v_1 X + v_2 (B-V)_{std} + v_3 X (B-V)_{std}, \qquad (5.4)$$

$$I_{inst} = I_{std} + i_0 + i_1 X + i_2 (V-I)_{std} + i_3 X (V-I)_{std}. \qquad (5.5)$$

In these equations the x_0 term is the *Zero Point*, which contains the basic correction for detector sensitivity, optical efficiency, and transparency of the atmosphere at the Zenith. The dependance of atmospheric transparency on the zenith angle of observation is corrected by the x_1 term, where $X = \sec(z)$. The fact that the change in transparency is wavelength dependant (*e.g.* sunsets are orange-red) is accounted for by the x_3 term. Finally, the prescriptions used for defining the filter bandpasses are approximations to the bandpasses used to define the standard system (*c.f.* Bessel 1990). The filter correction, x_2, should be constant for any given filter set but is a function of an object's color. However, telescope optics and detector responses also have wavelength variation in their efficiencies which has the same effect as a non-standard filter response. Thus, the filter coefficients can vary for a given filter set from telescope to telescope and detector to detector and need to be determined for each run.

Using the interactive non-linear least squares utility FITPARS within PHOTCAL I fit the instrumental standard star magnitudes to their standard magnitudes and colors with equations 5.2-5.5. During the fitting process a star more than 3 sigma away from the fit was removed and the fit was reiterated. Such deviations can be caused by cosmic ray hits on the stellar profile, CCD defects, or bad standards. I continued this procedure until there were no stars outside the 3 sigma limit. Typically I only removed one or two stars before meeting my fitting criteria. Because both the optics – telescope plus corrector – and detector are fixed for the PFC, I first fit equations 5.2–5.5 in the manner described above using all standards from both nights to establish the filter color coefficients. I then fit the standards from each individual night, fixing the x_2 terms to their previously determined values.

In Table 5.2 I have summarized the coefficients, RMS scatter, and standard deviations of the standard star photometry fits to equations 5.2–5.5. The small values of the filter color coefficients, the x_2 terms, indicate the high degree with which the filter prescriptions of Bessell (1990) and the response function of the CCD combine to represent the true filter response functions of the standard system. Furthermore the similarities of the remaining coefficients for the two photometric nights confirm their quality. Equations 5.2-5.5, along with these coefficients, are then inverted using the PHOTCAL task INVERTPARS for the actual transformation of the instrumental magnitudes to standard magnitudes and colors.

Using the inverted forms of equations 5.2–5.5 and the appropriate night's coefficients, the Praesepe calibration photometry was transformed onto the standard system. Where the same star was measured more than once I computed the mean and RMS scatter for its colors and magnitudes. The average scatter in the measured magnitudes and colors for these stars was <0.005 magnitude. When possible I chose these stars as my calibration source for the program fields, otherwise I chose well isolated uncontaminated single stars.

In Figure 5.1 I have plotted, for all standards observed, the residuals between the transformed magnitudes and colors and their standard values against the observed V magnitude. In all cases the only obvious systematic effect is the increased scatter at fainter magnitudes. Perhaps more importantly, there seems to be no systematic trends in the residuals as a function of color (Figure 5.2). It is clear from the flat distribution of the U-B residuals (Figure 5.2 bottom pannel) that the red leak correction to the instrumental U magnitude is effective over the

Table 5.2: Summary of the photometric coefficients, RMS scatter, and standard deviations for both nights combined and the two nights individually.

	Combined	10 Feb 1994	16 Feb. 1994
# of Stars	58	37	21
u_0	5.7828	5.8089	5.8779
u_1	0.4863	0.4787	0.3973
u_2	5.4304E-4	5.4304E-4	5.4304E-4
u_3	-0.0531	-0.0556	-0.0504
RMS(U)	0.0511	0.0385	0.0362
STDEV(U)	0.0532	0.0407	0.0393
b_0	4.3394	4.3676	4.3617
b_1	0.2657	0.2535	0.2443
b_2	-0.0645	-0.0645	-0.0645
b_3	-0.0218	-0.0186	-0.0232
RMS(B)	0.0329	0.0269	0.0155
STDEV(B)	0.0343	0.0285	0.0169
v_0	3.8710	3.8881	3.8585
v_1	0.1658	0.1580	0.1693
v_2	-4.7359E-4	-4.7359E-4	-4.7359E-4
v_3	0.0022	0.0070	4.0517E-5
RMS(V)	0.0313	0.0296	0.0170
STDEV(V)	0.0326	0.0311	0.0185
i_0	3.6484	3.6882	3.8787
i_1	0.0940	0.0810	-0.0906
i_2	-0.0184	-0.0184	-0.0184
i_3	-0.0073	-0.0108	-0.0169
RMS(I)	0.0494	0.0252	0.0376
STDEV(I)	0.0513	0.0266	0.0406

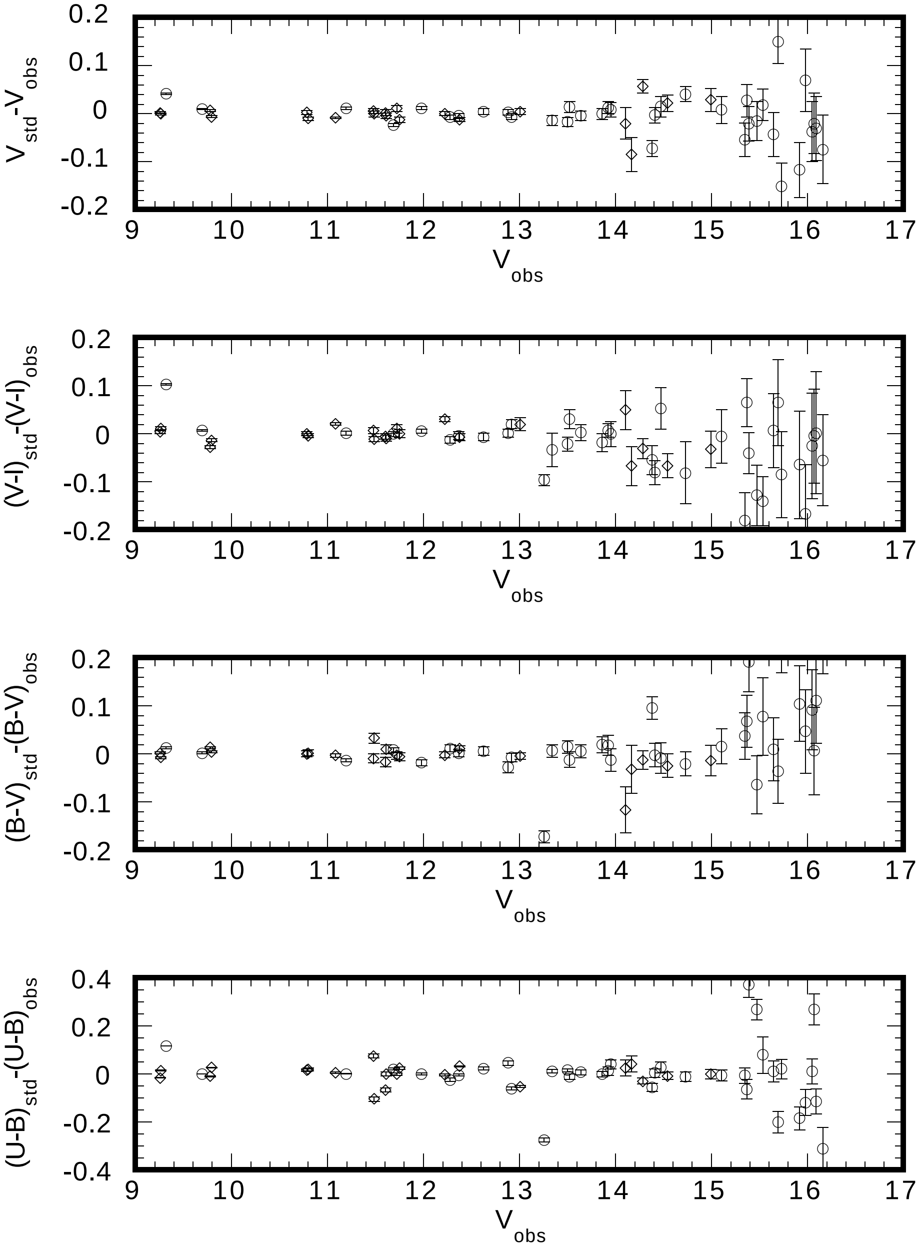

Figure 5.1: The residuals from the standard star photometry on 10 Feb. 1994 (open circles) and 16 Feb. 1994 (open diamonds) plotted against the observed V magnitude. The error bars represent the internal photometric error of each measurement for the standard stars observed.

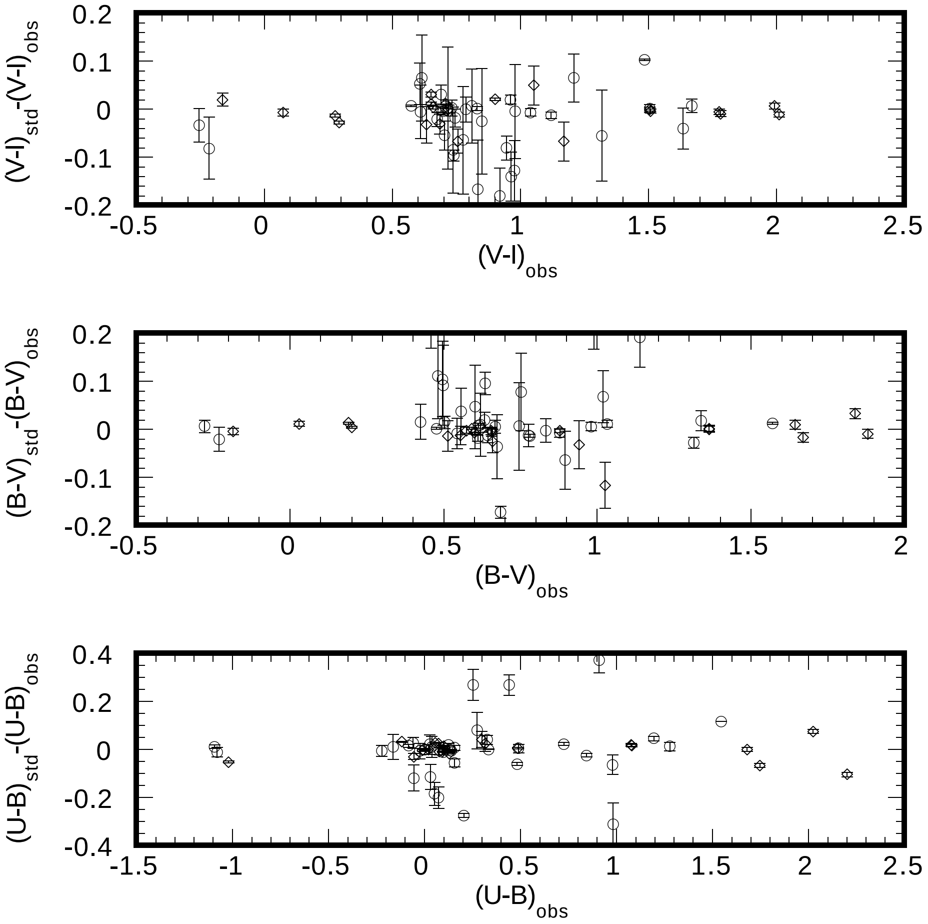

Figure 5.2: Same as in Figure 5.1, except the standard star residuals are plotted against their colors.

range of observed U-B colors. The red leak correction extends the usefulness of photometry with the Bessel (1990) U filter by at least one magnitude redward in U-B and perhaps by as much as 1.5-2 magnitudes to $(U-B)_{std} \sim 3.5$.

5.2.3 Program Photometry of the Praesepe

The present survey's program images can be divided into two groups: a short exposure group and a long exposure group. The short exposure group contains UBVI images in 3 of the Praesepe's central quadrants: Northwest, Northeast, and Southeast (see Figure 5.3). The long exposure group contains multiple images for each UBVI filter in 5 different fields: Northwest, Northeast, Southeast, North-Northwest, and North-Northeast. The short exposure set required no further processing and its field centers and exposure times are summarized in Table 5.3.

For the long exposure set it was necessary to register and coadd the individual filter images for each field prior to extracting the stellar photometry. For each field in the long exposure set a reference image was selected, usually the first U band exposure in the image series. On the reference image for each field I selected 30-50 moderately exposed isolated stars uniformly distributed as positional reference points. Using the APPHOT task CENTER in its interactive mode I then computed the x and y centroid for each of these stars. For each field I gave a list of these centers, a list of images, and a list of approximate x-y shifts for the other images in the field relative to the reference image to the IRAF task IMALIGN. With the estimated shifts as a first guess, IMALIGN computes the centroids and shifts for each star and each image in the list relative to the reference image. The final x-y shift for each image is determined from the mean of the individual shifts, weighted by their centering errors. Using a linear interpolation scheme for fractional pixel shifts, IMALIGN shifts each image accordingly. Finally, the image area around the border not common to all images was trimmed away, leaving a set of registered images of the same size for each field.

Table 5.3: Summary of the field centers, integration times, and area for the 3 short exposure image sets.

Field ID	RA (2000.0)	DEC (2000.0)	Filter	Total Exp. Time (s)	Area (Sq. Deg)
Praesepe NW	$8^h38^m12^m$	$19^\circ59'16''$	U	30	0.587
	"	"	B	5	"
	"	"	V	2	"
	"	"	I	1	"
Praesepe SE	$8^h40^m40^s$	$19^\circ19'24''$	U	30	0.587
	"	"	B	5	"
	"	"	V	3	"
	"	"	I	1	"
Praesepe NE	$8^h40^m43^s$	$20^\circ00'52''$	U	30	0.587
	"	"	B	5	"
	"	"	V	2	"
	"	"	I	1	"

I obtained the working image set for the survey by median combining the trimmed and registered images from the long exposure set on a filter-by-filter basis. I chose the median over the average because, even though the average has better statistics with a small number of images, it does not prove effective in the presence of cosmic ray hits or other spurious events. Because the individual images in the long exposure set were already close to the desired depth, using the median to combine the images did not significantly affect the final quality of the photometry.

The field centers, effective integration times, and net area covered for each long exposure field are summarized in Table 5.4. A map of this field is shown in Figure 5.3, where the total area encompassed by the heavy line is roughly 2.1 square degrees. The individual fields are indicated with lighter border lines, inset with their identifications. The amount of overlap in the short exposure set is nearly 10%, where the long exposure overlap is 25% by area.

It is now time to do some photometry. Extracting stellar photometry from the survey images listed in the previous two tables follows three basics steps: 1) Identify and locate all sources in each field and classify them as either stellar or non-stellar; 2) For all sources marked stellar extract their instrumental magnitudes using 2-dimensional point-spread-function (PSF) fitting; and 3) Transform the instrumental magnitudes onto the standard system from the calibration photometry discussed earlier.

The exact treatment of the short and long exposure image set differs only in the first step. For the short exposure set where galaxy contamination is slight, the source finding routine DAOFIND within DAOPHOT provides us with an adequate tool for this task. However, in the long exposure images where the number of galaxies excedes the number of stars, DAOFIND fails. In these images

Table 5.4: Summary of field centers, total integration times, and area for the 5 long exposure image sets.

Field ID	RA (2000.0)	DEC (2000.0)	Filter	Total Exp. Time (s)	Area (Sq. Deg)
Praesepe NW	$8^h38^m12^m$	$19^{\circ}59'16''$	U	5400	0.546
	"	"	B	1800	"
	"	"	V	1080	"
	"	"	I	720	"
Praesepe NNW	$8^h39^m27^s$	$20^{\circ}19'26''$	U	5400	0.564
	"	"	B	1800	"
	"	"	V	1080	"
	"	"	I	480	"
Praesepe SE	$8^h40^m40^s$	$19^{\circ}19'24''$	U	5400	0.567
	"	"	B	1800	"
	"	"	V	1080	"
	"	"	I	720	"
Praesepe NE	$8^h40^m43^s$	$20^{\circ}00'52''$	U	5400	0.533
	"	"	B	1800	"
	"	"	V	1080	"
	"	"	I	720	"
Praesepe NNE	$8^h41^m32^s$	$20^{\circ}22'39''$	U	5400	0.567
	"	"	B	1800	"
	"	"	V	1080	"
	"	"	I	720	"

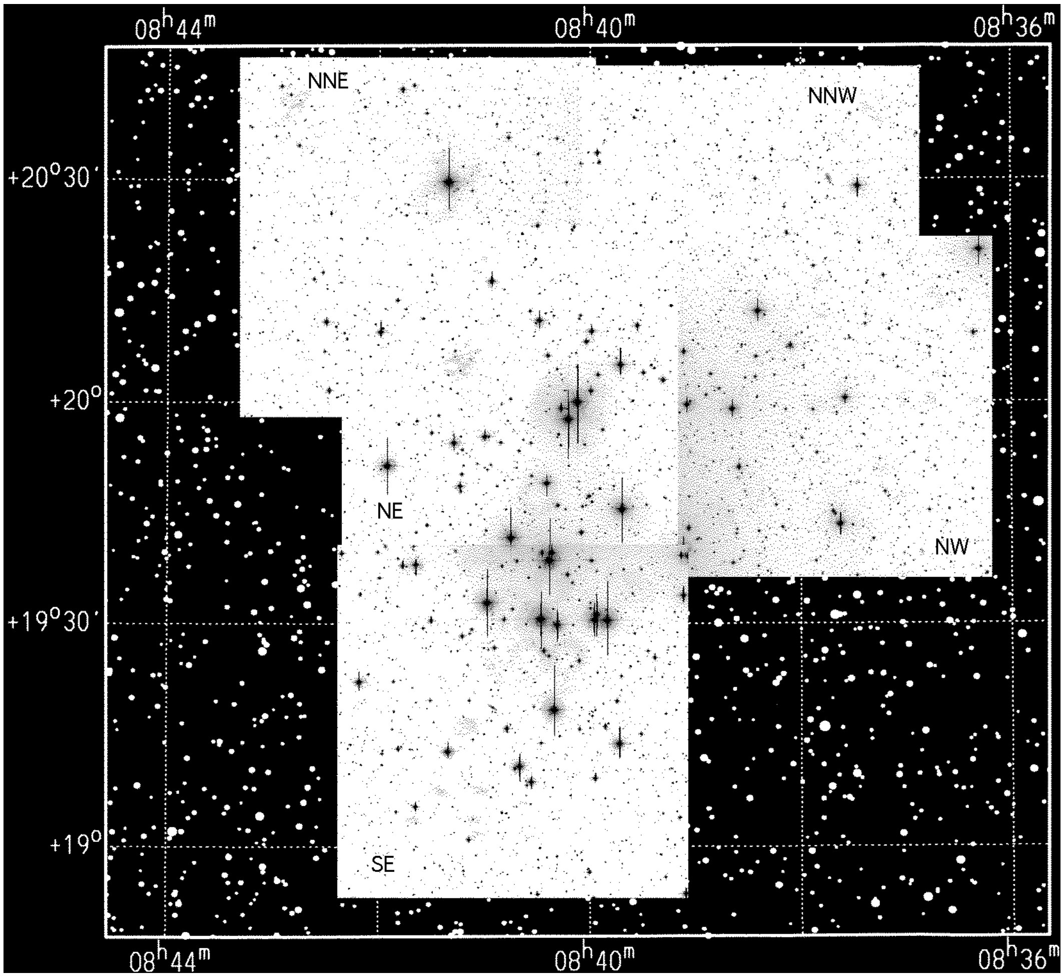
08h44m
08h40m
08h36m
+20°30'
+20°
+19°30'
+19°
NNE
NNW
NE
NW
SE
08h44m
08h40m
08h36m

Figure 5.3: The sky map (white on black) of the area surrounding the Praesepe showing the individual field locations (black on white imagery) and the boundary of the survey.

I have resorted to the more sophisticated source identification scheme called FOCAS, originally developed for identifying faint galaxies on digitized photographic plates.

For each field in the long exposure data set I created a composite image for input to FOCAS. The composite image is determined by throwing out the low pixel between the 4 filters and averaging the remaining three. The low pixel rejection prevents objects of extreme color from getting lost in the composite image, while the averaging makes the faint limit of the composite image deeper than any one of the single filter images. By performing the star-galaxy separation on the deeper composite image I ensure good separation below the limits of the individual images. Once FOCAS is run on an image, one is left with a catalog of sources and a myriad of statistics used in the classification process. From the catalog of each field I discarded the galaxies and generated a list of sources classified as stars, together with their centroided positions.

Next, I selected approximately 50 stars from each short exposure field and 100-150 stars in each long exposure field to define the average PSF in each image. If necessary I performed several iterations creating the average PSF in order to clean the region around the selected PSF reference stars of faint, undesired background stars. I used the initial list of stars generated by DAOFIND or FOCAS for each image to fit with the image's average PSF. After subtracting the fitted PSFs from the original image any, remaining stars are visually identified and added to the original list of stars. Starting with the U image I repeated the fit-inspect-update procedure for the B, V, and I images for each field, updating the field's star list as I went. Finally, I extracted the instrumental magnitudes by simultaneously fitting the final star list to each image's PSF, keeping only those stars successfuly measured in all 4 filters.

Using the Praesepe calibration stars in common with each field (approximately 30 stars per field), I then transformed the instrumental magnitudes for the program fields onto the standard system. Because the calibration stars are contained in the program fields, I needed only to determine the zero point between the instrumental and standard magnitudes in conjunction with the known filter color terms. I used equations 5.6 – 5.9,

$$U_{inst} = U_{std} + 0.000543(U - B) \tag{5.6}$$

$$B_{inst} = B_{std} - 0.0645(B - V) \tag{5.7}$$

$$V_{inst} = V_{std} - 0.000474(B - V) \tag{5.8}$$

$$I_{inst} = I_{std} - 0.0184(V - I) \tag{5.9}$$

to fit the filter zero points for each field, where the instrumental magnitudes are defined as they were for the standard star photometry. The cumulative photometry of more than 13,000 stars from both the long and short exposure fields is shown in the color-magnitude diagrams in Figures 5.4, 5.5, and 5.6.

There are several obvious features these three color-magnitude diagrams (CMD) have in common. One of the first things to note is the fact that the Praesepe's main sequence (arrowed) is clearly visible as a well–defined locus of stars, stretching diagonally and upward from the lower right toward the upper left portion of the CMDs. The effects of line blanketing in the U-B and B-V CMDs can be seen as an abrupt downward turn in the main-sequence locus near

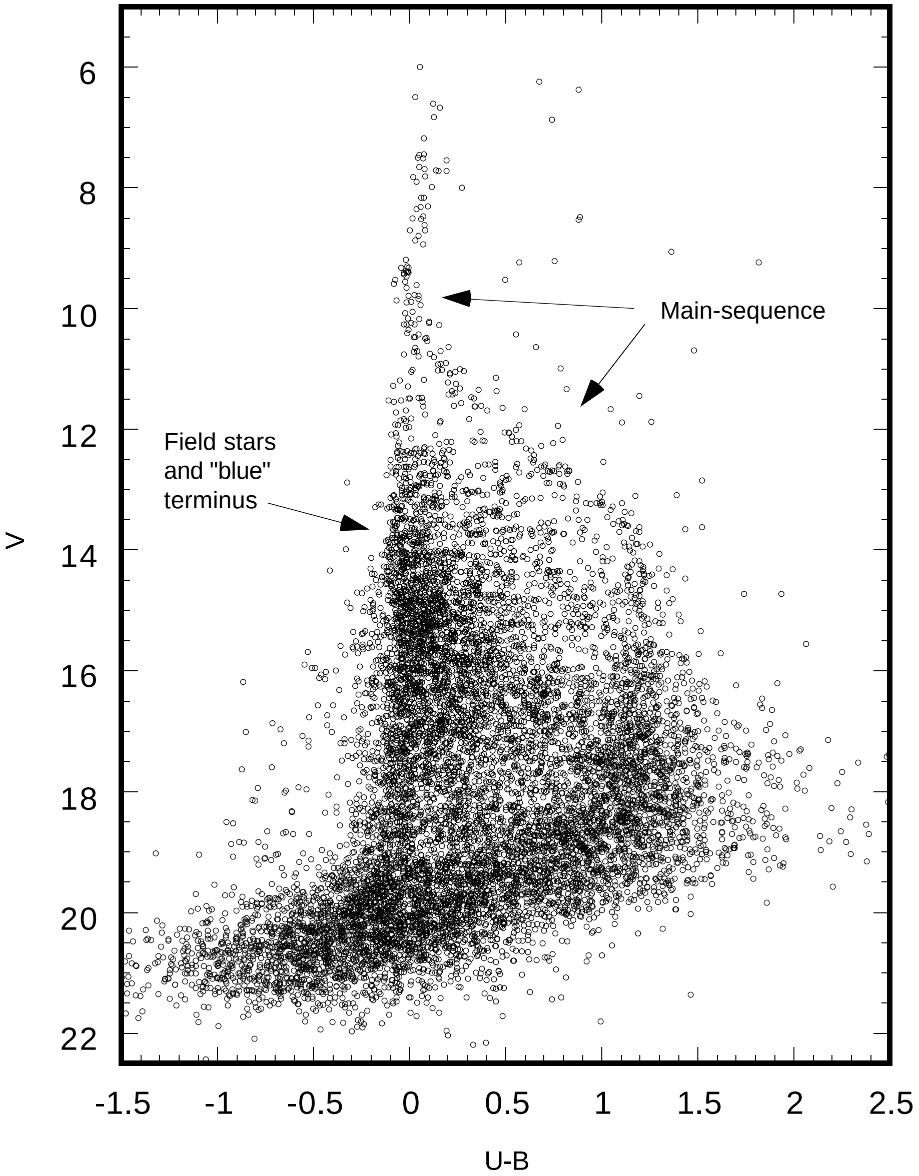

Figure 5.4: V vs U-B color-magnitude diagram for all stars measured in the survey of the Praesepe.

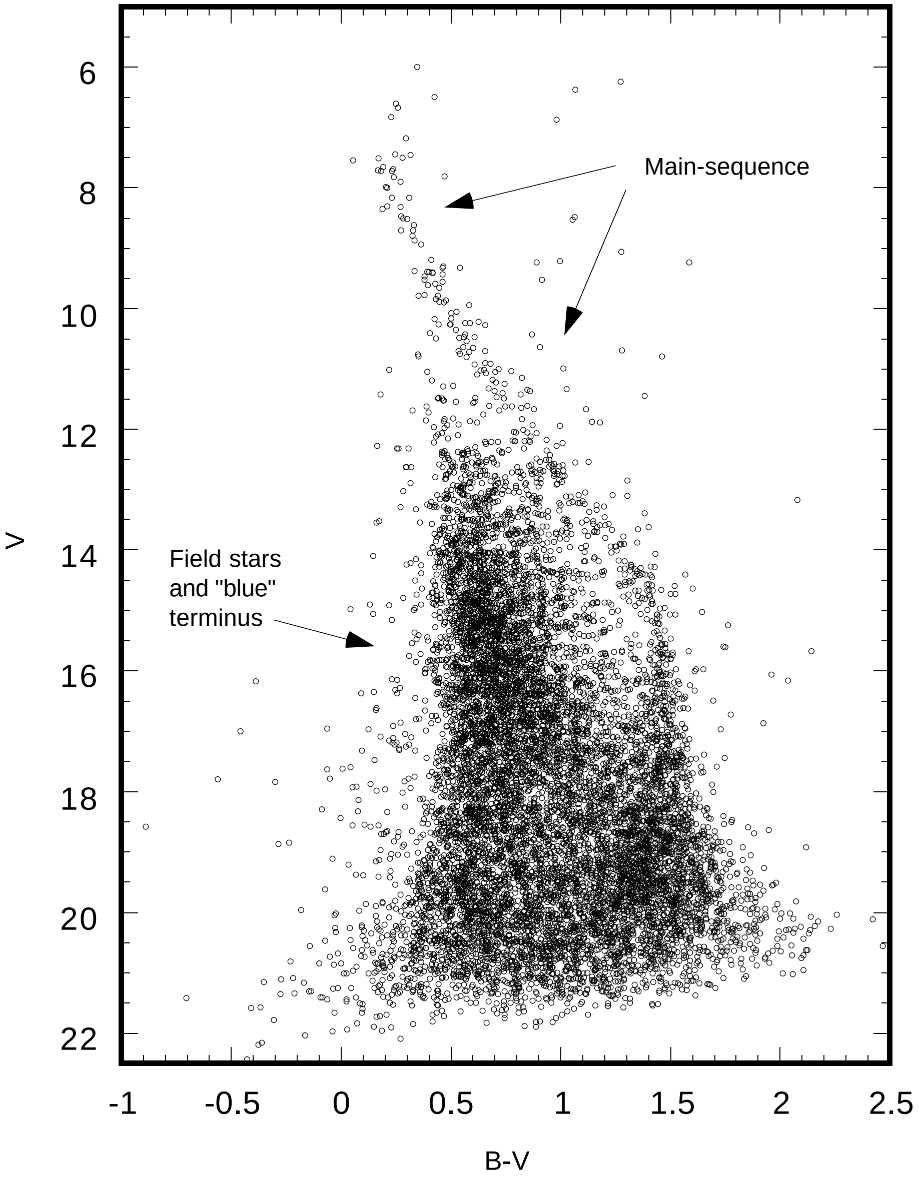

Figure 5.5: V vs B-V color-magnitude diagram for all stars measured in the survey of the Praesepe.

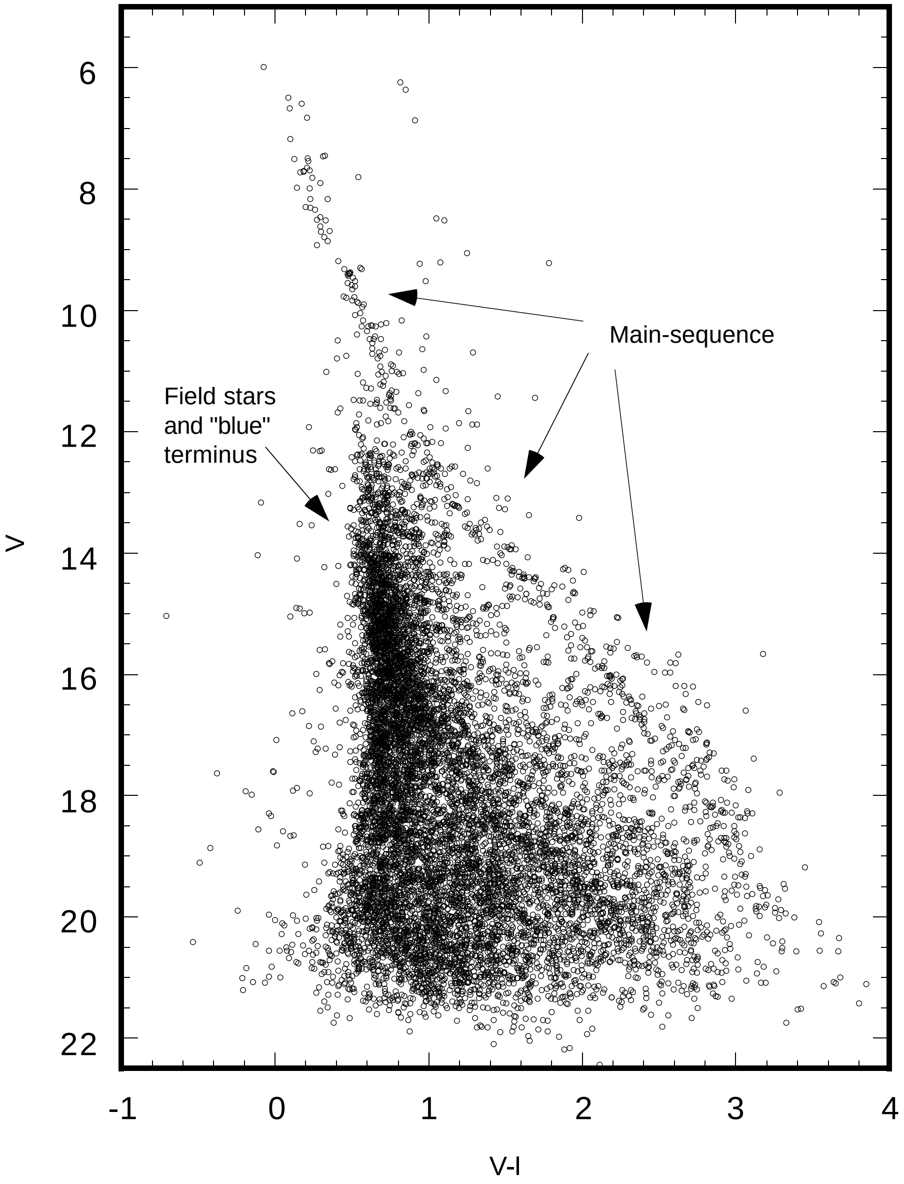

Figure 5.6: V vs V-I color-magnitude diagram for all stars measured in the survey of the Praesepe.

$U - B \approx 1.2$ and $B - V \approx 1.5$ respectively. Line blanketing does not effect the V-I color until extremely late spectral types. Consequently, we can see a well defined main-sequence almost to the limits of the photometry, where there may be the beginnings of a turndown near $V - I \sim 3$. Also evident, but less populated, is the sequence of binary stars located roughly 0.75 magnitudes above the main sequence in both the B-V and V-I CMDs.

We also see, immediately below the Praesepe's main-sequence, the very large number of foreground and background stars from the Galaxy. In each of the CMDs the Galaxy's field stars exhibit a "blue" terminus, indicated by the sharp decrease in the number of stars blueward of $U - B \sim -0.10$, $B - V \sim 0.45$, and $V - I \sim 0.55$. These colors are all consistent with a main-sequence turnoff color for the Galaxy's disk at an age of $\sim 10 - 12 Gyr$. There is also an increased number of stars on the blue side of this terminus at fainter magnitudes, and *among these are the white dwarf stars I am after*.

In addition, there are some features which are instrumental in nature, reflecting the limitations in the photometry. The most prominant of these are a large number of "blue" stars below $V \sim 19.5$ in the U-B CMD, which is caused by the growing scatter in the U photometry beyond this limit. The limiting U magnitude also accounts for the diagonal lower boundary of the photometry in the U-B CMD. The implied limit in U magnitude for useful photometry in this data is $U \approx 19.6$.

5.2.4 An Aside: Galactic Structure in the Direction of the Praesepe

In the V-I CMD there appears to be an enhancement in the number of field stars approximately four magnitudes below and roughly parallel to the Praesepe's main-sequence. Using the Praesepe's distance as reference, this "feature" is about 1100 parsecs away. This leads to the question: What (in the direction of the Praesepe) would be at this distance? The Galactic position of the Praesepe is $l = 206.00^{\circ}$ and $b = 33.17^{\circ}$, placing this feature at a distance of 920 parsecs away along the Galactic plane and 600 parsecs above it. This is entirely consistant with the outer edge of the Galactic disk with a scale height of 250 parsecs.

We can understand this feature in a qualitative sense if we consider how a fixed area, multi-color survey might sample a two component exponential distribution of stars, *i.e.* the Galactic Disk and Halo or Thick Disk. For this exercise I used the simple model developed by Kujiken and Gilmore (1989), where the density of stars is given by

$$\frac{v_0(z)}{v_0(0)} = 0.959e^{-z/249\,pc} + 0.041e^{-z/1000\,pc}, \tag{5.10}$$

where z is the height above the Galactic plane and v_0 is the number density of stars. The two distributions have characteristic scale heights of 249 and 1000 parsecs each. The volume element sampled by a survey between two distances, d_i and d_j, covering an area on the sky of A square degrees is expressed by

$$V_{ij} = 4/3\,\pi(d_j^3 - d_i^3)\frac{A}{41253}. \tag{5.11}$$

If I assume the density distribution given in equation 5.10 is the same for all spectral types I can compute the predicted number of stars in an area, having a solid angle Ω, as a function of distance modulus for a specific spectral type. The result of this calculation is shown in Figure 5.7 at three different scale heights – 200, 249, 300 parsecs, for the first component in equation 5.10. Where on the vertical axis *n* is defined by the normalized product of equations 5.10 and 5.11 divided by Ω, and the the horizontal axis is the average distance modulus between d_i and d_j. The number of stars seen in Figure 5.6 at a fixed V-I, which loosely translates into spectral type, has a similar trend as do the models shown in Figure 5.7. From this simple analytical model I confidently conclude that the feature in the V-I CMD is caused by the fact that we are "looking through" the disk

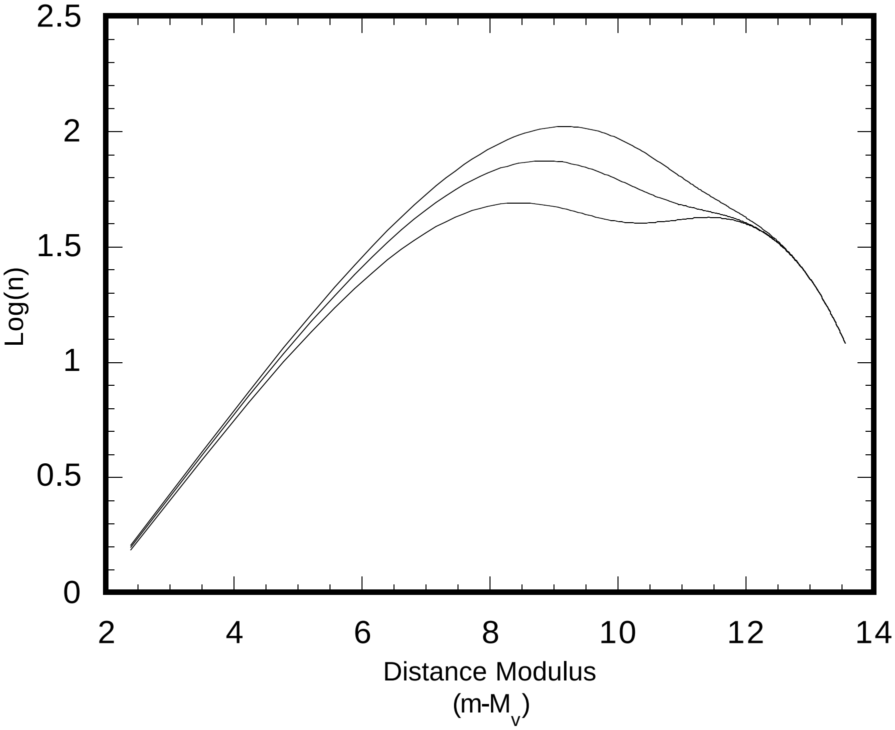

Figure 5.7: Normalized predicted star counts versus distance modulus for a two component exponential density distribution (see text).

component of our Galaxy. To my knowledge this has never been seen before. Furthermore, the difference in slope between the feature and Praesepe's main sequence is caused by a systematic change in scale height of the Galactic Disk as a function of spectral type as measured by V-I. The flatter slope of the feature suggests that low mass, redder stars tend to be more concentrated toward the Galactic plane.

The "edge of the disk" seen in the V-I CMD leads one to notice that the "blue terminus" is not straight, but has significant curvature. The location of the blue inflection point near V=14.5 appears to coincide with the extension of the feature just described. I speculate that the reason for this is that we are seeing a very blurred turnoff point for the Disk. On the one hand, the stars brighter than $V \sim 14.5$ are systematically more evolved than the turnoff, hence the terminus is redder than at $V \sim 14.5$. On the other hand, the stars fainter than $V \sim 14.5$ have lower masses than those near $V \sim 14.5$, leading again to the redder color of the terminus. However, the further we look below $V \sim 14.5$ the more the metal poor Halo population dominates the star counts, hence the move of the terminus towards the blue below $V = 18$.

It is clear from this simple exercise that, with careful modeling of the data, one can quantify what I have demonstrated qualitatively. It is also evident that high precision CCD photometry of the kind presented here can be used for detailed structure analysis of the Galaxy, beyond what has already been done with photographic data. A project designed specifically to use wide field CCD imagery with the PFC for a study of star counts to model Galactic structure would prove most interesting.

5.3 ANALYSIS OF THE PRAESEPE PHOTOMETRY

5.3.1 The Praesepe's Main-Sequence Age and Distance

The first step in this calibration of white dwarf and main-sequence ages is to use the data set to estimate the Praesepe's main-sequence age. The V vs B-V and V-I CMDs from the short exposure set are shown in Figure 5.8 and 5.9 respectively. In the B-V CMD the CCD photometry from this survey is overlayed with Johnson's (1952) photoelectric photometry. The excellent agreement in the locus of the Praesepe's main-sequence demonstrates that my CCD photometry has transformed well onto the standard broadband system. In addition, I have included the zero age main sequence (ZAMS) and 0.6, 0.8, and 1.0 Gyr isochrones from VandenBerg (1985) models in each CMD.

In the V-I CMDs the VandenBerg ZAMS is fit well to the observed main sequence locus at a distance for the Praesepe of 174 parsecs, corresponding to a distance modulus of 6.2 magnitudes. Other estimates, from either direct measurement or comparison with the Hyades, of the distance modulus to the Praesepe range from 6.1 to 6.4 magnitudes (Corbally and Garison 1986; Upgren Weis, and de Luca 1979; Crawford and Barnes 1969). The average distance modulus from these works is 6.25 magnitudes. The distance for the Praesepe from the V-I CMD and VandenBerg's isochrones is in good agreement with the other estimates. This is not true for the B-V CMD.

In the B-V CMD the VandenBerg ZAMS is best fit to the observed main sequence locus at a distance of 148 parsecs – a distance modulus of 5.85 (VandenBerg 1990). In the B-V CMD the ZAMS departs systematically

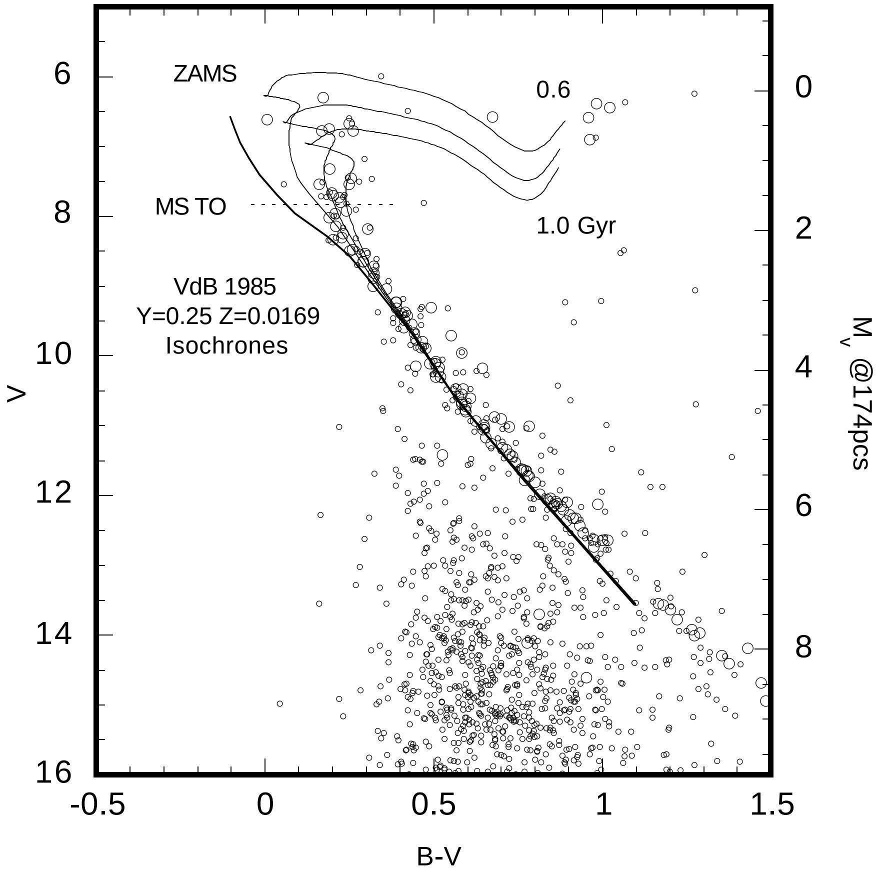

Figure 5.8: The B-V CMD from the short exposure set (small open circles) and Johnson's (1952) photoelectric photometry (large open circles). The locus of the Praesepe main-sequence in both data sets are in excellent agreement – indicating the CCD photometry from this work is on the standard UBVRI system. Superimposed on the data are the ZAMS (thick solid line) and 0.6, 0.8, and 1.0 Gyr isochrones (thin solid lines) from VandenBerg (1985) models. Also shown as a dashed line is the location of the main-sequence turn-off (MS TO) point.

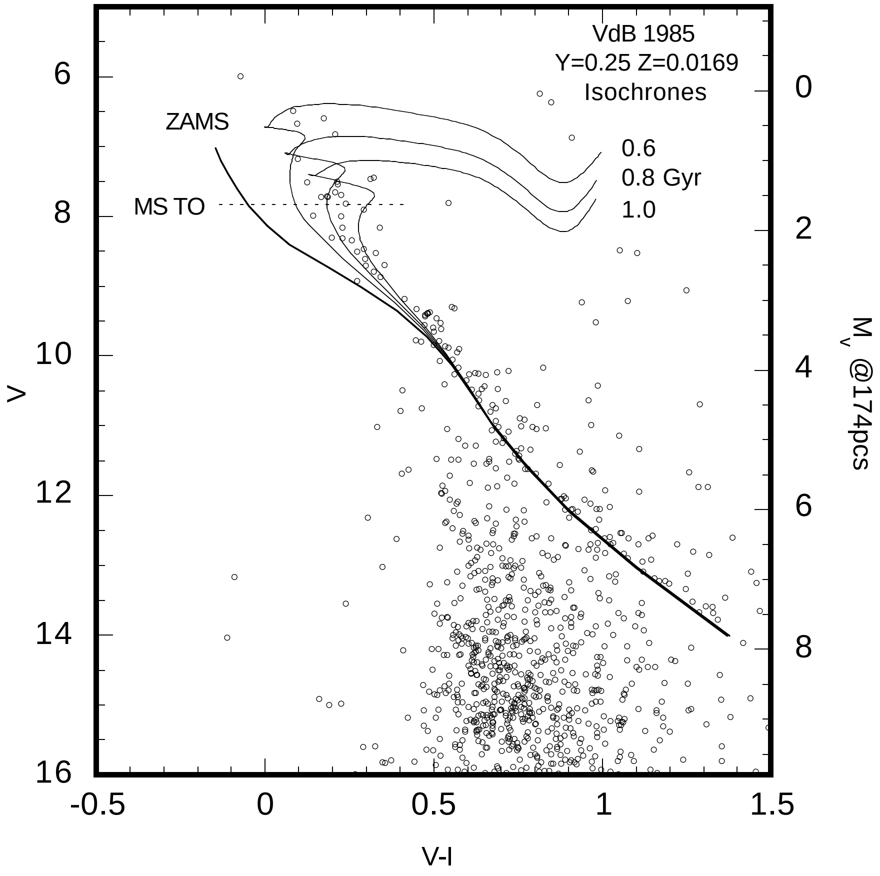

Figure 5.9: The V-I CMD from the short exposure image set (small open circles). As in Figure 5.8 the VandenBerg (1985) 0.6, 0.8, and 1.0 Gyr isochrones (thin solid lines) and ZAMS (thick solid line) are superimposed. The main-sequence turn-off (MS TO) is indicated by the dashed line.

below the Praesepes main sequence for $B-V \geq 0.7$, caused by inaccurate treatment of line blanketing in the model atmospheres used by VandenBerg. Line blanketing generally affects the blue portion of the stellar spectrum, hence the U and B magnitudes and colors. This has led others to sugest that the VandenBerg models are too blue. Since the distance to the Praesepe from the V-I CMD agrees well with other results, I infer that the discrepancy in the B-V CMD distance is in VandenBerg's B-Vcalibration. With a correction to VandenBerg's B-V colors of 0.1 magnitudes I get a good fit of the model ZAMS to the observed main sequence at a distance modulus of 6.2 magnitudes (Figure 5.8). This is the distance I will use later when isolating white dwarf candidates.

The age of the Praesepe from the B-V and V-I CMD can be found by comparing the location of main sequence stars within 2-3 magnitudes of the main sequence turn-off (MS TO) to the model isochrones. I determined the turn-off point, marked by a dashed line in figures 5.8 and 5.9, by interpolating Table 2 in Meynet *et al.* (1993) for a cluster age of $0.9 Gyr$. In the B-V CMD the stars near and above the MS TO indicate an age $> 0.8 Gyr$, while those below the MS TO indicate an age consistent with $0.6 Gyr$. However, in the V-I CMD the stars below the MS TO are more consistent with $0.8-1.0 Gyr$, and those above suggest an age $< 0.8 Gyr$.

We can see from the location of stars near the MS TO that it is difficult to assign a precise age to the Praesepe from matching model isochrones. This is true for most open clusters simply because they are too young to have a well defined turn-off. However, by taking the average positions of the stars around the MS TO I can get a reasonable age estimate for the Praesepe. From my photometry I estimate the Praesepe's main-sequence age to be $0.85 \pm 0.10 Gyr$, a value which I will use to compare against the white dwarf age later.

5.3.2 White Dwarf Candidate Selection from Photometry

In Chapter 4 I discussed at length the techniques available to identify white dwarf stars photometrically. In a star cluster we have an additional piece of information – distance. The distance determines where in the CMD the white dwarf track is located relative to apparent brightness. If it were not for contaminating objects like quasars and unresolved distant blue galaxies it would be possible to select cluster white dwarfs based solely on their position in the CMD. In this section I describe the steps I have taken to prune down the 13,000 stars measured to a few good white dwarf candidates.

In Figure 5.10 I show the V-I CMD along with the VandenBerg (1985) main-sequence isochrones and a mean white dwarf track. I computed the mean white dwarf track using the field white dwarfs identified in Monet *et al.* (1992) from trigonometric parallax measurements. In each 0.5 magnitude bin in M_v I calculated the average V-I color for the identified white dwarfs, producing a mean white dwarf track for the field. Shown in Figure 5.10 is this track translated by 6.2 magnitudes to the distance of the Praesepe. Already we can see by the location of the white dwarf track that we can eliminate most of the stars in Praesepe fields because they are either too bright or too red. We are also encouraged to see a handful of stars clustered around the white dwarf track. The problem is in where the white dwarf track meets the blue terminus of the Galaxy's field stars. From the CMD there is no way of telling a white dwarf from a field

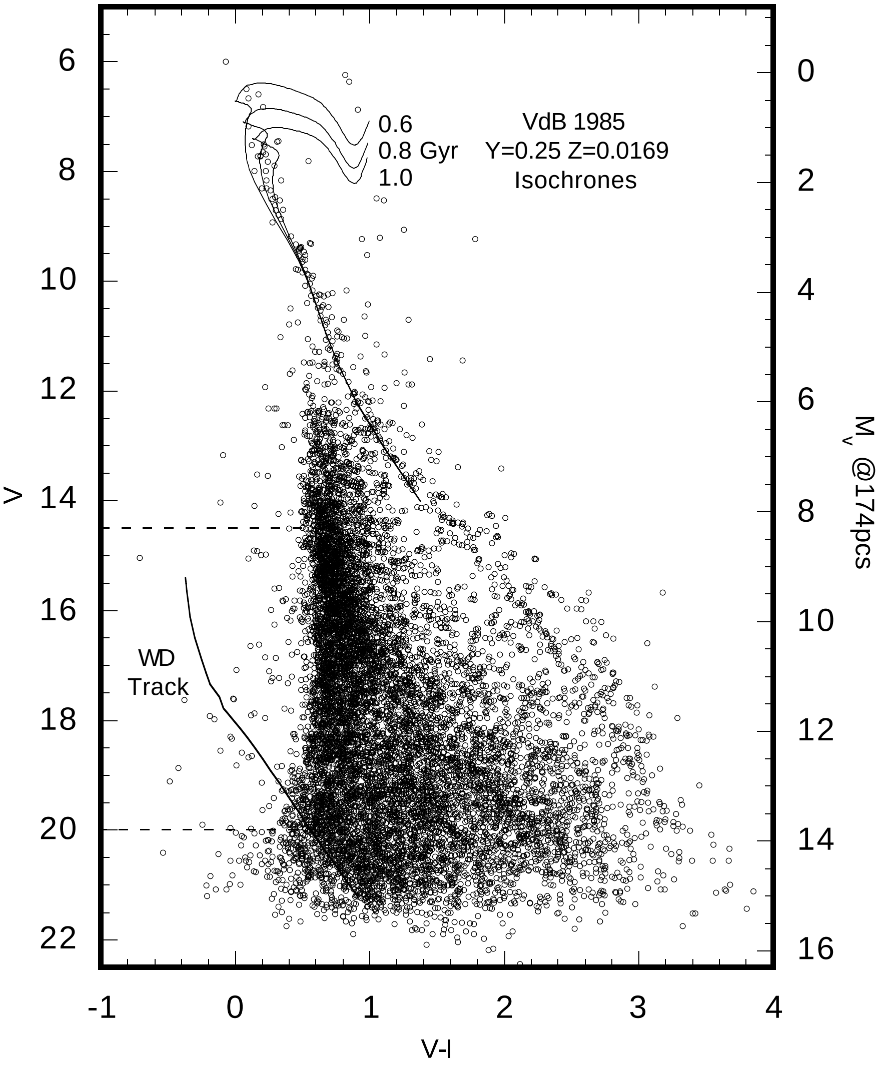

Figure 5.10: The grand V-I CMD of the Praesepe fields as in Figure 5.6 with VandenBerg's isochrones and the mean white dwarf evolutionary track from Monet *et al.* (1992 – thick solid line). The dashed lines represent the area of the first round of pruning described in the text.

star redward of $V - I \sim 0.4$. It is essential for the *white dwarf age* estimate to be able to say with certainty that there are or are not white dwarfs in this part of the CMD.

For the first round of pruning I have selected all stars with $14.5 \geq V \geq 20$ and $V - I \leq 0.6$ (shown as the dashed lines in Figure 5.10), essentially boxing in the white dwarf evolutionary track. At the Praesepe's distance, the lower limit, $V = 20$, corresponds roughly to a white dwarf having an age of $2.0 Gyr$ – more than twice the Praesepe's main-sequence age. The requirement that all selected stars must be bluer than $V - I = 0.6$ is set by the location of the Monet *et al.* white dwarf track. At $V = 20$ the $V - I$ color of the Monet *et al.* track is approximately 0.6. I conducted a similar pruning in the B-V and U-B CMD, using the same V limits and B-V and U-B limits chosen to have the same white dwarf temperature as $V - I = 0.6$; $B - V = 0.5$, and $U - B = -0.2$ respectively. My purpose for this first pruning is to reduce substantially the number of objects in the working list of candidates, hence easing the confusion in further tests.

I have compiled a subset of *UBVI* photometry for those objects which passed all three first round pruning criteria simultaneously. With this photometry subset I will proceed using the steps I detailed in Chapter 4 for identifying hotter white dwarfs with *UBVI* colors. The objects selected by the first criterion for hot white dwarfs, $U - V \leq 0$ and $B - V \leq -0.3$, are shown in Figure 5.11a,b. I have also included my model colors for DA white dwarfs and a black body distribution calculated in Chapter 4. It is clear from the classical two color diagram (bottom panel) that there are a substantial number of objects with *UBV* colors consistent with identification as white dwarfs.

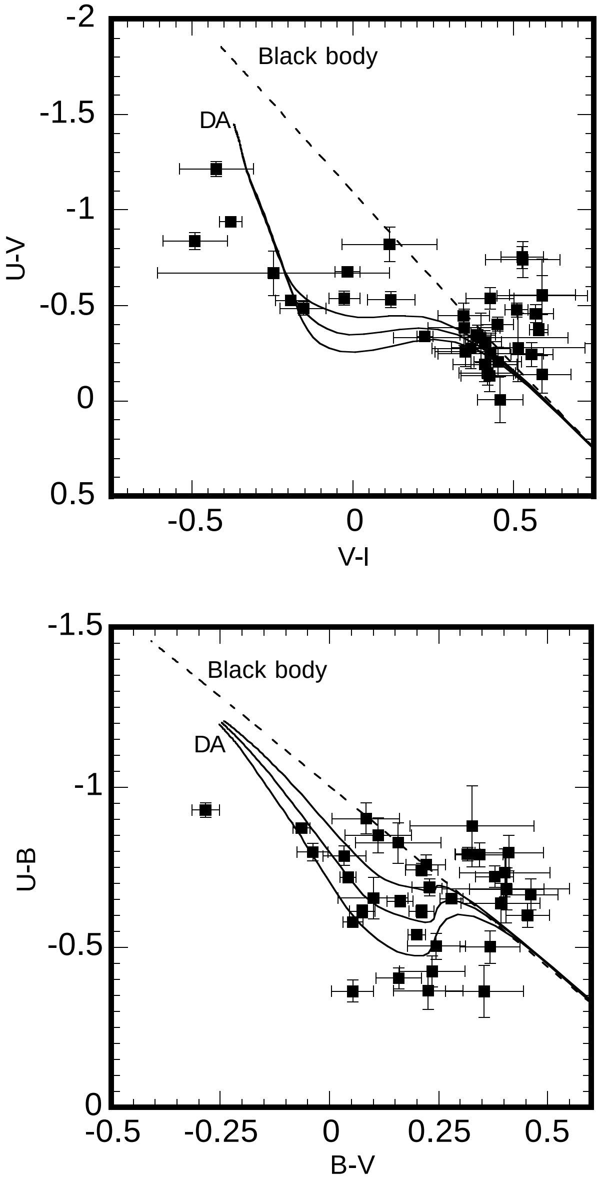

Figure 5.11a,b: The *UBVI* two color diagrams for the objects passing the first criterion of hot white dwarf selection: $U - V \leq 0$ and $B - V \leq -0.3$.

Following step two for the hot white dwarfs in Chapter 4, we turn our attention to the two color diagram of *UVI* shown in the top panel of Figure 5.11. At this point I have insisted that an object have at least its error bars touching either the model DA colors or the black body sequence to still be considered a candidate. This primarily eliminates those objects which lie redward of the blackbody sequence as well as two objects to the blue of the DA sequence, which I take to be main sequence stars. We can see that there are a number of candidates which appear to be of spectral type DA and one that is nonDA above ~10,000K. Below this temperature it is not possible to assertain spectral type within the errors of this broad band photometry. There is also evidence for a division in the photometry located near $V-I \approx 0.2$, $U-V \approx -0.5$. This may be indicative of the finite age of the Praesepe, but at this stage it is too early to tell.

I have plotted the remaining objects in the V versus $V-I$ color–magnitude diagram shown in Figure 5.12 along with the DA cooling sequences for $\log(g) = 7.5, 8.0$, and 8.5. The division in photometry that was suggested in the *UVI* two-color diagram is not evident here. Although it is possible to further reduce the candidate list by eliminating objects that lie below the white dwarf cooling tracks shown in Figure 5.12, there appears to be no obvious cut-off from which I can estimate an age. I have not excluded objects lying above the model cooling sequences because it is possible that they are white dwarfs of nonDA spectral types, or companions to low mass main sequence stars.

However, from photometry alone we have reduced the more than 13,000 objects observed to only 24 photometric white dwarf candidates. The photometry of these remaining objects are listed in Table 5.5. I am left with two choices now;

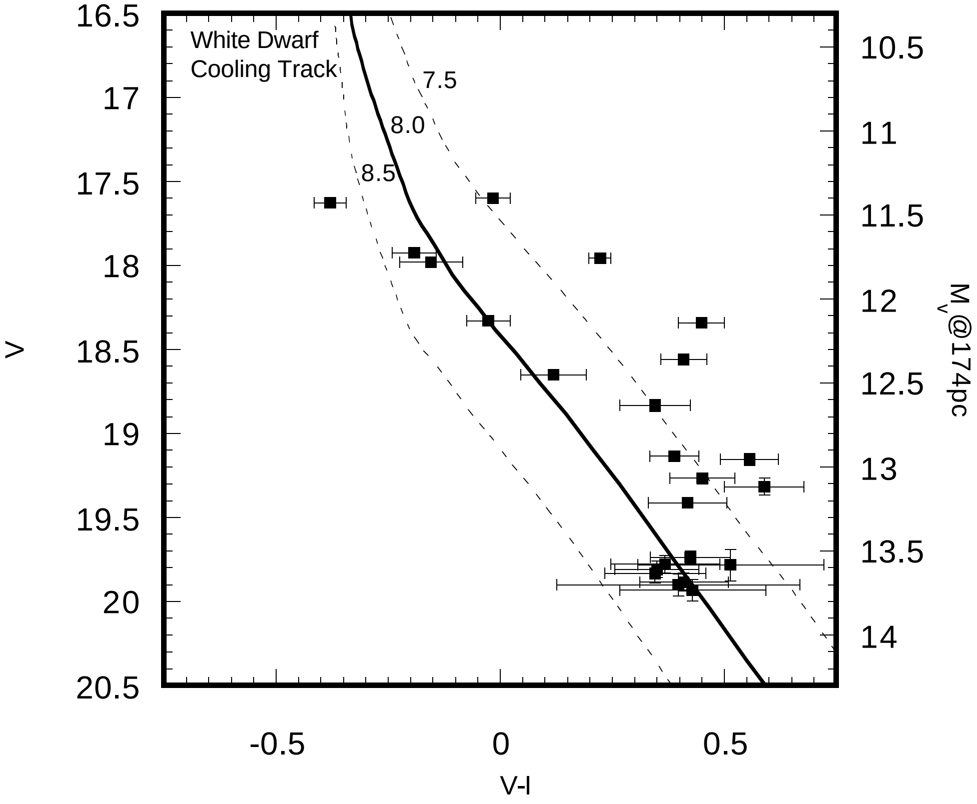

Figure 5.12: The V-I CMD for Praesepe white dwarf candidates satisfying both $U - V \leq 0$ and $B - V \leq -0.3$ color excess and *UVI* colors consistent with those of white dwarfs.

either spend more telescope time to investigate each of these candidates further (*i.e.* spectroscopy), or try to devise more group tests to determine which of the candidates are white dwarfs belonging to the Praesepe.

Table 5.5: Photometrically selected white dwarf candidates from the Praesepe survey.

Object ID	RA 2000 h:mm:ss.s	Dec. 2000 dd:mm:ss.s	V (err)	B-V (err)	U-B (err)	V-I (err)	U-V (err)
NE-908	8:40:28.1	19:43:34.4	17.60	0.04	-0.72	-0.02	-0.68
			(0.01)	(0.02)	(0.02)	(0.04)	(0.02)
SE-1712	8:39:36.5	19:30:43.2	17.63	-0.06	-0.87	-0.37	-0.93
			(0.01)	(0.02)	(0.02)	(0.04)	(0.03)
NE-1090	8:39:45.6	20:00:15.6	17.93	0.05	-0.58	-0.19	-0.53
			(0.02)	(0.02)	(0.02)	(0.05)	(0.03)
SE-664	8:41:39.8	19:00:07.5	17.96	0.20	-0.54	0.22	-0.34
			(0.01)	(0.02)	(0.01)	(0.03)	(0.02)
NNW-1145	8:39:45.6	20:00:15.6	17.98	0.16	-0.64	-0.15	-0.48
			(0.02)	(0.03)	(0.02)	(0.07)	(0.04)
NE-1155	8:39:47.2	19:46:11.8	18.33	0.08	-0.61	-0.03	-0.54
			(0.02)	(0.03)	(0.02)	(0.05)	(0.04)
NE-1290	8:39:56.3	20:03:41.3	18.56	0.05	-0.36	0.41	-0.31
			(0.03)	(0.05)	(0.03)	(0.05)	(0.06)
NNE-1371	8:41:13.9	20:30:18.6	18.65	0.21	-0.74	0.12	-0.53
			(0.03)	(0.04)	(0.02)	(0.07)	(0.04)
NNW-13	8:37:11.5	20:40:57.1	18.83	0.34	-0.79	0.35	-0.45
			(0.04)	(0.05)	(0.04)	(0.08)	(0.07)
NW-647	8:37:47.2	19:49:55.7	18.87	-0.28	-0.93	-0.42	-1.21
			(0.02)	(0.03)	(0.02)	(0.12)	(0.04)
SE-898	8:42:16.3	19:33:10.1	19.14	0.38	-0.72	0.39	-0.34
			(0.03)	(0.04)	(0.03)	(0.06)	(0.05)
NW-220	8:37:04.1	19:50:41.9	19.27	0.46	-0.67	0.45	-0.20
			(0.04)	(0.06)	(0.05)	(0.07)	(0.08)
NE-203	8:41:34.0	20:01:23.6	19.32	0.23	-0.37	0.59	-0.14
			(0.05)	(0.08)	(0.06)	(0.09)	(0.10)

Table 5.5 continued: Photometrically selected white dwarf candidates from the Praesepe survey.

Object ID	RA 2000	Dec. 2000	V	B-V	U-B	V-I	U-V
	h:mm:ss.s	dd:mm:ss.s	(err)	(err)	(err)	(err)	(err)
SE-440	8:41:22.9	19:11:16.3	19.41	0.36	-0.36	0.46	-0.01
			(0.03)	(0.09)	(0.08)	(0.07)	(0.12)
NNE-834	8:42:57.8	20:27:26.9	19.41	0.45	-0.60	0.42	-0.15
			(0.03)	(0.05)	(0.04)	(0.09)	(0.06)
SE-362	8:40:19.3	19:14:33.2	19.74	0.37	-0.50	0.42	-0.13
			(0.04)	(0.07)	(0.05)	(0.09)	(0.09)
NNE-733	8:42:26.9	20:33:20.1	19.78	0.41	-0.68	0.37	-0.28
			(0.05)	(0.09)	(0.07)	(0.12)	(0.11)
NNE-1767	8:40:09.1	20:15:48.3	19.78	0.40	-0.68	0.51	-0.28
			(0.09)	(0.15)	(0.11)	(0.21)	(0.18)
SE-31	8:41:11.0	19:38:31.8	19.81	0.25	-0.50	0.35	-0.26
			(0.05)	(0.07)	(0.04)	(0.09)	(0.08)
NNE-699	8:42:51.0	20:35:50.3	19.84	0.41	-0.80	0.35	-0.38
			(0.05)	(0.08)	(0.06)	(0.11)	(0.10)
SE-847	8:40:02.4	19:36:13.2	19.88	0.24	-0.43	0.41	-0.19
			(0.05)	(0.08)	(0.05)	(0.10)	(0.09)
NNW-285	8:38:31.6	20:17:18.0	19.90	0.16	-0.83	-0.25	-0.67
			(0.07)	(0.10)	(0.06)	(0.36)	(0.12)
NNW-58	8:39:04.8	20:34:33.6	19.90	0.40	-0.73	0.40	-0.33
			(0.07)	(0.10)	(0.08)	(0.27)	(0.13)
NNE-76	8:43:00.3	20:35:43.9	19.93	0.39	-0.64	0.43	-0.25
			(0.06)	(0.09)	(0.06)	(0.16)	(0.11)
NNE-1680	8:42:40.4	20:07:14.7	19.97	0.08	-0.90	0.12	-0.82
			(0.06)	(0.08)	(0.05)	(0.15)	(0.09)

5.3.3 Astrometry: Cluster Membership of Photometric Candidates

In §5.1 I stated that the Praesepe was one of the few open clusters in the sky known to exhibit measurable proper motion. During the 40+ years between epochs of the data presented here and the Palomar Observatory Sky Survey (POSS) the Praesepe has moved roughly 1.48 arcseconds in a direction ~250 degrees East of North.

The astrometry group in the Astronomy Department at the University of Texas maintains a PDS automated plate scanner. The PDS plate scanner is used for digitizing photographic plates to enable astrometric and/or photometric measurements. As part of this survey for white dwarfs in the Praesepe I asked Fritz Benedict and his student Randy Whited to digitize a region of the POSS plate containing the Praesepe. I was unaware at the time of my request just how daunting a task this was. As it turns out the area of my CCD survey is much larger than to what either Fritz or Randy were accustomed to dealing with. It was unknown whether or not the PDS scanner was up to the task.

Over the weekend of August 13-14 Randy started the PDS machine scanning a $1.5^\circ \times 1.5^\circ$ area centered on the Praesepe. We were pleasantly surprized when we saw a flawless image the following Monday. Using $25\mu m$ diameter spots on $25\mu m$ centers the area scanned resulted in an image 3500×3500 pixels in size. Several later attempts to scan a $2^\circ \times 2^\circ$ area have resulted in failure of one kind or another in the PDS scanner, proving to us just how "lucky" we were with the first scan. Unfortunately this left me with less than 100% coverage from the digitized POSS plate of the area covered by my survey.

Nonetheless, we now have a digitized image of the Praesepe from December 21/22, 1954 which we can compare against the current epoch CCD images of this survey. We can now separate the white dwarf candidates from field stars based on their proper motions.

Using the HST Guide Star catalog as our reference, we computed a plate solution for each epoch's imagery. The Praesepe field is one of the HST Guide Star Catalog's astrometric reference fields and has been calibrated to high precision. The RMS error for each solution was $\sim 0.2''$. Using these solutions we took our positions from the CCD data and computed their predicted positions on the POSS plate. What is shown in Figure 5.13 is the difference between the predicted X,Y coordinates and the measured coordinates on the digitized POSS plate, where the stars selected from near the main-sequence are plotted as small circles and white dwarf candidates listed in Table 5.5 are plotted as squares with error bars. The stars belonging to the Praesepe's main sequence form a clump near -0.7, 0.1, defining the motion of the cluster. I have plotted a circle having a radius equivalent to the half density width of the main sequence stars centered on their motion. The remaining field stars scatter about 0,0 and form a weak clump near 0.2, 0.1 from solar motion.

Of the 24 photometric white dwarf candidates we see that only four are within the circle and thus moving with the Praesepe, consistent with cluster membership. Two of these, NE-1090 and NNW-1145, are the same star located in the overlaping area between two fields. This leaves me with 3 unique candidates which have both photometric and kinematic characteristics for Praesepe white dwarfs. The positions of these three white dwarf candidates

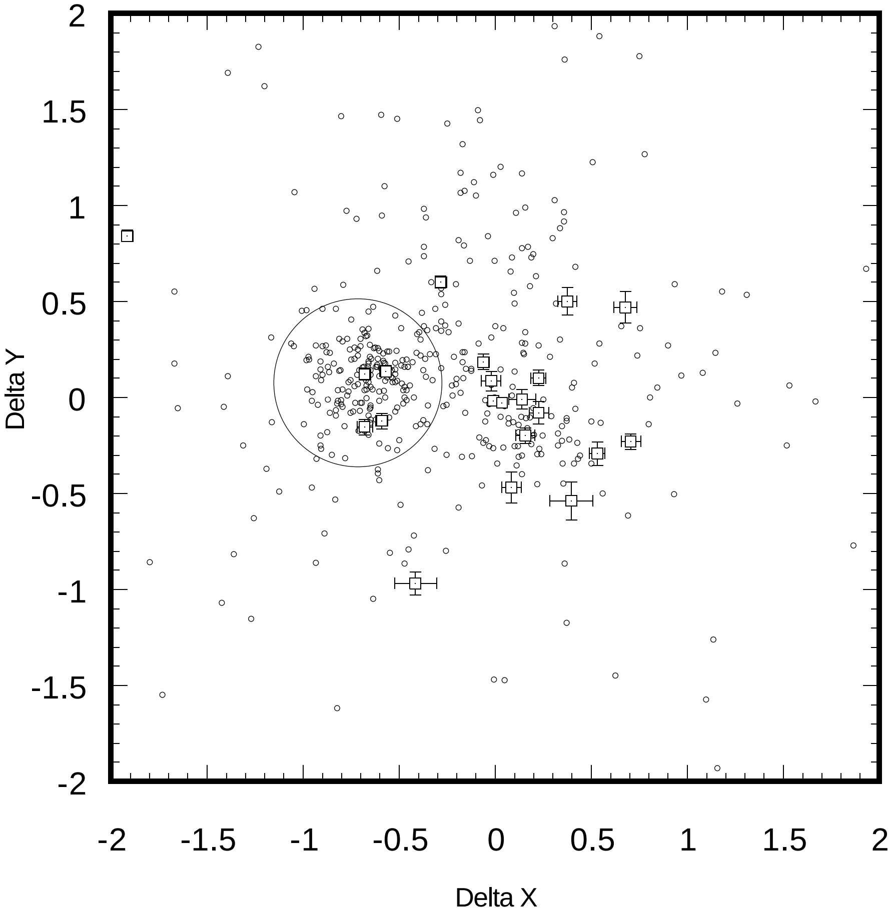

Figure 5.13: The instrumental proper motion vector point diagram for the photometric white dwarf candidates (squares plus error bars) and stars selected near the Praesepe main-sequence (open circles). The concentration of circles near -0.7,0.2 consists primarily of Praesepe main-sequence stars. A circle having a 3-sigma measurement error radius is centered on this concentration.

identify them as the three Eggen – Greenstein stars, EG-59, EG-60, and EG61, mentioned earlier. The candidate SE-1712 is the same star as LB-5893 listed in Anthony-Twarog (1984) as a Praesepe member was not confirmed in this proper motion measurement. I believe this to be caused by the presence of a nearby bright star, fouling the location of its center in either or both the CCD data and the plate scan. Because the proper motion of SE-1712 as measured by Luyten is consistemt with cluster membership I will retain it on my list of final white dwarf candidates in the Praesepe. In addition, upon visual inspection of SE-1712 in the PraesepeSE image and POSS scan it does show the correct proper motion to be a cluster member. Of the 24 photometric candidates two were outside our scanned area on the POSS plate, hence I could not evaluate them for kinematic membership with the cluster. NNW-13 is located very near the Northeast corner of the POSS plate containing the Praesepe and is just off the charts given in Luyten's Search for Faint Blue Stars XXXI and our plate scan of the POSS. The star SE-664, while outside our scan area, is within the search area of Luyten. No positive identification could be made on the basis of comparing my coordinates precessed to epoch 1950 and his listed coordinates. Because I could not explicitly eliminate them, these two stars have been retained on my list of candidates for final analysis.

The significance of this study is that no white dwarfs have been found at lower luminosities which pass both photometric and kinematic tests. All of the lower luminosity photometric candidates fail the proper motion test.

5.4 OTHER PRAESEPE WHITE DWARF CANDIDATES

There are two notable sources in the literature for white dwarf candidates in the Praesepe outside the area covered by this survey. The first is the work already mentioned by Anothony–Twarog (1984). One of the member candidates listed in her Table III, LB-1839, lies outside this survey in what would have been my South West field. The second source of Praesepe white dwarf candidates comes from spectroscopic observations by Wagner *et al*. (1986) of objects selected from the Case (Pesch and Sunduleak 1983; Sanduleak and Pesch 1984) and Kiso (Kondo *et al.* 1982) blue star surveys. They have identified three white dwarfs whose proximity to the Praesepe and cross identifications with Luyten's blue proper motion stars make them probable members.

5.5 CALCULATED ISOCHRONES FOR DA WHITE DWARF STARS

Before using the selected white dwarf candidates to estimate the Praesepe's age, we need to have the white dwarf equivalent of main-sequence isochrones. For my study of the Praesepe's white dwarf age I have calculated white dwarf isochrones with ages of $0.4-1.0Gyr$ in $0.1Gyr$ steps and $1.0-2.0Gyr$ in $0.2Gyr$ steps. In almost every case white dwarfs found in open clusters have spectral type DA - hydrogen dominated atmospheres. I have, therefore, selected the most recent white dwarf evolutionary models from Wood (1994), choosing model white dwarfs having a $10^{-4}M_{\odot}$ surface Hydrogen layer over a $10^{-2}M_{\odot}$ Helium layer, with a pure Carbon core, that span the mass range of $0.4-1.0M_{\odot}$ in steps of $0.1M_{\odot}$. These models are calculated in the theoretical $\log(L/L_{\odot})$ – T_{eff} plane and need to be transformed to the observable M_V – color

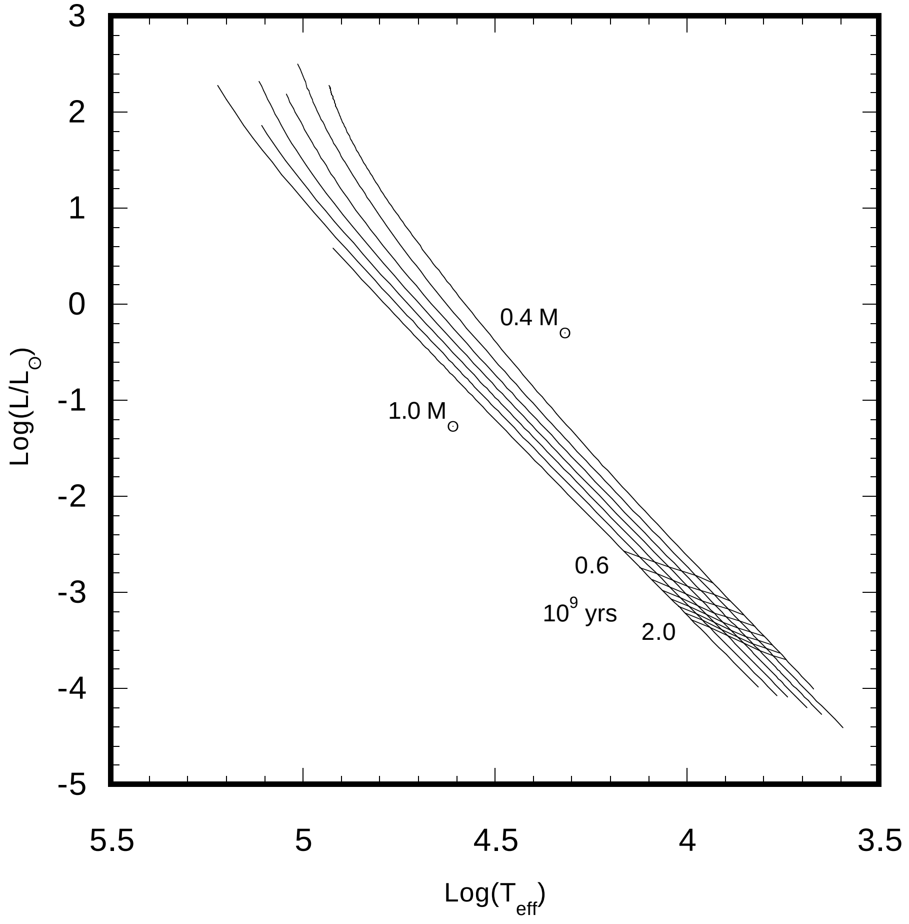

Figure 5.14: Wood's evolutionary models for $0.4-1.0M_{\odot}$ white dwarfs with the interpolated $0.6-2.0Gyr$ isochrones.

(U-B, B-V, V-I, etc.) plane to compare with the observed photometry presented here.

In transforming Wood's theoretical models onto observable planes I have followed three basic steps: First, I have used cubic-spline interpolations of $\log(L/L_{\odot})$ and T_{eff} versus $\log(\tau_{cool})$ to place the white dwarf evolution models onto a unifom time grid – the theoretical white dwarf isochrones. These are shown in Figure 5.14. Second, I computed M_V from $\log(L/L_\odot)$ using the bolometric correction data from Liebert, Dahn, and Monet (1988 – hereafter LDM88). In their paper on the white dwarf luminosity function LDM88 treat in detail the problem of estimating bolometric corrections for white dwarf stars. Using their data, Figure 2a and Tables 4 and 5 in LDM88, I have constructed an analytic relation between Mv and M_{bol} for hydrgen white dwarfs using a 4th order polynomial (Figure 5.15). Calculating M_{bol} from equation 5.12,

$$M_{bol} = -2.5\log\left(L/L_\odot\right) + 4.7, \tag{5.12}$$

I have evaluated this polynomial for M_v for the model isochrones. Third, I used the T_{eff} versus color relations for DA white dwarfs computed in Chapter 4 (Figures 4.3a, 4.3b, and 4.3c) to assign a specific V-I, B-V, or U-B to the model effective temperatures. The calculated DA white dwarf isochrones for M_v versus U-B, M_v versus B-V, and M_v versus V-I are shown in Figures 5.16, 5.17, and 5.18 respectively.

There are several immediate observations we can make. It is clear in Figure 5.16 that the M_v versus U-B isochrones cannot be used as a meaningful age descriminant because they are not single-valued. While not quite true for M_v versus B-V (Figure 5.17), the crowding of the isochrones near B-V=0.2 also make them poorly suited for age estimates. Clearly the best choice for estimating ages are the M_v versus V-I isochrones, shown in Figure 5.18. The behavior of these isochrones can be fully understood by noting the location of the hydrogen Balmer lines relative to the filter bandpasses as discussed in Chapter 4.

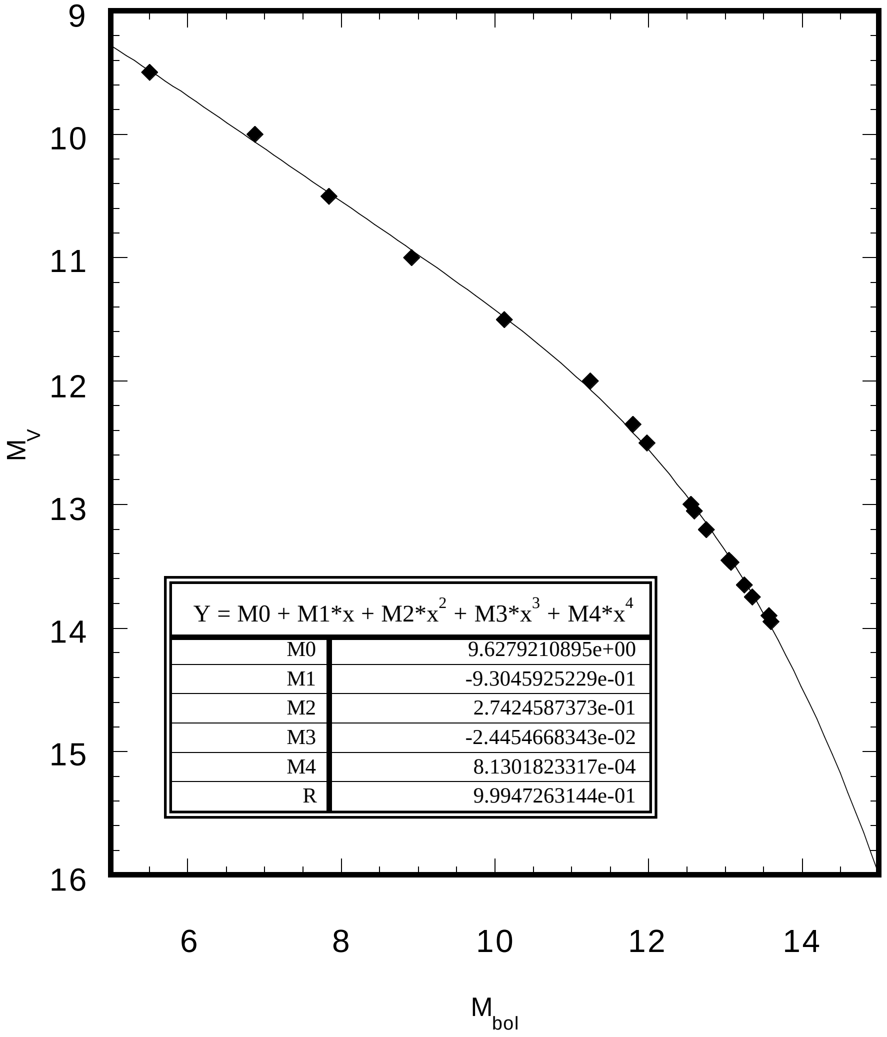

$Y = M0 + M1*x + M2*x^2 + M3*x^3 + M4*x^4$	
M0	9.6279210895e+00
M1	-9.3045925229e-01
M2	2.7424587373e-01
M3	-2.4454668343e-02
M4	8.1301823317e-04
R	9.9947263144e-01

Figure 5.15: The M_v versus M_{bol} data from Liebert, Dahn, and Monet (1988 - filled diamonds) fitted with a 4th order polynomial (solid line). The coefficients for the fit are given in the inset box.

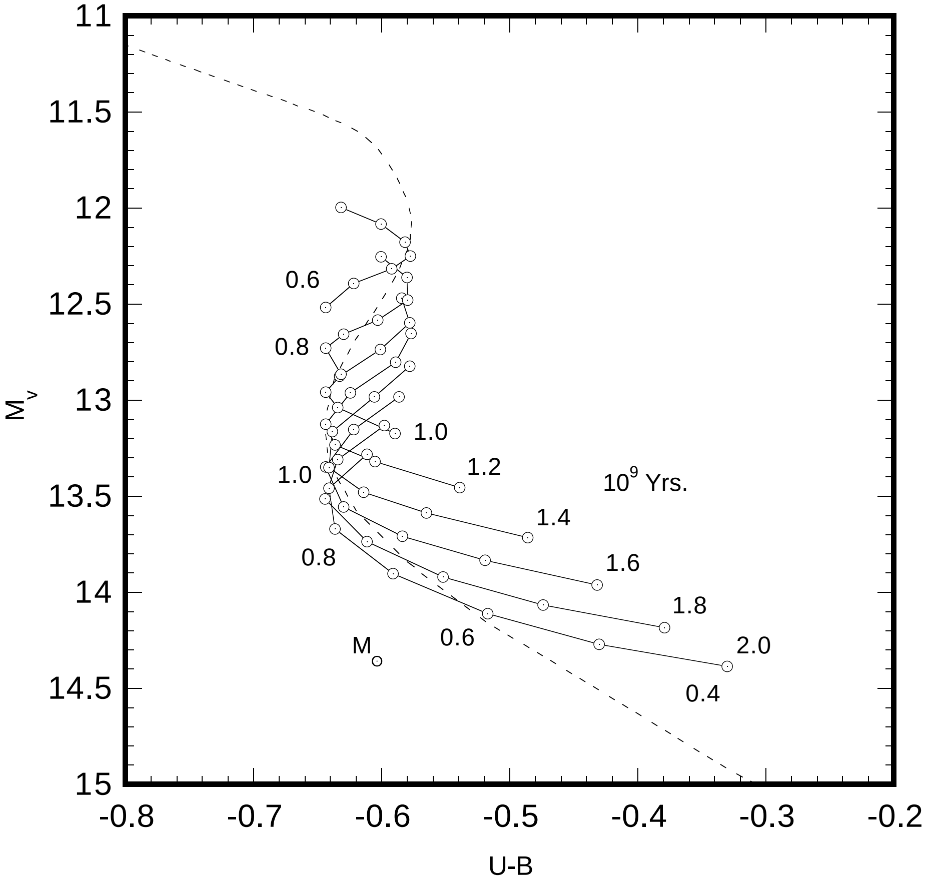

Figure 5.16: Calculated white dwarf isochrones in the M_v versus U-B color-magnitude plane.

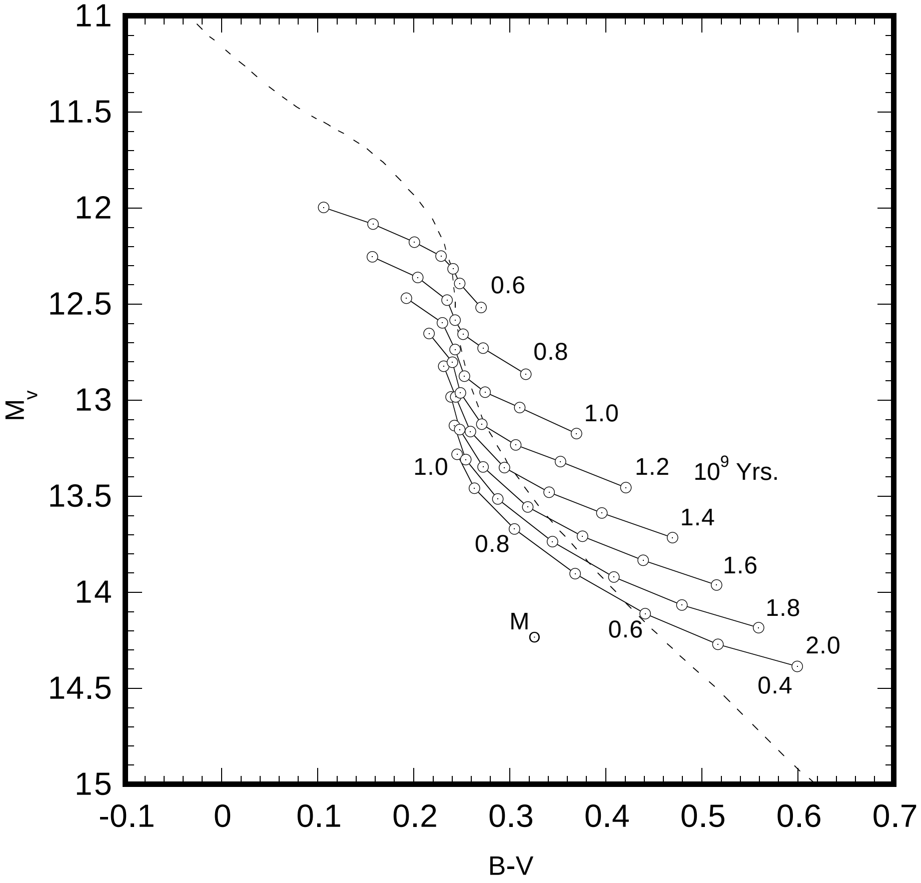

Figure 5.17: The same calculated WD isochrones as in Figure 5.16 transformed to the M_v versus B-V color-magnitude plane.

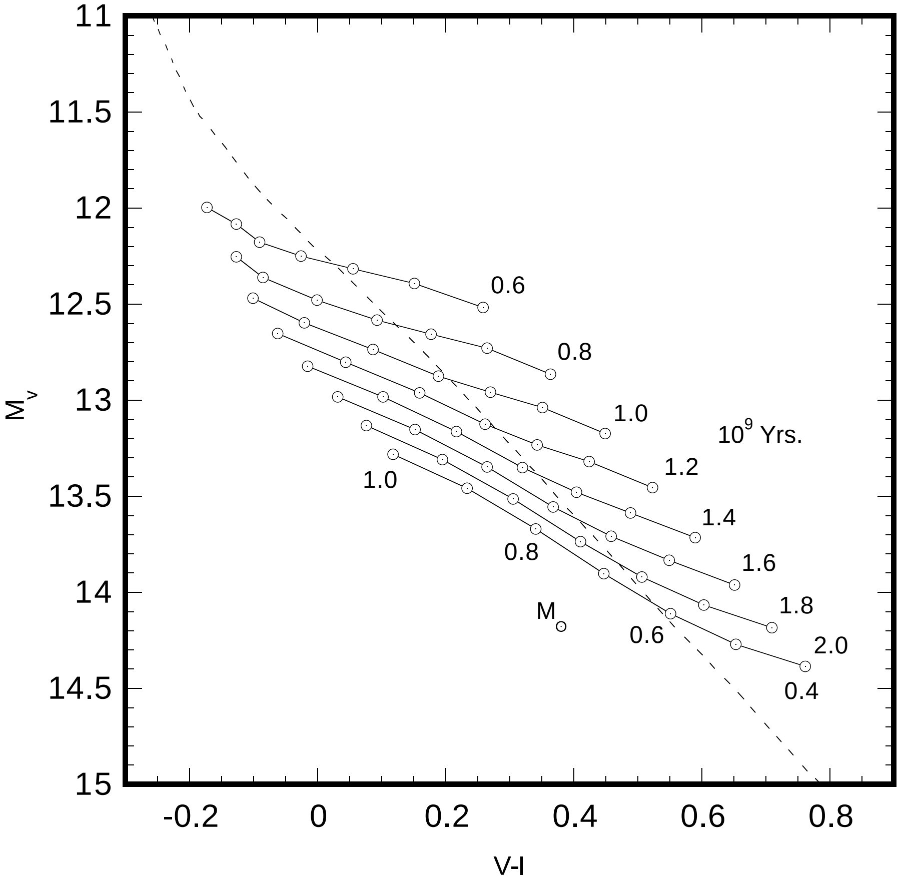

Figure 5.18: The same calculated WD isochrones as in Figure 5.16 transformed to the M_v versus V-I color-magnitude plane.

Our last step in preparing these isochrones is to be sure they agree with observations of white dwarfs in the field. In these figures I have included the single star sequence calibrated in M_v by an empirical fit to the Monet *et al.* (1992) M_v versus V-I white dwarf sequence with the white dwarf isochrones. The values for M_v in Monet *et al.* are determined from trigonometric parallax measurements which I regard as absolute. Bergeron, Saffer, and Liebert (1992 – hereafter BSL92), using line profile fits to DA white dwarfs, find that the mean mass for field white dwarfs is $0.54M_\odot$. Examining each of the figures above we can see the calculated isochrones and the location of the $\log(g) = 8.0$ sequence are in poor agreement with the result of BSL92.

However, since most DA white dwarfs have thick Hydrogen layers as demonstrated by Clemens (1994), then it is necessary to apply a correction to the results of BSL92 (who used a much thinner Hydrogen layer in their models). This implies a mean white dwarf mass nearer to $0.6M_\odot$. In this case the location of the $0.6M_\odot$ white dwarf sequence from the isochrones is in fair agreement with the $\log(g) = 8.0$ sequences. It is unlikely that these differences are in the color determination, otherwise the various checks made in Chapter 4 on the T_{eff}-color calibration could not have been met. It is more likely the differences arise from problems in estimating white dwarf bolometric corrections, thereby affecting M_v.

5.6 DISCUSSION OF RESULTS: THE PRAESEPE'S WHITE DWARF AGE

It now seems that I have the tools and information in hand to estimate the Praesepe's age from its white dwarf stars. In Table 5.6 I have combined photometry of the white dwarfs and candidates of this survey with the ones from the literature. For the objects out of the literature, in all cases only a V magnitude and $B-V$ color were listed. Because of the problems associated with the $B-V$ white dwarf isochrones I have used the model colors from Chapter 4 to estimate their $V-I$ color. These are indicated by values in parentheses. The photometric entries for EG-61, indicated by *, are the average between NE-1090 and NNW-1145. In column 4 I have indicated kinematic membership with a "Y", and if the spectral type is known it is given in column 5.

Table 5.6: The final composite list from this survey and the literature of white dwarfs and candidates for the Praesepe cluster. Entries with a ‡ are from Anthony-Twarog (1984) and † from Wagner *et al.* (1986).

Object ID	EG No.	LB No.	P.M. Mem.	Sp. Type	V	B-V	V-I
NE-908	59	390	Y	DA	17.60	0.04	-0.02
SE-1712	–	5893	Y‡	–	17.63	-0.06	-0.37
–	–	1876†	–	DA	17.69	0.15	(-0.12)
NE-1090 NNW-1145	61	393	Y	DA	17.96*	0.12*	-0.17*
SE-664	–	–	–	–	17.96	0.20	0.22
NE-1155	60	1847	Y	DA	18.33	0.08	-0.03
–	–	6072†	–	DA	18.73	0.24	(0.04)
–	–	1839‡	Y‡	–	18.83	0.23	(-0.01)
NNW-13	–	–	–	–	18.83	0.34	0.35
–	–	6037†	–	–	18.98	0.37	(0.46)

Before continuing with this discussion I need to have some idea of how many white dwarf stars are expected to be in the Praesepe. This estimate is necessary so that I can evaluate whether or not a significant number of white dwarf stars are missing from my list of candidates. There are two reasons why white dwarfs might have been missed. First, in some way the photometry may have overlooked some fraction of the white dwarf stars present, or there may remain a significant number of white dwarf stars outside my survey area. Second, as investigated by Weidemann *et al.* (1992) for the Hyades, it is possible that the oldest white dwarf stars may have been ejected from the cluster through dynamical interactions. While I am certain this effect is real I am not certain that it is as significant as Weidemann *et al.* suggest.

5.6.1 Predicted White Dwarf Numbers in the Praesepe

Using a similar approach to that of Anthony–Twarog (1984, hereafter AT84) I have estimated the expected number of white dwarf stars the Praesepe has produced to date. The basis of this estimate is that the mean luminosity function for open clusters derived by Taff (1974) is essentially universal for all open clusters. The assumption of universality is based on Taff's finding that of the 62 open clusters studied, all luminosity functions were similar except those of the richest clusters (>250 stars). In Taff's iterative approach, 10-12 clusters classified as very rich were consistently rejected, implying their LFs were somehow different from the others, leaving ~50 clusters from which the mean LF was computed. This argues that the resulting mean LF is universal, within the range of open cluster classes used by Taff. Included in Taff's final calculation of the mean LF was the LF from the Praesepe itself, further strengthening the assumption of universality.

The mean open cluster luminosity function from Taff is shown as filled diamonds in Figure 5.19 along with a best fit 3rd order polynomial. Adopting

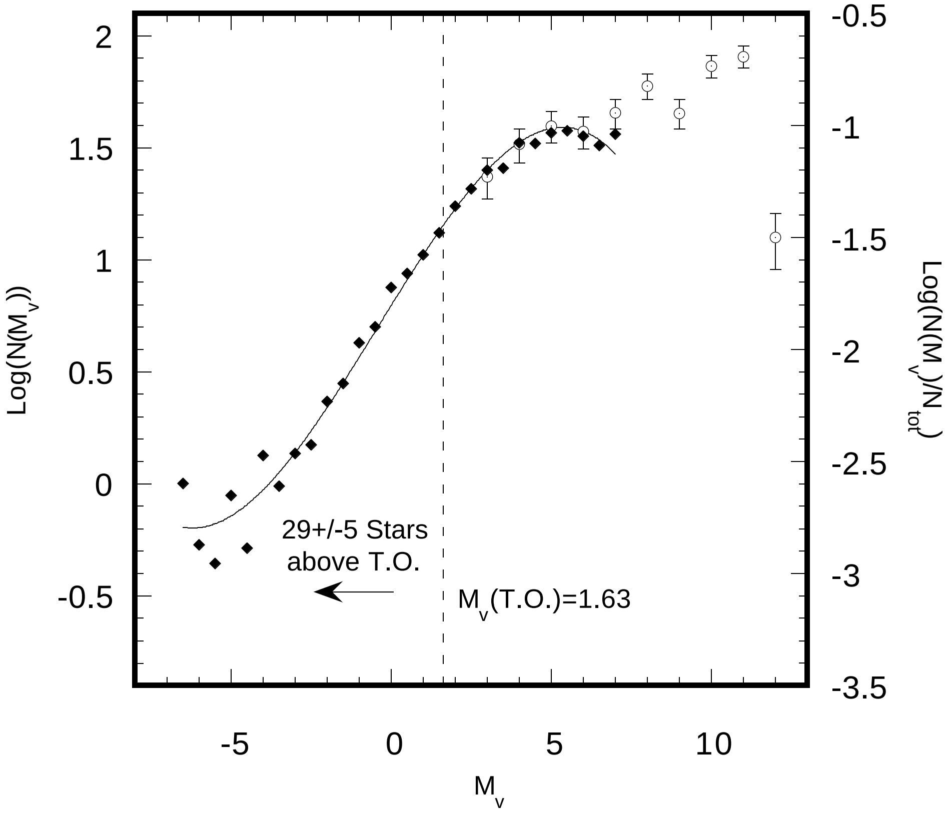

Figure 5.19: The mean open cluster luminosity function (filled diamonds) from Taff (1974) normalized to the observed Praesepe LF (circle-dots with error bars) of Jones and Stauffer (1991). The main-sequence turn-off point for the Praesepe is indicated by the dashed line. The integral of the Taff LF above the turn-off predicts 29 ± 5 *evolved* stars in the cluster.

the Taff LF in its functional form I have normalized it against the observed luminosity function from Jones and Stauffer (1991, hereafter JS91). The JS91 LF is the result of a proper motion study over a $4^{\circ} \times 4^{\circ}$ area, extending well into the cluster halo. The LF corrected for completeness (JS91 Table 6) is indicated in Figure 5.19 by the open circles with their accompanying error bars. Over the range of $2.5 \le M_v \le 6.5$ the JS LF contains 134 stars. Using a scaling factor of $\log(N) = 2.6$ I have integrated the Taff LF over the same range of absolute visual magnitude to get a predicted number of 134 stars – in order to obtain good agreement with the observed number of JS91. From this normalized LF I can now ask: how many stars are in the Praesepe which are more evolved than the cluster's turn-off point – the place in the observed color-magnitude diagram where stars have evolved away from the zero-age-main-sequence (ZAMS)?

Using the tables found in Meynet *et al.* (1993) I have estimated the absolute visual magnitude of the main sequence turn-off for the Praesepe at $0.9 Gyr$ to be $M_v(TO) = 1.63$ (the vertical dashed line in Figure 5.19), corresponding to a turn-off mass of $1.9 M_{\odot}$. I have calculated an estimate for the total number of "evolved" stars in the Praesepe by integrating the Taff LF above $M_v(TO) = 1.63$ through $M_v = -7$. If the Taff LF is a valid extension of the JS91 LF the Praesepe should contain 29 ± 5 "evolved" stars. The total number of stars observed in the Praesepe above $M_v = 1.63$ by Klein-Wassink (1927) is estimated to be $N_{evolve} = 21$. Similarly in Johnson's (1952) list of photoelectric photometry for the Praesepe the number of stars brighter than $M_v = 1.63$ is $N_{evolve} = 23$.

For the purpose of my estimate I take the number of "evolved" stars observed to be $N_{evolve} = 22 \pm 4$, where the uncertainty is the RMS of $\sqrt{N_{evolve}}$ and the difference between the counts of Klein-Wassink and Johnson. The difference in the observed number of evolved stars above the $M_v = 1.63$ turn-off and the calculated number of evolved stars is the number of evolved stars below $M_v = 1.63$ – the white dwarf stars. Using the arguments above I estimate the number of white dwarf stars in the Praesepe to be $N_{WD} = 7^{+9}_{-4}$. The lower limit is set by the 3 white dwarf stars previously known to be members of the Praesepe, while the upper limit is set by the extremes of my calculated and observed numbers for evolved stars. Of these it is possible and quite likely that some are members of binary systems and will not be recognized as single white dwarfs.

The 10 white dwarfs and candidates associated with the cluster is consistent with the total predicted number. Therefore, I conclude from this anlysis that I have not missed a substantial fraction of the Praesepe's white dwarf population. Furthermore, it is quite possible that the list in Table 5.6 is the entire white dwarf content of the Praesepe.

5.6.2 Estimating the White Dwarf Age.

The white dwarf age can be estimated now by examining the color magnitude diagrams from the data in Table 5.6 in reference to the white dwarf isochrones calculated earlier. I have assumed a distance to the Praesepe of 174 parsecs to place the white dwarf isochrones in the color–magnitude diagrams shown in Figures 5.20 and 5.21. In both $B - V$ and $V - I$ the chronometry is

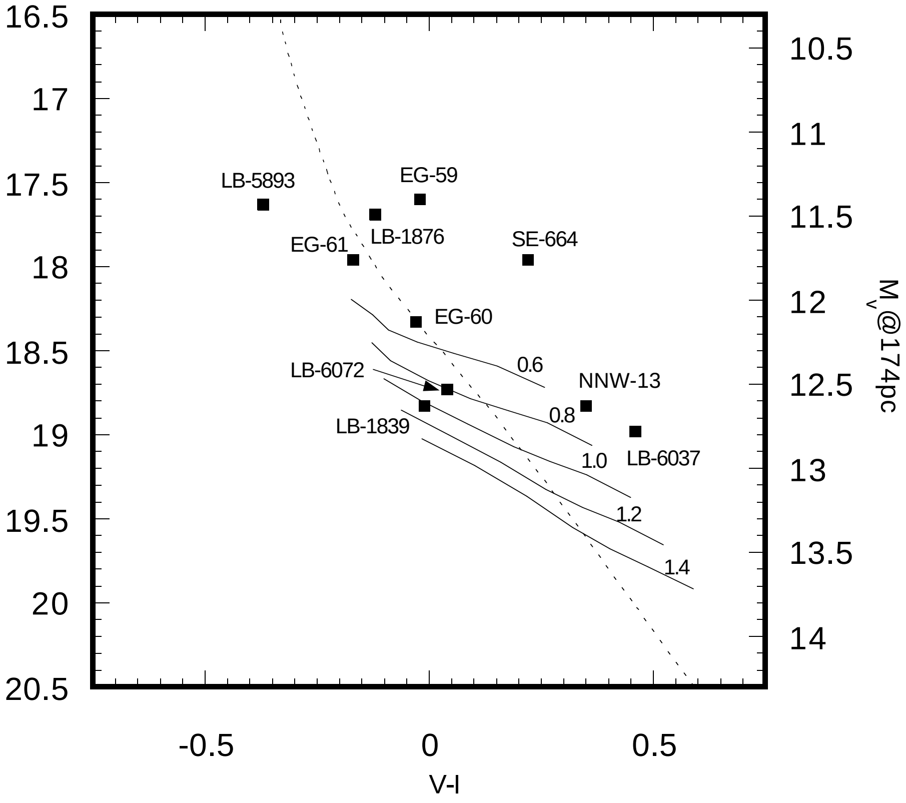

Figure 5.20: The V versus $V - I$ color–magnitude diagram for the white dwarfs and candidates (filled squares) listed in Table 5.6. Isochrones (solid lines) have their ages indicated by the numbers above them. A single star model evolution track for $\log(g) = 8.0$ (dashed line) is also shown.

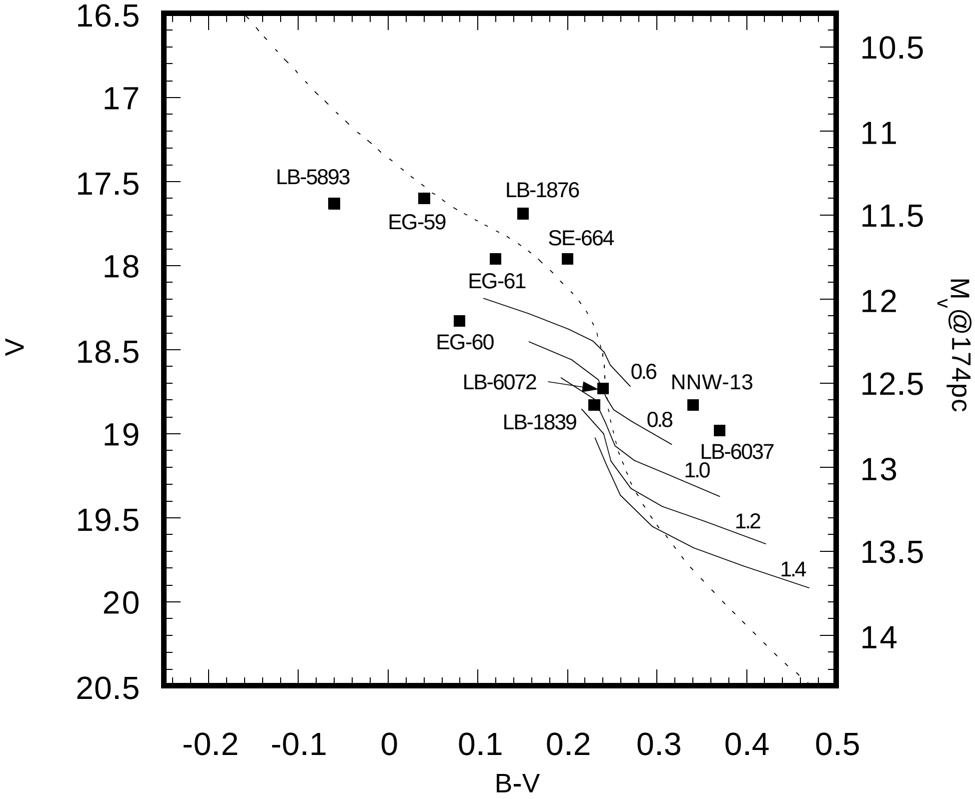

Figure 5.21: The V versus B-V color magnitude diagram for the Praesepe white dwarfs and candidates (filled squares). The isochrones and single star evolutionary track are as in Figure 5.20.

nearly identical with the two oldest objects being LB-1839 and LB-6072 at roughly 1.0 and 0.8 Gyr respectively, even though they are not the faintest objects in Table 5.6. It is worrisome that more of the white dwarf candidates in Table 5.6 do not have membership confirmation from proper motion. Additional observations in a field immediately West and East of my Praesepe SE field, where LB-1876 and LB-6072 respectively are located, along with a scan from the POSS plates would clarify this with certainty. However, taken at face value these data suggest the Praesepe white dwarf population has an age near 1.0 Gyr. By removing the oldest white dwarf, LB-1839, from the sample, I can make some estimate of the uncertainty in the above age. In this case the difference in age between LB-1839 and LB6072 is 0.2 Gyr. This is consistent with the main sequence isochrone age of 0.85 ± 0.10 estimated earlier.

Uncertainties in the distance modulus will have a systematic effect on the placement of the white dwarf isochrones, hence the inferred white dwarf age. At the age of the Praesepe's white dwarfs an uncertainty in distance of ~0.1 magnitudes translates into an uncertainty in age of roughly 0.1 Gyrs. For example, at a distance modulus of 6.3 the Praesepe's white dwarf age is near 0.9 Gyr. In addition, the systematic differences in the evolutionary and atmosphere models in estimating white dwarf luminosites cause roughly 0.10–0.15 Gyr uncertainty in the age of the Praesepe.

For the total uncertainty I take the RMS of the above uncertainties, which gives $\sigma_{total} = 0.27$ Gyr. Therefore, I have estimated the white dwarf age of the Praesepe to be 1.0 ± 0.27 Gyr.

5.7 CONCLUDING REMARKS

I have shown that it is possible to estimate the age of a star cluster from its white dwarf population. This method depends heavily on finding the oldest white dwarf and confirming its membership in the cluster. For this reason it will be difficult to apply this technique to the more sparse, young open clusters. However, by observing many of the younger clusters it should be possible to statistically constrain any zero point differences in the main sequence and white dwarf ages. Some work to this end has already been done by von Hippel (1994) with the Hubble Space Telescope on NGC-2477 and NGC-2420. Von Hippel concludes that the white dwarf populations in these two clusters are as old or slightly older than their main sequence isochrone ages.

It will be necessary to search additional clusters for white dwarfs in order to fully calibrate the white dwarf and stellar isochrone ages . This is especially true for the oldest clusters, where any systematic differences in time scales between these two age methods have had the most time to diverge to measurable levels. For the Galactic Disk this points immediately to the three oldest open clusters known: M-67, NGC-188, and NGC-6791. The ages and distances for these three clusters make it difficult, but not impossible, to look for the "bottom" of their white dwarf sequences with ground-based observations. At the distance to M-67 its oldest white dwarfs will have apparent magnitudes near 25th, while the bottom of the white dwarf cooling track in NGC-188 and NGC-6791 will be nearer to 26th magnitude. These limits are well within reach using the intermediate hydride band photometry technique described in Chapter 4 on a 4 meter class telescope at prime focus (*i.e.* the 4m telescope at Kitt Peak). However, careful comparison with adjacent fields will be necessary in order to evaluate the significance of field star and unresolved galaxy contamination.

6

White Dwarf Chronometry of the Galaxy

There are now two *different* ways to define the age of the galaxy, (*i.e.* via stellar isochrones applied to a distribution of stars, and from the white dwarf luminosity function), so the question naturally arises; do these methods give the same result? The answer to this question has come to the attention of the astronomical community as evidence for a conflict between globular cluster ages and recent estimates of the Hubble time (see Chapter 1; Jacoby 1994). The conflict arises from new estimates to the distance of the Virgo galaxy cluster using the Cepheid period–luminosity relation (Pierce *et al*. 1994; Freedman *et al*. 1994), which results in Hubble times much younger than the globular clusters. Can the globular cluster ages be wrong after 20+ years of acceptance? In this, the final chapter of my thesis I present a summary of this work and additional evidence that the globular cluster ages need a careful objective examination.

6.1 WHAT WE KNOW NOW.

As result of this thesis I have made a first comparison between the ages determined from stellar isochrones, and ages based on white dwarf cooling times.

I did this using the Praesepe galactic cluster as a place where both techniques could be applied simultaneously. The ages I have obtained for the Praesepe are:

1.0 ± 0.27 Gyr – the white dwarf age,

0.85 ± 0.10 Gyr – the main sequence stellar isochrone age.

Within their errors these ages agree with each other.

Concurrently with this work von Hippel (1994) has investigated two galactic clusters with the Hubble Space Telescope for their white dwarf content. His preliminary result indicates NGC 2477 and NGC 2420 have consistent ages from both stellar evolution and white dwarf cooling calculations. The oldest cluster NGC 2420 is estimated to be ~3 Gyrs old, so there is good agreement between ages determined by stellar evolution and white dwarf cooling calculations at least to 3 Gyrs. However, before we can draw further conclusions about the overall picture for the Galaxy's age from white dwarf stars, we must to extend the time baseline in our comparison of these two age–dating techniques. This is because the input physics of both stellar evolution and white dwarf cooling calculation changes dramatically for ages older than ~3 Gyrs.

In main sequence stellar models at a 3 Gyr turn–off, the energy production is predominantly from the CNO bi–cycle, but is beginning to be influenced by p–p chain hydrogen burning. By 4 Gyrs, stellar models at the turn–off are producing essentially all of their energy by p–p chain burning. Because the reaction rates for the p–p chain are difficult to measure in the laboratory, their rates are computed from theory, and therefore must be considered quite uncertain (Gough 1993). The ages of low mass stars (*i.e.* those found at the main–sequence turn–off in globular clusters) can therefore be significantly in error. Similarly, significant crystallization in white dwarf cooling models begins shortly after 3 Gyrs. The exact physical nature of the white dwarf crystallizing process is still uncertain. Whether a mixed composition white dwarf core crystallizes homogeneously or becomes stratified durring the process, can have significant effects on white dwarf cooling ages greater than 3 Gyrs.

The uncertainties outlined above underscore our need to cross-calibrate these two methods at older ages. I have outlined, at the end of Chapter 5, one approach for accomplishing this by investigating the white dwarf content of older star clusters. This would still leave us without a direct comparison between the Disk field age from the white dwarf luminosity function and the stellar isochrone ages. We must find some way of estimating the Disk's field star population from stellar isochrones.

6.2 AGE OF THE DISK FROM PRELIMINARY HIPPARCOS RESULTS

During my visit to Kiel, Germany for the 9th European Conference on White Dwarfs, Peter Thejll presented the color magnitude diagram shown in Figure 6.1. This color magnitude diagram (CMD) is a preliminary parallax solution of 5220 stars from the Hipparcos astrometry satellite project, with errors in parallax of $\sigma_\pi/\pi < 0.1$. The Hipparcos mission is to measure the parallax of ~100,000 stars to precision of 2–4 miliarcseconds, and from these parallaxes we can infer absolute visual magnitudes. This allows us to place these stars in a CMD in much the same way we do with star clusters. The majority of the stars in the Hipparcos Catalog are brighter than $V = 10$ and are almost entirely from the Disk population. We will see later that there are features in the data which

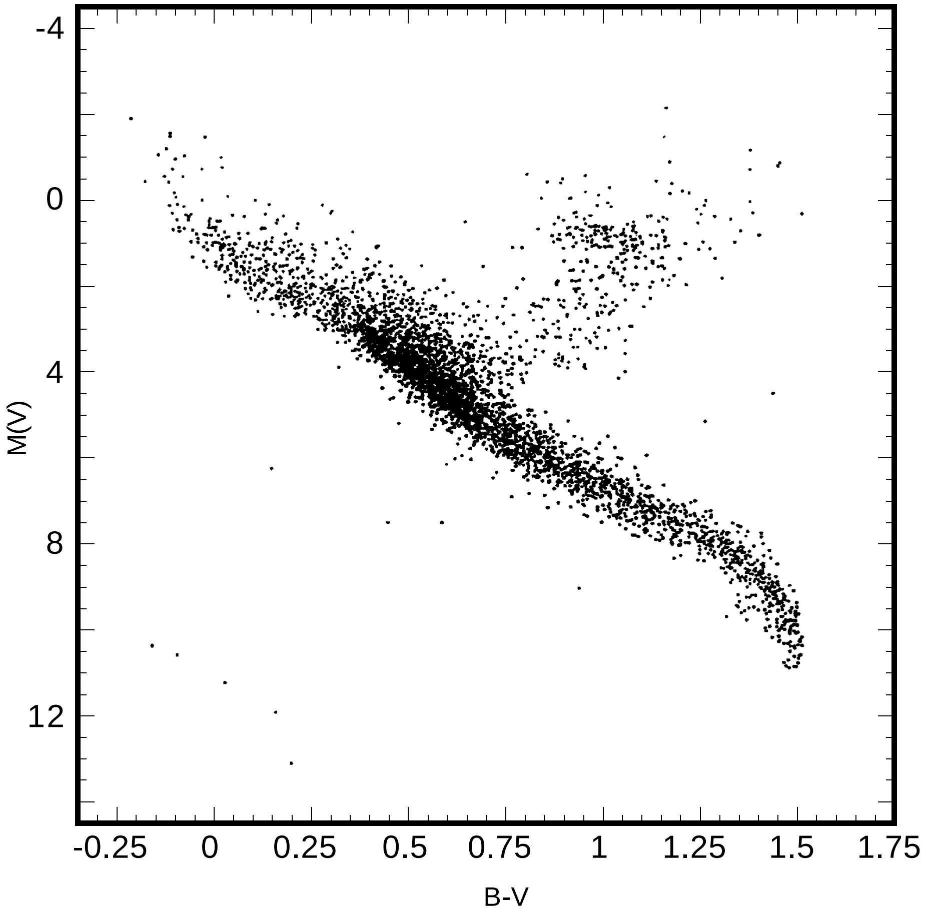

Figure 6.1: The preliminary Color-magnitude diagram of the solar neighborhood from the Hipparcos mission (Courtesy of Peter Thejll, NBI Copenhagen, Denmark).

confirm that the stars in this diagram are completely dominated by Disk stars. In addition to the Hipparcos data, I have overplotted on this diagram in Figure 6.2 the zero–age main sequence (ZAMS) isochrone along with those for 5, 10, and 15 Gyrs from VandenBerg (1985) for solar abundance stellar models.

The morphology of the CMD presented in Figure 6.1 bears a striking resemblance to both open and globular cluster diagrams, indicating the presence of both young and old stellar populations. It is tempting to try and estimate an age for the older population from the isochrones shown. However, we lack a well–defined turn off point, and the large apparent scatter in the data might make this seem impossible. Still, we can see by examining the base of the giant branch that its location – specifically its luminosity – is sensitive to age. It might be possible to construct a "pseudo–isochrone" age for the Disk population, thus providing the necessary counterpart to the Disk age from the white dwarf luminosity function. Before we can do this we need to convince ourselves of several things: 1) that the position of the models in the CMD are consistent with the observational data, 2) that the observations are not being contaminated by another stellar population that would affect our age estimate (*i.e.* Population II stars from the Halo), and 3) that the age–dependent effects produce observable features in a CMD for field stars.

At first glance it might appear that the location of the zero–age main sequence model, as indicated in Figure 6.2, is displaced from the locus of observed main sequence stars. It is, but that is exactly where it is supposed to be - on the blue edge of the observed main sequence distribution. Most things affecting a main sequence star's location in a CMD will place it on the red side of its nominal ZAMS. If we look carefully at the dispersion in the main sequence locus, we see that it is different above and below the indicated turn–off. The scatter above the turn–off is due primarily to evolutionary effects on the short–lived massive stars. The path a star takes in a CMD as it evolves *always* moves it initially towards redder colors relative to the ZAMS. Below the turn–off point

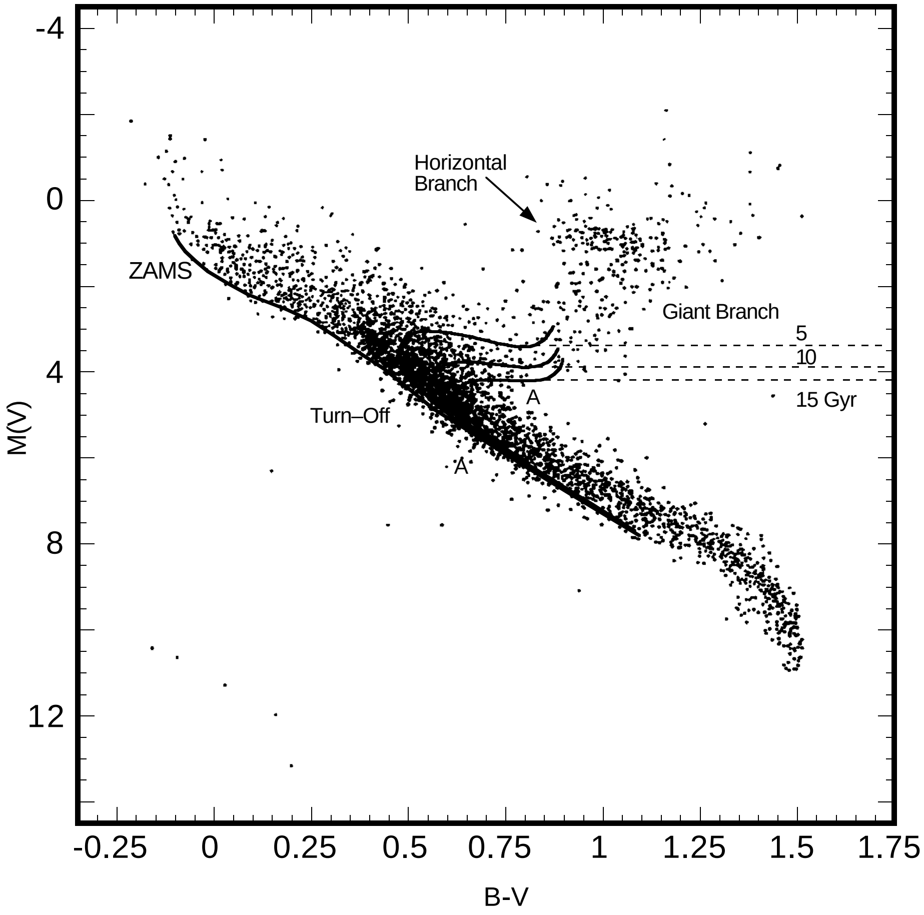

Figure 6.2: The color–magnitude diagram from the Hipparcos mission of the local field population with the ZAMS and isochrones from VandenBerg (1985) for 5, 10, and 15 Gyrs overplotted. See text for explanation.

the scatter results from a combination of evolution, duplicity, and differences in abundance patterns. For example, unresolved binaries with identical components have their ZAMS 0.75 magnitudes brighter than do single stars. There are very few ways to place a star bluer than its ZAMS in a CMD.

We notice, however, that there are a number of stars which do lie on the blue side of the ZAMS. I believe these to be low metalicity Population II stars from the Halo. The position of the ZAMS is bluer and more luminous with decreasing metal abundances (see Monet *et al.* 1992). I estimate that there are roughly roughly 100 or so stars immediately to the blue of the model ZAMS, which is consistent with the number to be expected from the ratio of Disk to Halo stars in the solar neighborhood and the total number of stars in this sample. As a check for the "purity" for these data in sampling the Disk, we note the red color of the horizontal branch stars, near $B-V \approx 1.0$. Compare this to the colors of horizontal branch stars of the metal poor Halo globular cluster M-5 shown in Figure 1.6. Also sensitive to metallicity is the slope of the giant branch; higher metal abundances result in a less–sloped giant branch. Once again, compare the giant branch in Figure 6.1 with the metal–poor cluster shown in Figure 1.6. I conclude from the limiting magnitude of stars measured by Hipparcos, the number of "blue" main sequence stars, and the morphology of the horizontal and giant branches that the CMD is dominated completely by Disk field stars. We can now use the CMD from Hipparcos to estimate an isochrone age for the Disk.

Normally, under the assumptions of coevolution and constant chemical make-up, we fit model isochrones to the locus of stars near a cluster's turn–off to estimate its age. However, in this case, the birthrate is essentially continuous which results in the "blurring" of the age–sensitive turn–off feature. Similarly, all the features in the Hipparcos CMD above the turn–off for the oldest stars are also blurred. For the same reasons that the upper main sequence is blurred in a way to form a "blue edge" at zero age, the base of the giant branch forms an edge at the oldest age. The dashed lines in Figure 6.2 indicate the trend with increasing age on the luminosity of the base of the giant branch. From the location of this older edge in the Hipparcos data it is apparent that there are stars with ages near 15 Gyr. I also note that the just below the 15 Gyr isochrone there is an abrupt change in the amount of scatter in the observed main sequence, near the place marked by AA. If we interpret this as where the contribution of evolutionary effects to the scatter end, this would imply stars ages older than 15 Gyr are present. From these data I estimate the Disk field star population has an isochrone age of 15 ± 2.5 Gyr.

It is important that I exercise some caution regarding the assumed metalicity of the sub–giant stars. By using the VandenBerg (1985) isochrones in Figure 6.2 I have made a critical assumption: that the stars at the edge of the sub–giant branch have solar abundances. If the abundance of these stars were something other than solar, then the age I infer would be altered. I can estimate the validity of this assumption and how it affects my age estimate by examining the color of the giant branch's red edge, which is sensitive primarily to metal abundance. In the Hipparcos CMD, the majority of giant branch stars along the red edge in the range $2 \le M_v \le 4$ are consistent with solar abundance. There are several redder giant stars in this region which would indicate a larger metal abundance. The giant stars in the region above (brighter) than $M_v \sim 2$ are more consistent with these more metal–rich stars. The estimated metallicity for these stars is $[Fe/H] \sim 0.3 - 0.4$, roughly 2 – 2.5 times solar.

The effect of increased metal abundance on my estimated age can be determined by comparing the solar abundance model isochrones from VandenBerg (1985) with the metal–rich model isochrone from VandenBerg and

Laskerides (1987). At 15 Gyr these models predict a decrease in luminosity of $M_{bol} \sim 0.1$ for a factor of two increase in metalicity beyond solar. Therefore, a younger model isochrone is needed to fit the location of the sub–giant branch's low luminosity edge. If the sub–giant stars have 2 – 2.5 time solar metal abundances, then the estimated Disk field age would be 1 – 1.5 Gyrs younger than for solar models, or ~13.5–14 Gyrs old.

Phelps *et al*. (1994) define a "Morphological Age Index" (MAI) based on the magnitude difference between the horizontal branch locus and the inflection point of the horizontal sub-giant branch, what they call δV. The mean absolute visual magnitude (M_v) of the horizontal branch of open clusters is given by Janes and Phelps (1994) as 0.95. This value is entirely consistent with the location of the horizontal branch in the Hipparcos color–magnitude diagram (see Figure 6.3a). The lower edge of the sub–giant branch in Figure 6.3a is approximately 3 magnitudes fainter than the horizontal branch. Using this as the oldest sub–giant inflection point, and allowing for the scatter in M_v observed in the horizontal branch, I obtain $\delta V \approx 3.0 \pm 0.2$ for the local field. According to Janes and Phelps (1994) this corresponds to a Morphological Age Index of 16 ± 4 Gyrs. Janes and Phelps (1994) caution that the Morphological Age Index is meant only for ranking cluster ages, and its absolute age calibration is somewhat suspect. Nevertheless, this would imply the Disk field population as sampled by the Hipparcos data has an morphological age as old as the globular cluster population (see Figure 6.3b), as measured by Chaboyer *et al*. (1992).

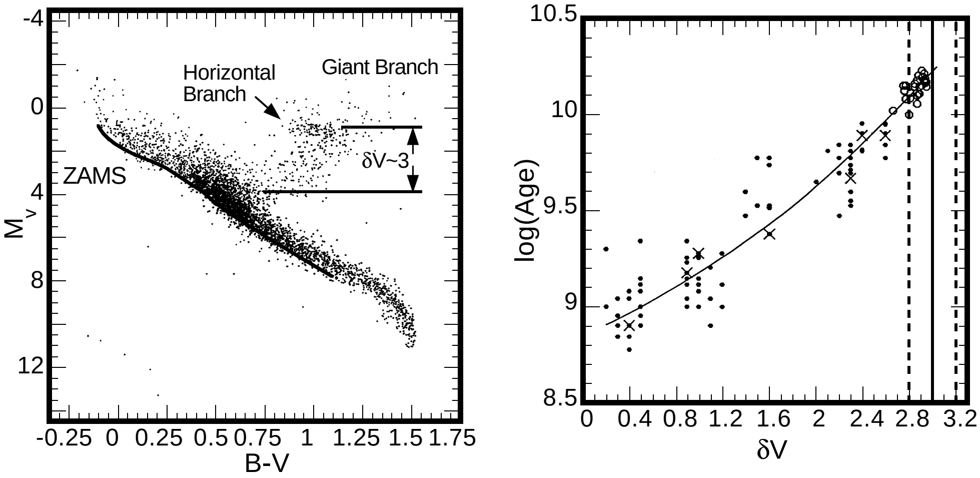

Figure 6.3a,b: The Morphological Age Index (δV) for the Hipparcos CMD (left) is compared to the cluster data from Janes and Phelps (1994 right). When measured this way the evolved population of the field is certainly older than the galactic open clusters (filled circles in 6.3b) and at least as old as the globular clusters (open circles in 6.3b).

6.4 CALIBRATION AND CONSTRAINTS OF AGES

We can now extend the time baseline for our age–age comparison, somewhat crudely, to calibrate out any real differences between isochrone ages for stars, and ages derived from the white dwarf luminosity function. In figure 6.4 I have placed my Praesepe and Disk field population ages (filled squares with errors) along with the two galactic clusters from von Hippel (open circles) on an "age–age" diagram. We can now compare stellar ages from isochrones and white dwarfs.

I have included in Figure 6.4 several analytical models which we can consider. The first, assumes that both stellar evolution and white dwarf cooling calculations give the same age (MAI=WD, short dashed line). This seems to be true for the three points determined from galactic clusters, but not true for the

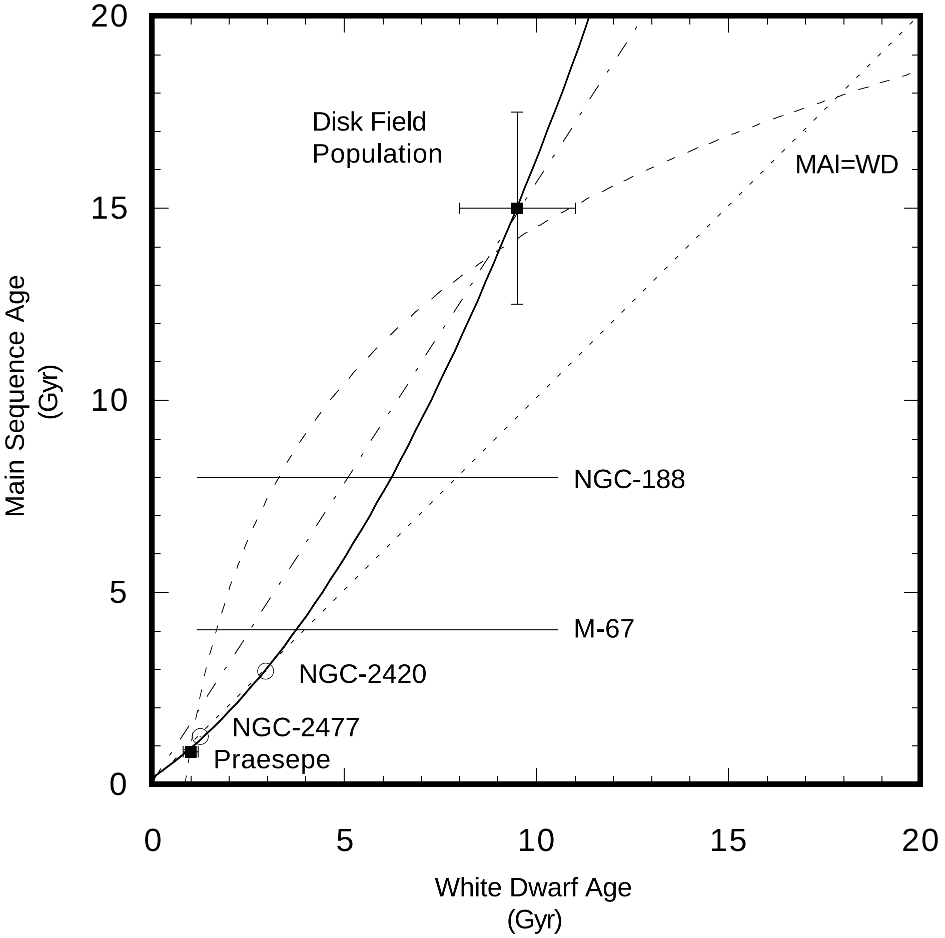

Figure 6.4: A preliminary look at the cross–calibration of white dwarf ages and stellar evolution ages. Shown are the calibration of the Praesepe and Disk from this work (filled squares) and the two additional galactic clusters from von Hippel (1994 open circles). The various model fits are described in the text.

Disk field star population. The next simplest model is a constant rate difference between stellar evolution and white dwarf cooling ages (indicated by the dot–dashed line). In this model the ages must agree at zero and at the oldest datum available, in this case the Disk field population. We can see a straight line through zero and the Disk age does not agree with the three data points from the galactic clusters. The failure of both of these simplistic model lends support to the idea discussed earlier, that a change in model physics is needed to alter the cross–calibration of age methods beyond a certain age.

I have included two additional models which are purely empirical. The first of these assumes the data for the Disk field and the ages for the globular clusters are essentially correct. If this model is to satisfy these two assumptions and pass near the origin it must have strong positive curvature (long dashed curve in Figure 6.4). Clearly, this model fails for the three galactic clusters. Finally, I have fit quadratic polynomial to the four data points (shown by the solid curve in Figure 6.4). The qualitative behavior of this fit is not without physical merit. If, as I have mentioned earlier, the p–p chain burning rates used in stellar models are wrong, then as we examine older and older stars these ages will begin to deviate from the white dwarf ages. We can see that the quadratic fit deviates from a slope of approximately one (MAI=WD) just beyond the cluster NGC 2420, when p–p chain burning starts becoming important. By the main sequence age of M67 p–p chain burning contributes approximate 50% of the model turn–off stars' luminosity, and by the age of NGC 188 the p–p chain produces essential all of the luminosity. From the location of NGC 188 in Figure 6.4 we can see that if its age can be estimated from its white dwarfs, then it would provide a key calibration point. With this point determined, it is possible that the cause of the apparent age discrepancy between globular cluster ages and recent estimates of the Hubble time could be resolved using ground–based telescopes.

6.4.1 Conclusions

Taking the quadratic relation at face value, I find there are some interesting consequences. This implies that the oldest globular clusters have ages on the white dwarf scale of roughly 11 Gyr, and there is no gap in ages between the Disk and Halo. If this is true then it would seem to support the idea of a virial collapse model for explaining the formation of the Galaxy, as was originally proposed by Eggen, Lynden–Bell, and Sandage (1962). It is interesting to point out the gap in cluster ages is centered just where the stellar models for the turnoff stars make the transition from CNO bi–cycle to p–p chain dominated energy production. In my opinion, the evidence for erroneous p–p chain rates in stellar model calculation is sufficient to make the globular cluster ages must be suspect.

Finally, making the same set of assumptions as by Winget *et al*. (1987), we can infer the age to the Universe. If we assume the time from the Big Bang to when galaxies started to form to be 1 Gyr, then the Universe's age is

$$12 \pm 2 \text{ Gyrs},$$

where the uncertainty is determined by the range of quadratic fits within the estimated errors.

Table 6.1: The ages of the different populations are summarized by what method was used to obtain them. If no age estimate has been made a "?" is indicated. The values in bold are those inferred from this work.

	Age Method (Gyrs)		
Stellar Population	Isochrones	Nuclear	**White Dwarf**
Disk – Field Stars	**15**	10–14	8–11
Disk – Open Clusters w Fe/O	6.5–7.5	?	–
w/o Fe/O	10–12		**6.5–7.7**
Praesepe	**0.85**		**1.0**
Thick Disk	8-11	?	**5–7**
Halo – Field Stars	<17–18	?	**<11**
Halo – Globular Clusters (Inner)	13–14	?	**8–9**
Halo – Globular Clusters (Outer)	13–17	?	**8–11**

Appendix A

Table A.1: $U-B$ colors versus T_{eff} for blackbody energy distribution (bb) and Bergeron *et al*. (1990) $\log(g) = 7.5$, 8.0, and 8.5 model DA atmospheres.

T_{eff}	U-B(7.5)	U-B(8.0)	U-B(8.5)	U-B(bb)
50000	-1.2065	-1.2015	-1.1965	-1.4552
49500	-1.2055	-1.2003	-1.1954	-1.4542
49000	-1.2046	-1.1991	-1.1942	-1.4532
48500	-1.2036	-1.1979	-1.1930	-1.4522
48000	-1.2025	-1.1967	-1.1918	-1.4511
47500	-1.2015	-1.1954	-1.1906	-1.4501
47000	-1.2004	-1.1941	-1.1893	-1.4490
46500	-1.1993	-1.1928	-1.1879	-1.4478
46000	-1.1981	-1.1914	-1.1865	-1.4467
45500	-1.1968	-1.1900	-1.1851	-1.4455
45000	-1.1955	-1.1885	-1.1835	-1.4443
44500	-1.1941	-1.1870	-1.1818	-1.4430
44000	-1.1926	-1.1854	-1.1801	-1.4418
43500	-1.1911	-1.1837	-1.1783	-1.4405
43000	-1.1895	-1.1820	-1.1764	-1.4391
42500	-1.1878	-1.1803	-1.1744	-1.4378
42000	-1.1860	-1.1785	-1.1723	-1.4364
41500	-1.1842	-1.1766	-1.1702	-1.4349
41000	-1.1824	-1.1746	-1.1680	-1.4334
40500	-1.1805	-1.1726	-1.1658	-1.4319
40000	-1.1785	-1.1705	-1.1635	-1.4303
39500	-1.1765	-1.1683	-1.1612	-1.4287
39000	-1.1744	-1.1661	-1.1588	-1.4271
38500	-1.1723	-1.1637	-1.1563	-1.4254
38000	-1.1700	-1.1612	-1.1536	-1.4236
37500	-1.1676	-1.1585	-1.1508	-1.4218
37000	-1.1650	-1.1556	-1.1477	-1.4199
36500	-1.1623	-1.1525	-1.1444	-1.4180
36000	-1.1593	-1.1492	-1.1408	-1.4160
35500	-1.1561	-1.1455	-1.1369	-1.4140

Table A.1: $U-B$ colors versus T_{eff} continued.

T_{eff}	U-B(7.5)	U-B(8.0)	U-B(8.5)	U-B(bb)
35000	-1.1525	-1.1415	-1.1325	-1.4119
34500	-1.1486	-1.1371	-1.1277	-1.4097
34000	-1.1444	-1.1324	-1.1223	-1.4075
33500	-1.1398	-1.1272	-1.1166	-1.4052
33000	-1.1348	-1.1217	-1.1103	-1.4028
32500	-1.1294	-1.1157	-1.1036	-1.4003
32000	-1.1237	-1.1093	-1.0965	-1.3977
31500	-1.1175	-1.1025	-1.0889	-1.3950
31000	-1.1109	-1.0953	-1.0808	-1.3923
30500	-1.1039	-1.0876	-1.0724	-1.3894
30000	-1.0965	-1.0795	-1.0635	-1.3865
29500	-1.0886	-1.0709	-1.0542	-1.3834
29000	-1.0803	-1.0619	-1.0445	-1.3802
28500	-1.0715	-1.0525	-1.0345	-1.3769
28000	-1.0623	-1.0426	-1.0240	-1.3734
27500	-1.0527	-1.0323	-1.0132	-1.3698
27000	-1.0428	-1.0216	-1.0021	-1.3660
26500	-1.0324	-1.0106	-0.99063	-1.3621
26000	-1.0217	-0.99921	-0.97886	-1.3580
25500	-1.0108	-0.98750	-0.96681	-1.3538
25000	-0.99950	-0.97550	-0.95450	-1.3493
24500	-0.98799	-0.96323	-0.94196	-1.3446
24000	-0.97623	-0.95070	-0.92917	-1.3398
23500	-0.96420	-0.93788	-0.91610	-1.3346
23000	-0.95187	-0.92475	-0.90269	-1.3292
22500	-0.93923	-0.91131	-0.88891	-1.3236
22000	-0.92626	-0.89752	-0.87471	-1.3176
21500	-0.91293	-0.88337	-0.86003	-1.3114
21000	-0.89922	-0.86884	-0.84482	-1.3048
20500	-0.88508	-0.85389	-0.82900	-1.2978
20000	-0.87050	-0.83850	-0.81250	-1.2904

Table A.1: $U-B$ colors versus T_{eff} continued.

T_{eff}	U-B(7.5)	U-B(8.0)	U-B(8.5)	U-B(bb)
19500	-0.85544	-0.82262	-0.79524	-1.2826
19000	-0.83991	-0.80613	-0.77716	-1.2744
18500	-0.82392	-0.78887	-0.75821	-1.2656
18000	-0.80750	-0.77065	-0.73833	-1.2562
17500	-0.79069	-0.75128	-0.71745	-1.2463
17000	-0.77350	-0.73050	-0.69550	-1.2357
16500	-0.75611	-0.70826	-0.67243	-1.2243
16000	-0.73917	-0.68544	-0.64831	-1.2121
15500	-0.72361	-0.66334	-0.62328	-1.1991
15000	-0.71050	-0.64350	-0.59750	-1.1850
14500	-0.70081	-0.62735	-0.57132	-1.1698
14000	-0.69409	-0.61460	-0.54567	-1.1534
13500	-0.68939	-0.60436	-0.52187	-1.1357
13000	-0.68550	-0.59550	-0.50150	-1.1163
12500	-0.68133	-0.58709	-0.48618	-1.0953
12000	-0.67738	-0.58011	-0.47631	-1.0722
11500	-0.67479	-0.57633	-0.47192	-1.0469
11000	-0.67500	-0.57800	-0.47300	-1.0190
10500	-0.67900	-0.58700	-0.48101	-0.98818
10000	-0.68500	-0.60200	-0.50100	-0.95392
9500.0	-0.69100	-0.62100	-0.52900	-0.91568
9000.0	-0.69200	-0.63699	-0.56199	-0.87278
8500.0	-0.68600	-0.64500	-0.58800	-0.82438
8000.0	-0.66700	-0.64099	-0.60099	-0.76944
7500.0	-0.63500	-0.62000	-0.59599	-0.70662
7000.0	-0.58600	-0.58000	-0.56700	-0.63424
6500.0	-0.52000	-0.51900	-0.51399	-0.55007
6000.0	-0.43300	-0.43499	-0.43399	-0.45118
5500.0	-0.32399	-0.32699	-0.32699	-0.33353
5000.0	-0.18800	-0.19000	-0.19100	-0.19150

Table A.2: $B-V$ colors versus T_{eff} for blackbody energy distribution (bb) and Bergeron *et al*. (1990) $\log(g) = 7.5$, 8.0, and 8.5 model DA atmospheres.

T_{eff}	B-V(7.5)	B-V(8.0)	B-V(8.5)	B-V(bb)
50000	-0.24200	-0.24700	-0.25300	-0.40815
49500	-0.24100	-0.24610	-0.25219	-0.40724
49000	-0.23998	-0.24518	-0.25137	-0.40630
48500	-0.23895	-0.24425	-0.25053	-0.40535
48000	-0.23789	-0.24330	-0.24968	-0.40437
47500	-0.23682	-0.24233	-0.24881	-0.40337
47000	-0.23572	-0.24133	-0.24791	-0.40235
46500	-0.23459	-0.24030	-0.24699	-0.40131
46000	-0.23343	-0.23924	-0.24603	-0.40024
45500	-0.23224	-0.23814	-0.24503	-0.39914
45000	-0.23100	-0.23700	-0.24400	-0.39802
44500	-0.22972	-0.23581	-0.24292	-0.39687
44000	-0.22839	-0.23457	-0.24179	-0.39569
43500	-0.22701	-0.23328	-0.24062	-0.39448
43000	-0.22559	-0.23195	-0.23940	-0.39324
42500	-0.22412	-0.23057	-0.23813	-0.39197
42000	-0.22259	-0.22914	-0.23680	-0.39067
41500	-0.22102	-0.22767	-0.23543	-0.38933
41000	-0.21940	-0.22616	-0.23401	-0.38796
40500	-0.21773	-0.22460	-0.23253	-0.38655
40000	-0.21600	-0.22300	-0.23100	-0.38510
39500	-0.21422	-0.22136	-0.22941	-0.38361
39000	-0.21237	-0.21966	-0.22776	-0.38209
38500	-0.21044	-0.21789	-0.22604	-0.38051
38000	-0.20840	-0.21603	-0.22423	-0.37889
37500	-0.20625	-0.21407	-0.22233	-0.37723
37000	-0.20396	-0.21199	-0.22033	-0.37551
36500	-0.20152	-0.20976	-0.21820	-0.37375
36000	-0.19889	-0.20737	-0.21595	-0.37193
35500	-0.19606	-0.20479	-0.21356	-0.37005

Table A.2: $B-V$ colors versus T_{eff} continued.

T_{eff}	B-V(7.5)	B-V(8.0)	B-V(8.5)	B-V(bb)
35000	-0.19300	-0.20200	-0.21100	-0.36811
34500	-0.18968	-0.19897	-0.20827	-0.36611
34000	-0.18611	-0.19570	-0.20536	-0.36405
33500	-0.18228	-0.19219	-0.20226	-0.36192
33000	-0.17818	-0.18844	-0.19898	-0.35972
32500	-0.17381	-0.18445	-0.19550	-0.35745
32000	-0.16918	-0.18022	-0.19182	-0.35509
31500	-0.16429	-0.17576	-0.18794	-0.35265
31000	-0.15913	-0.17107	-0.18384	-0.35013
30500	-0.15370	-0.16614	-0.17953	-0.34751
30000	-0.14800	-0.16100	-0.17500	-0.34480
29500	-0.14204	-0.15563	-0.17024	-0.34198
29000	-0.13582	-0.15006	-0.16527	-0.33906
28500	-0.12937	-0.14428	-0.16008	-0.33603
28000	-0.12268	-0.13830	-0.15469	-0.33287
27500	-0.11579	-0.13213	-0.14912	-0.32958
27000	-0.10871	-0.12580	-0.14337	-0.32616
26500	-0.10147	-0.11930	-0.13747	-0.32260
26000	-0.094080	-0.11265	-0.13142	-0.31888
25500	-0.086580	-0.10588	-0.12526	-0.31500
25000	-0.079000	-0.099000	-0.11900	-0.31094
24500	-0.071367	-0.092028	-0.11267	-0.30670
24000	-0.063667	-0.084959	-0.10625	-0.30226
23500	-0.055877	-0.077780	-0.099743	-0.29761
23000	-0.047969	-0.070476	-0.093124	-0.29273
22500	-0.039912	-0.063031	-0.086378	-0.28761
22000	-0.031671	-0.055429	-0.079487	-0.28223
21500	-0.023206	-0.047648	-0.072428	-0.27656
21000	-0.014474	-0.039666	-0.065180	-0.27060
20500	-0.0054237	-0.031459	-0.057713	-0.26430
20000	0.0040008	-0.023000	-0.050000	-0.25765

Table A.2: $B-V$ colors versus T_{eff} continued.

T_{eff}	B-V(7.5)	B-V(8.0)	B-V(8.5)	B-V(bb)
19500	0.013857	-0.014249	-0.042005	-0.25061
19000	0.024185	-0.0051334	-0.033683	-0.24316
18500	0.035020	0.0044370	-0.024984	-0.23524
18000	0.046404	0.014567	-0.015849	-0.22684
17500	0.058381	0.025376	-0.0062129	-0.21788
17000	0.071001	0.037001	0.0040007	-0.20834
16500	0.084303	0.049586	0.014912	-0.19814
16000	0.098269	0.063221	0.026795	-0.18721
15500	0.11285	0.077995	0.040017	-0.17549
15000	0.12800	0.094001	0.055001	-0.16289
14500	0.14361	0.11128	0.072113	-0.14931
14000	0.15948	0.12959	0.091168	-0.13463
13500	0.17531	0.14857	0.11178	-0.11872
13000	0.19077	0.16774	0.13343	-0.10144
12500	0.20541	0.18651	0.15549	-0.082600
12000	0.21870	0.20417	0.17714	-0.062010
11500	0.22998	0.21978	0.19736	-0.039409
11000	0.23842	0.23220	0.21486	-0.014523
10500	0.24300	0.23999	0.22799	0.012994
10000	0.24400	0.24300	0.23600	0.043548
9500.0	0.24700	0.24700	0.24300	0.077634
9000.0	0.25501	0.25600	0.25300	0.11585
8500.0	0.27200	0.27200	0.26900	0.15893
8000.0	0.29800	0.29800	0.29500	0.20779
7500.0	0.33300	0.33400	0.33100	0.26357
7000.0	0.38000	0.38100	0.38000	0.32771
6500.0	0.43800	0.44000	0.44000	0.40206
6000.0	0.51100	0.51300	0.51400	0.48905
5500.0	0.60100	0.60201	0.60400	0.59191
5000.0	0.71300	0.71400	0.71500	0.71502

Table A.3: $V-I$ colors versus T_{eff} for blackbody energy distribution (bb) and Bergeron *et al*. (1990) $\log(g)=7.5$, 8.0, and 8.5 model DA atmospheres.

T_{eff}	V-I(7.5)	V-I(8.0)	V-I(8.5)	V-I(bb)
50000	-0.36900	-0.36900	-0.36900	-0.41572
49500	-0.36864	-0.36864	-0.36852	-0.41466
49000	-0.36828	-0.36828	-0.36804	-0.41357
48500	-0.36791	-0.36791	-0.36755	-0.41245
48000	-0.36753	-0.36753	-0.36706	-0.41131
47500	-0.36714	-0.36715	-0.36656	-0.41015
47000	-0.36674	-0.36675	-0.36606	-0.40896
46500	-0.36633	-0.36634	-0.36555	-0.40774
46000	-0.36591	-0.36591	-0.36504	-0.40650
45500	-0.36546	-0.36546	-0.36452	-0.40522
45000	-0.36500	-0.36500	-0.36400	-0.40392
44500	-0.36452	-0.36451	-0.36347	-0.40258
44000	-0.36401	-0.36401	-0.36294	-0.40121
43500	-0.36348	-0.36347	-0.36239	-0.39981
43000	-0.36293	-0.36292	-0.36183	-0.39837
42500	-0.36235	-0.36233	-0.36125	-0.39690
42000	-0.36174	-0.36173	-0.36066	-0.39539
41500	-0.36110	-0.36109	-0.36004	-0.39384
41000	-0.36043	-0.36042	-0.35939	-0.39224
40500	-0.35973	-0.35973	-0.35871	-0.39061
40000	-0.35900	-0.35900	-0.35800	-0.38893
39500	-0.35823	-0.35824	-0.35725	-0.38721
39000	-0.35743	-0.35745	-0.35646	-0.38544
38500	-0.35659	-0.35662	-0.35563	-0.38362
38000	-0.35572	-0.35577	-0.35477	-0.38175
37500	-0.35482	-0.35488	-0.35388	-0.37982
37000	-0.35390	-0.35396	-0.35295	-0.37784
36500	-0.35295	-0.35302	-0.35200	-0.37580
36000	-0.35199	-0.35204	-0.35102	-0.37370
35500	-0.35100	-0.35103	-0.35002	-0.37153

Table A.3: $V - I$ colors versus T_{eff} continued.

T_{eff}	V-I(7.5)	V-I(8.0)	V-I(8.5)	V-I(bb)
35000	-0.35000	-0.35000	-0.34900	-0.36930
34500	-0.34898	-0.34894	-0.34796	-0.36700
34000	-0.34794	-0.34783	-0.34689	-0.36462
33500	-0.34685	-0.34666	-0.34576	-0.36217
33000	-0.34569	-0.34542	-0.34455	-0.35963
32500	-0.34445	-0.34407	-0.34323	-0.35701
32000	-0.34309	-0.34261	-0.34178	-0.35430
31500	-0.34160	-0.34099	-0.34017	-0.35150
31000	-0.33994	-0.33921	-0.33835	-0.34860
30500	-0.33808	-0.33722	-0.33631	-0.34560
30000	-0.33600	-0.33500	-0.33400	-0.34248
29500	-0.33365	-0.33252	-0.33138	-0.33925
29000	-0.33105	-0.32978	-0.32846	-0.33590
28500	-0.32820	-0.32679	-0.32527	-0.33242
28000	-0.32510	-0.32357	-0.32180	-0.32880
27500	-0.32176	-0.32011	-0.31810	-0.32504
27000	-0.31820	-0.31644	-0.31419	-0.32113
26500	-0.31443	-0.31258	-0.31008	-0.31705
26000	-0.31046	-0.30854	-0.30583	-0.31280
25500	-0.30631	-0.30433	-0.30145	-0.30837
25000	-0.30200	-0.30000	-0.29700	-0.30374
24500	-0.29755	-0.29555	-0.29251	-0.29890
24000	-0.29297	-0.29100	-0.28798	-0.29384
23500	-0.28827	-0.28635	-0.28340	-0.28854
23000	-0.28346	-0.28159	-0.27877	-0.28298
22500	-0.27854	-0.27673	-0.27406	-0.27715
22000	-0.27354	-0.27177	-0.26928	-0.27102
21500	-0.26846	-0.26671	-0.26440	-0.26458
21000	-0.26333	-0.26156	-0.25940	-0.25779
20500	-0.25817	-0.25632	-0.25428	-0.25063
20000	-0.25300	-0.25100	-0.24900	-0.24308

Table A.3: $V - I$ colors versus T_{eff} continued.

T_{eff}	V-I(7.5)	V-I(8.0)	V-I(8.5)	V-I(bb)
19500	-0.24782	-0.24560	-0.24355	-0.23508
19000	-0.24254	-0.24008	-0.23791	-0.22662
18500	-0.23699	-0.23442	-0.23205	-0.21764
18000	-0.23103	-0.22855	-0.22597	-0.20810
17500	-0.22444	-0.22243	-0.21963	-0.19795
17000	-0.21700	-0.21600	-0.21300	-0.18712
16500	-0.20847	-0.20916	-0.20606	-0.17556
16000	-0.19872	-0.20172	-0.19877	-0.16317
15500	-0.18760	-0.19343	-0.19110	-0.14988
15000	-0.17500	-0.18400	-0.18300	-0.13559
14500	-0.16072	-0.17308	-0.17434	-0.12017
14000	-0.14449	-0.16028	-0.16467	-0.10351
13500	-0.12596	-0.14511	-0.15333	-0.085437
13000	-0.10474	-0.12703	-0.13954	-0.065785
12500	-0.080348	-0.10536	-0.12235	-0.044341
12000	-0.052218	-0.079299	-0.10060	-0.020861
11500	-0.019679	-0.047873	-0.072848	0.0049470
11000	0.018070	-0.0099176	-0.037370	0.033430
10500	0.062004	0.036006	0.0080078	0.065005
10000	0.11200	0.089999	0.064000	0.10018
9500.0	0.16400	0.14700	0.12500	0.13956
9000.0	0.21800	0.20600	0.18900	0.18390
8500.0	0.27400	0.26600	0.25400	0.23416
8000.0	0.33300	0.32800	0.32000	0.29149
7500.0	0.39700	0.39400	0.38900	0.35742
7000.0	0.46900	0.46700	0.46400	0.43385
6500.0	0.55100	0.55000	0.54800	0.52332
6000.0	0.64800	0.64800	0.64700	0.62916
5500.0	0.76601	0.76501	0.76501	0.75589
5000.0	0.91100	0.91100	0.91100	0.90977

Appendix B

Table B.1: 0.6 Gyr isochrone for carbon core white dwarfs with 10^{-4}H over 10^{-2}He atmosphere cooling models of Wood (1994).

$M_\odot$	$\log(L/L_\odot)$	M_{bol}	M_v	$\log(T_{eff})$	$U-B$	$B-V$	$V-I$
0.4	-2.899	11.95	12.52	3.933	-0.644	0.270	0.258
0.5	-2.825	11.76	12.39	3.976	-0.622	0.248	0.151
0.6	-2.779	11.65	12.32	4.014	-0.592	0.241	0.056
0.7	-2.736	11.54	12.25	4.048	-0.577	0.228	-0.027
0.8	-2.689	11.42	12.18	4.083	-0.582	0.201	-0.091
0.9	-2.628	11.27	12.09	4.123	-0.600	0.157	-0.127
1.0	-2.566	11.12	12.00	4.166	-0.632	0.106	-0.173

Table B.2: 0.8 Gyr isochrone for carbon core white dwarfs with 10^{-4}H over 10^{-2}He atmosphere cooling models of Wood (1994).

$M_\odot$	$\log(L/L_\odot)$	M_{bol}	M_v	$\log(T_{eff})$	$U-B$	$B-V$	$V-I$
0.4	-3.086	12.41	12.87	3.888	-0.632	0.317	0.364
0.5	-3.016	12.24	12.73	3.930	-0.644	0.272	0.264
0.6	-2.976	12.14	12.66	3.966	-0.629	0.251	0.177
0.7	-2.937	12.04	12.58	3.999	-0.603	0.243	0.093
0.8	-2.877	11.89	12.48	4.036	-0.580	0.234	-0.001
0.9	-2.807	11.72	12.36	4.079	-0.580	0.204	-0.086
1.0	-2.739	11.55	12.25	4.123	-0.600	0.157	-0.127

Table B.3: 1.0 Gyr isochrone for carbon core white dwarfs with 10^{-4}H over 10^{-2}He atmosphere cooling models of Wood (1994).

$M_{\odot}$	$\log(L/L_{\odot})$	M_{bol}	M_v	$\log(T_{eff})$	$U-B$	$B-V$	$V-I$
0.4	-3.233	12.78	13.17	3.853	-0.590	0.370	0.449
0.5	-3.170	12.62	13.04	3.893	-0.634	0.310	0.351
0.6	-3.132	12.53	12.96	3.928	-0.644	0.274	0.270
0.7	-3.090	12.42	12.87	3.961	-0.633	0.253	0.189
0.8	-3.020	12.25	12.74	4.001	-0.601	0.243	0.087
0.9	-2.943	12.06	12.60	4.045	-0.578	0.230	-0.021
1.0	-2.869	11.87	12.47	4.091	-0.585	0.193	-0.101

Table B.4: 1.2 Gyr isochrone for carbon core white dwarfs with 10^{-4}H over 10^{-2}He atmosphere cooling models of Wood (1994).

$M_{\odot}$	$\log(L/L_{\odot})$	M_{bol}	M_v	$\log(T_{eff})$	$U-B$	$B-V$	$V-I$
0.4	-3.354	13.09	13.46	3.823	-0.539	0.421	0.523
0.5	-3.298	12.94	13.32	3.863	-0.605	0.352	0.424
0.6	-3.259	12.85	13.23	3.897	-0.636	0.306	0.343
0.7	-3.211	12.73	13.13	3.931	-0.644	0.271	0.261
0.8	-3.134	12.54	12.96	3.973	-0.624	0.249	0.159
0.9	-3.053	12.33	12.80	4.018	-0.589	0.241	0.044
1.0	-2.975	12.14	12.65	4.065	-0.577	0.216	-0.062

Table B.5: 1.4 Gyr isochrone for carbon core white dwarfs with 10^{-4}H over 10^{-2}He atmosphere cooling models of Wood (1994).

$M_\odot$	$\log(L/L_\odot)$	M_{bol}	M_v	$\log(T_{eff})$	$U-B$	$B-V$	$V-I$
0.4	-3.458	13.34	13.72	3.799	-0.486	0.469	0.590
0.5	-3.407	13.22	13.59	3.837	-0.565	0.396	0.489
0.6	-3.364	13.11	13.48	3.871	-0.614	0.341	0.404
0.7	-3.311	12.98	13.35	3.907	-0.641	0.295	0.320
0.8	-3.229	12.77	13.16	3.950	-0.638	0.259	0.217
0.9	-3.144	12.56	12.98	3.996	-0.606	0.244	0.102
1.0	-3.064	12.36	12.82	4.043	-0.578	0.231	-0.016

Table B.6: 1.6 Gyr isochrone for carbon core white dwarfs with 10^{-4}H over 10^{-2}He atmosphere cooling models of Wood (1994).

$M_\odot$	$\log(L/L_\odot)$	M_{bol}	M_v	$\log(T_{eff})$	$U-B$	$B-V$	$V-I$
0.4	-3.548	13.57	13.96	3.777	-0.432	0.515	0.651
0.5	-3.501	13.45	13.83	3.814	-0.519	0.439	0.548
0.6	-3.455	13.34	13.71	3.849	-0.584	0.376	0.458
0.7	-3.394	13.19	13.55	3.886	-0.630	0.319	0.368
0.8	-3.309	12.97	13.35	3.930	-0.644	0.272	0.265
0.9	-3.223	12.76	13.15	3.976	-0.622	0.248	0.152
1.0	-3.143	12.56	12.98	4.023	-0.586	0.239	0.031

Table B.7: 1.8 Gyr isochrone for carbon core white dwarfs with 10^{-4}H over 10^{-2}He atmosphere cooling models of Wood (1994).

$M_\odot$	$\log(L/L_\odot)$	M_{bol}	M_v	$\log(T_{eff})$	$U-B$	$B-V$	$V-I$
0.4	-3.627	13.77	14.19	3.759	-0.379	0.559	0.709
0.5	-3.584	13.66	14.07	3.794	-0.474	0.479	0.603
0.6	-3.532	13.53	13.92	3.830	-0.552	0.409	0.506
0.7	-3.465	13.36	13.74	3.869	-0.611	0.344	0.410
0.8	-3.379	13.15	13.52	3.913	-0.644	0.287	0.305
0.9	-3.293	12.93	13.31	3.959	-0.634	0.254	0.195
1.0	-3.214	12.73	13.13	4.006	-0.598	0.242	0.076

Table B.8: 2.0 Gyr isochrone for carbon core white dwarfs with 10^{-4}H over 10^{-2}He atmosphere cooling models of Wood (1994).

$M_\odot$	$\log(L/L_\odot)$	M_{bol}	M_v	$\log(T_{eff})$	$U-B$	$B-V$	$V-I$
0.4	-3.698	13.95	14.39	3.742	-0.330	0.599	0.761
0.5	-3.657	13.84	14.27	3.777	-0.430	0.517	0.653
0.6	-3.600	13.70	14.11	3.813	-0.517	0.441	0.551
0.7	-3.527	13.52	13.90	3.853	-0.591	0.368	0.447
0.8	-3.440	13.30	13.67	3.898	-0.637	0.305	0.341
0.9	-3.356	13.09	13.46	3.943	-0.641	0.263	0.233
1.0	-3.280	12.90	13.28	3.989	-0.611	0.245	0.118

References

Adams, W. S., 1914, *P. A. S. P.*, **26**, 198

Adams, W. S., 1915, *P. A. S. P.*, **27**, 236.

Allen, C. W., 1973, *Astrophysical Quantities, Third Ed.*, (the Athlone Press: London).

Anthony–Twarog, B. J., 1982, *Ap. J.*, **255**, 245.

Anthony–Twarog, B. J., 1984, *A. J.*, **89**, 276.

Armandroff, T. E., 1993, In *The Globular Cluster–Galaxy Connection*, ed G. H. Smith and J. P. Brodie, A. S. P. Conf. Ser., **48**, p48.

Armandroff, T. E., 1994, In *The Future Utilization of Schmidt Telescopes: I. A. U. Colloquium 148*, in press.

Baade, W., 1944, *Ap. J.*, **100**, 137.

Beauchamp, A. and Wesemael, F., 1994, In *Proceedings from The 9th European Workshop on White Dwarfs*, SpingerVerlag: Berlin, inpress.

Bencivenni, D., Caputo, F., Manteiga, M., and Quarta, M. L., 1991, *Ap. J.*, **380**, 484.

Bessell, M. S., 1990, *P. A. S. P.*, **102**, 1181.

Bessell, M. S., 1987, *P. A> S. P.*, **99**, 642.

Bergbusch, P. A., and VandenBerg, D. A., 1992, *Ap. J. Supp. Ser.*, **81**, 163.

Bergeron, P., Saffer, R. A., and Liebert, J., 1992, *Ap. J.*, **394**, 228.

Bergeron, P., Saumon, D., and Wesemael, F., 1994, *Ap. J.*, in press.

Bergeron, P., Wesemael, F., and Fontaine, G., 1991, *Ap. J.*, **367**, 253.

Berman, B. G., and Suchov, *A. A.*, 1991, A. S. S., **184**, 169.

Bolte, M., 1992, *P. A. S. P.*, **104**, 794.

Bowers, R. L., and Deeming, T., 1984, *Stars*, Jones and Bartlette Publishers: Boston.

Boyle, B. J., 1989, *M. N. R. A. S.*, **240**, 533.

Butcher, H. R., 1987, *Nature*, **328**, 127.

Chaboyer, B., Sarajedini, A., and Demarque, P., 1992, *Ap. J.*, **394**, 515.

Chabrier, G., Segretain, L., Hernanz, M., Isern, J., Mochkovitch, R., 1993, In *White Dwarfs: Advances in Observation and Theory*, ed M. A. Barstow, Kluwer Achademic Press: Dordrecht, p115.

Chandrasekhar, S., 1939, *An Introduction to the Study of Stellar Structure*, University of Chicago Press: Chicago.

Chandrasekhar, S., 1984, *Rev. Modern Physics*, **56**, 137.

Clark, J. P. A., and McClure, R. D., 1979, *P. A. S. P.*, **91**, 507.

Claver. C. F., Cornell, M. E., and Opal, C. B., 1990, In *Instrumentation in Astronomy VII*, ed. D. Crawford, SPIE Proceedings, **1235**, p253.

Clayton, D. D., 1968, 1983, *Principles of Stellar Evolution and Nucleosynthesis*, The University of Chicago Press: Chicago.

Clemens, J. C., Ph. D. Thesis: *The Origin and Evolution of the White Dwarf Stars*, The University of Texas at Austin: Austin Texas.

Corbally, C. J., and Garison, R. F., 1986, *A. J.*, **92**, 90.

Cox, J. P., and Giuli, R. T., 1968, *Principles of Stellar Structure*, Gordon and Breach: New York.

Crawford, D. L., and Barnes, J. V., 1969, *A. J.*, **74**, 818.

D' Antona, F., and Mazzitelli, I., 1978, *A. A.*, **66**, 453.

D'Antona, F., and Mazzitelli, I., 1990, *Ann. Rev. Ast. Astrophys.*, **28**, 139.

Da Costa, G. S., Armandroff, T. E., and Norris, J. E., 1992, *A. J.*, **104**, 154.

Dahn, C. C., Hinzen, P. M., Liebert, J., Stockman, H. S., and Spinrad, H., 1977, *Ap. J.*, **219**, 979.

Deeming, T. J., 1960, *M. N. R. A. S.*, **121**, 52.

Demarque, P., Green, E. M., and Guenther, D. B., 1992, *A. J.*, **103**, 151.

Dorman, B., Rood, R. T., and O'Connell, R. W., 1993, *Ap. J.*, **419**, 569.

Downes, R. A., 1986, *Ap. J. Supp. Ser.*, **61**, 941.

Eddington, A. S., 1926, *The Internal Constitution of the Stars*, Cambridge University Press: Cambridge, England.

Eggen, O. J., Lynden–Bell, D., and Sandage, A. R., 1962, *Ap. J.*, **163**, 748.

Eggen, O. J., and Greenstein, J. L., 1965, *Ap. J.*, **141**, 83.

Eggen, O. J., and Greenstein, J. L., 1967, *Ap. J.*, **150**, 927.

Evans, D. W., 1989, *A. A. Supp. Ser.*, **78**, 249.

Evans, D. W., 1992, *M. N. R. A. S.*, **255**, 521.

Felton, J. E., 1976, *Ap. J.*, **207**, 700.

Fenkart, R., 1989, *A. A. Supp. Ser.*, **81**, 187.

Fleming, T. A., Liebert, J., and green, R. F., 1986, *Ap. J.*, **308**, 176.

Fowler, R. H., 1926, *M. N. R. A. S.*, **87**, 114.

Fowler, W. A., 1987, *Q. J. R. A. S.*, **28**, 87.

Fowler, W. A., Caughlan, G. R., and Zimmerman, B. A., 1975, *Ann. Rev. Ast. Astrophys.*, **13**, 69.

Fowler, W. A., and Meisl, C. C., 1986, In *Cosmologi Processes*, eds. W. D. Arnett, C. J. Hansen, J. W. Truran, and S. Tsuruta (Utrech: VNU Science Press).

Freedman, W. L. *et al*., 1994, *nature*, **371**, 757.

Gafney, N. and Sneeden, C., 1991, *McDonald Observatory Internal Memorandum*, Quantitative Estimates of McDonald Observatory Seeing.

Geary, J. C., Torres, G., Latham, D. W., and Wyatt, W. F., 1990, In *CCDs in Astronomy*, ed. G. H. Jacoby, A. S. P. Conf. Ser., **8**, p. 43.

Giclas, H. L., 1971, In *I. A. U. Symposion 42, White Dwarfs*, ed. W. Luyten, p. 24.

Gilmore, G., and Reid, I. N., 1983, *M. N. R. A. S.*, **202**, 1025.

Gilmore, G., and Wyse, R. F. G., 1985, *A. J.*, **90**, 2015.

Gilmore, G., Wyse, R. F. G., and Kuijken, K., 1989, *Ann. Rev. Ast. Astrophys.*, **27**, 555.

Gough, D. O., 1993, In *Inside the Stars: IAU Colloquium 137*, eds W. W. Weiss and A. Baglin, ASP Conf. Series, **40**, 767.

Green, R. F., 1980, *Ap. J.*, **238**, 685.

Green, R. F., Schmidt, M., and Liebert, J., 1986, *Ap. J. Supp. Ser.*, **61**, 305.

Greenstein, J. L., 1971, In *IAU Symposium 42, White Dwarfs*, ed. W. Luyten, p. 46.

Greenstein, J. L., 1976, *A. J.*, **77**, 144.

Greenstein, J. L., 1984, *Ap. J.*, **276**, 602.

Guinan, E. F., and Smith., G. H., 1984, *P. A. S. P.*, **96**, 354.

Hartwick, F. D. A., Cowley, A. P., and Mould, J. R., 1984, *ap. J.*, **286**, 269.

Hayes, D. S., 1985, In *IAU Symposium 111: Calibration of Fundemental Stellar Quantities*, eds. D. S. Hayes, L. E. Pasinetti, and A. G. D. Phillip, Dordrecht: D. Reidel Pub. Co., p. 225.

Hernanz, M., Garcia-berrro, E., Isern, I., Mochlovitch, R., Segretain, L., and Chabrier, G., 1994, *Ap. J.*, **434**, 652.

Hesser, J. E., 1993, In *The Globular Cluster–Galaxy Connection*, ed G. H. Smith and J. P. Brodie, A. S. P. Conf. Ser., **48**, p1.

Iben, Jr., I., 1967, *Ap. J.*, **147**, 624.

Iben, Jr., I., 1994, In *Proceedings from The 9th European Workshop on White Dwarfs*, Springer–Verlag: Berlin, in press.

Iben, Jr., I., and Laughlin, G., 1989, *Ap. J.*, **341**, 312.

Iben, Jr., I., and Renzini, A, 1984, *Ann. Rev. Ast. Astrophys.*, **21**, 271.

Ishida, K., Mikami, T., Noguchi, T., and Maehara, H., 1982, *P. A. S. P.*, **34**, 381.

Jacoby, G. H., 1994, *Nature*, **371**, 741.

Janes, K., 1993, In*The Minesota Lectures on the Structure and Dynamics of the Milky Way* , Ed. R. M. Humphreys, A. S. P. Conf. Ser., **39**, 35.

Jarvis, J. F., and Tyson, J. A., 1981, *A. J.*, **86**, 476.

Johnson, H. L., 1952, *Ap. J.*, **116**, 640.

Jones, B. F., and Cudworth, K., 1983, *A. J.*, **88**, 215.

Jones, B. F., and Stauffer, J. R., 1991, *A. J.*, **102**, 1080.

Klein–Wassink, K. N., 1927, *Pub. Kaptayn Ast. Lab.*, No. **41**.

Koester, D., and Reimers, D., 1989, *A. A.*, **223**, 326.

Koester, D., and Reimers, D., 1985, *A. A.*, **153**, 260.

Koester, D., and Reimers, D., 1981, *A. A.*, **99**, 8.

Kondo, M., Watanabe, E., Yutani, M., and Noguchi, T., 1982, *P. A. S. J.*, **34**, 541.

Kovets, A., and Shaviv, G., 1976, *A. A.*, **52**, 403.

Kujiken, K., and Gilmore, G., 1989, *M. N. R. A. S.*, **239**, 571.

Lamb, D. Q., and Van Horn, H. M., 1975, *Ap. J.*, **200**, 306.

Landolt, A. U., 1983, *A. J.*, **88**, 439.

Landolt, A. U., 1992, *A. J.*, **104**, 340.

Larson, R. B., 1976, *M. N. R A. S.*, **176**, 31.

Larson, R. B., 1990, *P. A. S. P.*, **102**, 709.

Lesser, M. P., 1994, *W.W.W. URL:* ftp://ftp/frodo.as.arizona.edu/pub/ccdlab.html.

Liebert, J., 1979, In *IAU Colloquim No. 53: WHite dwarfs and Variable Degenerate Stars*, eds. H. M. Vann Horn and V. Weidemann, University of Rochester Press: Rochester, p. 146.

Liebert, J., 1980, *Ann. Rev. Ast. Astrophys.*, **18**, 363.

Liebert, J., 1990, Private communication.

Liebert, J., Dahn, C. C., and Monet, D. G., 1988, *Ap. J.*, **332**, 891.

Liebert, J., Dahn, C. C., and Monet, D. G., 1989, In *I. A. U. Colloquium #114: White Dwarfs*, ed. G. Wegner, Springer–Verlag: Berlin, p15.

Liebert, J., and Sion, E. M., 1995, In *The MK Process at 50 Years*, A. S. P. Conf. Ser., **60**, p64.

Liebert, J., Wesemael, F., Hansen, C. J., Fontaine, G., Shipman, H. L., Sion, E. M., Winget, D. E., and Green, R. F., 1986, *Ap. J.*, **309**, 241.

Luytern, W. J., 1958, *Vistas in Astronomomy*, **2**, 1048.

Luyten, W. J., 1962, *A Search for Faint Blue Stars*, No. 31, University of Minnesota Press: Minneapolis.

Luyten, W. J., 1975, *Proper Motion Survey with the 48 inch Schmidt Telescope*, XL, University of MInnesota Press: Minneapolis.

Luyten, W. J., 1979, *LHS Catalog* (2nd edition; Minneapolis: University of Minnesota).

Mackay, C. D., 1986, *Ann. Rev. Ast. Astrophys.*, **24**, 255.

Marshak, R. E., 1940, *Ap. J.*, **92**, 321.

Massey, P., 1992, *A Users Guide to CCD Reductions with IRAF*, National Optical Astronomy Observatories Pub.: Tucson.

Massey, P., and Davis, L. E., 1992, *A Users Guide to Stellar CCD Photometry with IRAF*, Notional Optical Astronomy Observatories Pub.: Tucson.

Mather, J. C. *et al.*, 1990, *Ap. J. Let.*, **354**, L37.

Mazzitelli, I., 1989, In *I. A. U. Colloquium #114: White Dwarfs*, ed. G Wegner, Springer–Verlag: Berlin, p341.

Mermilliod, J. C., Weis, E. W., Duquennoy, A., and Mayor, M., 1990, *A. A.*, **235**, 114.

Mestel, L., 1952, *M. N. R. A. S.*, **112**, 583.

Mestel, L., and Ruderman, M. A., 1967, *M. N. R. A. S.*, **209**, 511.

Meynet, G., Mermiliod, J. C., and Maeder, A., 1993, *A. A., SUpp. Ser.*, **98**, 477.

Mochkovitch, R., Garcia–Berro, E., Hernanz, M., Isern, I., and Panis, J. F., 1990, *A. A.*, **233**, 456.

Monet, D. G., Dahn, C. C., Veba, F. J., Harris, H. C., Pier, J. R., Luginbuhl, C. B., and Ables, H. D., 1992, *A. J.*, **103**, 638.

Norris, J, and Green, E. M., 1989, *Ap. J.*, **337**, 272.

O'Donoghue, D., Kilkenny, D., and Stonie, R. S., 1993, In *White Dwarfs: Advances in Observation and Theory*, ed. M. A. Barstow, p39.

Oswalt, T. D., and Smith, J. A., 1994, In *Proceedings from The 9th European Workshop on White Dwarfs*, SpingerVerlag: Berlin, inpress.

Peebles, P. J. E., Schramm, D. N., Turner, E. L., and Kron, R. G., 1991, *Nature*, **352**, 769.

Pesch, P., and Sanduleak, N., 1983, *Ap. J. Supp.*, **51**, 171.

Pierce, M. J. *et al.*, 1994, *Nature*, **371**, 385.

Renzini, A., 1986, In *Stellar Populations* , eds. C. A. Norman, A. Renzini, and M Tosi, p. 213.

Reimers, D., and Koester, D., 1988, *A. A.*, **202**, 77.

Reimers, D., and Koester, D., 1988, *A. A.*, **116**, 341.

Rich, R. M., 1988, *A. J.*, **95**, 828.

Rich, R. M., 1993, A. S. P. Conf. Ser., **49**, *Galaxy Evolution: The Mily Way Perspective* ed. S. R. Majewski, p65.

Romanishin, W., and Angel, J. R. P., 1980, *Ap. J.*, **235**, 992.

Rowan–Robinson, M., 1977, *Cosmology* (Oxford Physics Series; No. 15), Oxford University Press: Oxford, Great Britain.

Rowan–Robinson, M., 1988, *Space Science Reviews*, **48**, 1.

Ruiz, M. T., 1994, In *Proceedings from The 9th European Workshop on White Dwarfs*, Springer–Verlag: Berlin, in press.

Ruiz, M. T., Anguita, C., 1993, *A. J.*, **105**, 614.

Sandage, A., 1990, *J. R. A. S. C.*, **84**, 70.

Sanduleak, N., and Pesch, P., 1984, *Ap. J. Supp. Ser.*, **55**, 517.

Sarajedini, A., and Demarque, P., 1990, *Ap. J.*, **365**, 219.

Schmidt, M., 1959, *Ap. J.*, **129**, 243.

Schmidt, M., 1975, *Ap. J.*, **202**, 22.

Schramm, D. N., 1990, In *Astrophysical Ages and Dating Methods*, eds. E. Vangioni–Flam, M. Cassé, J. Audouze, and J. Tran Thanh Van, p365.

Schwan, H., 1991, *A. A.*, **243**, 386.

Schwartzschild, M., 1958, *Structure and Evolution of the Stars*, Princeton University Press: Princeton.

Searle, L., and Zinn, R., 1978, *Ap. J.*, **225**, 357.

Segretrain, L., Chabrier, G., Hernanz, M., Garcia–Berro, E., and Mochlovitch, R., 1994, *Ap. J.*, **434**, 641.

Sion, E. M., and Liebert, J., 1977, *Ap. J.*, **213**, 468.

Sion, E. M., Greenstein, J. L., Landstreet, J., Liebert, J., Shipman, H. L., and Wegner, G., 1983, *Ap J.*, **269**, 253.

Slattery, W. L., Doolen, G. D., and DeWitt, H. E., 1982, *Phys. Rev.*, **26**, 2255.

Stetson, P. B., 1987, *P. A. S. P.*, **99**, 191.

Taff, L. G., 1974, *A. J.*, **79**, 1280.

Takato, N., Akoi, T., Ichikawa, S., and Iye, M., 1990, In *Astronomical Instrumentation VII*, ed. D. Crawford, SPIE Proceedings, **1235**, p242.

Tammann, G. A., 1988, A. S. P. Conf. Ser., **4**,*The Extragalactic Distance Scale* eds. S. van den Berg and C. J. Pritchet, p282.

Tanamaha, C. M., Silk, J., Wood, M. A., and Winget, D. E., 1990, *Ap. J.*, **358**, 164.

Terndrup, D. M., 1988, *A. J.*, **96**, 884.

Trammell, S. R., 1994, Ph. D. Thesis, University of Texas at Austin: Austin, Texas.

Tully, R. B., 1990, In *Astrophysical Ages and Dating Methods*, Ed. E. Vangioni–Flam, M. Cassé, J. Audouze, and J. Tran Thanh Van, p3.

Upgren, A. R., Weis, E. W., and deLuca, E. E., 1979, *A. J.*, **84**, 1586.

Valdes, F., 1982, In *Instrumentation in Astronomy IV*, SPIE Proceedings, **331**.

VandenBerg, D. A., 1985, *Ap. J. Supp. Ser.*, **58**, 711.

VandenBerg, D. A., 1988, In *Calibration of Stellar Ages*, ed A. G. D. Phillip, p117, L. Davis Press: Schenectady, N.Y..

VandenBerg, D. A., 1990, *A. J.*, **100**, 445.

VandenBerg, D. A., 1991, In *The Formation and Evolution of Star Clusters*, ed. K. A. Janes, A. S. P. Conf. Sers., **13**, p183.

VandenBerg, D. A., 1992, *Ap. J.*, **391**, 685.

VandenBerg, D. A., 1991, In *The Formation and Evolution of Star Clusters*, Ed. K. A. Janes, A. S. P. Conf. Ser., **13**, 183.

van den Berg, S., 1989, *A. A. Rev.*, **1**, 111.

Van Horn, H. M., 1971, In *I. A. U. Symposium #42: White Dwarfs*, ed. W. Luyten, Reidel: Dordrecht., p97.

von Hippel, T., 1994, In *Proceedings from The 9th European Workshop on White Dwarfs*, Springer–Verlag: Berlin, in press.

Wagner, M. R., Sion, E. M., Liebert, J., Starrfield, S. G., and Zotov, N., 1986, *P. A. S. P.*, **98**, 552.

Wasserburg, G. J., Papanastassiou, D. A., Tera, F., and Hunkel, J. C., 1977, *Phil. Trans. R. Soc. Lond.*, **285**, 7.

Wegner, G., 1983, *Ap. J.*, **268**, 282.

Weidemann, V., 1967, *Z. f. Astrophysik*, **67**, 286.

Weidemann, V., 1971, In *I. A. U. Symposium #42: White Dwarfs*, ed. W. Luyten, Reidel: Dordrecht., p81.

Weidemann, V., 1990, *Ann. Rev. Ast. Astrophys.*, **28**, 103.

Weidemann, V., and Koester, D., 1983, *A. A.*, **121**, 77.

Weidemann, V., and Koester, D., 1984, *A. A.*, **132**, 195.

Weidemann, V., Jordan, S., Iben Jr., I., and Casertano, S., 1992, *A. J.*, **104**, 1876.

Winget D. E., Hansen, C. J., Liebert, J., Van Horn, H. M., Fontaine, G., Nather, R. E., Kepler, S. O., and Lamb, D. Q., 1987, *Ap. J. Let.*, **315**, L77.

Wright, E. L., *et al*., 1992, *Ap. J. Let.*, **396**, L13.

Wood, M. A., 1994, In *Proceedings from The 9th European Workshop on White Dwarfs*, Springer–Verlag: Berlin, in press.

Wood, M. A., 1992, *Ap. J.*, **386**, 539.

Wood, M. A., 1990, Ph. D. thesis, University of Texas: *Astero–Archaeology: Reading The Galactic History Recorded in the White Dwarf Stars*.

Vita

Charles Frederick Claver was born in Berkeley, California on 9 November 1962 to Jack Frederick Claver and Paulette Lucile Dodge Claver. He graduated from Ygnacio Valley High School in Concord, California in May 1981, and entered Diablo Valley Community College in the Fall of the same year. In the Fall of 1984 he transferred his education to the University of Texas at Austin, Texas. Prior to his moving to Texas he gained experience in industry as an optical fabrication technician, a professional photographer, and as a landscape architect. He graduated in the Spring of 1987 with a Bachelor of Arts in Astronomy with minors in Physics and Mathematics. While an undergraduate at the University of Texas, he began his present research in white dwarf stars and their ages. With this in mind, he stayed on after graduation and in the Fall of 1987 entered into graduate school in the Department of Astronomy of the University of Texas at Austin. While there, he worked as both a Research Assistant and Teaching Assistant. His dissertation research was supported by grants from the National Science Foundation through his thesis advisor R. E. Nather. He has made a major contribution to the research capabilities of McDonald Observatory through the construction of a significant piece of instrumentation. In the Fall of 1994 he was awarded the Benfield Scholarship for his dissertation work. He has happily become acquainted with Beth Clark and very much enjoys making orchids bloom, communicating with the world through amateur radio, and finding solace with his cat friend Denali.

Permanent address: 70 Big Bear Place N. W.
Issaquah, Washington 98027

This dissertation was typed by Charles F. Claver.